

Studies of materials for use in future
interferometric gravitational wave detectors

Iain William Martin

Department of Physics and Astronomy,
University of Glasgow

Presented as a thesis for the degree of Ph.D.
in the University of Glasgow, University Avenue,
Glasgow G12 8QQ.

February 14, 2009

Contents

Contents	i
List of Figures	vi
List of Tables	xvii
Acknowledgements	xviii
Preface	xx
Summary	xxii
1 Gravitational wave detection	1
1.1 Introduction	1
1.2 The nature of gravitational radiation	3
1.3 Sources of Gravitational Waves	4
1.3.1 Periodic sources	4
1.3.2 Burst sources	7
1.3.3 Stochastic gravitational wave background	8
1.4 Gravitational wave detection	9
1.4.1 Resonant bar detectors	9
1.4.2 Interferometric detectors	12
1.5 Limits to the sensitivity of long-baseline detectors	13
1.5.1 Gravitational gradient noise	14
1.5.2 Thermal noise	14
1.5.3 Seismic noise	15
1.5.4 Photoelectron shot noise	16
1.5.5 Radiation pressure noise	17
1.5.6 The Standard Quantum Limit	18

1.6	Interferometric techniques	20
1.6.1	Delay line interferometers	20
1.6.2	Faby-Perot arm cavities	21
1.6.3	Power recycling	22
1.6.4	Signal recycling	22
1.7	Current interferometric detectors	24
1.7.1	Second generation detectors	28
1.7.2	Future detectors	29
1.8	Conclusion	30
2	Thermal noise in gravitational wave detectors	31
2.1	Introduction	31
2.1.1	Brownian motion	31
2.1.2	The Fluctuation-Dissipation Theorem	32
2.2	Sources of mechanical dissipation	35
2.2.1	Dissipation from internal friction in materials	35
2.2.2	Harmonic oscillator with internal friction	36
2.2.3	The form of internal dissipation - Debye theory	38
2.2.4	Thermal noise associated with a single resonant mode	39
2.3	Relationship between mechanical loss and the quality factor	42
2.4	Thermoelastic damping	44
2.5	Thermal noise in a multi-resonance system	46
2.5.1	Inhomogeneous loss and coating thermal noise	48
2.5.1.1	Calculation of coating thermal noise	49
2.6	Thermoelastic noise	51
2.6.1	Coating thermoelastic noise	52
2.7	Suspension thermal noise sources	53
2.7.1	Pendulum mode	53
2.7.2	Violin modes of the suspension fibres	55
2.8	Total thermal noise in a detector mirror	55
2.9	Conclusion	56

3	Influence of temperature on the settling time of hydroxide-catalysis bonds	58
3.1	Introduction	58
3.2	The chemistry of hydroxide-catalysis bonding	61
3.3	Sample preparation	63
3.4	Variation of settling time with temperature	64
3.4.1	Experimental setup	64
3.4.2	Results	67
3.4.3	Analysis	67
3.5	Conclusion	71
4	Loss measurements using silica cantilevers at room temperature	72
4.1	Introduction	72
4.2	Mechanical loss of silica ribbons	73
4.2.1	Measuring mechanical loss	74
4.2.2	Experimental method	74
4.2.3	Semi-empirical model for intrinsic loss in fused silica	77
4.2.4	Mechanical loss of ribbons with ‘necks’	78
4.2.5	Gas damping	80
4.2.6	Welded silica ribbon	81
4.2.7	Coating loss measurements using silica cantilevers	84
4.3	Conductive coatings for charge mitigation in gravitational wave detectors	85
4.3.1	Charging issues in gravitational wave detectors	86
4.3.2	Charge mitigation	87
4.3.3	Experimental technique	87
4.3.4	Results	88
4.3.4.1	Optical requirements and absorption measurements	89
4.3.4.2	Mechanical loss measurements of SnO coatings	89
4.3.5	Coating loss analysis	90

4.3.6	Tin oxide coating loss results	93
4.3.7	Thermal noise modelling	94
4.3.8	Conclusion	98
4.4	Dissipation in optical coatings	98
4.4.1	Reflective dielectric coatings	99
4.4.1.1	Coating production	101
4.4.2	Mechanical dissipation in coating materials	101
4.4.2.1	Previous measurements of coating dissipation	102
4.4.3	Coating loss measurements using silica cantilever sub- strates	103
4.4.4	Coating loss measurements	107
4.5	Conclusion	110
5	Temperature dependence of the mechanical dissipation in tan- talum pentoxide coatings	112
5.1	Introduction	112
5.1.1	Measurements of the temperature dependence of coating dissipation	114
5.2	Initial measurements of the loss of doped tantalum pentoxide	116
5.2.1	Sample preparation	116
5.2.2	Experimental method	119
5.2.2.1	Readout system	120
5.2.2.2	Thermoelastic loss as a function of temperature	123
5.2.3	Results for cantilever A	125
5.2.3.1	Room temperature results	125
5.2.3.2	Measured loss as a function of temperature	126
5.2.4	Coating loss results for cantilever A	127
5.2.5	Coating loss results for cantilever B	131
5.2.6	Conclusion	134
5.3	Dissipation of a TiO ₂ -doped Ta ₂ O ₅ coating between 7 K and 300 K	135

5.3.1	Sample preparation	135
5.3.2	Experimental method	137
5.4	Results	137
5.4.1	Calculation of the coating loss	141
5.5	Analysis and Interpretation	141
5.5.1	Possible interpretation	146
5.6	Undoped tantala loss measurements	149
5.6.1	Experimental setup for cooling with liquid helium	149
5.6.2	Loss measurements of undoped tantala	151
5.6.3	Arrhenius plot analysis	156
5.6.4	Analysis of the distribution of potential battier heights	159
5.6.5	Comparison of tantala coatings at room temperature	163
5.7	The effect of heat treatment	164
5.8	Conclusions	170
6	Temperature dependence of the mechanical dissipation in silica coatings	173
6.1	Introduction	173
6.2	Coating thermoelastic loss	174
6.3	Results	176
6.4	Coating loss	182
6.4.1	Dissipation peak analysis	186
6.4.2	Silica coating loss above 200 K	187
6.5	Discussion - low temperature loss in silica	190
6.6	Multi-layer coating loss calculation	192
6.6.1	The mechanical loss of a multi-layer coating	193
6.6.2	Coating thermoelastic loss	196
6.6.3	Discussion	198
6.7	Conclusion	199
7	Conclusions	201
	Bibliography	205

List of Figures

1.1	<i>The effect of a gravitational wave with (a) the h_+ and (b) h_\times polarisation, incident normal to the page, on a ring of test particles.</i>	3
1.2	<i>A schematic diagram of a simple Michelson interferometer, consisting of a laser, beam splitter and two end mirrors.</i>	13
1.3	<i>Schematic diagram of two possible layouts for a delay line interferometer: (a) shows a folded arm scheme, while (b) illustrates a scheme in which the laser beam is reflected along each arm multiple times.</i>	21
1.4	<i>A schematic diagram of a Fabry-Perot interferometer, which uses Fabry-Perot cavities in each arm. The inner mirrors are partially transmissive to allow light to enter, and leave, the cavity.</i>	21
1.5	<i>A schematic diagram of a Michelson interferometer with a power recycling mirror at the input port, forming an optical cavity with the interferometer.</i>	23
1.6	<i>A schematic diagram of a Michelson interferometer with a signal recycling mirror at the output port. This mirror forms an optical cavity with the interferometer and allows the peak sensitivity to be tuned to specific frequency ranges.</i>	24
1.7	<i>The VIRGO interferometer at Cascina, Italy. Both 3 km long arms of the detector can be seen, meeting at the central station (right hand side) which houses the input and output optics. . . .</i>	24

1.8	<i>Left: A view along one 600 m long arm of the GEO 600 detector, with the end station housing the end test mass visible in the background. Right: A GEO 600 suspension, consisting of a triple pendulum, with a monolithic silica lowest stage.</i>	25
1.9	<i>The design sensitivity of GEO 600, showing the various noise curves for operation with signal recycling at 250 Hz de-tuning.</i>	26
1.10	<i>The typical amplitude strain sensitivity of GEO 600 in each of the science runs between 2002 and 2007.</i>	27
2.1	<i>(a) A schematic diagram of a mechanical oscillator with a complex spring constant $k(1 + i\phi)$. (b) A schematic diagram representing a standard anelastic solid, with an ideal spring connected in parallel with a spring-dashpot combination, where k_1 and k_2 are spring constants and α is the impedance of the dashpot.</i>	37
2.2	<i>Thermal noise displacement spectra for two mechanical oscillators each of $f_0=1$ kHz, $m =20$ kg at $T =290$ K and having differing mechanical loss. The solid, red line shows the thermal noise for a loss of $\phi = 1 \times 10^{-9}$ while the black, dashed line is for $\phi = 1 \times 10^{-7}$. The lower loss material has lower off-resonance thermal noise, as more of the thermal motion is concentrated close to the resonant frequency.</i>	42
2.3	<i>A schematic diagram of a bending mode of a rectangular cross-section bar.</i>	45
2.4	<i>Calculated levels of Brownian and thermoelastic thermal noise in a single suspended fused silica mirror, in an interferometer with a laser beam of radius $r_0 = 3.9$ cm, assuming a test mass loss of 5×10^{-9} and an ion-beam sputtered coating formed from alternating multi-layers of SiO_2 and Ta_2O_5.</i>	57
3.1	<i>The planned orbit of the three satellites forming the LISA gravitational wave detector.</i>	59

3.2	<i>The engineering model of the Lisa Pathfinder optical bench, which utilises fused silica optical components bonded to a Zerodur base plate.</i>	60
3.3	<i>A simplified diagram showing the surface of fused silica in a fully-hydrated state after cleaning. Note that the surface consists of OH groups attached to silicon atoms.</i>	62
3.4	<i>A simplified diagram of the etching stage of the bonding reaction. Hydroxide ions can etch into the surface of the silica by forming weak bonds with silicon atoms, weakening the Si-O bonds (a) resulting in silicate ions being released into solution (b).</i>	63
3.5	<i>Once the pH of the solution between the silica components has dropped below 11, the liberated $\text{Si}(\text{OH})_5^-$ molecules dissociate to form SiOH_4, which can hydrolyse to form polymer chains, eventually linking the two silica surfaces.</i>	64
3.6	<i>The mechanical excitation system developed to gently shake the upper silica block during bonding. The holder for the silica block was supported on one side by a rigid connection to a loudspeaker and on the other side by an elastic connection to a rigid clamp. A ‘flag’ attached to the top of the holder was used to monitor the motion of the block throughout the bonding process.</i>	65
3.7	<i>Schematic diagram of the temperature controlled glove box in which the experiment was carried out. The glove box was 1 m long, 40 cm deep and 50 cm high.</i>	66
3.8	<i>Typical plot of the measured oscillation amplitude of the upper silica block as a function of time during bonding. The point where the bond set can be clearly seen at approximately 360 seconds.</i>	68
3.9	<i>Plot of the measured settling time as a function of temperature for hydroxide-catalysis bonds made using 0.1 mol l^{-1} KOH solution, with an exponential fit.</i>	69

3.10	<i>Arrhenius plot of the settling time data, showing the logarithm of the settling time as a function of the reciprocal of the temperature, with linear fit excluding the room temperature measurement.</i>	70
4.1	<i>A schematic diagram of a silica ribbon (not to scale).</i>	73
4.2	<i>A schematic diagram of the experimental apparatus used to measure the mechanical loss of cantilever samples - not to scale.</i>	75
4.3	<i>A schematic diagram of the split photodiode arrangement used to measure the amplitude of oscillation of a cantilever.</i>	76
4.4	<i>A ringdown measurement for the the third bending mode at 1051 Hz. A sampling rate of 15 Hz was used, and the mechanical loss calculated from the fitted exponential decay constant.</i>	76
4.5	<i>(a) The flame-pulled ribbon section in the clamp. (b) The laser-pulled ribbon in the clamp.</i>	79
4.6	<i>Frequency dependence of the mechanical loss of a ribbon with a short neck fabricated with a laser pulling machine, compared to that of a ribbon with a longer neck fabricated with a flame pulling machine. Also shown are the losses predicted by Penn's model for both samples.</i>	80
4.7	<i>Left: Photograph of CO₂ laser welding. Right: Schematic diagram of laser welding apparatus.</i>	82
4.8	<i>(a) Photograph of the cantilever immediately after welding. (b) Photograph of the welded cantilever in the clamp.</i>	83
4.9	<i>Frequency dependence of the mechanical loss of a ribbon section welded to a silica slide, compared to that of a similar ribbon clamped at the neck region. Also shown are the losses predicted by Penn's model for both samples.</i>	84
4.10	<i>Microscope images of the welded silica cantilever.</i>	85
4.11	<i>Plot of the measured loss of four modes of sample 1 before and after coating with 25 nm of SnO.</i>	91

4.12	<i>A beam of thickness a and width b, with a thin coating of thickness t applied to one face, bent into an arc of radius R.</i>	92
4.13	<i>Plot of the calculated coating loss for each of the three SnO coatings studied.</i>	94
4.14	<i>The mechanical loss measured as a function of coating thickness, with a linear fit to the data. Each point indicates the mean loss measured for several modes of a sample.</i>	95
4.15	<i>(a) Microscope images of the surface of sample 3 after coating with tin oxide. (b) Higher magnification image of the tin oxide coating showing evidence of the formation of large crystals.</i> . . .	96
4.16	<i>Calculated levels of the Brownian thermal noise associated with a 100 nm and a 4 nm thick SnO coating on a fused silica mirror illuminated by a laser beam of radius $r_0=3.9$ cm, compared to the thermal noise arising from a multilayer HR coating.</i>	97
4.17	<i>A schematic diagram of a multi-layer reflective coating, composed of alternating layers of a high refractive index (n_H) and a low refractive index (n_L).</i>	100
4.18	<i>A schematic diagram of a simple ion-beam sputtering chamber.</i> .	100
4.19	<i>Plot of the lowest losses measured in the 7 welded silica membranes, compared with the losses measured in a welded ribbon section.</i>	105
4.20	<i>Plot of the coating loss factors for LMA F5** and F5*** tantala, measured using silica membrane substrates welded to silica clamping blocks.</i>	109
4.21	<i>Plot of the coating loss factors for undoped tantala, LMA F5* doped tantala and silica coatings, measured using unwelded membranes in the clamp developed by LMA.</i>	109
5.1	<i>Schematic diagram of cantilever sample A, 34 mm long, 10 mm wide and 92μm thick. The cantilever length is parallel to the $\langle 110 \rangle$ crystal axis and the surface is on the (100) plane.</i>	116

5.2	<i>(a) Cantilever A before coating. (b) Cantilever A after coating, clamped in preparation for mechanical loss measurements.</i>	118
5.3	<i>Schematic diagram of the cryostat, with an inset showing details of the clamp used to hold the cantilever samples.</i>	119
5.4	<i>Diagram of the photodiode sensor used to measure the displacement of the cantilever. The mask was made from electrical insulating tape, and the maximum width of the exposed photodiode (labelled a) was 1 mm. The laser spot diameter D was measured to be approximately 5 mm.</i>	120
5.5	<i>Circuit diagram for the photodiode circuit used to measure the amplitude of the cantilever displacement.</i>	121
5.6	<i>Plot of the response of the photodiode readout system used to measure the amplitude of the cantilever displacement.</i>	122
5.7	<i>Noise plot for the photodiode sensor used to sense the motion of the cantilever.</i>	122
5.8	<i>The frequency dependence of the calculated thermoelastic loss for cantilevers A and B (92 μm and 52 μm thick respectively). The arrows mark the first 6 bending frequencies of the samples.</i>	123
5.9	<i>Calculated thermoelastic loss as a function of temperature for three modes of silicon cantilever B.</i>	124
5.10	<i>Plot of room temperature loss measurements of cantilever A before and after coating with a 500 nm thick film of Ta_2O_5 doped with TiO_2.</i>	125
5.11	<i>Plot of the measured mechanical loss against temperature for the third bending mode of cantilever A before and after coating.</i>	126
5.12	<i>Plot of the measured mechanical loss of the fourth bending mode of cantilever A, before and after coating.</i>	127
5.13	<i>Plot of the calculated coating loss as a function of temperature for 3rd mode of cantilever A.</i>	128
5.14	<i>Plot of the calculated coating loss as a function of temperature for 4th mode of cantilever A.</i>	129

5.15	<i>Plot of the measured coating loss at approximately 1.9 kHz and the amplitude of the piezo signal detected at the start of each ringdown.</i>	130
5.16	<i>Plot of the measured loss for the fourth mode of cantilever B and its identical uncoated control sample.</i>	131
5.17	<i>Plot of the measured loss for the fifth mode of cantilever B and its identical uncoated control sample.</i>	132
5.18	<i>Plot of the coating loss for cantilever B at 777 Hz and 1280 Hz.</i>	133
5.19	<i>Plot of the coating loss for cantilever A at 1920 Hz and 3768 Hz, calculated using the lowest loss factors measured for the coated cantilever at each temperature.</i>	134
5.20	<i>Schematic diagram of the cryostat used to measure the doped tantala coating at Jena University, showing the laser interferometer readout system used.</i>	136
5.21	<i>Plot showing the temperature dependence of the measured mechanical loss of the first mode (~ 55 Hz) of the coated and uncoated cantilevers.</i>	138
5.22	<i>Temperature dependence of the measured mechanical loss of the second mode (~ 350 Hz) of the coated and uncoated cantilevers.</i>	138
5.23	<i>Temperature dependence of the measured mechanical loss of the third mode (~ 989 Hz) of the coated and uncoated cantilevers. .</i>	139
5.24	<i>Temperature dependence of the measured mechanical loss of the fourth mode (~ 1939 Hz) of the coated and uncoated cantilevers.</i>	139
5.25	<i>Temperature dependence of the measured mechanical loss of the fifth mode (~ 3184 Hz) of the coated and uncoated cantilevers. .</i>	140
5.26	<i>Temperature dependence of the dissipation of the doped Ta_2O_5 coating.</i>	142
5.27	<i>The mechanical loss peak measured in the doped Ta_2O_5 coating. For clarity, error bars are only shown for the fifth mode: these are typical of the errors in all of the points.</i>	143

5.28	<i>The fits used to determine the position of the mechanical loss peak in the doped Ta₂O₅ coating. Note the temperature at which the peak occurs increases with increasing mode frequency.</i>	144
5.29	<i>Arrhenius plot, showing a linear fit of ln(ω_0) against 1/T_{peak} for the dissipation peak.</i>	145
5.30	<i>Comparison of the measured dissipation peak to the theoretical peak obtained from the Arrhenius fit.</i>	146
5.31	<i>(a) Bright field TEM image of a tantalum layer (dark) and a silica layer (light) in a SiO₂ / Ta₂O₅ multi-layer coating, where the Ta₂O₅ layers are doped with 8% TiO₂ (b) convergent beam electron diffraction from a Ta₂O₅ layer showing just diffuse rings of intensity, confirming that this layer is amorphous. Both images were taken by Ian MacLaren of the solid state physics group at Glasgow University.</i>	147
5.32	<i>The addition of radiation shielding across the feed-through ports in the roof of the experimental chamber (a) and thermally anchoring wires to the base-plate (b) allowed the clamp to cool to 78 K, 6 degrees lower than the previous lowest temperature obtained.</i>	150
5.33	<i>Comparison of the loss of an undoped Ta₂O₅ and a Ta₂O₅ coating doped with 14.5 % TiO₂ at ~ 1000 Hz.</i>	152
5.34	<i>Comparison of the loss peak for an undoped Ta₂O₅ and a Ta₂O₅ coating doped with 14.5 % TiO₂ at ~ 1000 Hz.</i>	153
5.35	<i>Comparison of the loss of an undoped Ta₂O₅ and a Ta₂O₅ coating doped with 14.5 % TiO₂ at ~ 1900 Hz.</i>	153
5.36	<i>Comparison of the loss peak for an undoped Ta₂O₅ with a Ta₂O₅ coating doped with 14.5 % TiO₂ at ~ 1900 Hz.</i>	154
5.37	<i>Comparison of the loss peak for an undoped Ta₂O₅ with a Ta₂O₅ coating doped with 14.5 % TiO₂ at ~ 1900 Hz.</i>	154
5.38	<i>Comparison of the loss of an undoped Ta₂O₅ and a Ta₂O₅ coating doped with 14.5 % TiO₂ at ~ 3200 Hz.</i>	155

5.39	<i>Comparison of the loss peak for an undoped Ta_2O_5 with a Ta_2O_5 coating doped with 14.5 % TiO_2 at ~ 355 Hz.</i>	155
5.40	<i>The polynomial fits used to determine the position of the dissipation peak for the second and third bending modes.</i>	156
5.41	<i>The polynomial fits used to determine the position of the dissipation peak for the fourth and fifth bending modes.</i>	157
5.42	<i>Comparison of the Arrhenius plots of $\ln(\omega_0)$ against $1/T_{peak}$ for the dissipation peaks in TiO_2 doped Ta_2O_5 and undoped Ta_2O_5.</i>	158
5.43	<i>A schematic diagram of an asymmetric double well potential, with a potential barrier V and an asymmetry Δ.</i>	159
5.44	<i>Plot of the loss data used to calculate the barrier height distribution for pure tantalum, titania doped tantalum and silica.</i>	161
5.45	<i>Plot of the calculated potential barrier height distribution function $g(V)f_0$ as a function of barrier height for pure tantalum, titania-doped tantalum and silica.</i>	162
5.46	<i>Comparison of the coating losses measured at room temperature for Formula 5, Formula 5** and undoped Ta_2O_5 coatings.</i>	163
5.47	<i>Measurements of the mechanical loss of the second bending mode (at approximately 350 Hz) of three cantilevers coated with undoped Ta_2O_5 and heated to 300, 600 and 800 °C respectively.</i>	166
5.48	<i>Measurements of the mechanical loss of the third bending mode (at approximately 1000 Hz) of three cantilevers coated with undoped Ta_2O_5 and heated to 300, 600 and 800 °C respectively.</i>	166
5.49	<i>Measurements of the mechanical loss of the fourth bending mode (at approximately 1960 Hz) of three cantilevers coated with undoped Ta_2O_5 and heated to 300, 600 and 800 °C respectively.</i>	167
5.50	<i>Measurements of the mechanical loss of the fifth bending mode (at approximately 3200 Hz) of three cantilevers coated with undoped Ta_2O_5 and heated to 300, 600 and 800 °C respectively.</i>	167
5.51	<i>Arrhenius plot for the dissipation peak observed at ~ 30 K for an undoped tantalum coating heat treated at 300 °C</i>	168

5.52	<i>Transmission electron microscope and EELS images of an undoped tantala coating annealed to 800° C.</i>	170
6.1	<i>Comparison of the coating thermoelastic loss at 290 K calculated for a 500 nm thick SiO₂ coating and a 500 nm thick Ta₂O₅ coating.</i>	177
6.2	<i>Temperature dependence of the coating thermoelastic loss calculated for three modes of the SiO₂ coated silicon cantilever.</i>	178
6.3	<i>Plot of the measured loss for the first mode of the cantilever coated with silica and of the uncoated control sample.</i>	178
6.4	<i>Plot of the measured loss for the second mode of the cantilever coated with silica and of the uncoated control sample.</i>	179
6.5	<i>Plot of the measured loss for the third mode of the cantilever coated with silica and of the uncoated control sample.</i>	179
6.6	<i>Plot of the measured loss for the fourth mode of the cantilever coated with silica and of the uncoated control sample.</i>	180
6.7	<i>Plot of the measured loss for the fifth mode of the cantilever coated with silica and of the uncoated control sample.</i>	180
6.8	<i>Calculated dissipation of the silica coating for the first mode at 59 Hz.</i>	183
6.9	<i>Calculated dissipation of the silica coating for the second mode at 355 Hz.</i>	184
6.10	<i>Calculated dissipation of the silica coating for the third mode at 995 Hz.</i>	184
6.11	<i>Calculated dissipation of the silica coating for the fourth mode at 1920 Hz.</i>	185
6.12	<i>Calculated dissipation of the silica coating for the fifth mode at 3175 Hz.</i>	185
6.13	<i>Arrhenius plot for the low temperature dissipation peak in the silica coating.</i>	186

6.14	<i>Plot comparing the initial measurements of the temperature dependence of the coating loss with the measurements repeated at room temperature.</i>	188
6.15	<i>Plot of the repeated room temperature measurements of the coating loss. Shown for comparison are the loss factors presented in Chapter 4 for a silica coating on a silica cantilever substrate and Penn's coating loss data, measured at room temperature also using silica substrates.</i>	189
6.16	<i>A comparison of the dissipation measured for the ion-beam sputtered silica coating with dissipation measured in other types of silica.</i>	191
6.17	<i>The measured coating loss for the silica and tantala coatings at ~ 1 kHz which was used in the multi-layer coating loss calculation.</i>	194
6.18	<i>The expected loss in a 31 layer $\text{SiO}_2/\text{Ta}_2\text{O}_5$ coating, calculated from the single layer results, compared with the loss measured in such a multi-layer coating by Yamamoto et al.</i>	195
6.19	<i>Plot showing Yamamoto's coating loss measurements at 1.1 kHz and the calculated coating thermoelastic loss in (i) a 31 layer $\text{SiO}_2/\text{Ta}_2\text{O}_5$ coating on a sapphire substrate at room temperature and (ii) a $\text{SiO}_2/\text{Al}_2\text{O}_3$ coating on a sapphire substrate as a function of temperature.</i>	197

List of Tables

4.1	<i>Dimensions of the two ribbons with necks.</i>	78
4.2	<i>Summary of thickness and mean mechanical loss for the three tin oxide coating samples.</i>	94
4.3	<i>The average mechanical loss (calculated for all mode frequencies studied) of several coatings applied to silica membranes. All coatings were 0.5 μm thick: the membranes were 110 μm thick.</i>	110
5.1	<i>Properties of the silicon cantilevers A, B and C.</i>	118
5.2	<i>The temperature at which the dissipation peak occurs and the peak magnitude of the dissipation for each mode of the cantilever coated with doped Ta_2O_5 measured in Jena.</i>	144
6.1	<i>Material properties for silicon, silica and tantala at 290 K, used in the calculation of the coating thermoelastic loss.</i>	175
6.2	<i>The coating loss factors for each mode at room temperature, calculated using the data from the repeated loss measurements of the coated cantilever. Also shown is the calculated thermoelastic coating loss for each mode frequency.</i>	189
6.3	<i>Material properties of sapphire used to calculate coating thermoelastic loss.</i>	197

Acknowledgements

Firstly, I would like to thank my supervisor Professor Sheila Rowan, for all of her help and advice over the course of my PhD. My second supervisors Professor Jim Hough and Dr Caroline Cantley were also great sources of inspiration and encouragement. I thoroughly enjoyed my PhD, and am very grateful to have had the opportunity to work in the Institute for Gravitational Research.

The work presented in this thesis was carried out with the support of a PPARC (latterly STFC) CASE studentship in conjunction with the Rutherford-Appleton Laboratory. Many thanks to Justin Greenhalgh, Tim Hayler and Ian Wilmut at RAL. I would like to thank the cryogenics group of the Solid State Physics Institute at Jena University for the opportunity to work with them for a month, and especially to Ronny Nawrodt and Christian Schwarz for their wonderful hospitality.

I am very grateful to Stuart Reid and Alastair Heptonstall for all of their good advice and for many useful discussions: both were a pleasure to work with. Thanks also to Alan Cumming who shared an office with me from the start and offered much good-humoured practical assistance and support when things didn't work. Colin Craig and Stephen Craig deserve special thanks for always managing to get last-minute technical jobs done so well. I would also like to thank Adam Woodcraft for his advice on all things cryogenic and for being willing to spend several late nights in the lab while showing me the ropes with liquid helium transfers.

Others I would like to thank include Eleanor Chalkley, for sharing an office and a lab; David Crooks, for his help at the start and for introducing me to

espresso; Christian Killow and Ewan Fitzsimmons, fellow drinkers of lots of coffee; and all the occupants of room 427a. My friends Gordon, Craig, Robert, Andy, Jen, Jenn and Jennifer and the regular Wednesday night pub trips did a great job of keeping me sane. My sister Kirsty, though long-ago lost to biochemistry, has often commiserated with me on the trials and tribulations of doing an experimental PhD, which seem to be similar across all disciplines. Thanks to my parents for all of their help, advice and support with everything I've done over the years. I am particularly grateful to my Mum for proof reading this thesis, and to my Dad for getting me interested in science in the first place. Finally, I would like to thank my partner Mairi for all of her love, support and understanding over the past few years.

Preface

This thesis is an account of work carried out in the Institute for Gravitational Research at the University of Glasgow between October 2004 and August 2008, involving studies of materials for use in future gravitational wave detectors.

In Chapter 1 the nature and origin of gravitational waves is discussed, various detection techniques are summarised and the status of current and planned gravitational wave detectors reviewed.

In Chapter 2 the theory of thermal noise, its relationship to mechanical dissipation and its influence on the displacement sensitivity of interferometric gravitational wave detectors is discussed.

In Chapter 3 an investigation into the extension of the settling time of hydroxide catalysis bonds by cooling is presented. This work was carried out jointly with S. Reid, who additionally constructed the low temperature environment and optical readout system which were used.

In Chapter 4 the development of a technique to measure the mechanical dissipation of optical and conductive coating materials applied to silica cantilever substrates is discussed. A. Heptonstall fabricated the silica ribbon fibres used and assisted in welding them to silica slides using a CO₂ laser. Some of the measurements of the dissipation of optical coatings were carried out jointly with P. Holt. The conductive SnO coatings were fabricated by S. Reid, who also measured the coating thickness. L. Cunningham measured the resistivity of the coatings, and the optical absorption was measured by A. Markosyan at Stanford University. The mechanical loss measurements and analysis were carried out by the author.

In Chapter 5 studies of the temperature dependence of mechanical dissipation in Ta₂O₅ (tantala) coatings applied to thin silicon substrates are presented. This work was largely carried out in Glasgow using a cryostat initially set up by S. Reid and modified by the author to allow cooling to liquid helium temperatures. In addition, measurements of the dissipation of a TiO₂-doped Ta₂O₅ coating were carried out at the University of Jena by the author, R. Nawrodt and C. Schwarz. Analysis of the data was performed by the author, with input from S. Rowan and J. Hough. One data point used in the analysis was derived from similar measurements at Glasgow by E. Chalkley. TEM microscope and electron diffraction images of the coatings were taken by I. MacLaren, R. Bassiri and J. Scott.

In Chapter 6 measurements of the temperature dependence of mechanical dissipation in an SiO₂ (silica) coating are presented. These measurements were also performed at the University of Jena, by the author, R. Nawrodt and C. Schwarz. Calculations of the expected level of coating thermoelastic loss in the coated sample were carried out by the author, using published literature. The analysis was carried out by the author following discussions with S. Rowan and J. Hough.

Summary

Gravitational waves, predicted by the theory of General Relativity, are fluctuations in the curvature of space-time which arise from the asymmetric acceleration of mass. While gravitational waves have yet to be detected directly, measurements of the inspiral rate of a binary pulsar system have provided strong evidence for their existence and a world-wide effort to develop more sensitive detectors is ongoing. In addition to testing predictions of General Relativity, observation and analysis of gravitational waves from astrophysical sources will provide new insights into a wide range of phenomena including black holes, neutron stars and supernovae.

Gravitational waves are quadrupole in nature, and therefore produce fluctuating tidal strains on space. Long baseline gravitational wave detectors aim to measure this effect using laser interferometry to measure fluctuations in the relative separation of free masses, coated to form highly reflective mirrors and suspended as pendulums at the ends of perpendicular arms up to 4 km in length. There are currently several long baseline gravitational wave detectors in operation around the world, including the three LIGO detectors in the US, the UK/German GEO600 detector near Hannover and the French/Italian Virgo detector near Pisa.

The strain expected from gravitational waves is very small, of order $\approx 10^{-22}$. The magnitude of the resultant displacement is such that the thermal motion of the mirrors and their suspensions forms an important limit to detector sensitivity. The level of thermal noise is related to the mechanical dissipation of the materials used in the test mass and the mirror coatings.

The research presented focuses on the characterisation and reduction of the mechanical loss of materials for use in the construction of the interferometer mirrors, with the aim of reducing the level of thermal noise in future gravitational wave detectors. An introduction to gravitational waves, possible astrophysical sources and the techniques used in both interferometer and bar detectors is given in Chapter 1. Chapter 2 discusses thermal noise, one of the major limits to sensitivity in interferometric gravitational wave detectors, and its relationship to the mechanical loss of the materials used in the detector mirrors.

The technique of hydroxide catalysis bonding was used to allow the construction of low thermal noise monolithic silica mirror suspensions in the GEO 600 detector. Hydroxide catalysis bonding is also of interest for the space based gravitational wave detector LISA, which requires the rigid attachment of many precisely aligned optical components to a Zerodur base plate. In Chapter 3, an investigation of the dependence of the settling time of the bond on temperature is presented, and the results used to calculate the activation energy associated with the bonding reactions.

Recent research has suggested that the thermal noise associated with the ion-beam sputtered mirror coatings applied to the test masses will limit the sensitivity of planned ‘second generation’ detectors in their most sensitive frequency band. Current gravitational wave detectors use multi-layer dielectric mirror coatings formed from alternating layers of ion-beam sputtered silica (SiO_2) and tantala (Ta_2O_5). Research carried out by the Institute for Gravitational Research in Glasgow in collaboration with colleagues in the US has shown that the mechanical dissipation of these coatings arises predominantly in the tantala layers, and that the dissipation can be reduced by ~ 40 to 50% by doping the tantala with titania (TiO_2). However, neither the process responsible for mechanical dissipation in tantala or the mechanism by which titania doping reduces the dissipation is clearly understood.

In Chapter 4, the fabrication of silica cantilevers for use in measurements of the mechanical loss of various coatings is discussed. In addition to measurements of the dissipation of single layer coatings of silica and tantala at room temperature, a study of the dissipation of conductive SnO coatings is presented. SnO coatings may be of interest for the mitigation of electrostatic charging, which can result in excess noise and control problems in gravitational wave detectors. The results indicate that thin layers of SnO may meet the mechanical and optical specifications for use in the second generation Advanced LIGO detectors.

Studies of the temperature dependence of the mechanical dissipation of tantala coatings are presented in Chapter 5. A peak in the dissipation was found at approximately 20 K. Analysis of this peak provides insight into possible dissipation mechanisms in ion-beam sputtered tantala, suggesting that it may involve the reorientation of molecules in double-well potential systems. The width of the dissipation peak suggests that there is a broad distribution of potential barrier heights, probably arising from the amorphous structure of the coating. Doping tantala with titania is shown to increase the average activation energy of the dissipation process by $\sim 33\%$, in addition to reducing the magnitude of the dissipation. Further experiments to study the effect of heat treatment on the low temperature mechanical dissipation of tantala coatings are described. An improved understanding of mechanical dissipation in ion-beam sputtered tantala, based on the results presented here, may enable the sensitivity of future gravitational wave detectors to be increased through the development of coatings with lower mechanical loss.

In Chapter 6 measurements of the temperature dependence of the dissipation of a silica coating are presented, and the possible effect of coating thermoelastic loss on the measurements is assessed. Using the measurements from this chapter and Chapter 5, the expected temperature dependence of the dissipation in a silica/tantala multi-layer coating is calculated. The results suggest

that the multi-layer coating loss increases with decreasing temperature to a peak at approximately 20 K.

Chapter 1

Gravitational wave detection

1.1 Introduction

The existence of gravitational waves is a prediction of Einstein's General Theory of Relativity [1], which describes the force of gravity as arising from curvature in space-time created by the presence of mass. A direct consequence of this theory is that the acceleration of asymmetric masses should produce fluctuations in the curvature of space-time, or gravitational waves, propagating at the speed of light. Due to the nature of gravity, very large masses and accelerations are required to produce detectable gravitational waves. Thus the only likely sources of detectable gravitational radiation are astrophysical events such as supernovae, orbiting and coalescing binary neutron stars and merging black holes.

Gravitational waves produce fluctuating tidal forces on masses in their path. Due to the relative weakness of gravitational interaction with matter, these tidal forces are predicted to be very small, making gravitational radiation exceptionally challenging to detect. However, as a consequence of the same weak interaction with matter, gravitational waves are not as susceptible to scattering and absorption as electromagnetic radiation, making them a potentially invaluable tool in astronomy.

Gravitational waves have not yet been directly detected, although extensive experimental efforts to do so are ongoing, originating from work by Joseph

Weber in the 1960s [2]. However, compelling evidence for the existence of gravitational radiation has been provided by studies of the binary pulsar PSR 1913 + 16, discovered in 1974 by Hulse and Taylor [3, 4]. Analysis of the decay rate of the binary orbital period has shown that this system is losing energy and angular momentum at almost precisely the rate predicted by models for the emission of gravitational radiation [5, 6, 7]. In the decades following this discovery, considerable progress has been made towards the direct detection of gravitational waves. The first generation of broad-band gravitational wave detectors began to acquire observational data in 2002. While no detection has been achieved after several years of observation, the data obtained have put scientifically meaningful constraints on astrophysical models of various sources. Significant upgrades to improve the sensitivity of the first generation of detectors are in the advanced planning stages, and it is widely expected that these upgrades will enable the first detection of gravitational waves.

Detection of gravitational waves, and observation of their polarisation states and velocity, will allow the predictions of General Relativity to be directly verified. Of greater significance is the exciting prospect of gravitational wave astronomy. Signals from a wide variety of astrophysical sources including neutron stars, binary compact objects, supernovae, black holes and gamma ray bursts may be detected, greatly increasing our knowledge of these phenomena. A gravitational background radiation field, analogous to the the cosmic microwave background but originating earlier in the history of the universe, has been predicted. Detecting these primordial gravitational waves would be of great cosmological significance, perhaps placing constraints on inflation theories and providing information on the large scale structure of the universe. Finally, it should be remembered that previous major advances in astronomy have often resulted in new and unexpected observations, such as the discovery of pulsars. Gravitational waves will provide a radically new way of observing the universe, and it is possible that unexpected sources will be discovered.

1.2 The nature of gravitational radiation

Gravitational radiation is produced by the acceleration of mass, in a similar way to the production of electromagnetic radiation by the acceleration of charge. However, the dominant component of a radiated electromagnetic field is dipole radiation. A gravitational dipole moment analogous to an electric dipole can be defined, but the conservation of momentum implies that it must remain constant, precluding the existence of gravitational dipole radiation. Fundamentally, this difference arises from the existence of both positive and negative electric charge, whereas only positive mass can occur. There are no conservation laws to prevent higher moments of mass distributions from varying, and variations in gravitational quadrupole moment are predominantly responsible for the emission of gravitational radiation.

The quadrupole nature of gravitational waves implies that they can only be generated by the acceleration of an *asymmetric* mass and are typically emitted at twice the oscillation frequency of the source. A gravitational wave exerts differential strains along perpendicular paths in space, as shown in Figure 1.1. This figure shows the effect of a gravitational wave travelling perpendicular to the page on a ring of masses of diameter L . The perpendicular axes of the ring

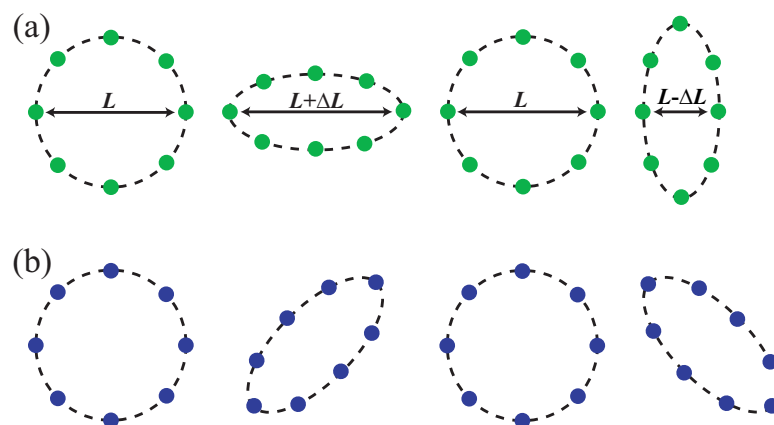


Figure 1.1: *The effect of a gravitational wave with (a) the h_+ and (b) h_\times polarisation, incident normal to the page, on a ring of test particles.*

are alternatively extended and compressed by ΔL . The total strain is given by:

$$h = \frac{2\Delta L}{L}, \quad (1.1)$$

where h is the amplitude of the gravitational wave.

Long baseline gravitational wave detectors aim to measure this effect using laser interferometry to measure fluctuations in the relative separation of free masses located at the ends of perpendicular arms. Currently there are several such interferometric detectors in operation (some are currently being up-graded) including the 600 m long GEO 600 detector in Germany [8], the two 4 km long and one 2 km long LIGO detectors in the United States [9], the French-Italian VIRGO detector in Italy [10] and the TAMA detector in Japan [11]. These detectors have all reached, or closely approached, their design sensitivities, with the lowest strain sensitivity of $\sim 2 \times 10^{-23} \text{ Hz}^{-\frac{1}{2}}$ being achieved by one of the LIGO detectors at its most sensitive frequencies. The principles of laser interferometry and the design of these detectors is discussed in Section 1.4.2. First, a more detailed overview of various possible sources of gravitational waves is given.

1.3 Sources of Gravitational Waves

Many astrophysical and cosmological sources of gravitational radiation have been predicted. These can be conveniently grouped according to the type of signal they are expected to emit.

1.3.1 Periodic sources

Periodic sources emit gravitational waves continuously at an essentially constant frequency, with the most likely sources in the detection band of current detectors being rotating single neutron stars and low mass X-ray binaries (LMXBs) [12]. Neutron stars are formed from the supernova remnants of stars

of between ~ 1.4 and ~ 24 solar masses. As a neutron star cools, a solid crust forms, while the inner regions of the star are thought to remain in a liquid phase. For a single neutron star to emit gravitational radiation, it must have a quadrupole moment resulting from an axial asymmetry. Three major mechanisms of gravitational wave emission have been postulated: non-axisymmetric distortions of the crust, internal modes of the star and free precession of the star.

Non-axisymmetric distortions of a single neutron star could arise from either elastic strains or from magnetic fields. Elastic strains may be caused by the gradual spin-down of the star or may be ‘frozen’ into the crust during the formation of the star. The gravitational wave amplitude, h , of waves produced by these distortions is given by:

$$h = \frac{4\pi^2 G}{c^4} \frac{I_{zz} f^2}{d} \epsilon, \quad (1.2)$$

where I_{zz} is the principal moment of inertia of the star, ϵ is the ellipticity, d is the distance of the star from Earth, G is the gravitational constant, c is the speed of light, and f is the gravitational wave frequency, which is twice the rotational frequency of the neutron star [12]. The actual ellipticity of neutron stars is highly uncertain, but is likely to be limited by the breaking strain of the crust. Certain proposed exotic stars, such as postulated ‘solid strange quark stars’ [13], could potentially support larger ellipticities than a neutron star [14]. Indeed, it is possible that such stars may be identified for the first time from their gravitational wave signal. Another possible source of ellipticity is a strong internal magnetic field [15], which can be caused by differential rotation as the neutron star forms. The ellipticity can be increased if the toroidal component of the magnetic field is aligned towards the equator of the star.

Oscillations in the fluid interior of a neutron star, most likely axial pulsation modes (also known as ‘r-modes’), could also emit gravitational waves [16, 17]. This is thought to be particularly likely in newly formed or rapidly accreting neutron stars.

The third possible emission mechanism for a single neutron star is free precession [18], a wobble of the star which occurs when the symmetry axis and rotation axis do not coincide. The expected gravitational wave amplitude is:

$$h_{\text{precession}} = 10^{-27} \left(\frac{\theta_w}{0.1} \right) \left(\frac{1 \text{ kpc}}{d} \right) \left(\frac{\nu}{500 \text{ Hz}} \right)^2, \quad (1.3)$$

where θ_w is the amplitude of this wobble in radians and ν is the orbital frequency [12, 19].

One neutron star, the Crab pulsar, is thought to be one of the most promising candidates as a local source of gravitational waves. Radio observations have shown that the spin frequency of this pulsar is decreasing at a rate of $3.7 \times 10^{-10} \text{ Hz s}^{-1}$. If it is assumed that this spin-down is entirely due to the loss of energy by gravitational radiation, then an upper limit of $h = 1.4 \times 10^{-24}$ can be placed on the gravitational wave amplitude at Earth [20].

Finally, LMXBs are thought to be good candidate sources of gravitational radiation [21]. These are systems in which a neutron star accretes matter from a binary companion star (often a main sequence star or a red giant). The stream of superheated matter emits intense X-rays as it falls into the neutron star. Guided by magnetic fields, the accreted material could accumulate to form denser regions on the surface of the neutron star. The resulting distortion of the neutron star would increase the quadrupole moment leading to the emission of gravitational waves.

Another possible emission mechanism was predicted by Wagoner [22], who demonstrated that an accreting neutron star could gain enough angular momentum to surpass the Chandrasekhar-Friedman-Schutz (CFS) limit [23, 24], at which point its rotation would become non-axisymmetric, leading to the emission of gravitational waves. These neutron stars, known as Wagoner stars, are particularly interesting as the gravitational wave amplitude would be related to the observed X-ray flux from the system.

1.3.2 Burst sources

Certain rapid events, such as supernovae and the coalescence of compact binary stars [25], will produce short bursts of gravitational waves rather than continuous signals. Bursts of gravitational waves are significantly more likely to be detected if the expected waveform can be calculated and used as a template for the data analysis procedures.

Over half of all stars are thought to occur in binary systems, in which two stars orbit their common centre of mass. Binaries consisting of a pair of compact objects (i.e. neutron stars or black holes) have been widely studied as sources of gravitational waves. As mentioned in the introduction, the orbital decay of the binary pulsar PSR 1913+16 has been measured to be within 0.2 % of the rate predicted from the emission of gravitational waves [7]. As gravitational radiation carries away orbital energy and angular momentum from a binary system, the two compact objects move closer together and orbit more rapidly until they finally coalesce. During the last few thousand orbits before coalescence (corresponding to a time of only a few seconds) the frequency sweeps up from ~ 10 to ~ 300 Hz [25]. This rapid ‘chirp’ signal occurs in the frequency band of current ground based detectors. The approximate strain amplitude expected from inspiralling neutron stars can be shown to be [26]:

$$h \approx 10^{-23} \left(\frac{100 \text{Mpc}}{d} \right) \left(\frac{M_b}{1.2 M_\odot} \right)^{\frac{5}{3}} \left(\frac{f}{200 \text{Hz}} \right)^{\frac{2}{3}}, \quad (1.4)$$

where $M_b = (M_1 M_2)^{3/5} / (M_1 + M_2)^{1/5}$ is known as the mass parameter of the binary, and M_1 and M_2 are the masses of the two neutron stars.

The final coalescence event is not yet well understood, making it difficult to search for the emitted gravitational wave signal. However, the inspiral phase can be modelled [27] and by tracking the changing frequency of the inspiral, it may also be possible to detect the final merger event.

Binary systems consisting of a black hole and a neutron star, or of two black holes, have not been observed; however, they are expected to exist, although

with a lower occurrence than neutron star binaries. Due to the greater density and mass of a black hole, the gravitational wave amplitude from binary black holes is expected to be about 4 times larger than from binary neutron stars, making these inspirals promising candidates for detection.

An important property of inspiralling binary systems is that they are ‘standard candles’ for gravitational wave emission. If the time dependence of both the frequency and amplitude of the signal are measured, then the distance of the system can be calculated from the intensity of the detected gravitational waves. Thus, if enough events are measured to high enough red-shift, the extracted distances may allow a new, independent measure of the Hubble constant [26].

Bursts of gravitational waves may also be emitted by core collapse supernovae. These occur when a star of greater than ~ 8 solar masses has used all of its available nuclear fuel, so that radiation pressure can no longer prevent the stars gravitational collapse. The core implodes rapidly, until the density of nuclear material is reached. At this point the outer layers effectively bounce off the core in a violent explosion, leaving the remnant of the core exposed as a neutron star or perhaps a black hole. If there is any asymmetric distribution of mass during the supernova, perhaps related to the angular momentum of the stellar core, then gravitational waves will be emitted. Detection of gravitational waves from supernovae may provide unique information, unavailable through electromagnetic observations, about the processes involved in the collapse of stellar cores [28].

1.3.3 Stochastic gravitational wave background

The superposition of gravitational waves from many unresolved sources is predicted to form a stochastic, or random, background signal, significantly below the instrument noise level in first generation interferometers. This background will include signals from astrophysical sources, such as faint and unresolved

neutron star signals. It is also expected to contain gravitational radiation from sources in the very early universe. The cosmic microwave background radiation, produced approximately 10^5 years after the Big Bang, was famously detected by Penzias and Wilson in 1964 [29, 30]. An analogous cosmological gravitational background field has been predicted, originating from an earlier time, possibly as little as 10^{-35} seconds after the Big Bang. Detection of this background radiation would allow unique insight into the very early universe.

Many possible cosmological sources of gravitational waves have been proposed, including the amplification of quantum vacuum fluctuations during inflation, pre-big bang models, the decay of cosmic strings and phase transitions in the early universe. Reviews of these, and other possible sources and methods for their detection, can be found in Allen [31] and in Abbott et al [32]. Inflationary models have been studied extensively and many make detailed predictions about the expected gravitational wave spectrum, while it has been calculated that any gravitational waves produced at $\approx 10^{-25}$ seconds would be red-shifted into the detection band of current ground based interferometers.

The amplitude of the stochastic background is expected to be significantly smaller than the sensitivity of current detectors. However, it may be possible to detect it by cross-correlating the data from two detectors. Assuming the detectors are widely separated, so that the instrument noise is uncorrelated, this technique can significantly increase the sensitivity of the search. This method has already been used to place constraints on cosmic string models [32].

1.4 Gravitational wave detection

1.4.1 Resonant bar detectors

The first gravitational wave detectors were proposed by Joseph Weber in 1960 [2]. Weber's technique involved monitoring the oscillations of solid bodies

for evidence of interaction with a gravitational wave. Initially, Weber and his colleagues looked for evidence of excitation of the normal modes of the Earth by low frequency gravitational waves [33]. At the same time, Weber began attempts to detect tidal strains in large cylindrical aluminium bars, which were isolated from external mechanical and acoustic noise sources [34]. Piezoelectric crystals bonded around the centre of the bar were used to monitor the oscillations of its fundamental mode. A gravitational wave of sufficient amplitude passing through the bar would be expected to excite this mode, with the changes to the amplitude and phase of the motion being detected by the piezoelectric sensors.

In 1968 Weber observed multiple coincident events between two bars separated by 2 km [35], which he believed were possibly due to gravitational waves. The following year, Weber took data from larger bars, approximately 66 cm in diameter and up to 1.5 m long, located approximately 1000 km apart in Maryland and Illinois. The bars were resonant at 1660 Hz, a frequency at which gravitational waves were believed to be emitted during a core collapse supernova. Weber again reported coincident readings between these detectors, at a rate of approximately one per day [36, 37], which he claimed were due to gravitational waves.

With interest in the field growing, several laboratories around the world attempted to repeat Weber's measurements. However, various research groups including those at Yorktown Heights [38, 39], Bell Labs [40], Moscow [41] and Glasgow [42] failed to verify Weber's results. Calculations suggested that Weber's bar detectors had a strain sensitivity of $\sim 10^{-16}$ for millisecond pulses, whereas sensitivities in the order of 10^{-23} were thought to be required to enable regular detection of gravitational waves from astrophysical sources. It was clear that the sensitivity of the detectors had to be improved by many orders of magnitude if gravitational waves were to be discovered.

Two strategies were adopted to develop more sensitive detectors: the first

was to reduce the level of noise in bar detectors; the second involved moving to a new type of detector using laser interferometry as discussed in the following section. The sensitivity of resonant bars was limited by thermally excited vibrations of the bar and by electronic noise in the detector circuits, and research focused on the use of cryogenic cooling to reduce these effects. Several low temperature bar detectors were constructed including the Allegro detector at Louisiana State University [43], the EXPLORER and NAUTILUS detectors built by the University of Rome [44, 45], the NIOBE detector at the University of Western Australia [46] and the AURIGA detector built by the Universities of Padua and Trento [47, 48]. In recent years, strain sensitivities approaching 10^{-20} for millisecond pulses have been reached [45, 49]. Observational runs involving two or more bars have been undertaken, but, although coincident events have been observed, there has been no compelling evidence of the detection of gravitational waves. Spherical bar detectors, which give superior performance in determining the directionality of any signal, have been developed at the University of Leiden in the Netherlands [50] and at the University of Sao Paulo, Brazil [51].

Bar detectors have relatively narrow operational bandwidths centered on the resonant mode of the bar; the resonant frequency is typically chosen to optimise the sensitivity for a particular type of source. While Cerdonio et al [52] have suggested a method of increasing the bandwidth using a dual resonant mass detector, lack of broadband sensitivity remains a significant disadvantage of bar detectors. As broadband interferometric detectors (discussed in the following section) have surpassed the sensitivity of bar detectors continued funding of the bars has become limited, and only AURIGA, EXPLORER and NAUTILUS are still in operation [53].

1.4.2 Interferometric detectors

At the same time as the sensitivity of bar detectors was being increased a new type of detector using laser interferometry to measure the distance between two widely separated masses was developed. Since gravitational waves produce strains in space (i.e. a fractional change in length) the resulting absolute displacement can be increased by increasing the separation of the masses. This technique, first proposed by Gertsenshtein and Pustovoit in 1962 [54], was also very attractive as it could provide high sensitivities over a large range of frequencies [55].

The design of these detectors is based on a Michelson interferometer, shown in Figure 1.2. A beam splitter is used to divide the incident laser light into two beams, directed along the two perpendicular arms of the interferometer. At the end of the arms, the light is reflected back towards the beam splitter by the test mass mirrors, which are suspended as pendulums to provide seismic isolation. At the beam splitter the reflected light is recombined and the resulting interference pattern directed onto a photodiode.

Due to their quadrupole nature, polarised gravitational waves propagating perpendicular to the plane of the interferometer will increase the length of one arm by δL and reduce the length of the perpendicular arm by δL , as illustrated in Figure 1.1. The change in arm lengths results in a relative phase shift between the two reflected beams, causing a change in the intensity of the interference fringe on the photodiode. In practice, feedback signals are used to control the positions of the mirrors to keep the output ‘locked’ onto a certain point on the interference pattern; usually a dark fringe (see Section 1.5.4). Information about the differential motion of the mirrors, including any gravitational wave signals, will therefore be encoded in the control signal.

Robert Forward and his colleagues constructed the first prototype gravitational wave detector using laser interferometry in the early 1970s [56, 57], although the sensitivity was limited by the low power of the He-Ne laser and

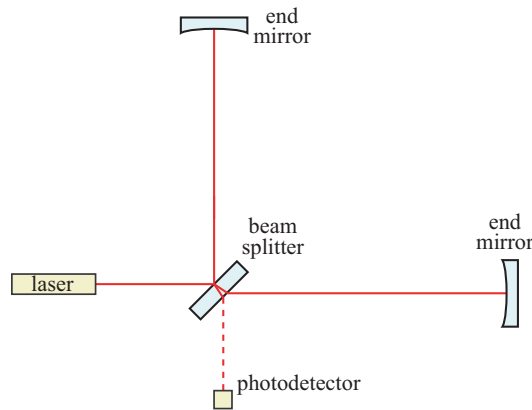


Figure 1.2: A schematic diagram of a simple Michelson interferometer, consisting of a laser, beam splitter and two end mirrors.

the short arm length. In 1975 a 3 m prototype interferometer was developed at the Max Planck Institute for Astrophysics in Munich [58], while a 1 m detector was built at the University of Glasgow [59]. These initial prototypes were followed by a 10 m interferometer at Glasgow [60], a 40 m instrument at the California Institute of Technology and a 30 m prototype at the Max Planck Institute of Quantum Optics in Garching [61]. After the development of these interferometers, the technology was thought to be sufficiently advanced to allow the construction of longer base-line interferometers which would have a realistic chance of detecting gravitational waves. Thus, in the mid 1990s, construction of several detectors with arms between 600 m and 4 km long was begun at various sites around the world. A brief summary of this first generation of long baseline gravitational wave detectors is given in Section 1.7.

1.5 Limits to the sensitivity of long-baseline detectors

In principle the sensitivity of a laser interferometer monitoring strains in space should be limited by the Heisenberg Uncertainty Principle. In practice, however, a number of other factors can limit the sensitivity of an interferome-

ter, and reaching the quantum limit poses a significant challenge. The major sources of noise are described in the following sections.

1.5.1 Gravitational gradient noise

Fluctuations in the local gravitational field can directly induce motion in the interferometer test masses, resulting in a form of displacement noise in the interferometer known as gravity-gradient noise [62, 63]. This noise source is potentially significant at frequencies $\lesssim 20$ Hz, and, since the test masses cannot be shielded from gravitational fields, effectively sets a lower limit on the low-frequency sensitivity achievable on Earth. Indeed, due to the level of low frequency gravity-gradient noise on Earth, experiments to detect gravitational waves at frequencies below ~ 1 Hz have to be carried out in space (see Chapter 3).

Locally fluctuating gravitational fields can be produced by either density fluctuations in the ground or air surrounding the interferometer, or by the motion of other masses (perhaps passing cars, people, or aeroplanes flying overhead) in the vicinity. Surface waves in the top-most layers of the Earth's crust, created by the impact of ocean waves, are a major source of gravity-gradient noise [64]. The gravity-gradient noise spectrum is below the initial sensitivity of the first generation of long baseline interferometers [63], although it is expected to limit the low frequency sensitivity of the planned second generation of detectors.

1.5.2 Thermal noise

Thermal noise, arising from the thermally driven motion of the molecules in the test masses and their suspensions, is one of the major limits to the sensitivity of gravitational wave interferometers at frequencies up to several hundred Hertz. Thermal excitation drives the various resonant modes of the suspended mirror, with each mode having on average $\frac{1}{2}k_B T$ of thermal energy associated with it.

Since the internal modes are typically at high frequencies outwith the gravity wave detection band, the thermal noise results from the tails of the resonance peaks. It is possible to shape the thermal noise spectrum and concentrate the majority of the thermal motion close to the resonances, thus reducing the off-resonance motion in the operation band of the detector. This is achieved by using materials of ultra-low mechanical loss, typically fused silica, for the test mass mirrors. Fused silica suspension fibres are also used in the GEO 600, and are planned for use in future gravitational wave detectors such as Advanced LIGO and Advanced VIRGO. Thermal noise and mechanical dissipation are discussed more extensively in Chapter 2.

1.5.3 Seismic noise

The effects of the continual motion of the ground, with amplitudes in the micrometer range, is a major low-frequency limit which must be overcome in a gravitational wave detector. Seismic noise between approximately 1 and 10 Hz largely arises from wind and human activity such as traffic and industry [64]. Below 1 Hz vibrations from ocean waves travelling as surface waves in the Earth's crust produce the micro-seismic background, with peaks in amplitude at 0.08 Hz and 0.16 Hz [64]. Even at a relatively low-noise location on the Earth's surface, the seismic noise spectrum is approximately $10^{-7} f^{-2} \text{m Hz}^{-\frac{1}{2}}$ in all dimensions [65]. If the disturbance to each test mass must be less than approximately $3 \times 10^{-20} \text{m Hz}^{-\frac{1}{2}}$ [66], then at 20 Hz for example, the seismic noise in the horizontal direction must be reduced by a factor of approximately 8×10^9 . This horizontal isolation can be achieved relatively easily by suspending the test masses as pendulums. Above the resonant frequency of the pendulum, the transfer function between horizontal motion of the suspension point and the pendulum mass is proportional to $1/f^2$, providing a high degree of horizontal isolation. In any pendulum system there is likely to be a degree of coupling between vertical and horizontal motion, typically of order 10^{-3} [66, 67], making

it important to also provide a significant level of vertical isolation. This can be achieved by suspending the test mass on a spring, most usually of the cantilever type.

The requirements of horizontal and vertical seismic isolation lead to complex pendulum systems consisting of several stages. In GEO 600, for example, a triple pendulum design is used, with the test mass suspended, via an intermediate mass, from cantilever springs on an upper mass [68]. This upper mass is itself suspended from cantilever springs at the top of the pendulum structure. This entire structure is hung from a plate resting on both passive and active anti-vibrational damping stages. The VIRGO detector, which was designed to operate to frequencies below 10 Hz, uses a seven stage pendulum system for horizontal isolation, with six of the upper stages hung from cantilever springs for vertical isolation [69].

To reduce motion at the pendulum frequency, active damping of the pendulum mode is employed. Further ‘pre-isolators’ are required to reduce low frequency motion at the micro-seismic peak and thus to reduce the necessary dynamic range of the servo systems used to hold the optical cavities on resonance. Many forms of low frequency isolator are used. In VIRGO, tall inverted pendulums are used with seismometers and actuators to provide feedback in the horizontal direction and with cantilever springs of reduced stiffness in the vertical direction. GEO 600 also uses a system of seismometers and actuators below the passive isolation stage, while a new active hydraulic pre-isolation system, situated outside the vacuum, is being developed for Advanced LIGO [70].

1.5.4 Photoelectron shot noise

Gravitational wave detectors operate with the interferometer locked at a particular point on an interference fringe. Any intensity changes at the interferometer output port are sensed with a photodiode, allowing a feedback signal

to be derived which is then applied, with appropriate phase, to a transducer capable of moving one of the interferometer mirrors. Changes in the lengths of the interferometer arms can be detected by monitoring the feedback signals. It has been shown [71] that the best signal-to-noise ratio is obtained by locking the interferometer close to a dark fringe.

Shot noise in the detected photo-electrons is one limit to the sensitivity of this optical readout scheme, where the photo-electrons are assumed to obey Poisson statistics. If the laser has a mean power P and wavelength λ , then the mean number of photons passing through the interferometer in an observing time τ , corresponding to a bandwidth $\Delta f = 1/2\tau$, is $N = P\tau/h\nu$. Statistical fluctuations in the number of photons detected by the photodiode can limit the sensitivity of the detector. If the photoelectrons follow Poisson statistics, the average magnitude of these fluctuations is \sqrt{N} , leading to a limit to the accuracy with which the differential displacement Δx of the mirrors can be determined. In a simple Michelson interferometer this limit is given by [71]:

$$\Delta x = \left(\frac{\hbar c \lambda \Delta f}{4\pi P \cos^2(\phi/2)} \right)^{\frac{1}{2}}, \quad (1.5)$$

where ϕ is the phase difference between the light in the two arms of the interferometer and $\hbar = h/(2\pi)$ is the reduced Planck constant. It can be seen that the effects of shot noise can be reduced by increasing the light power and that, as mentioned above, the best sensitivity is obtained by operating the interferometer close to a null point in the interference pattern where $\phi = 0$.

1.5.5 Radiation pressure noise

Fluctuations in radiation pressure on the interferometer mirrors can produce a differential displacement between the two mirrors. For a simple Michelson interferometer the resulting differential displacement sensitivity limit, Δx , at a frequency ω can be shown to be:

$$\Delta x = \left(\frac{16\pi\hbar P \Delta f}{\lambda m^2 \omega^4 c} \right)^{\frac{1}{2}}, \quad (1.6)$$

where P is the laser power and m is the mass of the mirror. A formal quantum mechanical treatment of an interferometer has shown that this fluctuating radiation pressure force arises from zero-point fluctuations of the amplitude of the vacuum electromagnetic field, entering the interferometer at the beam-splitter via the output port [72, 73]. If this light has the correct phase it will increase the light intensity in one of the interferometer arms while decreasing the intensity in the other arm, producing anti-correlated fluctuations of the light intensity in each arm. These intensity fluctuations are the differential driving force which results in radiation pressure noise.

The same quantum mechanical treatment of an interferometer shows that the shot noise actually arises from fluctuations in the *phase* of the vacuum field entering the interferometer at the beam-splitter [72, 73].

1.5.6 The Standard Quantum Limit

It has been shown, as discussed in the previous section, that the radiation pressure fluctuations and shot noise in an interferometer arise from orthogonal fluctuations in the vacuum field entering the dark port of the beam-splitter [72, 73]. They are therefore statistically independent of each other and thus Equations 1.5 and 1.6 can be combined additively to give a total quantum sensitivity limit of:

$$(\Delta x)^2 = \frac{\hbar c \lambda \Delta f}{4\pi P \cos^2(\phi/2)} + \frac{16\pi \hbar P \Delta f}{\lambda m^2 \omega^4 c}, \quad (1.7)$$

Since radiation pressure noise is proportional to the laser power, while the shot noise varies as the inverse of the laser power, it follows that at any frequency of observation there will be an optimum power for which the total quantum noise is a minimum [71]. By minimising the above expression with respect to P , this optimum power can be shown to be:

$$P_{optimum} = \frac{\lambda m \omega^2 c}{8\pi} \quad (1.8)$$

At this power, the apparent total ‘quantum’ limit to the detectable differential displacement can be found from Equation 1.7 [71]:

$$\Delta x = \left(\frac{4\hbar\Delta f}{m\omega^2} \right)^{\frac{1}{2}}. \quad (1.9)$$

This is often referred to as the Standard Quantum Limit (SQL). In fact, it is not necessarily a true limit to sensitivity.

The SQL arises only if the optical noise sources - photon shot noise and radiation pressure noise - are uncorrelated. These optical noise sources are a result of fluctuations in the vacuum field entering the dark port of the interferometer, with fluctuations in the phase quadrature responsible for shot noise and fluctuations in the amplitude quadrature responsible for radiation pressure noise. If the balance of the fluctuations in the two quadratures of the vacuum field can be changed, it is possible to reach the SQL at a lower power than derived above. This can be achieved through the use of squeezed states of light, which reduce the noise in one quadrature while increasing the noise in the orthogonal quadrature [73]. The injection of a squeezed vacuum field at the dark port of the beam-splitter can therefore reduce the dominant form of optical noise at a particular frequency, allowing the SQL to be reached at a lower power than derived above.

In principle the SQL can actually be overcome by introducing correlations between the shot noise and radiation pressure [74]. This is an example of the principle of quantum non-demolition, first suggested by Braginsky [75], in which the quantum properties of a measurement apparatus are prevented from ‘demolishing’ the quantum state of the system which they are measuring.

Correlations between the two optical noise sources in an interferometer can be introduced using at least two methods. The optical cavities can be designed so that the optical field is strongly coupled to the mechanical system through an optical spring effect, described for example by Corbitt and Mavalvala [76]. These effects can be enhanced through the use of optical bars and optical

levers [77, 78]. Signal recycling (see Section 1.6.4), as used currently in the GEO 600 detector, can also introduce correlations between the shot noise and radiation pressure noise, leading to the possibility of achieving sensitivities below the SQL [79]. Another possible method of introducing such correlations is to measure the output signal after suitable filtering at optical frequencies through the inclusion of a long filtering Fabry-Perot cavity [80].

1.6 Interferometric techniques

A number of techniques can be used to improve the sensitivity of the basic Michelson interferometer layout shown in Figure 1.2. As discussed above, long interferometer arms are desirable to increase the absolute displacement caused by a gravitational wave. However, the curvature of the Earth and other geographical (and cost) factors limit the practical arm length to kilometer-scales. Additionally, extremely high laser powers are required to overcome the shot noise sensitivity limit in a simple Michelson detector. The laser power requirement can be significantly reduced if the laser beam is allowed to pass up and down each arm many times, as the apparent displacement of the mirror is multiplied by the number of times the light is reflected from it. This can be achieved by a delay line configuration or by the use of Fabry-Perot cavities in the interferometer arms.

1.6.1 Delay line interferometers

The effective arm-length of an interferometer can be increased by folding the optical path so that the light is reflected from the test mass mirror more than once. This is known as a delay-line interferometer [55]. Two possible delay line configurations are shown in Figure 1.3. The total phase change due to a gravitational wave builds up with each reflection, as long as the total storage time of the light in the arm is less than half of the period of the gravitational

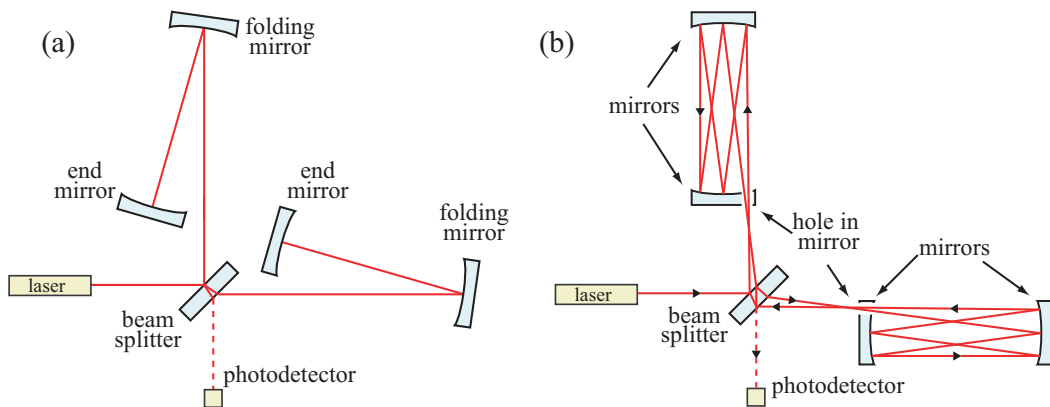


Figure 1.3: *Schematic diagram of two possible layouts for a delay line interferometer: (a) shows a folded arm scheme, while (b) illustrates a scheme in which the laser beam is reflected along each arm multiple times.*

wave. Multiple beam delay lines were used in some prototype gravitational wave detectors [58, 59, 61] but scattering proved to be a significant noise source in these designs. The GEO 600 detector, however, makes use of a folding mirror design (Figure 1.3 (a)) to double the effective arm-length of the detector [8].

1.6.2 Fabry-Perot arm cavities

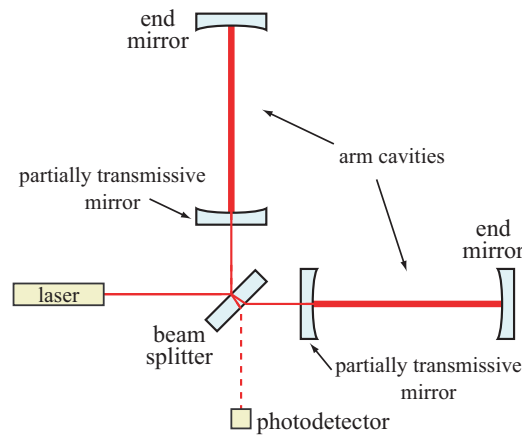


Figure 1.4: *A schematic diagram of a Fabry-Perot interferometer, which uses Fabry-Perot cavities in each arm. The inner mirrors are partially transmissive to allow light to enter, and leave, the cavity.*

An alternative scheme, used in the LIGO, VIRGO and TAMA detectors,

is a Fabry-Perot Michelson interferometer. In this configuration, Fabry-Perot optical cavities are used to form the arms of the interferometer, as shown in Figure 1.4. The laser beam is reflected back and forwards along itself in the cavity, resulting in light building up in the cavity. The input mirror of each cavity is partially transmissive, to allow some light to enter and leave the arm. The effective number of bounces along the cavity is determined by the optical properties of the mirrors. If the arm length changes, perhaps due to interaction with a gravitational wave, the resulting phase change is enhanced with each bounce the light makes along the cavity.

1.6.3 Power recycling

An interferometer is typically operated close to a dark fringe to minimise the photon shot noise, with most of the input light returned towards the laser. However, this light can be reused by placing another mirror (the power recycling mirror) between the laser and the beam splitter, thus reflecting the output light back into the interferometer, as shown in Figure 1.5. The interferometer can effectively be considered as a mirror when operated on a dark fringe, and the presence of the power recycling mirror forms a cavity between it and the interferometer. As light builds up in this cavity, more power is incident on the interferometer, resulting in higher light powers in the arms and increased sensitivity.

1.6.4 Signal recycling

In addition to recycling the light at the input port of the interferometer, it is possible to recycle the ‘signal’ light at the output port [81, 82]. A detector is normally operated locked close to a null in the interference pattern; a gravitational wave, or indeed any other differential motion of the test masses, produces a change in the phase of the light being recombined at the beam splitter, resulting in light leaking out of the output port. In the frequency domain,

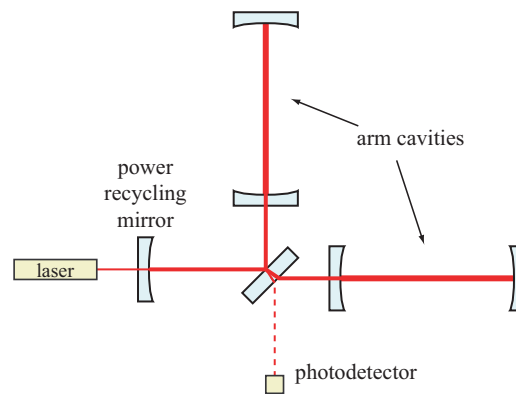


Figure 1.5: *A schematic diagram of a Michelson interferometer with a power recycling mirror at the input port, forming an optical cavity with the interferometer.*

this phase change creates sidebands on the ‘carrier’ laser light at the frequency of the gravitational wave. These sidebands do not interfere destructively, and so appear at the output of the interferometer.

A mirror placed between the output port of the beam splitter and the photodiode detector will effectively form a cavity with the interferometer, as shown in Figure 1.6. A signal sideband will be reflected back into the interferometer, where it resonates, increasing the signal size in a certain bandwidth. By changing the position of the signal recycling mirror to adjust the length of the signal recycling cavity, the frequency at which the interferometer is most sensitive can be tuned.

Three modes of signal recycling operation can be obtained by precise tuning of the position of the signal recycling mirror: broad-band signal recycling, resonant sideband extraction and de-tuned operation [83, 84, 85].

Narrow band signal recycling (from de-tuned operation) can be useful to provide increased sensitivity at frequencies where sensitivity is normally limited by shot noise and can be used in searches for continuous sources at specific frequencies. Signal recycling with a larger bandwidth can be used to optimise the detector frequency response to the signals expected from broadband and ‘chirp’ sources. Currently only the GEO 600 detector uses signal recycling [86].

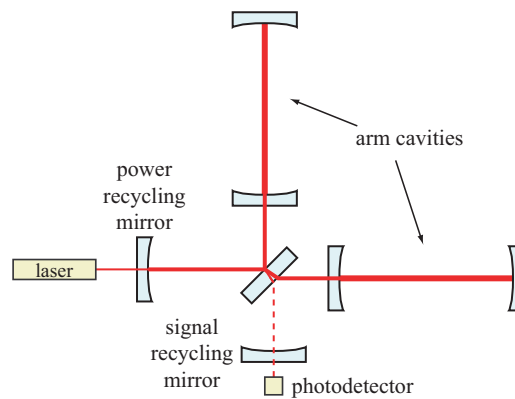


Figure 1.6: A schematic diagram of a Michelson interferometer with a signal recycling mirror at the output port. This mirror forms an optical cavity with the interferometer and allows the peak sensitivity to be tuned to specific frequency ranges.

1.7 Current interferometric detectors

The construction of a number of long-baseline gravitational wave detectors was begun in the mid-1990s at several sites around the world. The Laser Interferometer Gravitational Wave Observatory (LIGO) in the US consists of two widely separated detector facilities, one near Baton Rouge, Louisiana and the other near Hanford, Washington. Both sites have an interferometer with



Figure 1.7: The VIRGO interferometer at Cascina, Italy. Both 3 km long arms of the detector can be seen, meeting at the central station (right hand side) which houses the input and output optics.



Figure 1.8: *Left: A view along one 600 m long arm of the GEO 600 detector, with the end station housing the end test mass visible in the background. Right: A GEO 600 suspension, consisting of a triple pendulum, with a monolithic silica lowest stage.*

4 km long arms, while the Hanford site also houses a 2 km long detector within the same vacuum system. The French/Italian VIRGO detector near Pisa, shown in Figure 1.7, has 3 km long arms and makes use of a seven stage mirror suspension system to reduce seismic noise, allowing operation at frequencies down to 10 Hz. Two prototype Japanese detectors called TAMA and CLIO have been constructed [11, 87]. TAMA is located at the Tokyo Astronomical Observatory and has an arm length of 300 m, CLIO is situated in Kamioka mine where the seismic noise is two orders of magnitude lower than at the TAMA site. CLIO is intended to demonstrate the use of cryogenically cooled sapphire mirrors, and there are plans to adopt the design for a 3 km detector known as LCGT, also to be constructed in Kamioka mine [88].

The detectors discussed so far all make use of Fabry-Perot arm cavities and power recycling to increase the circulating laser power, and the mirrors are suspended by metal wires. The German / British GEO 600 detector (see Figure 1.8), situated near Hannover, makes use of several different techniques. GEO 600 uses a four pass delay line optical layout, with an effective arm length

of 1200 m, and includes a signal recycling mirror, allowing the peak sensitivity and detection bandwidth to be tuned to different frequencies. Thermal noise is reduced through the use of ultra low loss silica fibres to suspend the mirrors. Figure 1.9 shows the design sensitivity of GEO 600, operated with signal recycling de-tuned at 250 Hz.

Since the late summer of 2002, the LIGO detectors have completed five ‘science runs’, in which coincident data was taken over extended periods of time. The most recent science run involved observations by the LIGO detectors, GEO 600 and VIRGO, and ended in October 2007 after almost two years of data taking. GEO 600, TAMA and the ALLEGRO and AURIGA bar detectors took part in previous runs. Between the science runs, commissioning work was undertaken and the sensitivities of the various detectors was improved. Figure 1.10 shows the typical sensitivity of the GEO 600 detector during each science run. The results of the science runs have been used to

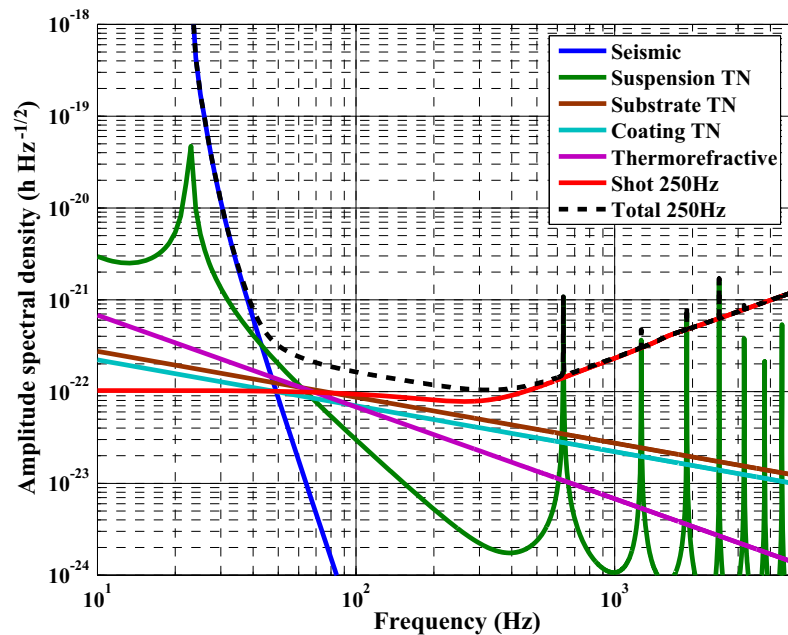


Figure 1.9: *The design sensitivity of GEO 600, showing the various noise curves for operation with signal recycling at 250 Hz de-tuning.*

set new limits on various astrophysical sources. For example, data from the

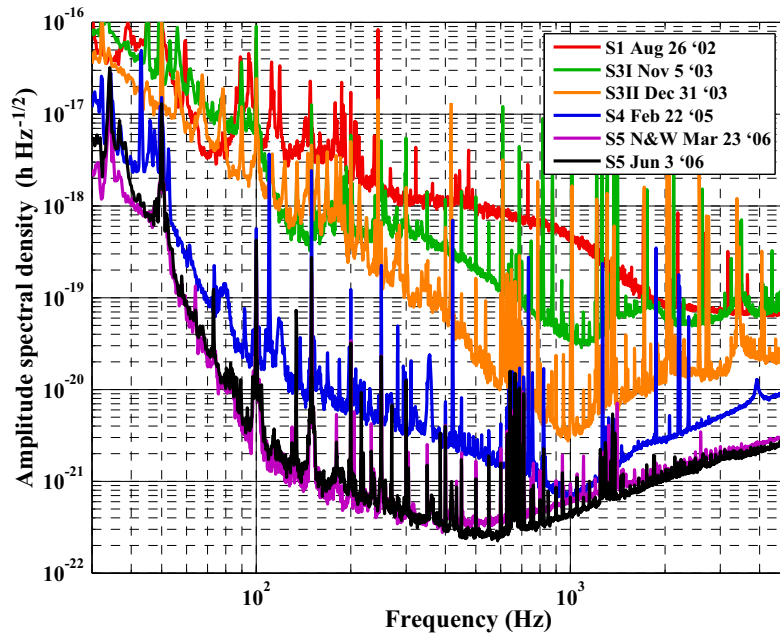


Figure 1.10: *The typical amplitude strain sensitivity of GEO 600 in each of the science runs between 2002 and 2007.*

fifth science run have been used to place a new upper limit on gravitational wave emission from the Crab pulsar [20], beating the spin-down limit, derived by assuming that all of the energy loss is due to gravitational radiation, by a factor of ~ 4 . This result, which assumes that the gravitational wave and electromagnetic emissions are phase-locked, implies that less than 6 % of the energy loss responsible for the spin-down is emitted as gravitational waves [20].

Many other interesting analyses have been performed, including searches for gravitational waves associated with gamma-ray bursts [89, 90] and SGR 1806-20, a hyperflare originating from a galactic neutron star [91]. In addition, cross-correlation searches for a stochastic background of gravitational waves have begun to explore the parameter space of models of gravitational radiation from cosmic strings [32].

1.7.1 Second generation detectors

There are plans in place for significant upgrades to both the LIGO and VIRGO detectors, known as Advanced LIGO and Advanced VIRGO. The Advanced LIGO project [92] aims to increase the peak sensitivity of the LIGO detectors by more than a factor of ten, increasing the volume of space from which gravitational waves could be detected by a factor of order one thousand. The second detector at the Hanford site will be increased in length from 2 km to 4 km. Each Advanced LIGO detector will incorporate a signal recycling mirror at the output port, allowing the interferometer response to be tailored to the type of source being searched for. The input laser power will be increased by a factor of 20, and the circulating power in the interferometer arms will be ~ 830 kW, compared to the initial LIGO value of ~ 10 kW. The 11 kg silica mirrors used in the initial LIGO detectors will be replaced with 40 kg mirrors of larger radius to reduce thermal noise and radiation pressure noise. The mirrors will be suspended from fused silica fibres based on those used in GEO 600, which will be supplied by the Institute for Gravitational Research in Glasgow. A complete suspension will consist of four pendulum stages, with an improved seismic isolation system designed to reduce the seismic cut-off frequency from 40 Hz to 10 Hz.

The installation of Advanced LIGO is planned to begin in 2011, with the initial tuning of the detectors expected to occur in 2013. Prior to the installation of Advanced LIGO facilities, a series of upgrades are being implemented to create Enhanced LIGO detectors which will be used for more science runs between 2009 and 2011. Similar plans are in place for the upgrade of the VIRGO detector to Advanced VIRGO.

GEO 600, with its shorter arms, will not be able to match the sensitivity of the second generation detectors. However, GEO 600 will operate (with some low-level commissioning work) while the LIGO detectors are off-line for the Enhanced LIGO installation to provide an ‘Astrowatch’ capability. In

the future, GEO 600 may be used to test new technologies, materials and interferometric techniques for use in the proposed third generation of detectors.

1.7.2 Future detectors

A number of factors suggest that improvements to the sensitivity of the second generation detectors will be challenging. At frequencies below ~ 400 Hz, the sensitivity is expected to be limited by thermal noise, particularly that arising from the optical coatings, while photon shot noise will be the major limitation at higher frequencies. Thermal noise can, in principle, be reduced by cooling the mirrors and by using materials of low mechanical loss at low temperature. Fused silica is not a promising candidate material for cooling as it is known to have a large mechanical loss peak at approximately 40 K [93].

The effects of shot noise can be reduced by increasing the laser power. However, the thermo-mechanical properties of silica make it likely that any increase of laser power beyond the Advanced LIGO design would result in significant thermal deformation of the mirrors, making stable operation of the interferometer difficult [94, 95]. Thus a material with a lower thermal expansion coefficient and higher thermal conductivity would be desirable if substantially higher laser powers are to be used.

The use of silicon optics has been proposed, as silicon is likely to meet both the low temperature thermal noise requirements and to have the ability to withstand high laser powers [94]. Silicon is not transparent to 1064 nm light, which is used in current gravitational wave detectors. However, current interferometer designs could incorporate silicon optics if a laser wavelength of 1.5 μm was used. Alternatively, interferometers using an all reflective topology based on diffractive optics have been proposed [96, 97].

Improved low-frequency sensitivity could be obtained by building future detectors underground, where levels of seismic noise are significantly lower. This approach, along with the use of cryogenic cooling, has been used for the

Japanese prototype CLIO, which is located in Kamioka mine. The same mine is the proposed location for the planned Large-Scale Cryogenic Gravitational Wave Telescope (LCGT) detector [88]. A major European Commission design study for a third generation detector known as the Einstein Telescope (ET) is currently underway with participation from groups across Europe [98].

1.8 Conclusion

Over the past eight years, the first generation of long-baseline interferometric gravitational wave detectors have been commissioned and have closely approached or achieved their design sensitivities. Several science runs have taken place in which various instruments in the world-wide network of detectors have operated in coincidence for extended periods. While gravitational waves have not yet been detected, analysis of the data obtained has allowed astrophysically useful upper limits to be placed on the gravitational wave emission of several sources. The next generation of detectors, consisting of major upgrades to the current LIGO and VIRGO detectors, are expected to begin operation before 2015, and it is widely expected that they will detect the first gravitational wave signals, heralding a new era in astronomy. Several challenges must be overcome to significantly improve upon the sensitivities of the second generation detectors. In particular, thermal noise is likely to limit detector sensitivity at low frequencies, while improved sensitivity at high frequency will require the thermal loading effects associated with high laser power to be overcome.

Chapter 2

Thermal noise in gravitational wave detectors

2.1 Introduction

Thermal noise arising from the thermal motion of the molecules in the mirrors and their suspensions sets an important limit to the sensitivity of interferometric gravitational wave detectors at frequencies up to approximately 500 Hz. The equipartition theorem states that any mechanical system will have a mean value of $\frac{1}{2}k_{\text{B}}T$ of thermal energy associated with each degree of freedom. This energy is stored in vibrations of the molecules making up the system, resulting in thermally induced motion of the macroscopic system. In the mirror suspensions of a gravitational wave detector, the thermal energy will excite the resonant modes of the test mass and the suspension fibres, resulting in a source of displacement noise in the measured position of the mirror faces. This noise can be of the same order as the displacement which would be caused by a gravitational wave, making reduction of thermal noise within the operational bandwidth of gravitational wave detectors an important area of research.

2.1.1 Brownian motion

Thermal motion in a mechanical system was first reported by the botanist Robert Brown in 1828 after he observed the irregular motion of pollen grains

and dust suspended in water [99]. Despite studies by a number of scientists, the source of this ‘Brownian motion’ remained unknown for several decades. Experiments by Gouy and Exner established that the motion was more rapid in less viscous liquids, and that the velocity of the dust particles rose as the temperature of the liquid was increased [100, 101]. However, it was not until 1905 that a full mathematical treatment of Brownian movement was presented in Einstein’s well-known paper [102]. Einstein realised that the motion arose from fluctuations in the rate of collisions between water molecules and the pollen grains, and showed that as a result of these impacts the grains lost kinetic energy. This was the first time that a dissipation process, in this case the loss of energy due to the viscosity of the fluid, had been related to random fluctuations, here the random displacement of the pollen grain.

An electrical equivalent to Brownian motion was discovered in 1927, when J. B. Johnson observed random voltage fluctuations across a resistor [103]. These fluctuations were shown to result from the thermal motion of the atoms in the conductor [104, 105], and to be related to the temperature T , the resistance of the wire R and the bandwidth of the measurement Δf as follows:

$$V^2(f) = 4k_B T R \Delta f. \quad (2.1)$$

2.1.2 The Fluctuation-Dissipation Theorem

Both Brownian motion and Johnson noise in a resistor show a link between fluctuations (in the position of a particle or of the voltage across a resistor) and dissipation (energy loss due to the viscosity of the fluid or the electrical resistance). More generally, all of the parameters which characterise a linear system in thermal equilibrium are found to undergo spontaneous thermally driven fluctuations, whose magnitude and frequency spectrum are related to the dissipative (i.e. real) part of the impedance of the system. The Fluctuation-Dissipation Theorem, derived by Callen et al in a series of papers in 1951-52 [106, 107, 108], states that the power spectral density $S_f(\omega)$ of the fluctuating

thermal force on a system is given by:

$$S_f(\omega) = 4k_B T \Re\{Z(\omega)\}, \quad (2.2)$$

where $Z(\omega)$ is the impedance of the system, defined as:

$$Z(\omega) \equiv F(\omega)/v(\omega), \quad (2.3)$$

for a force $F(\omega)$ applied to the system resulting in motion with a velocity of amplitude $v(\omega)$. Alternatively, the theorem can be written in terms of the power spectral density of the fluctuating motion of the system $S_x(\omega)$:

$$S_x(\omega) = \frac{4k_B T \Re\{Y(\omega)\}}{\omega^2}, \quad (2.4)$$

where $Y(\omega)$, the mechanical admittance of the system, is equal to $Z^{-1}(\omega)$. It is therefore possible to estimate the thermal noise spectrum of a mechanical system if the macroscopic impedance of the system can be determined.

It has been shown that the level of thermal noise in a system is related to the real (dissipative) part of the mechanical admittance of the system - also known as the mechanical conductance. By definition, this is related to the damping coefficient of the system. Thus the level of thermal noise is also related to the level of damping, or dissipation, present in the system. This can be illustrated clearly by considering the example of a damped harmonic oscillator [65]. Neglecting the fluctuating force responsible for thermal noise, the equation of motion of a damped harmonic oscillator of resonant frequency ω_0 and mass m is:

$$F = m\ddot{x} + b\dot{x} + kx, \quad (2.5)$$

where b is the damping coefficient and $k = m\omega_0^2$ is the spring constant of the oscillator. The displacement x and acceleration \ddot{x} of the oscillator can be expressed in terms of the velocity \dot{x} as follows:

$$x = \frac{\dot{x}}{i\omega} \quad \text{and} \quad \ddot{x} = i\omega\dot{x}. \quad (2.6)$$

The impedance can then be calculated from its basic definition:

$$Z \equiv \frac{F}{\dot{x}} \quad (2.7)$$

$$= \frac{mi\omega x}{\dot{x}} + \frac{b\dot{x}}{\dot{x}} + \frac{kx}{i\omega\dot{x}} \quad (2.8)$$

$$= b + i\omega m + \frac{k}{i\omega}, \quad (2.9)$$

from which the real part can be seen to be simply b . Application of the Fluctuation-Dissipation Theorem (Equation 2.2) allows the power spectral density of the fluctuating thermal force to be calculated:

$$S_f(\omega) = 4k_B T b. \quad (2.10)$$

To calculate the power spectral density of the thermal displacement of the system, the mechanical admittance $Y = Z^{-1}$ of the system must be calculated:

$$Y = \frac{1}{b + i\omega m - ik/\omega} \quad (2.11)$$

$$= \frac{b - i\omega m + ik/\omega}{b^2 + (\omega m - k/\omega)^2}. \quad (2.12)$$

The real part of the admittance is therefore given by:

$$\Re\{Y\} = \frac{b}{b^2 + (\omega m - k/\omega)^2}, \quad (2.13)$$

and can be substituted into Equation 2.12, to give the power spectral density of the thermal noise:

$$S_x(\omega) = \frac{k_B T b}{\omega^2 (b^2 + (\omega m - k/\omega)^2)}. \quad (2.14)$$

This simple example illustrates that the real part of the impedance of a mechanical system is related to the level of damping in the system. The concept of mechanical dissipation and its relationship to thermal noise in gravitational wave detectors will be discussed in detail throughout the rest of this chapter.

2.2 Sources of mechanical dissipation

It has been shown that the level of thermal noise in a mechanical system is related to the level of dissipation in the system. Broadly speaking there are two types of mechanical dissipation: external dissipation, in which energy is lost into the environment and internal dissipation, in which energy is ultimately lost as heat within the system.

A suspended test mass in a gravitational wave detector has many potential external sources of energy dissipation. Perhaps the most obvious analogy to the original pollen grain observations is gas damping [93], in which friction from gas molecules dissipates energy from the test mass pendulum. Other sources of external dissipation may include friction at the pendulum suspension points and recoil loss, in which energy is lost from the pendulum into the surrounding support structure [109]. External sources of damping can be minimised by careful design of the pendulum system. Gas damping, for instance, is reduced by operating the interferometer in ultra-high vacuum conditions. If these external sources of damping are suitably reduced, the dominant source of thermal noise will be the internal dissipation which occurs in the mirror and suspension fibres.

2.2.1 Dissipation from internal friction in materials

Internal dissipation arises from a process called anelasticity [110]. In an ideal elastic solid, an applied stress σ instantaneously creates a strain ϵ in the material, with Hooke's law defining the relationship between stress and strain as $\sigma = \epsilon Y$ where Y is the elastic modulus. For an anelastic material (i.e. most real materials), the stress-strain relationship is not instantaneous and the strain response will lag behind the applied stress, developing over a finite relaxation time. A periodic stress applied to the material can be written as:

$$\sigma = \sigma_0 e^{i\omega t}, \quad (2.15)$$

where σ_0 is the stress amplitude and ω is the angular frequency of the oscillation. Since the stress-strain relationship is linear, the resulting strain will also be periodic with the same angular frequency, but with a phase lag with respect to the stress. This can be expressed as:

$$\epsilon = \epsilon_0 e^{i\omega t - \phi}, \quad (2.16)$$

where ϕ is the angle by which the strain lags behind the stress, known as the loss angle. It can be shown that the loss angle, also described as the internal friction of the material, is a measure of the fractional energy dissipated per cycle of oscillation [110].

Anelasticity, and hence internal friction, can arise from many internal properties of a material which are a function of the internal stress [110, 111]. These internal degrees of freedom include the temperature and the density of point defects, dislocations and grain boundaries. If the internal stress in the material is altered, these properties typically require a finite period of time over which to respond to the new state of stress. The process by which internal degrees of freedom change often involve energy barriers which must be crossed, resulting in an exponential relaxation to the new equilibrium value, with a characteristic time τ . In many cases, the relaxation time obeys the Arrhenius equation [112]:

$$\tau = \tau_0 e^{\Delta E/k_B T}, \quad (2.17)$$

where ΔE is the energy barrier which must be overcome and τ_0 represents the characteristic time between attempts at crossing the barrier.

2.2.2 Harmonic oscillator with internal friction

Internal friction in a material has been shown to arise from the time delay between an applied stress and the development of the associated strain. In the frequency domain this appears as a phase lag ϕ between the applied force F and the response of the system x . This can be represented by a modified

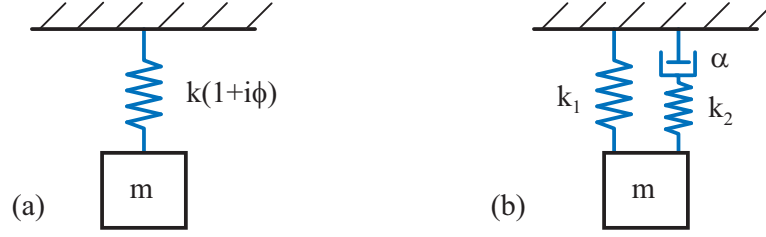


Figure 2.1: (a) A schematic diagram of a mechanical oscillator with a complex spring constant $k(1 + i\phi)$. (b) A schematic diagram representing a standard anelastic solid, with an ideal spring connected in parallel with a spring-dashpot combination, where k_1 and k_2 are spring constants and α is the impedance of the dashpot.

version of Hooke's law, involving a complex spring constant, as shown in Figure 2.1(a):

$$F = -k(1 + i\phi(\omega))x. \quad (2.18)$$

If the resonant modes of the suspended mirror system in a gravitational wave detector are modelled as harmonic oscillators with internal damping, the equation of motion can be written as:

$$m\ddot{x} = -k(1 + i\phi(\omega))x + F. \quad (2.19)$$

Using the standard expressions relating the acceleration and displacement to the velocity of a harmonic oscillator (see Equation 2.6), the force F on the oscillator can be expressed as:

$$F = i\omega m\dot{x} + \frac{k}{i\omega}(1 + i\phi(\omega))\dot{x}, \quad (2.20)$$

from which the impedance $Z = F/\dot{x}$ can be seen to be:

$$Z = \frac{k - \omega^2 m + ik\phi(\omega)}{i\omega}. \quad (2.21)$$

This expression can be inverted to give the admittance, which, after rationalising the denominator is:

$$Y = \frac{\omega k \phi(\omega) + i(\omega k - m\omega^3)}{(k - m\omega^2)^2 + k^2 \phi^2(\omega)}, \quad (2.22)$$

from which the real part can be seen to be:

$$\Re\{Y\} = \frac{\omega k \phi(\omega)}{(k - m\omega^2)^2 + k^2 \phi^2(\omega)} \quad (2.23)$$

Application of the Fluctuation-Dissipation Theorem shows that the thermal noise power spectral density is given by:

$$S_x(\omega) = \frac{4k_B T \Re\{Y(\omega)\}}{\omega^2} \quad (2.24)$$

$$= \frac{4k_B T k \phi(\omega)}{\omega [(k - m\omega^2)^2 + k^2 \phi^2(\omega)]}. \quad (2.25)$$

This expression can be simplified by noting that $k = \omega_0^2 m$, to give the following expression for the thermal noise spectral density of an oscillator of resonant frequency ω_0 , in terms of its mass and mechanical loss:

$$S_x(\omega) = \frac{4k_B T}{\omega} \frac{\omega_0^2 \phi(\omega)}{m[\phi^2(\omega)\omega_0^4 + (\omega_0^2 - \omega^2)^2]}. \quad (2.26)$$

2.2.3 The form of internal dissipation - Debye theory

The complex spring constant given in Equation 2.18 is usually an excellent approximation of anelastic effects [111]. It is not, however, exact, and a more accurate model of an anelastic solid can be obtained by considering an ideal

spring connected in parallel with a combination of a spring and a dashpot of impedance α , as shown in Figure 2.1 (b). Zener [113] showed that, for an anelastic solid with no other similar relaxation times, this model results in a loss angle ϕ with a characteristic frequency dependence, given by:

$$\phi \approx \Delta \frac{\omega\tau}{1 + \omega^2\tau^2} \quad (2.27)$$

where $\Delta \equiv k_2/k_1$ is the relaxation strength, and $\tau = \alpha/k_2$ is the relaxation time. The dissipation peaks at a frequency $\omega_{\text{peak}} = \tau^{-1}$: this is known as a Debye peak. Many authors have reported that the internal friction in a wide variety of materials is largely independent of frequency [114, 115, 116, 117, 118, 119, 120]. Since an anelastic relaxation process results in the dissipation having a Debye peak at a characteristic frequency, this result may at first be surprising. However, a material may have several Debye peaks at frequencies separated by many orders of magnitude. At frequencies far from any of the peaks, the combined effect of the tails of these peaks is effectively constant with frequency. The operating frequency band of gravitational wave detectors (from ~ 10 Hz to several thousand Hz) usually lies in such a region. One anelastic relaxation process, known as thermoelastic damping, gives rise to a dissipation peak which can lie in or close to this frequency band. Thermoelastic damping is discussed in Section 2.4.

2.2.4 Thermal noise associated with a single resonant mode

A mirror suspension system in a gravitational wave detector has many resonant modes which can be thermally excited. These modes include the pendulum mode of the suspension, the bending modes (or ‘violin’ modes) of the suspension fibres and the internal modes of the mirror itself. Of these, usually only the violin modes occur at frequencies which lie within the sensitive detection band of the interferometer. The mirror suspension is typically designed such

that its pendulum modes occur at frequencies below the detection band, while the internal modes of the mirrors occur at several tens of kilohertz, well above the detection band. For the pendulum modes and the internal mirror modes, since the peak thermal noise occurs far from the interferometer detection band, it is therefore the off-resonance thermal noise which sets a limit to detector sensitivity.

Equation 2.26 can be simplified by approximation to examine the three cases of interest discussed above: that is, the thermal noise at frequencies far below, equal to and far above the resonant frequency of a mode. First, consider the thermal noise at frequencies far below the resonance, ie $\omega \ll \omega_0$:

$$S_x(\omega) = \frac{4k_B T}{\omega} \frac{\omega_0^2 \phi(\omega)}{m[\phi^2(\omega)\omega_0^4 + (\omega_0^2 - \omega^2)^2]} \quad (2.28)$$

$$\approx \frac{4k_B T}{\omega} \frac{\omega_0^2 \phi(\omega)}{m(\phi^2(\omega)\omega_0^4 + \omega_0^4)} \quad (2.29)$$

$$\approx \frac{4k_B T \phi(\omega)}{m\omega\omega_0^2(\phi^2(\omega) + 1)}. \quad (2.30)$$

Now if $\phi^2(\omega) \ll 1$, which is a valid assumption for the low loss materials used in the mirrors of gravitational wave detectors, the thermal noise spectral density can be approximated as:

$$S_x(\omega) \approx \frac{4k_B T}{m\omega_0^2} \frac{\phi(\omega)}{\omega}, \quad (2.31)$$

This equation can be used to calculate the thermal noise in the gravitational wave detection band from an internal resonance of the mirror. The thermal noise at frequencies well above a resonance can be calculated in a similar way. In this case $\omega \gg \omega_0$ and thus Equation 2.26 can be approximated as:

$$S_x(\omega) \approx \frac{4k_B T \phi(\omega)\omega_0^2}{m\omega[\omega^4 + \omega_0^4\phi^2(\omega)]}, \quad (2.32)$$

Again assuming that $\phi^2(\omega) \ll 1$, this can be simplified to:

$$S_x(\omega) \approx \frac{4k_B T \omega_0^2 \phi(\omega)}{m\omega^5}. \quad (2.33)$$

Equations 2.31 and 2.33 show that at frequencies far from a resonance, the thermal noise power spectral density due to that resonance is directly proportional to the mechanical loss $\phi(\omega)$. Off-resonance thermal noise can therefore be reduced by using materials with a low mechanical loss. However, since the total thermal energy associated with the resonance is $\frac{1}{2}k_B T$, it follows that the noise spectral density close to the resonance frequency must be very high. In this case, $\omega = \omega_0$ and Equation 2.26 becomes:

$$S_x(\omega) = \frac{4k_B T}{m\omega_0^3 \phi(\omega_0)}, \quad (2.34)$$

and it can be seen that the power spectral density of thermal motion at the resonant frequency of a mode is inversely proportional to the mechanical loss.

Reducing the mechanical loss effectively confines more of the thermal motion into a narrow frequency band centred on the resonance, resulting in a narrower and higher thermal noise peak at the resonant frequency and lower off-resonance thermal noise. This is demonstrated in Figure 2.2, which shows the thermal displacement noise spectrum for a mode of two otherwise identical mechanical oscillators with different mechanical loss factors. It was mentioned above that several violin modes of the suspension fibres typically occur within the gravitational wave detection band. The use of low loss suspension materials ensures that the thermal noise peaks from the violin modes are suitably narrow, and thus they can be easily removed from the interferometer signal by notch filtering, with minimal reduction of the useful bandwidth of the detector.

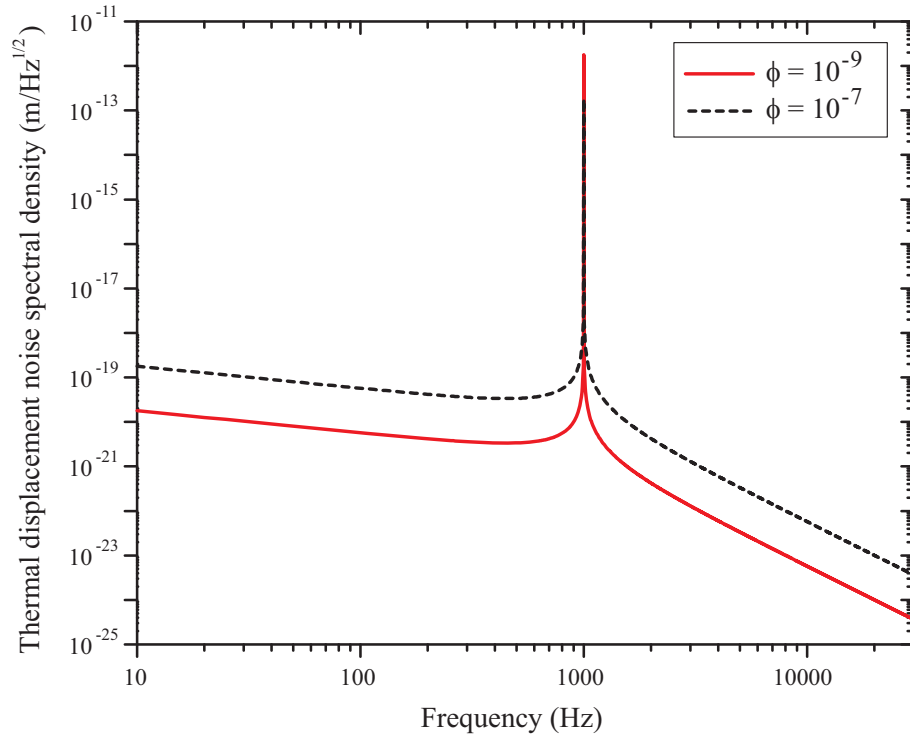


Figure 2.2: *Thermal noise displacement spectra for two mechanical oscillators each of $f_0=1$ kHz, $m=20$ kg at $T=290$ K and having differing mechanical loss. The solid, red line shows the thermal noise for a loss of $\phi = 1 \times 10^{-9}$ while the black, dashed line is for $\phi = 1 \times 10^{-7}$. The lower loss material has lower off-resonance thermal noise, as more of the thermal motion is concentrated close to the resonant frequency.*

2.3 Relationship between mechanical loss and the quality factor

The mechanical quality factor, Q is a dimensionless quantity related to the dissipation of an oscillator at a resonant frequency, f_0 :

$$Q(f_0) \equiv 2\pi \frac{E_{\text{stored}}}{E_{\text{lost per cycle}}} \equiv \frac{f_0}{\Delta f}, \quad (2.35)$$

where E_{stored} is the total energy stored in the oscillator, $E_{\text{lost per cycle}}$ is the energy dissipated with each cycle of oscillation and Δf is the width of the resonance peak measured at half of its maximum power. Thus it can be seen that oscillators with low levels of energy dissipation will have narrow resonances.

From this definition, the quality factor can be related to the loss angle (the angle by which the induced strain lags behind the stress applied to a system) by considering the energy stored and dissipated in an oscillating system. For a mechanical oscillator of angular frequency ω_0 with displacement $x = Ae^{i\omega_0 t}$ where the restoring force is given by $F_R = -kx$, the stored potential energy is given by:

$$E_{\text{stored}} = \frac{1}{2}kA^2, \quad (2.36)$$

where A is the amplitude of the oscillation. The energy lost per cycle can be found by including the effect of the dissipative part of the spring constant (using Equation 2.18).

$$\begin{aligned} F_R &= -k(1 + \phi(\omega_0))x \\ &= -kAe^{i(\omega_0 t + \phi(\omega_0))} \\ &= -kA\{\cos(\omega_0 t + \phi(\omega_0)) - ikA \sin(\omega_0 t + \phi(\omega_0))\}. \end{aligned} \quad (2.37)$$

The real part of this expression can be integrated to find the work done in one period of oscillation, T :

$$\begin{aligned} W &= \int F_R dx \\ &= \int -kA \cos(\omega_0 t + \phi(\omega_0)) dx \\ &= \int_0^T kA \cos(\phi(\omega_0)t + \phi(\omega_0)) A \omega_0 \sin \omega_0 t dt \\ &= \frac{1}{2}k\omega_0 A^2 T \sin \phi(\omega_0). \end{aligned} \quad (2.38)$$

Therefore the quality factor (Equation 2.35) is given by:

$$\begin{aligned}
 Q &= \frac{2\pi k A^2}{k\omega_0^2 A^2 T \sin \phi(\omega_0)} \\
 &= \frac{1}{\sin \phi(\omega_0)} \\
 &\approx \frac{1}{\phi(\omega_0)}, \tag{2.39}
 \end{aligned}$$

when $\phi(\omega_0)$ is small. Thus the mechanical loss can be determined by measuring the quality factor of an oscillator at its resonant frequencies. If the damping is assumed to be essentially frequency independent (i.e. structural damping) then the mechanical loss at frequencies of interest for gravitational wave detectors can be approximated from these measurements. Alternatively, the loss can be measured over a range of frequencies by measuring many modes of a variety of samples of different sizes.

2.4 Thermoelastic damping

Thermoelastic damping is an anelastic relaxation process related to the flow of heat in a material, and arises from the coupling of temperature and strain in a body via the thermal expansion coefficient. Thermoelastic dissipation in thin beams and fibres was studied by Zener, who calculated the differential heating across a fibre as it vibrates [121, 122]. If a thin beam is deflected into an arc, the part of the beam under compression will heat up, while the opposite side of the beam will expand under tension and cool down, as shown in Figure 2.3. A thermal gradient is therefore created, leading to the flow of heat across the thickness of the beam. If, instead of undergoing a static deflection, the beam is vibrating there will be an oscillating heat flow as each side of the beam is compressed and stretched in turn. This heat flow is a source of dissipation, and will have a peak at a frequency related to the time taken for heat to flow across the beam.

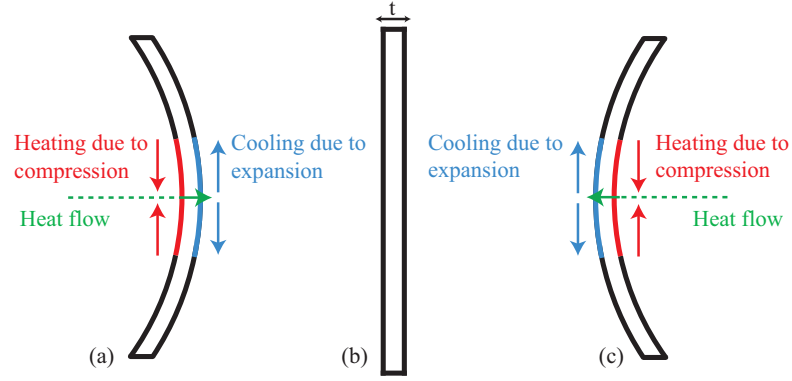


Figure 2.3: A schematic diagram of a bending mode of a rectangular cross-section bar. Initially (a), the bar is at maximum deformation with one side warming up under compression while the other side cools under tension. As the bar oscillates through the un-deflected position (b) and bends in the opposite direction (c), the heating and cooling, and thus the direction of heat flow, is reversed.

When the beam, or indeed any body, is at rest, localised statistical temperature fluctuations throughout the material result in deformation of the material, with the strain produced being governed by the thermal expansion coefficient, $\alpha = l^{-1} \frac{dl}{dT}$. The level of thermoelastic dissipation in a flexure is calculated by Zener [121, 122] to be:

$$\phi(\omega) = \frac{Y\alpha^2 T}{\rho C} \frac{\omega\tau}{1 + \omega^2\tau^2}, \quad (2.40)$$

where Y is Young's modulus, ρ is density, C is specific heat capacity and τ is the relaxation time. The relaxation time is related to the time taken for heat to flow across the beam, and sets a characteristic frequency $f_{char} = (2\pi\tau)^{-1}$ at which the maximum thermoelastic loss occurs. For a rectangular cross section fibre, known as a ribbon, the relaxation time can be shown to be:

$$\tau = \frac{\rho C t^2}{\pi^2 \kappa}, \quad (2.41)$$

where t is the thickness of the ribbon and κ is thermal conductivity [110]. For a circular cross section fibre of diameter d , the thermoelastic relaxation time

is given by [110]:

$$\tau = \frac{\rho C d^2}{13.55 \kappa}. \quad (2.42)$$

This theory has direct application in the estimation of the thermoelastic thermal noise in the mirror suspension fibres used in gravitational wave detectors. Recent work has extended this theory to include the effects of the temperature dependence of the Young's modulus, with the interesting result that the effective thermal expansion coefficient of a suspension fibre material could be set to zero if an appropriate stress is applied to a fibre [123]. It is therefore possible that careful design of the suspension fibres could lead to the nulling of suspension thermoelastic noise.

2.5 Thermal noise in a multi-resonance system

The thermal noise model described by Equation 2.26 is appropriate for a single resonance of a mechanical system. In practice, the laser beam reflected from the front face of the mirror in a gravitational wave detector senses the total thermal displacement arising from a large number of the resonant modes of the suspended mirror. Early models assumed that the motion of each mode was uncorrelated and that the total thermal noise power spectral density could be calculated simply by summing the contribution of each individual mode [111] as calculated using Equation 2.31. Gillespie and Raab [124] derived the following expression for the total power spectral density of the thermal motion associated with the internal resonant modes of a mirror:

$$S_x(\omega) = \sum \frac{4k_B T \phi_n(\omega)}{\alpha_n m \omega_n^2 \omega}, \quad (2.43)$$

where ϕ_n is the loss factor of the n^{th} mode of resonant frequency ω_n . α_n represents the coupling between a particular mechanical mode of the mirror and the laser beam [124].

However, the assumption that the modes are uncorrelated implies that each mode has a separate Langevin thermal driving force, which is only the case if

the mechanical dissipation is homogeneously distributed throughout the test mass [125]. In the case of spatially inhomogeneous dissipation which occurs, for example, due to the presence of lossy mirror coatings or at the attachment points of the suspension fibres, it is possible that the thermal motion of different modes may have some correlation, thus making the simple mode summation technique inadequate to predict the expected thermal noise levels correctly. This was pointed out by Levin [125], who along with others [126, 127] has developed an alternative, direct method of calculating the internal thermal noise which can account for the distribution of loss throughout the system and for the precise shape of the laser beam.

Levin's approach involves the direct application of the fluctuation dissipation theorem to the interferometer readout of the position of the test mass face, weighted by the Gaussian intensity profile of the sensing laser beam. To calculate the thermal noise a notional pressure, of the same spatial profile as the intensity of the laser beam spot on the test mass, is applied to the front face of the test mass and the resulting power dissipated in the mass is calculated. Application of the fluctuation dissipation theorem then allows the power spectral density of thermal displacement, $S_x(f)$, to be calculated as:

$$S_x(f) = \frac{2k_B T W_{\text{diss}}}{\pi^2 f^2 F_0^2}, \quad (2.44)$$

where F_0 is the peak amplitude of the notional oscillatory force and W_{diss} is the power dissipated in the mirror. The dissipated power is given by:

$$W_{\text{diss}} = 2\pi f \int_V \epsilon(x, y, z) \phi(x, y, z, f) dV, \quad (2.45)$$

where ϵ is the energy density of the elastic deformation under the peak applied pressure F_0 . For spatially homogeneous loss, the formula for W_{diss} becomes:

$$W_{\text{diss}} = 2\pi f U_{\text{max}} \phi(f), \quad (2.46)$$

where U_{max} is the total energy associated with the peak elastic deformation of the test mass.

If the laser beam radius is considerably smaller than the radius of the test mass, the test mass can be modelled as being half-infinite and U_{\max} can be calculated from elasticity theory [126, 127]. In this case, the power spectral density of the Brownian thermal noise, $S_x^{ITM}(f)$, can be shown to be [126]:

$$S_x^{ITM}(f) = \frac{2k_B T}{\pi^{3/2} f} \frac{1 - \sigma^2}{Y w_0} \phi_{\text{substrate}}(f), \quad (2.47)$$

where $\phi_{\text{substrate}}(f)$ is the mechanical loss of the test-mass material, Y and σ are the Young's modulus and Poisson's ratio of the material respectively and w_0 is the radius of the laser beam where the *electric field* has fallen to $1/e$ of the maximum intensity.¹

An expression for the thermal noise power spectral density of a finite sized test mass, $S_x^{\text{FTM}}(f)$, was also derived by Bondu et al [126], and corrected by Liu and Thorne [127]:

$$S_x^{\text{FTM}}(f) = \frac{4k_B T}{\pi f} \phi_{\text{substrate}}(f) (U_o + \Delta U), \quad (2.48)$$

where the term $(U_o + \Delta U)$ represents the elastic deformation energy, defined explicitly by Liu and Thorne [127].

The half-infinite mass approximation is found to over-estimate the thermal noise power spectral density, $S_x^{ITM}(f)$. Liu and Thorne calculate a correction factor, C_{FTM} , to Equation 2.47 for the finite test-mass case, such that $S_x^{\text{FTM}}(f) = C_{\text{FTM}}^2 S_x^{ITM}(f)$. For an Advanced LIGO type mirror, they found that this correction factor varied between 0.96 and 0.66 for beam radii ranging from 1 to 6 cm respectively.

2.5.1 Inhomogeneous loss and coating thermal noise

Equations 2.44 and 2.45 show that the level of thermal noise is directly related to the power dissipated in the test mass when a notional oscillating pressure

¹The radius at the point where the *intensity* has fallen to $1/e$ of the maximum value, $r_0 = w_0/\sqrt{2}$, is also widely used in thermal noise literature.

is applied to the surface. The power dissipated at any point in the mass is proportional to both the elastic energy associated with the deformations caused by the pressure and the mechanical loss at that point [125, 127]. Since most of the deformation occurs close to the point where the pressure is applied, it follows that a source of dissipation located close to the front face of the mass will contribute more to the thermal noise read out by the laser beam than an identical source of dissipation located further from the front face. The spatial distribution of mechanical loss throughout the volume of a test-mass must therefore be considered when calculating the expected level of thermal noise. Thus to reduce thermal noise, sources of dissipation should ideally be located as far as possible from the front surface of the test mass.

This realisation is of great significance, as interferometric gravitational wave detectors require the use of multi-layer dielectric coatings to form highly reflecting mirrors on the front faces of the test masses. The dissipation of these coatings has been shown to be in the order of $2 - 4 \times 10^{-4}$ [128, 129, 130, 131]. This is several orders of magnitude higher than the dissipation of the silica substrate material, which may be as low as $\sim 1 \times 10^{-9}$ [132]. Thermal noise associated with the reflective coatings will therefore potentially be the dominant source of thermal noise in a gravitational wave detector. This has led to a programme of research, involving a number of research groups worldwide, aimed at quantifying and studying ways of reducing the mechanical dissipation of the coating materials, and is the motivation for much of the work presented in this thesis.

2.5.1.1 Calculation of coating thermal noise

Nakagawa et al [133] applied Levin's method to approximate the thermal noise in a coated mirror by modelling a multi-layer reflective coating as a thin surface layer of thickness d and mechanical loss ϕ_{coating} , with the same material properties as the test-mass substrate. Nakagawa showed that the total power

spectral density of the thermal noise associated with such a mirror is given by:

$$S_x^{total}(f) = \frac{2k_B T}{\pi^{3/2} f} \frac{1 - \sigma^2}{w_0 Y} \left(\phi_{\text{substrate}} + \frac{2}{\sqrt{\pi}} \frac{(1 - 2\sigma)}{(1 - \sigma)} \frac{d}{w_0} \phi_{\text{coating}} \right), \quad (2.49)$$

where $\phi_{\text{substrate}}$ is the mechanical loss of the mirror substrate material.

In Harry et al [128] an expression incorporating the effects of the layer structure of the reflective coating and the differing material properties of the coating and the substrate is derived. Since the reflective coating is not homogeneous, but is made of alternating layers of two materials (SiO_2 and Ta_2O_5), possible anisotropy of the coating mechanical loss factor must be taken into account. Harry et al consider the coating mechanical loss factor to have two components, ϕ_{\perp} and ϕ_{\parallel} , associated with strains parallel and perpendicular to the coating surface respectively. The Brownian thermal noise power spectral density of a coated mirror can be shown to be [128]:

$$\begin{aligned} S_x(f) = & \frac{2k_B T}{\pi^{3/2} f} \frac{1 - \sigma^2}{w_0 Y} \left\{ \phi_{\text{substrate}} + \frac{1}{\sqrt{\pi}} \frac{d}{w_0} \frac{1}{YY'(1 - \sigma'^2)(1 - \sigma^2)} \right. \\ & \times [Y'^2(1 + \sigma)^2(1 - 2\sigma)^2 \phi_{\parallel} \\ & + YY'\sigma'(1 + \sigma)(1 + \sigma')(1 - 2\sigma)(\phi_{\parallel} - \phi_{\perp}) \\ & \left. + Y^2(1 + \sigma')^2(1 - 2\sigma')^2 \phi_{\perp}] \right\}, \quad (2.50) \end{aligned}$$

where f is the frequency in Hz, T is the temperature in Kelvin, Y and σ are the Young's modulus Poisson's ratio of the substrate, Y' and σ' are the Young's modulus Poisson's ratio of coating, ϕ_{\parallel} and ϕ_{\perp} are the mechanical loss values for the coating for strains parallel and perpendicular to the coating surface, d is the coating thickness and w_0 is the laser beam radius. In the case where $Y' = Y$, $\sigma' = \sigma$ and $\phi_{\perp} = \phi_{\parallel}$, this equation agrees with the result of Nakagawa et al (Equation 2.49).

Harry et al note that for fused silica substrates coated with alternating layers of SiO_2 and Ta_2O_5 , the Poisson's ratio of the coating is likely to be small enough that Equation 2.50 can be approximated to within $\approx 30\%$ by

setting $\sigma' = \sigma = 0$ [128]:

$$S_x(f) = \frac{2k_B T}{\pi^{3/2} f} \frac{1}{w_0 Y} \left\{ \phi_{sub} + \frac{1}{\sqrt{\pi}} \frac{d}{w_0} \left(\frac{Y'}{Y} \phi_{\parallel} + \frac{Y}{Y'} \phi_{\perp} \right) \right\}. \quad (2.51)$$

This expression is a significant simplification of Equation 2.50, and is useful for estimating the expected level of thermal noise. It should be noted that Equations 2.49 to 2.51 all represent the sum of the power spectral density of Brownian thermal noise from the coating and the substrate. The thermal noise power spectral density associated with the coating alone can be obtained explicitly by expanding the second term in Equation 2.51:

$$S_x(f) = \frac{2k_B T}{\pi^2 f Y} \frac{d}{w_0^2} \left(\frac{Y'}{Y} \phi_{\parallel} + \frac{Y}{Y'} \phi_{\perp} \right). \quad (2.52)$$

It can be seen that the coating thermal noise is a function of the Young's modulus of the substrate material and thus the same coating may have a different level of thermal noise when applied to different substrates.

It is interesting to note that the coating thermal noise varies as w_0^{-2} while the substrate thermal noise, arising from the homogeneous dissipation in the test mass itself, varies as w_0^{-1} . Thus one possible way to reduce thermal noise in general, and coating thermal noise in particular, is to use laser beams of larger radius. In addition, the standard Gaussian beam profile is not optimum from a thermal noise perspective, as it averages the thermal displacement of the test mass over a relatively small region. The use of different beam geometries is an area of active research [134, 135, 136, 137, 138, 139].

2.6 Thermoelastic noise

Thermoelastic dissipation has been discussed in the context of flexural vibrations of a thin beam, in which energy is dissipated as the result of heat flow from the side of the beam under compression to the side under tension. Thermoelastic dissipation is also of relevance when considering the expected thermal noise

of the test mass mirrors in gravitational wave detectors. Deformations associated with statistical fluctuations in the temperature of a mirror will result in displacements of the front face of the mirror, through the coefficient of thermal linear expansion of the mirror substrate. In certain crystalline materials which are of interest for use as mirror substrates such as sapphire [140] and silicon [95], this thermoelastic thermal noise is likely to be more significant than Brownian thermal noise. The power spectral density of thermoelastic thermal noise, $S_{\text{TE}}(f)$ in a mirror (approximated as half-infinite with respect to the radius of the laser beam incident on it) has been calculated by Braginsky et al [140] to be:

$$S_x^{\text{TE}}(f) = \frac{\sqrt{2}}{\pi^{5/2}} \frac{k_B T^2 \alpha^2 (1 + \sigma)^2 \kappa}{\rho^2 C^2 r_0^3 f^2}, \quad (2.53)$$

where α is the coefficient of linear thermal expansion, C is specific heat capacity, κ is thermal conductivity, ρ is density and r_0 is the radius of the laser beam at which the intensity has fallen to $1/e$ of the maximum value. This expression is strictly only accurate in the case where the test mass is large with respect to the size of the laser beam spot. A correction factor for the case of a finite sized test mass was derived by Liu and Thorne [127]. This factor is dependent on the test mass dimensions, and for typical test masses is of the order of unity.

2.6.1 Coating thermoelastic noise

In a coated test mass additional thermoelastic effects resulting from the differing thermo-mechanical properties of the coating and the substrate have been shown to occur [141, 142]. The power spectral density of the thermoelastic thermal noise arising from the presence of the coating has been shown by Fejer and Braginsky [141, 142] to be given by:

$$S_x(f) \approx \frac{8k_B T^2}{\pi \sqrt{\pi f}} \frac{d^2}{w_0^2} (1 + \sigma_s)^2 \frac{C_{\text{avg}}^2}{C_s^2} \frac{\alpha_s^2}{\sqrt{\kappa_s C_s}} \tilde{\Delta}^2, \quad (2.54)$$

where the subscript s denotes a property of the substrate and where $\tilde{\Delta}^2$ is given by:

$$\tilde{\Delta}^2 \equiv \left\{ \frac{C_s}{2\alpha_s C_{\text{avg}}} \left(\frac{\alpha}{1-\sigma} \left(\frac{1+\sigma}{1+\sigma_s} + (1-2\sigma_s) \frac{Y}{Y_s} \right) \right)_{\text{avg}} - 1 \right\}^2. \quad (2.55)$$

In these equations the averaging takes into account the relative thicknesses of the alternating coating layers. The form of the averaging operation is given by [142]:

$$(X)_{\text{avg}} \equiv \frac{d_a}{d_a + d_b} + \frac{d_b}{d_a + d_b}, \quad (2.56)$$

where the coating is considered to consist of alternating layers of two types of material, labelled a and b, which are d_a and d_b in thickness respectively.

2.7 Suspension thermal noise sources

Thermal noise resulting from the test mass and coating materials was discussed in the previous section. Thermal noise associated with the resonant modes of the suspension system is considered briefly here.

2.7.1 Pendulum mode

As noted in Chapter 1, the mirrors in a gravitational wave detector are suspended as pendulums to attenuate seismic noise. The thermal noise associated with the pendulum mode of the suspended mass is a function of the mechanical loss of the material of the suspension fibres. However, most of the energy in a pendulum is stored as potential energy via the Earth's gravitational field rather than in the elastic deformation of the suspension wire material. Only the fraction of the total energy which is stored in the suspension fibres can thus be dissipated. This results in the loss factor of a pendulum being lower than that of the material used in the fibres suspending it. It can be shown [111] that the loss of a pendulum is related to the loss of the suspension fibre

material by:

$$\phi_{\text{pend}}(\omega_0) \simeq \phi_{\text{material}}(\omega_0) \frac{k_{\text{fibre}}}{k_{\text{grav}}}, \quad (2.57)$$

where k_{fibre} is the elastic spring constant of the wire and k_{grav} is the effective ‘spring constant’ associated with the gravitational field, that is $k_{\text{grav}} = mg/l$ where m is the mass of the mirror and l is the length of the wire. The elastic spring constant for a pendulum suspended from n wires is:

$$k_{\text{fibres}} = \frac{n\sqrt{TYI}}{2l^2}, \quad (2.58)$$

where T is the tension in each wire, Y is the Young’s modulus and I is the moment of inertia of the wire cross section. Thus the mechanical loss of the pendulum is found to be:

$$\phi_{\text{pend}}(\omega_0) \simeq \phi_{\text{mat}}(\omega_0) \frac{n\sqrt{TYI}}{2mgl}. \quad (2.59)$$

The factor by which the loss of the material is reduced is known as the dilution factor D which, noting that $mg/n = T$, can be expressed as:

$$D = \frac{2l\sqrt{T}}{\sqrt{YI}}. \quad (2.60)$$

This analysis assumes that each wire bends only at the top, close to the suspension point. It can be generalised by introducing a factor ξ which takes the value $\xi = 1$ if the wires are constrained to bend only at the top and $\xi = 2$ if the wires can bend at both the top and bottom [143]:

$$\phi_{\text{pend}}(\omega_0) \simeq \phi_{\text{mat}}(\omega_0) \frac{\xi n\sqrt{TYI}}{2mgl}. \quad (2.61)$$

The power spectral density of the pendulum thermal noise in the gravitational wave band (at frequencies significantly higher than the pendulum frequency, ω_0) can be found using Equation 2.33:

$$S_x(\omega) \approx \frac{4k_B T \phi_{\text{pend}}(\omega) \omega_0^2}{m \omega^5} \quad (2.62)$$

$$\approx \frac{2k_B T \xi n \sqrt{TYI} \omega_0^2}{m^2 g l \omega^5} \phi_{\text{mat}}(\omega), \quad (2.63)$$

where m is the mass of the test mass and ω is the angular frequency in the operating band of the detector.

2.7.2 Violin modes of the suspension fibres

Finally, the effect on the displacement of the front face of the mirror of the suspension fibres vibrating in their ‘violin’ modes must be taken into account. The violin modes form a harmonic series, with many modes typically lying within the interferometer’s operating frequency band. As with the pendulum mode, the loss of a violin mode is reduced from the intrinsic loss of the material by some dilution factor. Assuming that the loss in the suspension fibres is spatially homogeneous, and that the rocking mode of the pendulum is constrained, then the loss of the first violin mode will be twice that of the pendulum mode [120, 143]. The violin mode thermal displacement couples to the displacement of the test mass with a suppression factor m/m_{fibre} , where m is the mass of the pendulum and m_{fibre} is the mass of the suspension fibre [144].

For a low loss silica suspension, the thermally induced motion of the test mass due to the violin modes will be concentrated in a narrow bandwidth around the violin frequencies, resulting in several spikes of noise in the detector readout. However, these violin mode thermal noise peaks can easily be notch filtered out of the interferometer signal [145], with only a small reduction in the useable bandwidth of the detector.

2.8 Total thermal noise in a detector mirror

To calculate the total thermal noise in a single interferometer mirror, the thermally driven motion of the various resonances of the system must be appropriately combined. The various contributions to the total thermal displacement noise can be summarised as follows:

- Substrate thermal noise

- Due to intrinsic mechanical loss of the test mass material (Equation 2.47).
- Due to thermoelastic effects arising from temperature fluctuations in the test mass (Equation 2.54).
- Coating thermal noise
 - Due to the intrinsic mechanical loss of the coating materials (Equation 2.52).
 - Due to thermoelastic effects arising from temperature fluctuations and the differing thermodynamic properties of the coating and substrate (Equation 2.54).
- Suspension thermal noise
 - Due to the pendulum mode (Equation 2.63).
 - Due to violin modes of the suspension fibres (Section 2.7.2).

The thermal noise expected in a typical mirror for use in the second generation gravitational wave detectors has been calculated by Rowan et al [146], using a laser beam radius of $r_0 = 3.9$ cm [92], and is shown in Figure 2.4.

2.9 Conclusion

Thermal noise from the mirrors and the lower stages of their suspensions is one of the most important limits to the sensitivity of interferometric gravitational wave detectors. The level of thermal noise in the detector operating band is related to the mechanical loss of the materials used in the test-mass pendulums, with low loss materials resulting in lower thermal noise. However, the spatial distribution of the dissipation is also extremely important. Specifically, sources of dissipation located close to the reflecting surface of the mirror

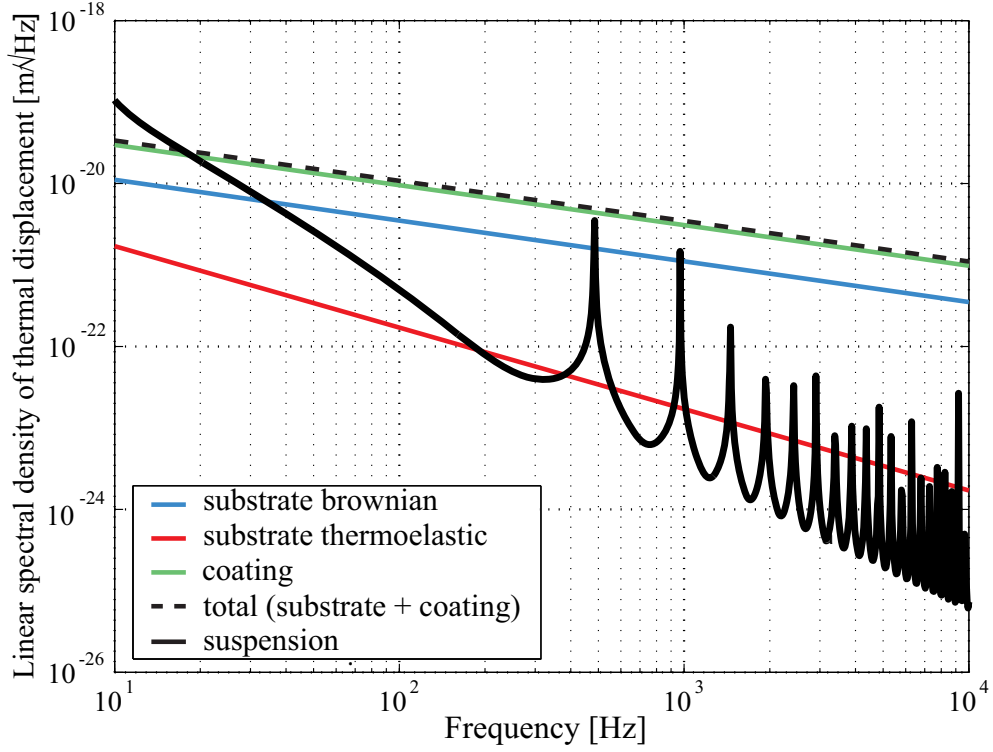


Figure 2.4: *Calculated levels of Brownian and thermoelastic thermal noise in a single suspended fused silica mirror [146], in an interferometer with a laser beam of radius $r_0 = 3.9$ cm, assuming a test mass loss of 5×10^{-9} [132], and an ion-beam sputtered coating formed from alternating multi-layers of SiO_2 and Ta_2O_5 [130].*

have a larger contribution to the total thermal noise sensed by the laser. The multi-layer dielectric coatings applied to the front face of the test-mass, which are known to be significantly more lossy than the silica test-mass substrate, are therefore expected to be a particularly important source of thermal noise in future detectors, limiting the achievable sensitivity over a significant portion of the detection band. Finding methods of reducing the dissipation of the reflective coatings is therefore one of the most important challenges for future generations of detectors.

Chapter 3

Influence of temperature on the settling time of hydroxide-catalysis bonds

3.1 Introduction

Hydroxide-catalysis bonding can be used to join rigidly materials which can be hydrated and dehydrated in the presence of a hydroxide catalyst. Initially developed and patented by Jason Gwo at Stanford University for assembling the fused silica star-tracking telescope of the Gravity Probe-B mission [147, 148, 149], the technique was further developed in Glasgow University for use in the construction of the quasi-monolithic suspensions in the GEO 600 gravitational wave detector [150, 151]. In this detector, fused silica fibres suspend the silica test mass. To avoid welding the fibres directly to the test mass, potentially introducing thermal stress and increasing the mechanical loss, they are welded to small silica ‘ears’ attached to the sides of the test masses by hydroxide-catalysis bonding. Variants of this technique are planned for use in both Advanced LIGO and Advanced VIRGO [152].

In addition, hydroxide-catalysis bonding is also planned for use in the space based gravitational wave detector LISA (Laser Interferometer Space Antenna) [153, 154]. LISA is designed to search for gravitational waves at frequencies

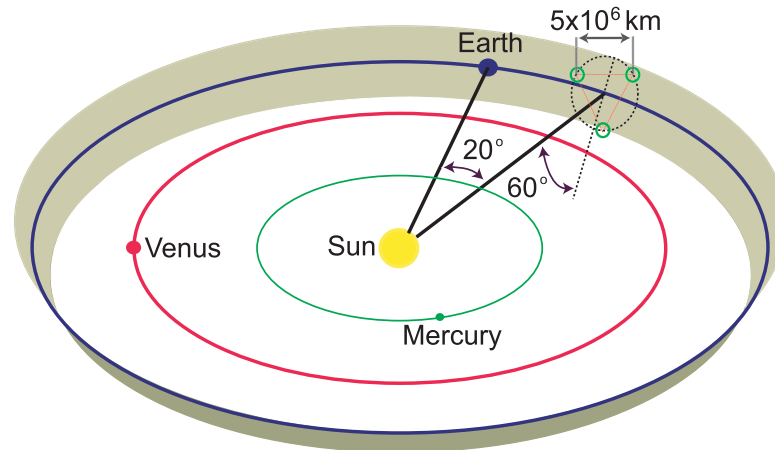


Figure 3.1: *The planned orbit of the three satellites forming the LISA gravitational wave detector.*

below ~ 1 Hz, which are not detectable on Earth due to the sensitivity barrier at low frequencies (below ~ 10 Hz) formed by gravity gradient fluctuations [63]. In addition to eliminating terrestrial gravity gradient noise, operating the detector in space allows the interferometer arms to be very long, matching the wavelength of the gravitational waves being searched for. Possible sources which may be detected by LISA include short period galactic binaries (e.g. binary white dwarfs) and the coalescence of massive black holes at the centres of merging galaxies [155].

LISA will consist of three spacecraft located at the corners of an equilateral triangle with sides 5 million kilometers long, as shown in Figure 3.1. Each spacecraft will have two optical assemblies inside arms at 60° to each other. These assemblies consist of a telescope, pointing at one of the other two spacecraft, and an optical bench containing a test-mass cage and other optical components. The arm-length is measured as the distance between the freely floating test masses within each spacecraft. Two separate lasers are located on each spacecraft, and can be phase-locked in order to behave like the beam-splitter in a Michelson interferometer. Drag-free control techniques will be used to keep each spacecraft ‘centered’ on the test masses without touching

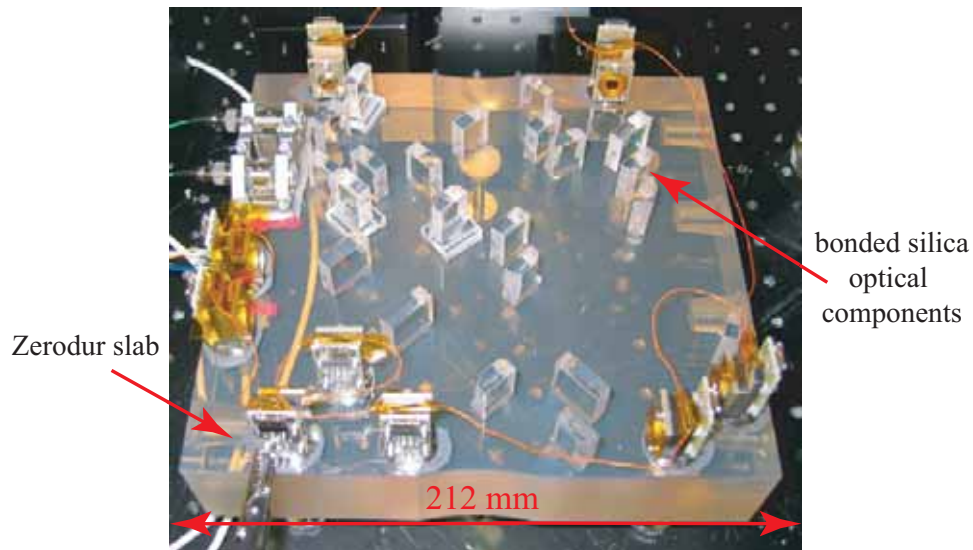


Figure 3.2: *The engineering model of the Lisa Pathfinder optical bench, which utilises fused silica optical components bonded to a Zerodur base plate.*

them, ensuring that the test masses are isolated from external disturbances and remain ‘freely floating’. The whole interferometer will follow an Earth-like orbit around the sun, lagging about 20° behind the Earth. In total, the three spacecraft form three separate, but not independent, interferometers, sensitive to gravitational waves between approximately 1 and 1×10^{-5} Hz [154].

To verify aspects of the technology developed for LISA, a demonstration mission known as LISA Pathfinder is planned [156]. This will involve the launch of a single spacecraft to test some of the critical components, including laser stabilisation, the phase readout of interferometric signals and drag-free control. The LISA spacecraft will each use local interferometers to measure the phase of the light received from the other two spacecraft. A similar interferometer will be required for the LISA Pathfinder mission. The success of both missions relies on the mechanical stability of the optical benches on which these interferometers are mounted [157], with the bench having to survive launch into space.

The design of the optical bench incorporates a low thermal expansion Zerodur base-plate to which silica optical components are attached using hydroxide-

catalysis bonding, as shown in Figure 3.2. At room temperature, the bonds set rigidly in a few tens of seconds [147, 158], allowing only a short time window for the precision alignment of the components. This chapter describes an experiment investigating the possibility of extending the settling time by carrying out the bonding process at lower temperatures. The experiment was undertaken jointly by the author and another PhD student [159].

3.2 The chemistry of hydroxide-catalysis bonding

Hydroxide catalysis bonding was developed for jointing oxide materials such as fused silica. Ideally, the surfaces of the material to be bonded should be flat to approximately $\lambda/10$ (where λ is 633 nm), and thoroughly cleaned to be free of any contaminants. A small volume (typically $0.4\mu\text{l}/\text{cm}^2$ [158]) of aqueous hydroxide solution, such as sodium or potassium hydroxide, is placed onto one surface immediately before the components to be bonded are brought together. The bonding solution is normally centrifuged and filtered to remove any undissolved particles.

If the surfaces are sufficiently flat and clean, the bonding solution spreads out between the surfaces, where it reacts with the silica to form a silicate gel which hardens over time to form a very strong, yet very thin, bond between the two surfaces. Recent measurements suggest that bonds between fused silica components are typically between 30 and 100 nm in thickness [160].

At room temperature, the silica components can be moved (parallel to the plane of the bond) for ≈ 1 minute after the bonding solution is applied; after this time, the bond ‘sets’ quite rigidly, although it takes several weeks until the bond reaches maximum strength.

A series of chemical reactions are involved in the formation of a hydroxide-catalysis bond. The first stage is *hydration* of the silica surfaces. The surface

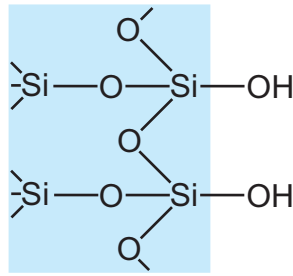
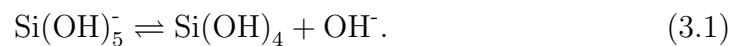


Figure 3.3: A simplified diagram showing the surface of fused silica in a fully-hydrated state after cleaning. Note that the surface consists of OH groups attached to silicon atoms.

of silica is hydrophilic, and on exposure to water, or hydroxide ions, hydration will occur, with the attraction of OH^- ions to fill any open bonds. Fully hydrated silica, as shown in Figure 3.3, typically has 4 to 6 silanol (Si-OH) groups per nm^2 [161]. Any contaminants on the surface will inhibit this hydration, potentially obstructing the formation of the bond. The silica surfaces are therefore cleaned thoroughly prior to bonding to remove any contaminants, as described in Section 3.3.

When the bonding solution comes into contact with the silica, the OH^- ions etch the surface, as shown in Figure 3.4. The etching process is initiated by OH^- ions forming weak bonds with silicon atoms on the surface of the silica. As a result, the original Si-O bonds in the silica are weakened, leading to the possibility of a silicate ($\text{Si}(\text{OH})_5^-$) molecule breaking from the surface. As the etching process continues, a quantity of these liberated $\text{Si}(\text{OH})_5^-$ molecules become available in solution. When the pH of the solution drops below 11, the silicate molecule hydrolyses to form monosilicic acid ($\text{Si}(\text{OH})_4$) and a hydroxide ion, as shown in Equation 3.1:



Once the concentration of $\text{Si}(\text{OH})_4$ reaches approximately 1 - 2 %, silanol groups on adjacent $\text{Si}(\text{OH})_4$ molecules can link together by dehydration to

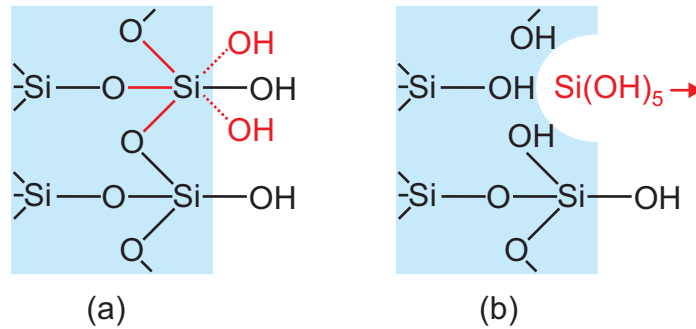


Figure 3.4: A simplified diagram of the etching stage of the bonding reaction. Hydroxide ions can etch into the surface of the silica by forming weak bonds with silicon atoms, weakening the Si-O bonds (a) resulting in silicate ions being released into solution (b).

form a siloxane bridge (Si-O-Si) [162]. Repeated dehydration results in the formation of a network of silicate-like polymer chains, as shown in Figure 3.5. At the surfaces of the silica, exposed silanol groups can similarly dehydrate to link the surface silicon atoms to the polymer chains, resulting in a rigid polymer network between the two surfaces. It should be noted that Figure 3.5 is significantly simplified with only one polymer chain shown. In reality, many cross-linked chains would be present.

If it is assumed that the conversion of $\text{Si}(\text{OH})_5^-$ to $\text{Si}(\text{OH})_4$ and the subsequent polymerisation is fast in comparison to the rate of etching of $\text{Si}(\text{OH})_5^-$ from the silica surface, then the settling time can reasonably be defined as the time taken for the silicate to start converting to silicic acid, which occurs when the pH drops below 11. The assumption that the etching process is the rate determining step for the formation of the bond has been experimentally verified [163].

3.3 Sample preparation

Appropriate preparation of the silica surfaces is critical to the success of the bonding process and the formation of strong, reliable bonds. A global surface

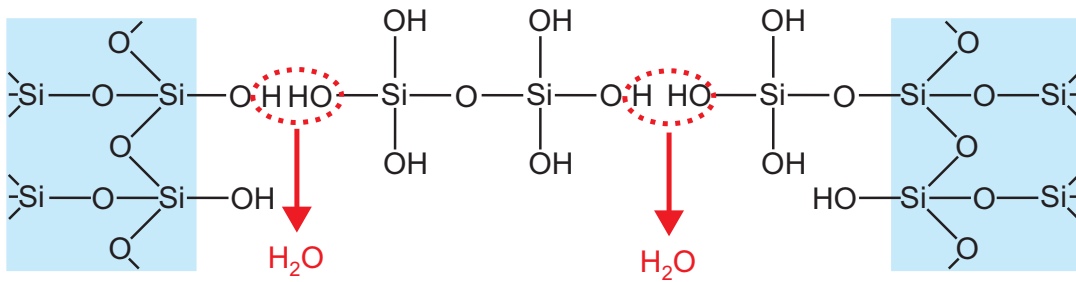


Figure 3.5: *Once the pH of the solution between the silica components has dropped below 11, the liberated $\text{Si}(\text{OH})_5^-$ molecules dissociate to form SiOH_4 , which can hydrolyse to form polymer chains, eventually linking the two silica surfaces.*

flatness of approximately $\lambda/10$ (where λ is 633 nm) is required to ensure successful bonding [151]. The flatness is normally measured with an interferometer prior to bonding.

The cleanliness of the surfaces is also important, to ensure that the silica is free from chemical and particulate contaminants and to enable full hydration. To this end, a specific cleaning procedure has been developed. The samples are rinsed with deionised water before the bonding surfaces undergo a light abrasive cleaning with a paste of cerium oxide rubbed over the surface for approximately 20 to 30 seconds. After cleaning the surface with deionised water, any remaining cerium particles are removed with a paste of sodium bicarbonate. After a final rinse with deionised water, the samples are dried with a single wipe from a non-abrasive cloth dampened with methanol.

3.4 Variation of settling time with temperature

3.4.1 Experimental setup

This experiment was designed to investigate whether cooling could extend the length of time during which the position of bonded components can be

adjusted. The settling time was defined as the time between the start of the bonding reaction and the point where the silica pieces could no longer be easily moved relative to one another. This was measured by applying an oscillating force of constant amplitude to one of the pieces and monitoring the amplitude of the motion as the bond formed.

Small silica blocks, of dimensions $10 \times 10 \times 5$ mm, were bonded to silica discs of 24.5 mm diameter. A silica block was placed in a small holder, attached on one side via a rigid connection to a loudspeaker and on the other side by an elastic connection to a fixed clamp, as shown in Figure 3.6. This setup allowed an oscillating horizontal force to be applied to the silica block. A silica disc was rigidly clamped beneath the block, and the bonding solution placed between the samples as they were brought into contact. A split-photodiode readout system (see Figure 4.3) was used to measure the amplitude of the motion of a ‘flag’ attached to the holder for the silica block.

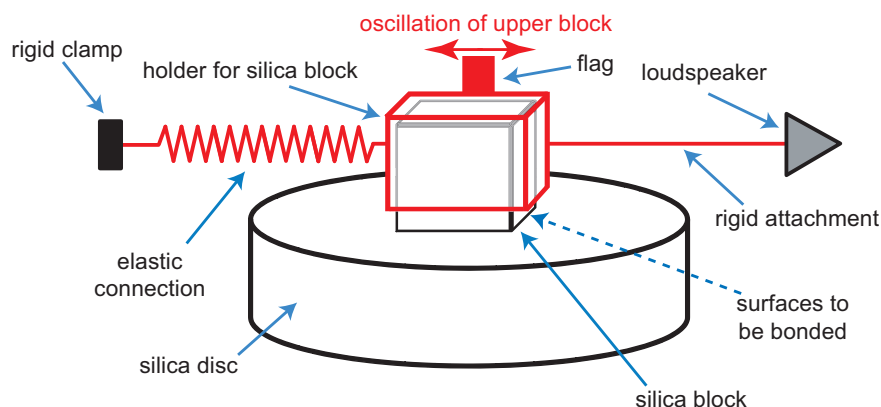


Figure 3.6: *The mechanical excitation system developed to gently shake the upper silica block during bonding. The holder for the silica block was supported on one side by a rigid connection to a loudspeaker and on the other side by an elastic connection to a rigid clamp. A ‘flag’ attached to the top of the holder was used to monitor the motion of the block throughout the bonding process.*

An oscillation frequency of 14 Hz was used as this frequency was found to couple well to the sample holder, providing both a large enough amplitude

of motion and a clean sinusoidal readout signal. The initial amplitude of the motion of the upper sample was typically between 100 and 500 μm . The amplitude was observed to slowly decrease by approximately a factor of five as the bond solidified, before the motion suddenly stopped entirely as the bond set. The time taken to reach this point where motion stopped was taken as the settling time of the bond. The bonding was carried out in a temperature

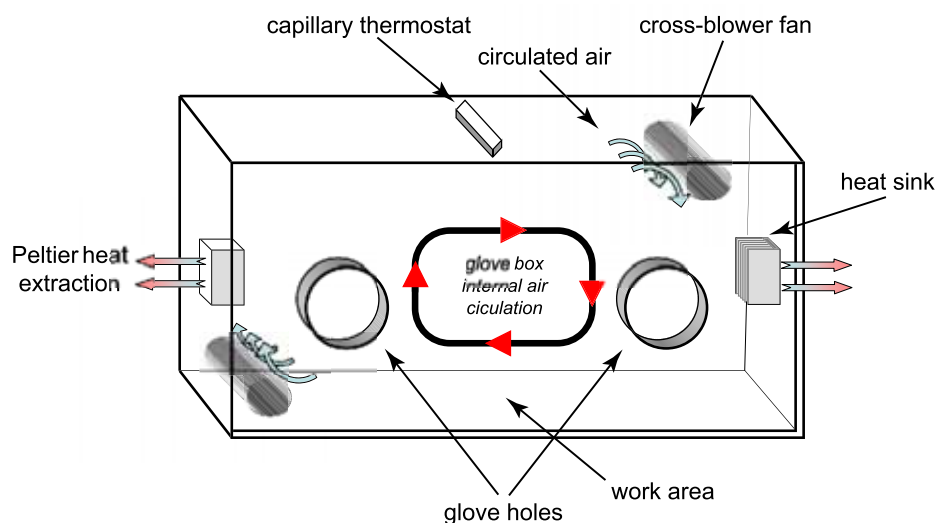


Figure 3.7: *Schematic diagram of the temperature controlled glove box in which the experiment was carried out. The glove box was 1 m long, 40 cm deep and 50 cm high.*

controlled glove-box constructed by S. Reid [159]. The interior of the glove box was cooled using two internal cross-blower fans to circulate the air over heat-sinks cooled by Peltier devices, as shown in Figure 3.7. A capillary thermostat was used to sense the internal temperature, which was controlled by regulating the power to the Peltier devices. Temperatures between 0 and 20°C could be obtained, with a typical stability of $\pm 0.1^\circ\text{C}$. The silica samples and the bonding solution were placed within the glove-box at least ten minutes prior to bonding, to allow them to achieve thermal equilibrium.

3.4.2 Results

A series of measurements of the bonding time were taken at 0, 5, 10, 15 and 20°C, using 0.1 mol l⁻¹ potassium hydroxide (KOH) bonding solution. KOH was chosen as the literature suggests that this solution produces the strongest bonds [149]. A typical plot of the amplitude of motion of the upper block as a function of time is shown in Figure 3.8. The point where the bond sets can be clearly seen at the right of this graph, where the amplitude of the upper silica block suddenly drops to zero. On several occasions, the sample was observed to stop moving as if the bond had set when in fact the bonding solution was still fluid. This was possibly due to small rough areas (or high areas) of the silica surfaces coming into contact, or due to particulate contaminants between the samples. In these cases the silica block was tapped gently and it resumed shaking: the settling times were found to be similar to those measured for samples which did not experience this problem.

Between 8 and 10 settling time measurements were made at each temperature point. The mean settling time was found to increase with decreasing temperature, as shown in Figure 3.9. The error bars in this plot are the standard error calculated from the data taken at each temperature.

3.4.3 Analysis

For a general chemical reaction:



the *rate equation* [164] links the rate at which the reaction occurs to the concentrations of the reactants as follows:

$$\tau = k(T)[A]^\alpha[B]^\beta, \quad (3.3)$$

where [A] and [B] are the concentrations of reactants A and B, $k(T)$ is the rate constant for the reaction, and the exponents α and β describe the order

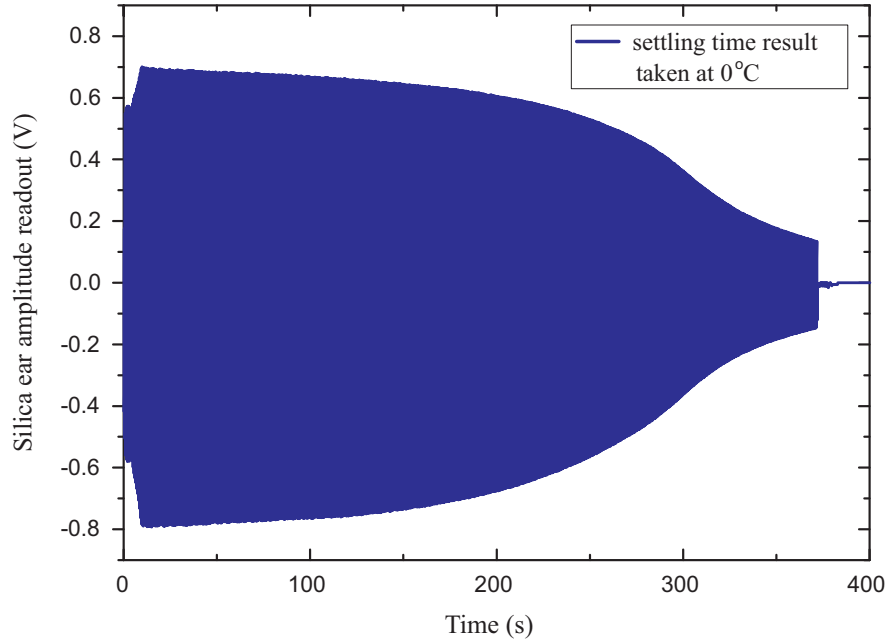


Figure 3.8: *Typical plot of the measured oscillation amplitude of the upper silica block as a function of time during bonding. The point where the bond set can be clearly seen at approximately 360 seconds.*

of the reaction with respect to each reactant. The temperature dependence of the rate constant $k(T)$ is generally described by the Arrhenius equation:

$$k(T) = Ce^{-E_a/k_B T}, \quad (3.4)$$

where E_a is the activation energy of the reaction, k_B is the Boltzmann constant, T is temperature in Kelvin and C is a constant known as the frequency factor [112, 165]. Thus for the general reaction above, the rate can be expressed as:

$$\tau = Ce^{-E_a/k_B T}[A]^\alpha[B]^\beta. \quad (3.5)$$

Assuming that hydroxide catalysis bonding is a first order reaction, depending only on the concentration of the OH ions, then the reaction rate is:

$$\tau = Ce^{-E_a/k_B T}[\text{OH}]. \quad (3.6)$$

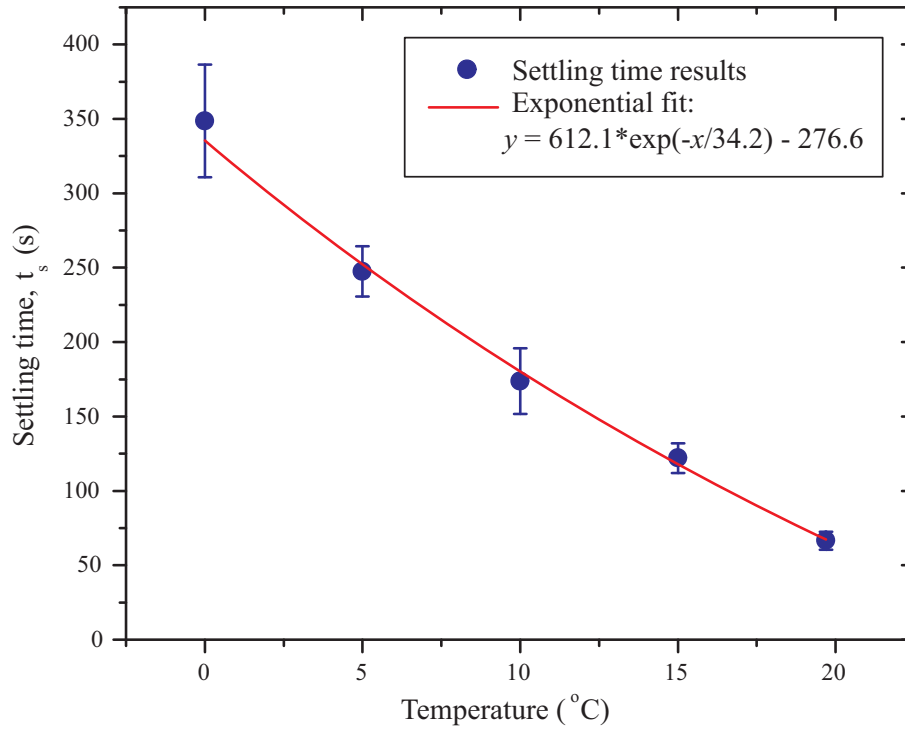


Figure 3.9: Plot of the measured settling time as a function of temperature for hydroxide-catalysis bonds made using 0.1 mol l^{-1} KOH solution, with an exponential fit.

The settling time, t_s can reasonably be assumed to be inversely proportional to the reaction rate:

$$t_s \propto \tau^{-1}, \quad (3.7)$$

which, when substituted into Equation 3.6, gives the following expression for the bonding reaction rate:

$$t_s = C' \frac{e^{E_a/k_B T}}{[\text{OH}]}, \quad (3.8)$$

where C' is a constant. Taking the natural logarithm yields the following:

$$\ln t_s = \ln C' - \ln [\text{OH}] + \frac{E_a}{k_B T}. \quad (3.9)$$

Since all of the bonds were made with the same concentration of potassium hydroxide solution (0.1 mol l^{-1}), the OH concentration at the start of each reaction was the same. Similarly, since the settling point was defined as the

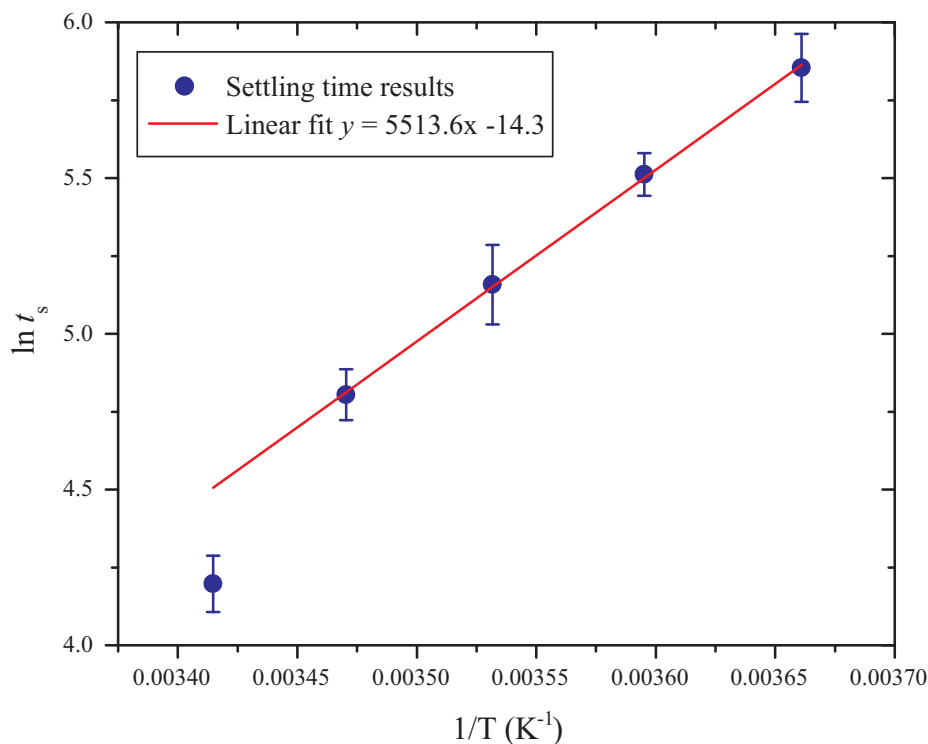


Figure 3.10: Arrhenius plot of the settling time data, showing the logarithm of the settling time as a function of the reciprocal of the temperature, with linear fit excluding the room temperature measurement.

time at which the pH dropped below 11, the concentration of OH at the end of each bonding reaction was the same. Therefore the average OH ion concentration throughout the bonding process can be considered constant for all of the bonds which were made. Hence, from Equation 3.9, it can be seen that a graph of $\ln(t_s)$ against $1/T$ should be a straight line with gradient E_a/k_B . This plot (see Figure 3.10) shows a clear linear relationship, with the exception of the data taken at 20°C, which lies some distance below the line fitted to the other data points.

There were two differences in the experimental procedure used for the 20°C measurement which might explain this discrepancy. Firstly, the settling times at 20°C were not measured within the temperature controlled glove-box. It is possible that, on transferring the apparatus into the glove-box, the actuation

system or the readout was accidentally altered, giving a slightly different result for the settling time. Secondly, the potassium hydroxide solution used for these bonds was not filtered, leading to the possibility that particulate contaminants (perhaps undissolved potassium hydroxide) were present in the solution, possibly affecting the settling time. Given these factors and the strong linear relationship of the remainder of the data, the room temperature measurement was disregarded and a straight line fitted to the data measured at 15, 10, 5 and 0 °C. The line has a gradient of 5514, corresponding to an activation energy of 0.48 ± 0.01 eV per molecule of OH^- , or alternatively $(4.58 \pm 0.08) \times 10^4$ J per mole. It should be noted this is not the activation energy reaction for a single reaction, but rather for the compound reaction of etching and polymerisation resulting in the formation of the bond.

3.5 Conclusion

It has been demonstrated that the settling time for a hydroxide catalysis bond can be increased by reducing the temperature at which the bonding is carried out. For the 0.1 mol l^{-1} KOH bonding solution studied here, the settling time increased by a factor of ~ 5 to 370 seconds on cooling from 20 °C to 0 °C. This method may have applications in increasing the time available for the precise alignment of optical components during the construction of rigid optical benches in projects such as LISA. The calculation of the activation energy for the bonding reaction may also be useful in comparative investigations of the properties and chemistry of hydroxide catalysis bonds between other materials such as silicon, which is of interest for use in future gravitational wave detectors.

Chapter 4

Loss measurements using silica cantilevers at room temperature

4.1 Introduction

In Chapter 2, the relationship between the thermal noise in a gravitational wave detector and the mechanical loss of the materials used in the suspended mirrors was discussed. The thermal noise arising from any particular source of loss, which is sensed by the laser, is dependent on the proximity of the source of loss to the front face of the mirror. Thus the mechanical loss of the reflective mirror coatings applied to the front face of the test mass is particularly significant. In this chapter a method of studying the mechanical loss of coating materials is described, in which thin silica cantilever samples are used as substrates to which coatings are applied. Preliminary measurements of the mechanical loss of both optically reflective, and conductive tin oxide coatings for charge mitigation, are presented, and the same technique is applied to estimate the loss associated with a polished silica surface. Firstly, the development of silica cantilever samples and the experimental method used to measure the mechanical loss will be discussed.

4.2 Mechanical loss of silica ribbons

Thin rectangular cross-section silica fibres (known as ‘ribbons’) were developed in the Institute for Gravitational Research in Glasgow for possible use in the final stage of the test mass suspensions for Advanced LIGO [166, 167], but also form useful substrates for the study of the mechanical loss of coating materials. Coating loss can be calculated from measurements of the loss of the substrate before and after application of the coating. Fused silica is a good choice of substrate as it is known to have a low mechanical loss at room temperature [93, 132] thus ensuring high sensitivity to the loss of the coating material.

Most of the ribbons studied were fabricated using a machine developed by Alastair Heptonstall [166]. A hydrogen-oxygen flame is used to melt the central portion of a silica slide ($1 \times 11 \times 75$ mm), which is then rapidly pulled into a long, thin ribbon using motorised clamps. The resulting ribbons are approximately 60 cm long, 1 to 2 mm wide and 110 μm thick, as shown in Figure 4.1. The tapered regions at each end of the ribbon are known as ‘necks’. Initial studies were carried out to assess the level of mechanical loss of silica ribbons and determine the optimum geometry of sample for use in coating loss measurements.

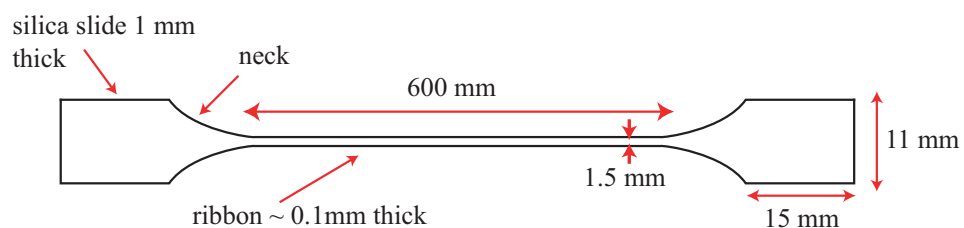


Figure 4.1: A schematic diagram of a silica ribbon (not to scale).

4.2.1 Measuring mechanical loss

The mechanical dissipation (also known as the mechanical loss), $\phi(\omega)$, of a resonant mode of system at angular frequency ω_0 is defined as:

$$\phi(\omega_0) = \frac{E_{\text{dissipated}}}{2\pi E_{\text{stored}}}, \quad (4.1)$$

where E_{stored} is the total energy stored in the vibrating system and $E_{\text{dissipated}}$ the energy dissipated with each cycle of oscillation.

Dissipation can be measured using a ‘ring-down’ method, in which a resonant mode of a sample is excited and the amplitude of the resulting motion is allowed to decay freely. For a resonant mode of angular frequency ω_0 , excited to an initial amplitude A_0 , the time dependence of the amplitude decay $A(t)$ is given by:

$$A(t) = A_0 e^{-\phi(\omega_0)\omega_0 t/2}. \quad (4.2)$$

The loss factor of a resonance may thus be found from measurements of the amplitude of the decaying resonant motion as a function of time.

4.2.2 Experimental method

Cantilever samples consisting of a length of silica ribbon, the neck region and the remnant of the silica slide were produced by carefully cutting a ribbon at the desired distance from the neck (see Figure 4.1). The silica slide was held horizontally in a stainless steel clamp, from which the ribbon section projected. The mechanical loss factors of the bending modes of the ribbon sample could then be measured. The frequency of the n^{th} bending mode of a cantilever of thickness a , length L , Young’s modulus Y and density ρ is given by [168]:

$$\omega_n = (k_n L)^2 \frac{a}{2\sqrt{3}L^2} \left(\frac{Y}{\rho}\right)^{1/2}, \quad (4.3)$$

in which $k_n L = 1.875$ ($n=1$), 4.694 ($n=2$), 7.853 ($n=3$), 10.996, ($n=4$) and 14.137 ($n=5$). For $n > 5$, $k_n l$ can be approximated as $k_n l = (2n - 1)\pi/2$ [169].

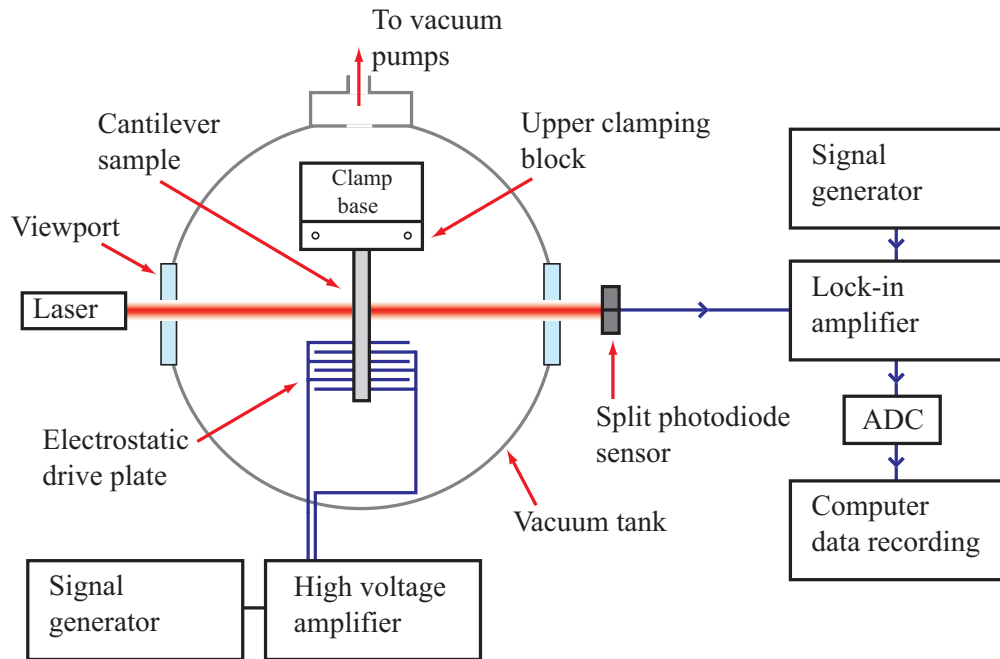


Figure 4.2: A schematic diagram of the experimental apparatus used to measure the mechanical loss of cantilever samples - not to scale.

Figure 4.2 shows a schematic diagram of the apparatus used to measure the mechanical loss factors of the bending modes of silica cantilevers. After a cantilever was clamped, the clamp was placed on a suspended table inside a vacuum tank, which was evacuated to a pressure of approximately 1×10^{-6} mbar. The bending modes of the cantilever were excited in turn by applying an oscillating high voltage signal at the frequency of a resonant mode, with a d.c. off-set of approximately 700 V, to an electrostatic drive plate located approximately 5 mm below the cantilever.

The amplitude ring-down of an excited mode was recorded by illuminating the cantilever with a diode laser beam and monitoring the resulting shadow with a split photodiode sensor, illustrated in Figure 4.3. The signals from the two halves of the photodiode were subtracted and amplified. A lock-in amplifier was used to multiply the resulting signal with a generated sine wave differing in frequency by 2 Hz. This produced a signal, proportional to the

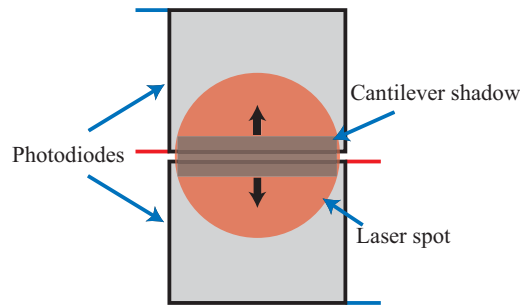


Figure 4.3: A schematic diagram of the split photodiode arrangement used to measure the amplitude of oscillation of a cantilever .

displacement of the cantilever, at a beat frequency of 2 Hz, which was digitally sampled and recorded with a computer. The dissipation was calculated from an exponential fit to the amplitude ring-down using Equation 4.2; an example of a typical ring-down is shown in Figure 4.4.

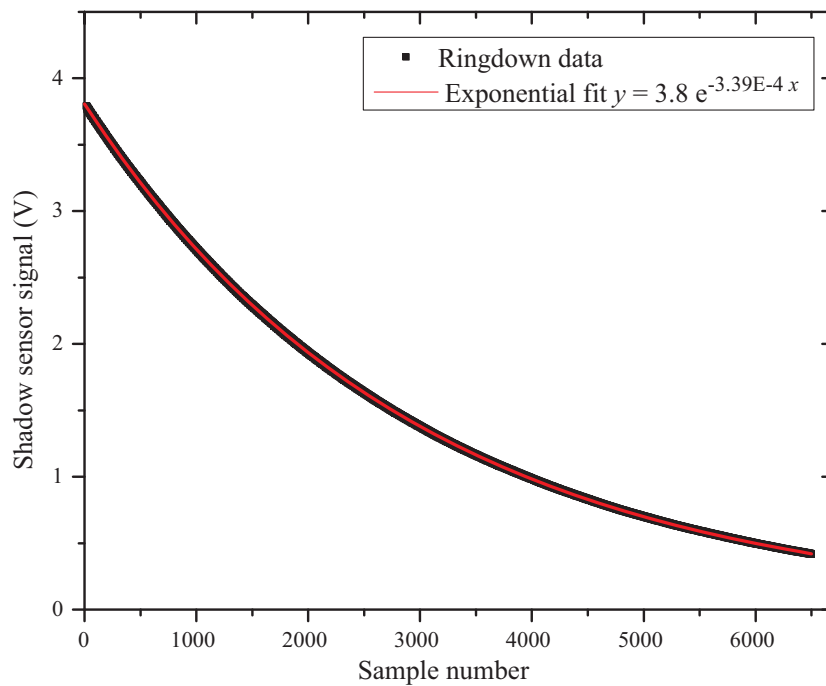


Figure 4.4: A ringdown measurement for the the third bending mode at 1051 Hz. A sampling rate of 15 Hz was used, and the mechanical loss calculated from the fitted exponential decay constant.

The loss measured in this way is the sum of all of the energy dissipation

mechanisms in the sample, including intrinsic dissipation within the material and any excess dissipation, which can arise from a number of sources and must be suitably minimised. A model for the intrinsic dissipation of fused silica is described in the next section, after which the mechanical loss results for the first two ribbon samples is presented.

4.2.3 Semi-empirical model for intrinsic loss in fused silica

Penn et al [170] have formulated a semi-empirical model for the dissipation in fused silica, based on a study of the experimental loss factors measured by several groups. The intrinsic loss, $\phi\left(f, \frac{S}{V}\right)$, is considered to have contributions from three dissipation processes: dissipation in the bulk of the material, in the surface of the material and thermoelastic dissipation, which is discussed in detail in Section 2.4. The total loss is given by:

$$\phi\left(f, \frac{S}{V}\right) = C_1 \frac{S}{V} + C_2 f^{C_3} + C_4 \phi_{\text{thermoelastic}}, \quad (4.4)$$

where $\phi_{\text{thermoelastic}}$ is the thermoelastic loss, S and V are the surface area in mm^2 and the volume in mm^3 respectively. The coefficients C_n are obtained empirically and depend on the type and condition of the silica. The term $C_1 \frac{S}{V}$ describes the loss associated with the surface of a silica sample. The mechanical loss of the surface is often significantly different to that of the bulk material [171]. This is postulated to arise from factors such as small surface cracks, surface roughness and the increased likelihood of the presence of impurities. The term $C_2 f^{C_3}$ represents the bulk loss of fused silica. The bulk loss is thought to be related to certain molecules (or larger structural units) which can have two energetically stable states (e.g. one model involves two possible Si-O bond angles [172]), separated by a potential barrier [171, 173]. In response to an applied strain these atoms can move between the stable states, resulting in the

dissipation of energy ¹. The amorphous structure of fused silica results in a distribution of the heights of the potential barriers. The frequency dependence of the loss can be found from measurements of this distribution [173].

The results presented here are for ribbons fabricated from Heraeus Suprasil 312, for which the values of the coefficients C_n are taken to be: $C_1 = 6.5 \times 10^{-9}$ m, $C_2 = 7.6 \times 10^{-12}$, $C_3 = 0.77$ and $C_4 = 1$ [170].

4.2.4 Mechanical loss of ribbons with ‘necks’

Initially the loss factors of two silica ribbon cantilevers were studied. The first ribbon was fabricated with the flame pulling machine as described in Section 4.2, while the second ribbon was fabricated using a similar system in which a CO₂ laser rather than a flame was used to heat the silica. The dimensions of the ribbons are given in Table 4.1. The ribbon from the laser-based pulling machine had a significantly shorter neck than the ribbon produced with the flame pulling machine (see Figure 4.5).

	Flame-pulled ribbon	Laser-pulled ribbon
Length	60 ±0.5 mm	48 ±0.5 mm
Width	1.11 ±0.01 mm	5.98 ±0.01 mm
Thickness	110 ±5 μm	120 ±5 μm

Table 4.1: *Dimensions of the two ribbons with necks.*

It was possible to measure the lengths of the cantilevers to an accuracy of ± 0.5 mm without contacting the surfaces. The width and thickness of the cantilevers were measured with a micrometer after the mechanical loss factors had been measured.

The loss factors of the first six bending modes of each ribbon were measured using the ring-down technique described in Section 4.2.1. Each measurement

¹Asymmetric double-well potential models for the dissipation mechanism in silica are discussed in more detail in Section 5.5.1.

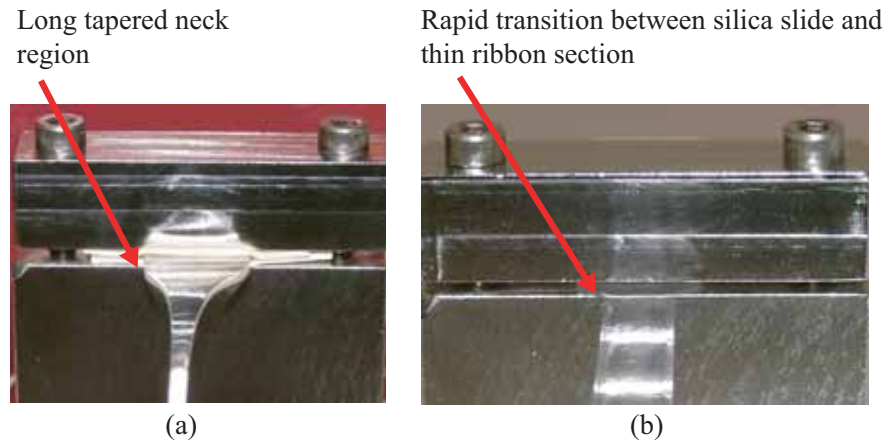


Figure 4.5: (a) *The flame-pulled ribbon section in the clamp.* (b) *The laser-pulled ribbon in the clamp.*

was repeated five times, and the standard error calculated from the spread of the data. The measured mechanical losses of these ribbons were compared to the values obtained from Penn's model, as shown in Figure 4.6. In both cases, the measured loss factors were substantially higher than those predicted by the model, although the loss of the laser-pulled ribbon was generally closer to the predicted values at high frequency.

This excess loss may arise from some degree of movement of the cantilever in the clamp, resulting in frictional stick-slip loss [174]. Measurements by Quinn et al have shown that stick-slip losses can be reduced by having a large difference in thickness between the clamping block and the cantilever itself [174], which ensures that the bending point occurs outwith the jaws of the clamp. This reduces the shear stress at the edge of the clamp, which in turn reduces the tendency of the ribbon to slip [175]. Both of the samples had an extensive neck region over which the clamping block gradually thins and narrows to form the ribbon. Thus there was very little difference in thickness between the clamping point and the adjacent ribbon section, suggesting that stick-slip effects may indeed be a significant loss mechanism. Furthermore, due to the different manufacturing processes, the laser-pulled ribbon had a

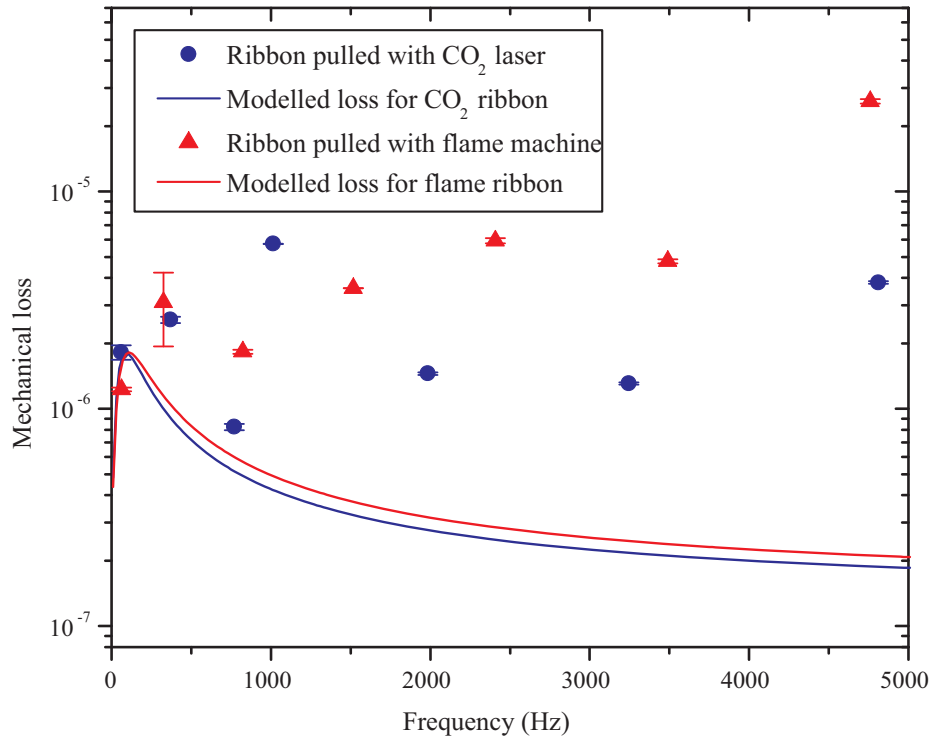


Figure 4.6: *Frequency dependence of the mechanical loss of a ribbon with a short neck fabricated with a laser pulling machine, compared to that of a ribbon with a longer neck fabricated with a flame pulling machine. Also shown are the losses predicted by Penn's model for both samples.*

significantly shorter neck, while the flame-pulled ribbon had a long neck over which the thickness decreases more gradually (see Figure 4.5). This suggests that the lower loss of the laser-pulled ribbon at high frequency may be due to reduced levels of friction in the clamp, arising from the larger difference in thickness on either side of the clamping point. The high loss measured at 1014 Hz for the laser-pulled ribbon is likely to be the result of energy coupling into a resonant mode of the clamping structure. This effect is discussed in more detail by Reid [159] and in Section 5.2.4.

4.2.5 Gas damping

To ensure that the measured loss factors are not limited by frictional damping from residual gas molecules, suitably low vacuum pressure must be reached.

The loss due to gas damping, ϕ_{gas} , can be approximated to be [175]:

$$\phi_{\text{gas}} \approx \frac{AP}{m\omega} \sqrt{\frac{M}{RT}}, \quad (4.5)$$

where A is surface area, P is pressure, m is the mass of the cantilever, ω is the angular frequency of the resonant mode, M is the mass of one mole of the gas, R is the gas constant and T temperature. The loss associated with gas damping is proportional to $1/\omega$: gas damping is therefore more likely to influence loss measurements at low frequency. The first bending mode of the sample studied were at approximately 50 Hz. At this frequency the loss predicted by the semi-empirical model is of the order of 1.4×10^{-6} . To ensure that the gas damping is at least an order of magnitude lower than this, a gas pressure of less than $\approx 2 \times 10^{-3}$ mbar is required, assuming that the residual gas molecules are nitrogen. The pressure in the vacuum chamber routinely reached $\approx 1 \times 10^{-6}$ mbar, so gas damping effects are considered to have been negligible for all of the modes studied.

4.2.6 Welded silica ribbon

One possible source of the difference between the loss factors measured in the ribbon cantilevers and the values predicted by the semi-empirical model was frictional loss in the clamp. In an effort to improve the isolation of a vibrating ribbon from the clamp, a new type of cantilever which did not have a ‘neck’ region was fabricated. First, a 1 mm wide ribbon was pulled using the flame machine and cut carefully in half with clean pliers. The free end of the ribbon was welded onto a section of silica slide using a CO_2 laser, as shown in Figure 4.7. The section of silica slide was thoroughly cleaned with chloroform and methanol, and placed in a clamp. A second clamp was used to hold a length of silica ribbon in the correct position for welding. Both clamps were mounted on horizontal and vertical translation stages, to allow the samples to be moved relative to the laser beam. The best results were obtained by heating the slide

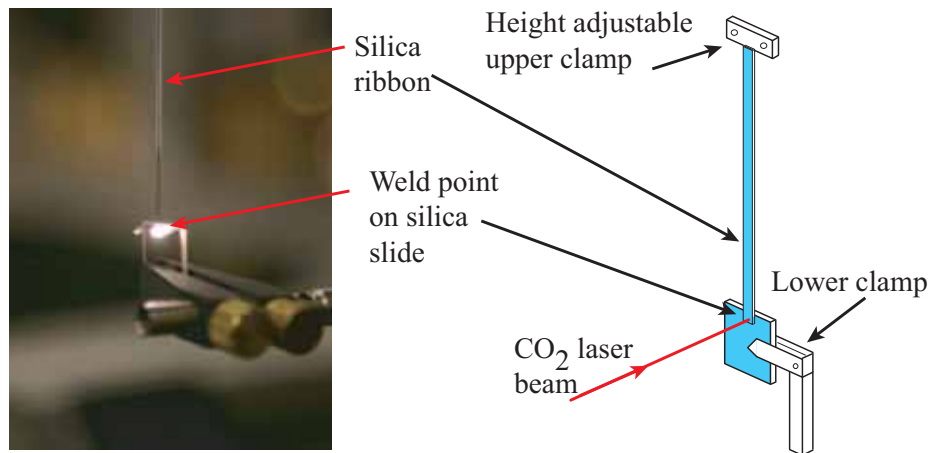


Figure 4.7: *Left: Photograph of CO₂ laser welding. Right: Schematic diagram of laser welding apparatus.*

immediately below the weld region for approximately 20 seconds with a low power ($\sim 15 - 20\text{W}$) before the samples were lowered so that the end of the ribbon was directly heated by the laser beam. After a further 10 to 20 seconds of heating, the laser power was increased incrementally over 30 seconds to a maximum of 30 W. The silica ribbon was then cut to form a 7 cm long cantilever sample welded to a clamping block. The welded sample is shown in Figure 4.8.

The section of silica slide was used as a clamping block, with the sample clamped directly behind the weld region. This sample therefore had a significantly sharper transition between the flexing cantilever and the thicker clamping block with the aim of reducing the level of stick-slip loss in the clamp. The ribbon was measured to be $110 \pm 5 \mu\text{m}$ thick with a micrometer. The thickness was also calculated from the measured resonant frequencies of each of the first 9 modes using Equation 4.3. The average thickness obtained was $113 \pm 3 \mu\text{m}$.

The loss factors measured for this ribbon were considerably lower than the previous measurements for the necked ribbon samples, as shown in Figure 4.9.

At low frequencies, the loss factors of the welded ribbon follow the modelled curve closely, while at higher frequencies they are approximately a factor of two above those predicted by the model.

There are several possible sources of this residual excess loss. During the welding process, parts of the sample were contaminated with silica vapour, which may increase the loss associated with the cantilever surface (see Figure 4.10). The ribbon section was cut with pliers and it is possible that the surface close to the location of the cut was damaged slightly, again producing a source of excess loss. It is also likely that the weld itself is a source of some additional loss, as measurements of welded cylindrical fibres have shown a degree of loss associated with the weld [176]. The modes at 1056 Hz and 2728 Hz show evidence of higher levels of excess loss. The 1056 Hz mode is close to the frequency at which excess loss was observed in the laser pulled ribbon, providing a further suggestion that there may have been energy loss into a mode of the clamp at a nearby frequency.

The results for this welded sample suggest that frictional losses in the clamp can be reduced by the use of a thick clamping block with a sharp transition in

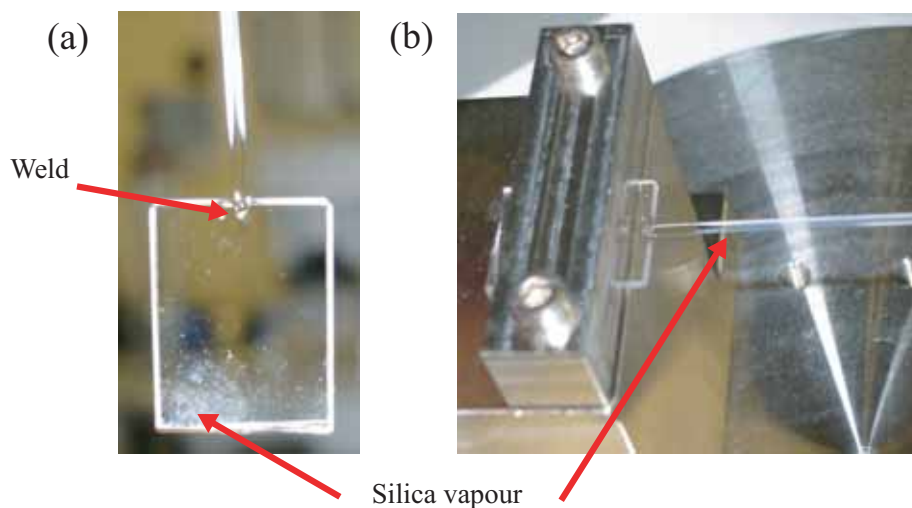


Figure 4.8: (a) Photograph of the cantilever immediately after welding. (b) Photograph of the welded cantilever in the clamp.

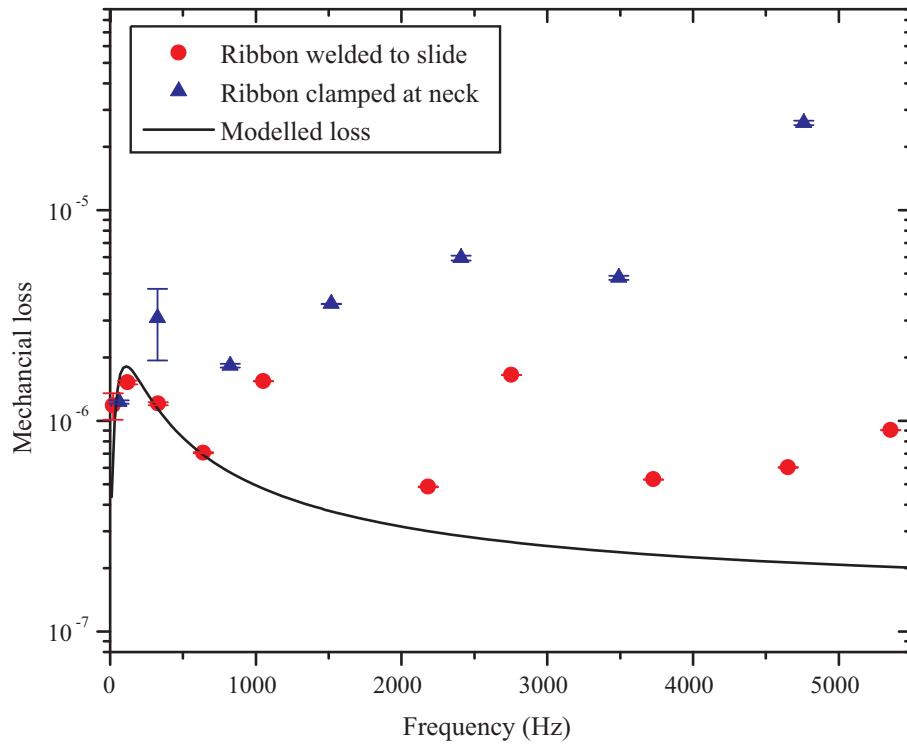


Figure 4.9: *Frequency dependence of the mechanical loss of a ribbon section welded to a silica slide, compared to that of a similar ribbon clamped at the neck region. Also shown are the losses predicted by Penn’s model for both samples.*

thickness to the cantilever.

4.2.7 Coating loss measurements using silica cantilevers

It has been shown that a level of mechanical loss close to that predicted by Penn’s semi-empirical model can be measured in silica cantilever samples produced by laser-welding a silica ribbon to a 1 mm thick section of silica slide. The low loss of these samples makes them of interest for use in experiments to measure losses associated with both surface effects in silica and with coatings of various types. In the following section, loss measurements of conductive tin oxide coatings, which may be of interest for the mitigation of charging effects in the test masses and suspensions of future gravitational wave detectors, are

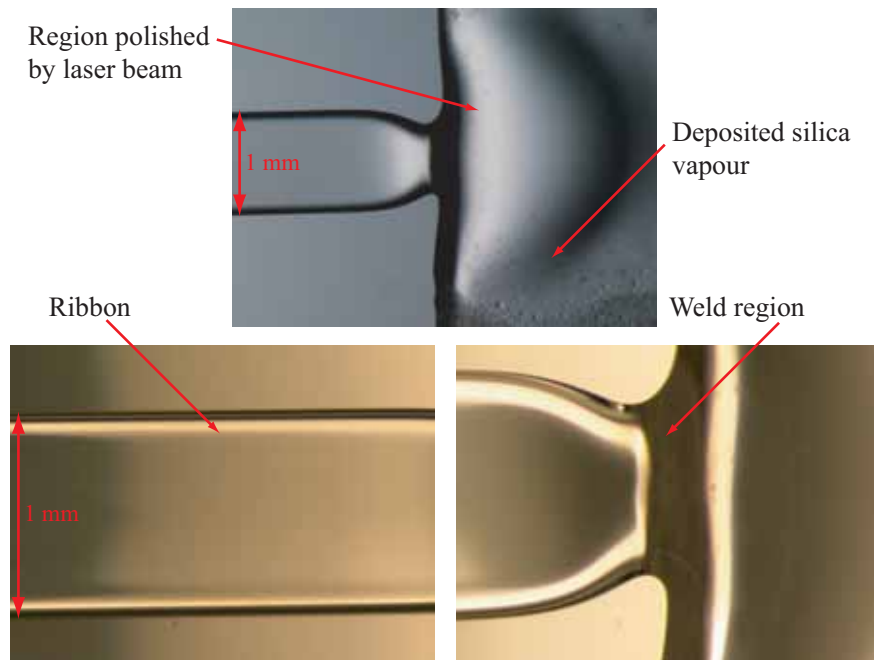


Figure 4.10: *Microscope images of the welded silica cantilever.*

described. Silica cantilevers were also used to measure the loss of single layers of the optical coating materials used in gravitational wave detectors; the results are presented in Section 4.4.

4.3 Conductive coatings for charge mitigation in gravitational wave detectors

Electrostatic charging of the test masses can be a significant problem in a gravitational wave detector, potentially resulting in increased levels of displacement noise [177] and in difficulties with the interferometer control systems [178]. A fused silica test mass suspended in ultra-high vacuum is a very well electrically isolated system, particularly if suspended on silica fibres, as is the case with GEO 600 and the planned Advanced LIGO and Advanced VIRGO detectors. It is therefore possible that high levels of electrostatic charge with long decay times will arise. Indeed, in laboratory experiments the charge of fused

silica masses suspended in a vacuum has been observed to increase continuously over several months, with occasional large jumps of charge [179, 180]. There are many mechanisms by which the mirrors could become charged including friction from evacuating and venting of the vacuum tanks, by touching an earthquake stop² or from interactions with cosmic rays [181]. One possible solution is the application of a conductive coating to the test mass and suspension fibres, which would allow the dispersal of any charges as they are accumulated.

4.3.1 Charging issues in gravitational wave detectors

Charging of the test masses and suspensions can lead to several potential problems in a gravitational wave detector. Electrostatic damping may occur if charges on the mirror interact with surrounding structures, reducing the quality factor of the modes of the suspended mirror [182, 183, 184] and therefore resulting in higher levels of thermal noise in the detector. Fluctuating electric fields associated with charge migration across the mirror or suspension surfaces can lead to an additional source of displacement noise [177, 185].

Charging can also lead to control issues, with electrostatically induced displacement of the mirrors potentially resulting in calibration errors, difficulties in controlling the mirror position and locking the interferometer. Charging-related control problems have recently been experienced at the GEO 600 detector [178]. In GEO 600, electrostatic actuators located on the reaction mass suspended immediately behind each test mass, are used to control the longitudinal position of the test mass. After a power cut at the GEO 600 site in 2006, a test mass was found to have touched the electrostatic actuator and become charged. The charged mirror was found to significantly affect the performance of the electrostatic actuators, and the detector could not be locked using the standard locking parameters.

²Earthquake stops are designed to limit the swing of the test-mass in the event of excessive seismic excitation.

Similar charging events are thought to have been observed at the LIGO Livingston detector [186], with the charging occurring when the test mass made contact with an earthquake stop. The suspension resonant frequencies were observed to increase after this event, and the noise spectrum was altered significantly. After venting the vacuum chambers, both the suspension frequencies and the noise spectrum returned to normal. It is clear therefore that the development of charge mitigation techniques is of considerable importance for future gravitational wave detectors.

4.3.2 Charge mitigation

There are several possible methods of reducing the effects of charging of the mirror suspension in a gravitational wave detector. Experiments carried out in Glasgow demonstrated that illumination with UV radiation could control the level of charge on a Macor pendulum suspended on silica fibres [182]. The same technique was used to discharge the positively charged GEO 600 test mass referred to above.

A method of charge mitigation commonly used for dielectric materials under vacuum is the application of a thin, slightly conductive coating of a material such as tin oxide [187]. This technique would have the advantage of preventing charge accumulating on the test mass. For such a system to be implemented in a gravitational wave detector, the conductive coating would have to meet stringent thermal noise requirements, and, for application to the front face of the mirror, optical loss requirements. In the following sections measurements of the mechanical loss of tin oxide coatings will be presented, and their potential thermal noise contribution in a gravitational wave detector calculated.

4.3.3 Experimental technique

Fused silica cantilevers, similar to those described in Section 4.2.6, were used to investigate the mechanical loss of the SnO coatings. Several 50 mm sections

of ribbon, 1.5 mm wide and ≈ 0.11 mm thick, were welded to fused silica clamping blocks of approximate dimensions ($10 \times 10 \times 1$) mm, using a CO₂ laser as described in Section 4.2.6. The mechanical loss of several modes of each ribbon was measured before and after coating with tin oxide.

Tin oxide coatings were produced using pulse spray pyrolysis, a technique in which a thin film is deposited by spraying a solution onto a heated surface where the constituents react to form the desired coating compound [188]. Spray pyrolysis is often used for depositing high quality, low cost transparent oxide films [187, 189, 190], and is an established method for applying conductive tin oxide coatings to glass [191].

Various precursor solutions can be used to deposit tin oxide films including SnCl₂, SnCl₄ and SnF₂ [192, 193]. The coatings measured here were deposited using a pyrolysis solution of 0.1 mol l⁻¹ tin (II) chloride dissolved in methanol, which reacted on, or immediately above, the silica surface to form tin oxide as shown below:



The deposition was carried out by Stuart Reid with assistance from the author. The silica samples were heated to 600°C in a ceramic tube oven. Small quantities of the tin chloride solution were sprayed into the oven using an airbrush nozzle with dry nitrogen gas as the carrier gas, in pulses of 1 second duration. The distance between the nozzle and the samples was approximately 20 to 30 cm, and the pulses were separated by 10 second intervals to minimise evaporative cooling of the samples. It was found that approximately 10 to 15 ml of tin chloride solution was required to deposit ~ 100 nm of coating.

4.3.4 Results

Measurements with a four point probe carried out by Liam Cunningham showed that the resistivity of the coatings were between 3.4×10^{-3} and 9.5×10^{-3} Ω cm. The variations in resistivity are possibly explained by variations in the

temperature of gas carrying the SnCl_2 vapour resulting in variations in the thickness or quality of the coating, as observed by Ishida et al when depositing coatings under similar conditions [194]. The lowest resistivity measured is consistent with the values reported by Shalama et al in similar coatings [195].

4.3.4.1 Optical requirements and absorption measurements

To achieve desired levels of shot-noise limited performance in gravitational wave detectors substantial light powers must be supported in the arms of the interferometers. The optical mirror coatings used place a limit on the maximum achievable power, as heating due to absorption in the coatings can lead to thermal deformation of the optics [94], resulting in instabilities within the laser cavities. For example, the planned Advanced LIGO detectors have a design requirement that the mirror coatings within the Fabry-Perot arm cavities have an absorption of less than 1 ppm to allow the cavity to maintain 830 kW of circulating laser power [92].

Several silica disks coated with SnO were sent to collaborators at Stanford University for measurements of the SnO absorption at 1064 nm. Values as low as 60 ppm absorption were measured for the ~ 100 nm thick SnO coatings [196]. This level of absorption clearly rules out the use of these SnO coatings on top of the HR mirror coatings. However a coating placed beneath the HR mirror coating would only be exposed to the laser power external to the cavity, approximately 1 kW in the case of Advanced LIGO [92], resulting in a reduction in the absorbed power by a factor of ≈ 800 . It is thus possible, in principle, to place a conductive tin oxide coating below the multi-layer optical coating without exceeding the absorption requirements for Advanced LIGO.

4.3.4.2 Mechanical loss measurements of SnO coatings

In this section, measurements of the mechanical loss of SnO coatings are presented and used to estimate the thermal noise contribution of a tin oxide

coating on the front face of a test mass. Three silica cantilevers were coated with SnO in separate pyrolysis runs. Several partially masked ‘witness samples’ (25 mm diameter silica disks) were included in each coating run. The coating thickness was obtained from measurements of the step height between the masked and the coated regions of the witness samples carried out by Stuart Reid using a Talysurf stylus profiler. Thicknesses ranging from 25 nm to 1.6 μm were measured for coatings produced at different times, with the typical variation of coating thickness between samples in a single coating run being $\sim 10\%$.

The loss of several bending modes of each cantilever (up to the 6th mode where possible) was measured before and after coating. The loss of the tin oxide layer was calculated using the difference in the measured loss of each mode, as explained in the following section. The measured loss factors for one of the cantilevers, which was coated with 25 nm of SnO, are shown in Figure 4.11. The loss of this cantilever after coating generally tended to decrease with increasing frequency, with the exception of loss measured for the 3.6 kHz mode, which is significantly higher. No large increase in loss was observed at similar frequencies in the other coated cantilevers, so it seems possible that the high value of loss measured was due to energy loss into the clamping structure at this frequency.

4.3.5 Coating loss analysis

The measured loss of a coated cantilever arises from the loss of both the cantilever substrate and the loss of the coating material. As the coating is thin in comparison to the cantilever, only a small fraction of the energy associated with a resonant mode of the cantilever is stored in, and thus can be dissipated in, the coating layer. It can be shown that the measured loss of the coated cantilever $\phi(\omega_0)_{\text{coated}}$ is related to the loss of the substrate $\phi(\omega_0)_{\text{substrate}}$ and

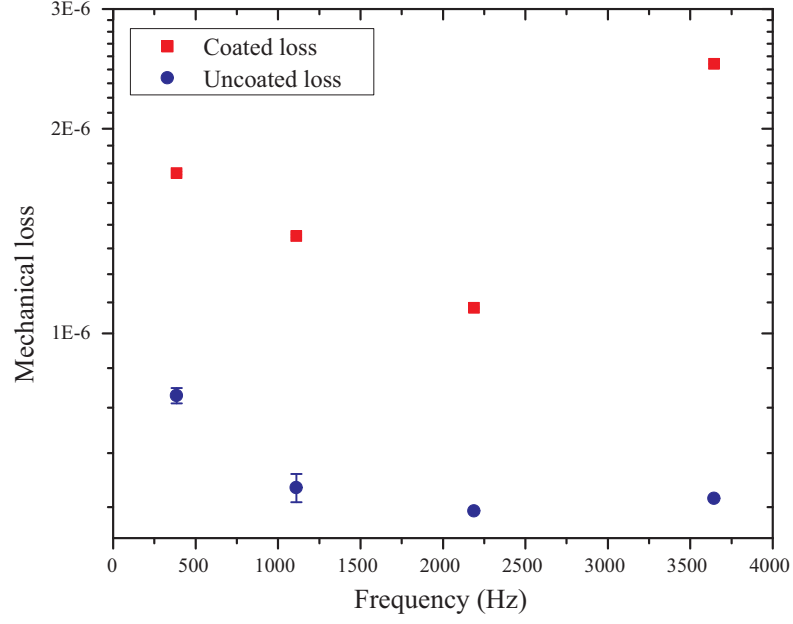


Figure 4.11: *Plot of the measured loss of four modes of sample 1 before and after coating with 25 nm of SnO.*

the intrinsic loss of the coating material $\phi(\omega_0)_{\text{coating}}$, as follows [197]:

$$\phi(\omega_0)_{\text{coated}} = \phi(\omega_0)_{\text{substrate}} + \frac{E_c}{E_s} \phi(\omega_0)_{\text{coating}}, \quad (4.7)$$

where E_c/E_s is the ratio of the energy stored in the coating layer to the energy stored in the cantilever substrate. This energy ratio can be calculated by considering a bar of length L , thickness a and width b , with a thin coating of thickness t on one surface, bent into an arc of a circle of radius R , as shown in Figure 4.12.

The energy stored in the coating layer is given by:

$$E_c = \frac{Y_c A}{2L} \Delta L^2 \quad (4.8)$$

$$= \frac{Y_c t b}{2L} \Delta L^2, \quad (4.9)$$

where the cross sectional area of the coating, A , is given by $A = tb$, Y_c is the Young's modulus of the coating and the change in length, ΔL , is given by:

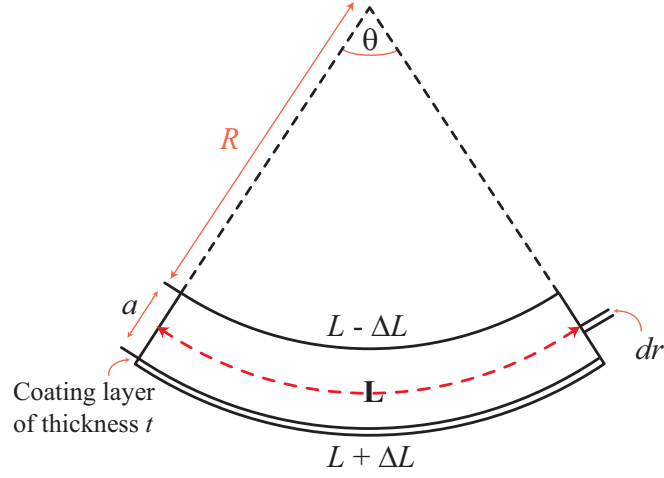


Figure 4.12: A beam of thickness a and width b , with a thin coating of thickness t applied to one face, bent into an arc of radius R .

$$\Delta L = \frac{a}{2}\theta. \quad (4.10)$$

Similarly, the energy stored in the half of the beam under compression may be written as:

$$dE = \frac{Y_s b \Delta L^2}{2L} dr, \quad (4.11)$$

where Y_s is the Young's modulus of the substrate and $\Delta L = (r-R)\theta$. Integrating over half of the beam gives:

$$\frac{E_s}{2} = \int_R^{R+\frac{a}{2}} \frac{Y_s b \theta^2}{2L} (r-R)^2 dr = \frac{1}{48} \frac{Y_s b \theta^2 a^3}{L}. \quad (4.12)$$

If it is assumed that the energy stored in the half of the beam under tension is equal to the energy stored under compression, the total stored energy in the beam is twice that calculated in Equation 4.12. From Equations 4.12 and 4.9, the ratio of the energy stored in the coating to that stored in the substrate can be shown to be:

$$\frac{E_c}{E_s} = \frac{3Y_c t}{Y_s a}. \quad (4.13)$$

Since the shape of each bending mode of a cantilever is made up of a number of such arcs, the energy ratio could be expected to remain constant for each

mode. This has been confirmed by finite element analysis [198]. Rearranging Equation 4.7 and substituting for the energy ratio gives the following expression for the coating loss:

$$\phi(\omega_0)_{coating} = \frac{Y_s a}{3Y_c t} (\phi(\omega_0)_{coated} - \phi(\omega_0)_{substrate}). \quad (4.14)$$

4.3.6 Tin oxide coating loss results

Equation 4.14 was used to calculate the coating loss of the three SnO coatings from the loss factors of the cantilevers before and after deposition of the coating. The Young's modulus of the tin oxide coating was taken to be 100 ± 10 GPa [199]. The calculated coating loss factors are shown in Figure 4.13. The loss of the 25 nm thick SnO film was significantly lower than that of the thicker films below 2.5 kHz. The high coating loss measured at 3.6 kHz for the 25 nm coating arises from the anomalously high loss measured for this mode after the cantilever was coated. As discussed in Section 4.2.4, this high loss is possibly related to frequency dependent energy loss into the clamping structure. The large error in the coating loss in Figure 4.11 arises primarily from the combination of the uncertainties in the Young's modulus and thickness of the tin oxide films.

Table 4.2 summarizes the thickness, energy ratio and average loss across all of the measured modes for the three coatings measured. It can be seen in Figure 4.14 that the average loss appears to have a linear dependence on the coating thickness. It is possible that this apparent dependence of the loss on coating thickness is due to structural differences in the thicker coatings. On examination under an optical microscope, the thicker coatings were found to contain many large grain-like structures, shown in Figure 4.15. Particularly large crystal structures were observed near the free end of the cantilever (i.e. the opposite end from the weld). These structures were not observed in the 25 nm thick coating.

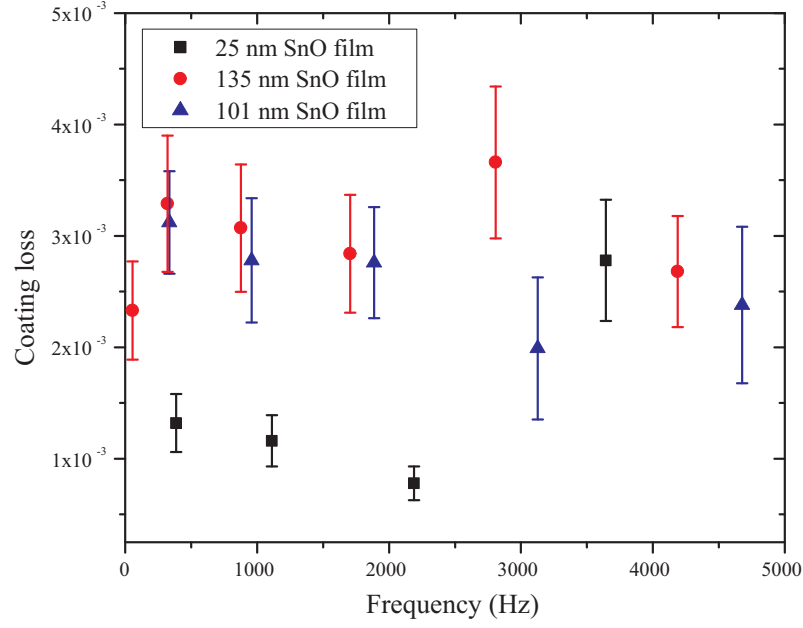


Figure 4.13: Plot of the calculated coating loss for each of the three SnO coatings studied.

The mean mechanical loss calculated for all of the modes of the three samples studied was $(2.4 \pm 0.2) \times 10^{-3}$. This is of the same order as measurements of the dissipation of SnO₂ films at higher frequencies (between 5 and 20 kHz) reported by Mitrokhin et al [200].

	Sample 1	Sample 2	Sample 3
SnO coating thickness	25 ± 2.5 nm	101 ± 10 nm	135 ± 14 nm
$E_{\text{coating}}/E_{\text{substrate}}$	0.69×10^{-3}	2.72×10^{-3}	3.07×10^{-3}
Mean mechanical loss of SnO	$(1.5 \pm 0.3) \times 10^{-3}$	$(2.6 \pm 0.2) \times 10^{-3}$	$(3.0 \pm 0.2) \times 10^{-3}$

Table 4.2: Summary of thickness and mean mechanical loss for the three tin oxide coating samples.

4.3.7 Thermal noise modelling

The level of thermal noise associated with an SnO coating applied to the front surface of a test mass in a gravitational wave interferometer can be calculated

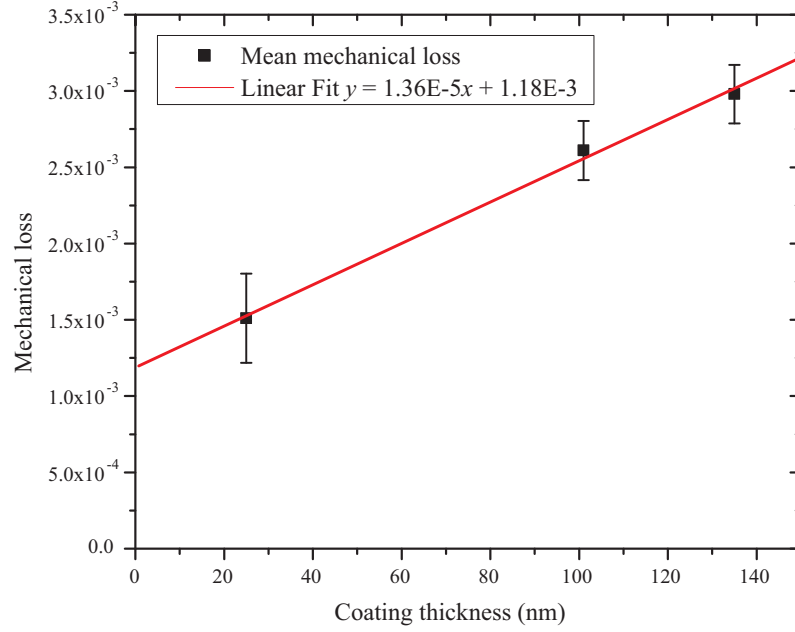


Figure 4.14: *The mechanical loss measured as a function of coating thickness, with a linear fit to the data. Each point indicates the mean loss measured for several modes of a sample.*

from the measured mechanical loss using Equation 2.52. Assuming that the mechanical losses associated with strains parallel and perpendicular to the coating surface are identical, $\phi_{\parallel} = \phi_{\perp}$, this equation becomes:

$$S_x(f) = \frac{2k_B T}{\pi^2 f} \frac{d}{Y w_0^2} \left(\frac{Y'}{Y} + \frac{Y}{Y'} \right) \phi, \quad (4.15)$$

where f is frequency, T is temperature in Kelvin, Y and Y' are the Young's modulus values for the substrate and coatings respectively, ϕ is the mechanical loss of the SnO coating, d is the coating thickness and w_0 is the radius of the interferometer laser spot in terms of electric field amplitude. The loss of the coating was taken to be the mean mechanical loss measured for all of the modes of the three samples: $\phi = 2.4 \times 10^{-3}$.

Since thermal noise associated with the optical coatings is expected to set the primary limit to the sensitivity of future detectors in their most sensitive frequency band, it is desirable for the magnitude of any additional thermal

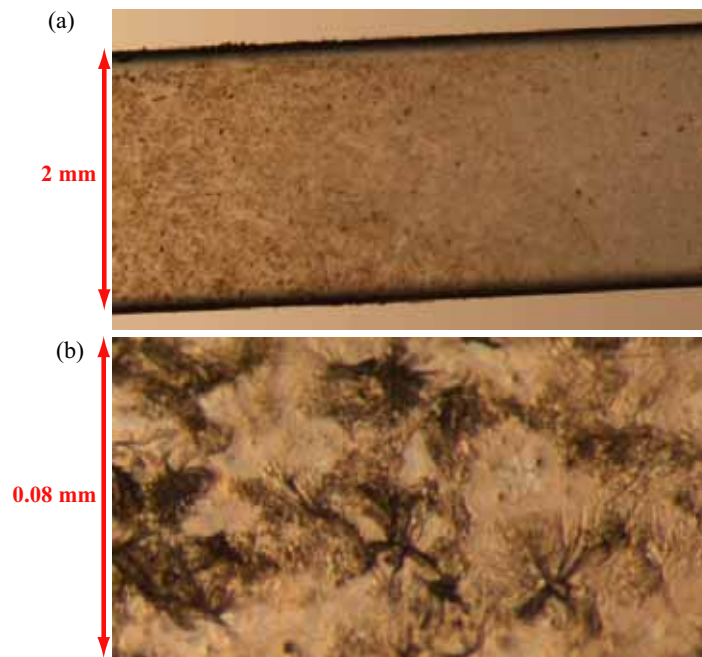


Figure 4.15: (a) Microscope images of the surface of sample 3 after coating with tin oxide. (b) Higher magnification image of the tin oxide coating showing evidence of the formation of large crystals.

noise (e.g. from SnO coatings) to be at least an order of magnitude lower than this. This is a general design requirement of the Advanced LIGO detectors. Figure 4.16 shows the calculated linear spectral density of the Brownian thermal noise associated with two different thicknesses of SnO coating applied to the front face of a detector mirror. Also shown is the Brownian thermal noise arising from a standard silica-tantala multi-layer reflective coating. It can be seen that for a 100 nm thick SnO coating the associated thermal noise is only a factor of ~ 2 lower than the noise from the reflective coating. To ensure the thermal noise associated with an SnO coating would be a factor of ten lower than the reflective coating thermal noise, as required for the Advanced LIGO design, a thickness of ≈ 4 nm of SnO would be necessary. This is approximately five times thinner than the thinnest coating produced by spray pyrolysis to date, and further work would be needed to establish if such a thin coating could be produced and to study its optical, mechanical and electrical

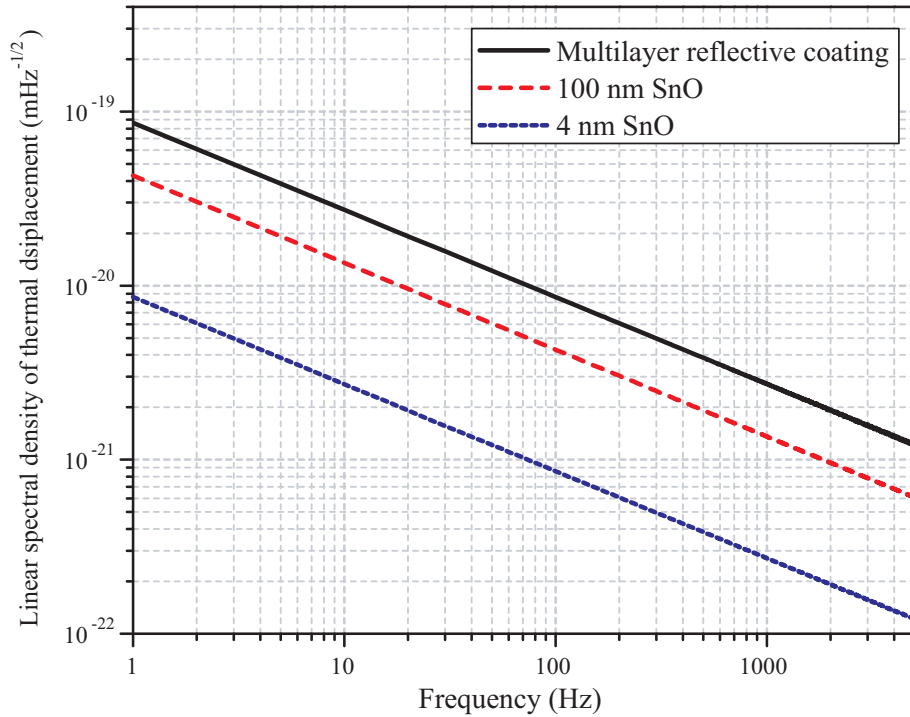


Figure 4.16: *Calculated levels of the Brownian thermal noise associated with a 100 nm and a 4 nm thick SnO coating on a fused silica mirror illuminated by a laser beam of radius $r_0=3.9$ cm, compared to the thermal noise arising from a multilayer HR coating.*

properties. Studies of mechanical loss in SnO coatings deposited by alternative methods may also be of interest, although it should be noted that similar losses to those presented here have been measured in SnO films deposited by magnetron sputtering [200].

As noted previously, the mechanical dissipation of the SnO coatings was observed to have some dependence on the film thickness. Further investigation to confirm this relationship is required. However, if confirmed it would potentially allow the target thermal noise to be met by a slightly thicker coating. This may be of some importance if the optical and electrical properties are found to also depend on the thickness of the coating. The linear fit in Figure 4.14 gives the following relationship between the mechanical loss, ϕ , and

thickness in meters, t , of an SnO coating:

$$\phi = 1.36 \times 10^4 t + 1.18 \times 10^{-3}, \quad (4.16)$$

from which the loss of a 4 nm thick coating can be found to be 1.24×10^{-3} , a factor of 1.9 lower than the mean loss used above. This would result in a reduction in the linear spectral density of thermal displacement associated with the coating by a factor of 1.38 (since the linear thermal spectral density, x , is defined as $x(f) = \sqrt{S_x(f)}$). The loss-thickness relationship can be substituted into Equation 4.15 to calculate the coating thickness required for a particular level of thermal noise. The maximum coating thickness compatible with the Advanced LIGO noise target is found to be 7.4 nm.

4.3.8 Conclusion

Initial investigations have shown that conductive tin oxide coatings applied to the test-mass mirrors beneath the reflective mirror coatings could potentially fulfill both the optical absorption and thermal noise requirements for future gravitational wave detectors. The use of these coatings could mitigate both control problems and increased levels of thermal noise associated with electrostatic charging of the mirrors. Coatings of less than 10 nm in thickness would be required to meet the thermal noise specifications of future detectors, necessitating further studies of the properties of very thin SnO coatings.

4.4 Dissipation in optical coatings

As discussed in Chapter 2, the thermal noise arising from the mechanical loss in the mirror coatings is expected to limit the sensitivity of the next generation of gravitational wave detectors between several tens and several hundreds of Hertz. In this section, experiments using silica cantilevers to measure the loss factors of single layers of the individual coating materials will be described.

4.4.1 Reflective dielectric coatings

Interferometric gravitational wave detectors require mirrors with a very high reflectivity, as discussed in Chapter 1. Metallic coatings are not suitable due to high levels of absorption [201], potentially resulting in excessive thermal deformation in the mirror and damage to the coating. Dielectric coatings, however, tend to have lower absorption levels and are more durable than metallic coatings [201]. Highly reflecting dielectric coatings consist of alternating layers of two dielectric materials with different refractive indices. The optical thickness of each layer is generally $\lambda/4$, where λ is the wavelength to be reflected: 1064 nm in the case of the Nd:YAG lasers used in gravitational wave detectors.

Optical thickness, δ , is related to the actual thickness of the layer, t , by:

$$\delta = nt, \quad (4.17)$$

where n is the refractive index of the layer. An illustration of a quarter-wavelength reflective coating is shown in Figure 4.17.

The total reflectivity of the coating is related to the difference in the refractive indices of the alternating layers. For a laser beam in a medium with refractive index n_0 incident on a multi-layer coating with an even number, $2N$, of layers of refractive indices n_H and n_L with $n_H > n_L$, the reflectivity of the coating is given by [202] :

$$R_{2N} = \left(\frac{n_s f - n_0}{n_s f + n_0} \right)^2, \quad (4.18)$$

where n_s is the refractive index of the substrate and $f = (n_H/n_L)^{2N}$. For an odd number, $2N + 1$, of layers this expression becomes:

$$R_{2N+1} = \left(\frac{n_H^2 f - n_0 n_s}{n_H^2 f + n_0 n_s} \right)^2. \quad (4.19)$$

The reflectivity of the coating can therefore be increased either by increasing the number of pairs of high and low index layers or by increasing the difference between the refractive indices of the layers. For a given reflectivity the number of layers, and thus the thickness of the coating, can be reduced by using materials with a large difference in refractive index.

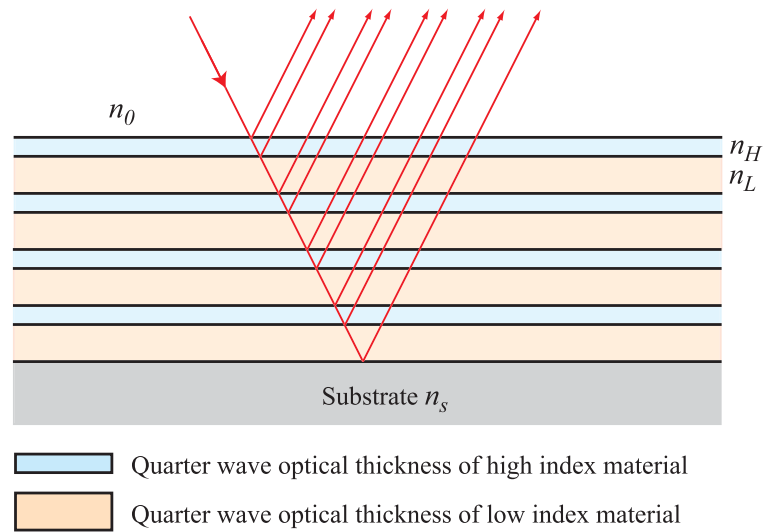


Figure 4.17: A schematic diagram of a multi-layer reflective coating, composed of alternating layers of a high refractive index (n_H) and a low refractive index (n_L).

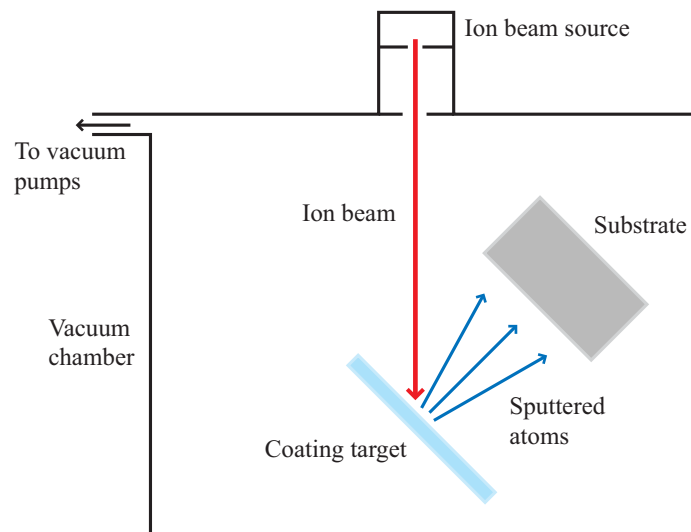


Figure 4.18: A schematic diagram of a simple ion-beam sputtering chamber.

4.4.1.1 Coating production

All current gravitational wave detectors use multi-layer dielectric coatings formed from alternating layers of silica (SiO_2) and tantalum pentoxide (Ta_2O_5). These layers are deposited by ion-beam sputtering. In this technique, a beam of ions is accelerated towards a target of the coating material. On impact, the ions eject atoms from the surface of the target, which travel to the substrate where they condense, gradually forming a uniform coating layer. A simple schematic of an ion beam sputtering system is shown in Figure 4.18. Tantalum pentoxide coatings are usually produced using a tantalum metal target with a small amount of oxygen present in the deposition chamber [203]. The sputtered tantalum atoms react with the oxygen atoms and are subsequently deposited as tantalum pentoxide. The coatings studied in this these were deposited using argon ions as the sputtering species.

Ion-beam sputtering has several advantages over other thin film deposition methods. Since the sputtered ions have a relatively high energy (several eV), the coating atoms adhere more strongly to the substrate and the coatings tend to have a denser structure [204]. In addition, the optical absorption of ion-beam sputtered coatings is significantly lower than for coatings deposited with other techniques such as electron beam deposition [205]. Post-deposition thermal annealing is used in most optical coatings to reduce optical absorption losses [203].

4.4.2 Mechanical dissipation in coating materials

As discussed in Chapter 2, recent research has shown that thermal noise associated with the Brownian motion of the ion-beam sputtered cavity mirror coatings of amorphous oxide materials sets a fundamental limit to the sensitivity of interferometric gravitational wave detectors [128, 129, 206, 207]. In addition to gravitational wave detectors, similar amorphous oxide coatings are utilised in the laser cavities used in the development of highly frequency-stabilised lasers

for high-resolution optical spectroscopy [208], fundamental quantum measurements, optical frequency standards [209, 210] and quantum information science [211]. These systems are currently limited, or expected to soon be limited, by thermal noise in the cavity mirror coatings.

It is clearly of major importance to a range of precision measurement systems to determine the exact level of dissipation, and thus thermal noise, expected from specific coatings, to understand the mechanism responsible for this dissipation and to study possible methods of reducing it.

4.4.2.1 Previous measurements of coating dissipation

Previous studies have shown that dissipation in the commonly-used SiO_2 / Ta_2O_5 coatings is dominated by the dissipation in the coating materials, and is not significantly affected by friction at the layer interfaces or by the coating/substrate interface [130, 131]. It has also been shown that the dissipation of the Ta_2O_5 layers is significantly larger than that of the SiO_2 layers, and some evidence of a small frequency dependence of the coating loss has been observed [131, 212]. Currently a number of research groups worldwide are involved in a programme of research aimed at understanding the mechanical dissipation of the coating materials and studying ways of reducing it. One approach has involved the reduction of the total Ta_2O_5 content of a multi-layer coating, using an optimisation technique which varies the number and thickness of coating layers to minimise the mechanical loss for a given reflectivity [213]. Modelling has suggested that a reduction of approximately 14 % in the coating dissipation may be achievable using this technique.

Another approach has been to attempt to reduce the mechanical loss of the Ta_2O_5 layers by doping. It has been shown that the dissipation of a SiO_2 / Ta_2O_5 coating can be reduced by up to $\sim 40\%$ by doping the Ta_2O_5 with titanium dioxide (TiO_2) [214]. The lowest coating loss factor measured by Harry et al [214] was 1.7×10^{-4} , for a coating which was doped with TiO_2 to a level of $(24 \pm 2)\%$ Ti cation concentration. However, there is no clear

correlation between the concentration of TiO_2 dopant and the magnitude of the reduction in dissipation and, as yet, the exact mechanism by which this doping reduces the dissipation is not clearly understood.

4.4.3 Coating loss measurements using silica cantilever substrates

Most coating loss experiments to date have focussed on multi-layer coatings applied to samples with a comparatively small surface to volume ratio. The experiments presented in this thesis were designed to study the dissipation of single layers of either Ta_2O_5 or SiO_2 , thus allowing these materials to be studied independently of each other. The coatings studied were applied to thin substrates, between approximately 50 and 100 nm in thickness. Thin substrates are desirable to ensure a relatively high fraction of the total elastic energy associated with a resonant mode is stored in the coating, thus increasing the effect of the intrinsic loss of the coating on the loss factor of a coated cantilever.

In this section, measurements of the mechanical loss of single layers of optical coating materials applied to silica cantilevers will be described. This work was carried out in collaboration with LMA, a coating vendor in Lyon [215]. Colleagues at LMA had developed an experiment to measure the loss of coatings applied to silica membranes (45 mm long, 10 mm wide and ≈ 0.11 mm thick) fabricated by mechanically polishing silica wafers. After manufacture, the membranes were annealed at 1000°C for approximately ten hours.

The measurement technique used by LMA involved directly clamping the membranes in a highly polished steel clamp. In an effort to obtain better isolation from the clamp, six of these membranes were sent to the lab in Glasgow, where they were attached to clamping blocks of approximate dimensions $10\text{ mm} \times 10\text{ mm} \times 1\text{ mm}$ using the CO_2 laser welding technique described in Section 4.2.6.

The loss of the first six bending modes of the uncoated welded samples was measured at room temperature, initially by the author and latterly with the assistance of another student, P. Holt [216]. To test the level of clamping loss in these samples, one membrane was welded to a 5 mm thick silica block. This resulted in no significant difference to the measured loss, suggesting that adequate isolation from the clamping structure was provided by the 1 mm thick clamping blocks.

The lowest loss factors measured in the set of seven membranes are compared to data for an identical un-welded membrane clamped directly in the LMA clamp in Figure 4.19. The loss of the welded ribbon discussed in Section 4.2.6 is also included for comparison. Welding the membranes to clamping blocks can be seen to significantly reduce the measured mechanical loss, suggesting that the clamping block may reduce recoil and frictional losses into the clamp. However, the loss of the welded LMA membranes was significantly higher than the loss of the welded silica ribbon. It is possible that this difference is related to the different surfaces of the two types of sample. The polishing process used to fabricate the LMA membranes may have left a damaged surface which could be more lossy than the smooth surface of a flame pulled ribbon.

The loss of the damaged surface layers can be estimated by comparing the results to the Penn model (Equation 4.4) and the experimental data for a flame-pulled silica ribbon (Section 4.2.6). The modelled loss obtained from the bulk and thermoelastic terms of Penn's model were subtracted from the measured loss of each mode to find the level of 'excess loss' present. Excess loss is defined here as the sum of the loss associated with the surface, ϕ_S , and any loss due to the weld region or the clamp, ϕ_{other} :

$$\phi_{\text{excess}} = \phi_S + \phi_{\text{other}}. \quad (4.20)$$

Thus the total measured loss can be represented by:

$$\phi_{\text{measured}} = \phi_{\text{thermoelastic}} + \phi_{\text{bulk}} + \phi_{\text{excess}}, \quad (4.21)$$

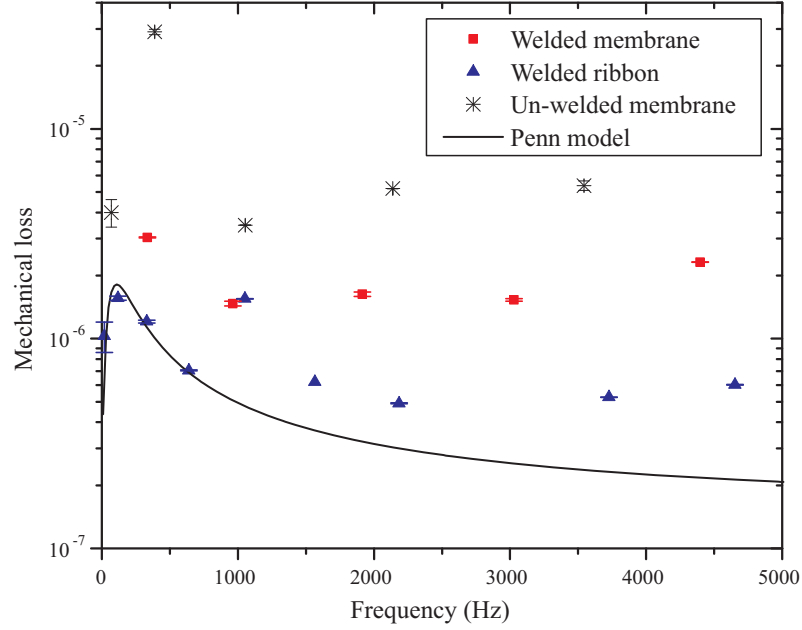


Figure 4.19: *Plot of the lowest losses measured in the 7 welded silica membranes, compared with the losses measured in a welded ribbon section.*

where ϕ_{measured} is the measured loss for a mode and $\phi_{\text{thermoelastic}}$ and ϕ_{bulk} are the thermoelastic and bulk loss terms from Penn's model.

A simple model for the surface loss assumes that there is a surface layer of thickness h , which is lossier than the bulk of the material, with a dissipation factor of ϕ_{surface} [217]. It is important to distinguish between ϕ_{surface} , which is the actual loss of the surface layer (which would be obtained if the surface could be removed from the sample and measured independently) and ϕ_S , the part of the total measured loss which is due to surface loss. Following the argument in Section 4.3.5 for a coated beam, the contribution ϕ_S of the surface loss to the total loss of the cantilever is related to the loss factor of the surface layer, ϕ_{surface} , by the ratio of the energy stored in the surface layer to the energy stored in the bulk of the cantilever:

$$\phi_S = \frac{E_{\text{surface}}}{E_{\text{bulk}}} \phi_{\text{surface}}. \quad (4.22)$$

Assuming that the Young's modulus of the surface layer is identical to that of

the bulk of the ribbon, the energy ratio given by Equation 4.13 can be corrected by a factor of two to account for the presence of the lossy surface layer on both sides of the ribbon, giving the following expression for the surface loss:

$$\phi_S \doteq 6 \frac{h}{a} \phi_{\text{surface}}, \quad (4.23)$$

where a is the thickness of the ribbon. Here, the portions of the surface associated with the thin edges of the ribbons and membranes are ignored.

Measurements by Heptonstall et al suggest the product $h\phi_{\text{surface}}$ in flame-pulled silica ribbons is $\approx 3 \times 10^{-12}$ m [217]. Using this value, the weld or clamp loss associated with the ribbon cantilever, ϕ_{other} can be estimated using Equation 4.21, using the average experimental loss factor at frequencies above the thermoelastic peak. Further assuming that this weld loss is identical for the ribbon and the membrane sample, the surface loss, ϕ_S in the membrane can be calculated using Equation 4.21, to give a value of 1.23×10^{-6} . The value of $h\phi_{\text{surface}}$ can then be calculated using Equation 4.23, giving $h\phi_{\text{surface}} = (2.3 \pm 0.2) \times 10^{-11}$ m.

Studies of fused silica suggest that an appropriate thickness for the lossy surface layer in flame-pulled silica fibres is $\sim 1 \mu\text{m}$ [218]. This lossy layer could arise from chemical contaminants or from absorption of water from the flame used to heat the silica prior to pulling the fibre. It is also possible that stress arising as the molten ribbon cools could alter the loss of a surface layer [217, 218].

Studies of the thickness of a damaged layer in silica caused by polishing have been carried out as part of the Gravity Probe B mission, with the layer thickness found to be approximately twice the diameter of the polishing particles used [219]. Thus for the polished surface of the membrane, which was polished with particles of diameter $\sim 1 \mu\text{m}$ [216], $h = \sim 2 \mu\text{m}$. These values for the thickness of the lossy surface layers give the following surface losses:

$$\phi_{\text{surface(ribbon)}} = (3 \pm 0.2) \times 10^{-6}, \quad (4.24)$$

$$\phi_{\text{surface(membrane)}} = 1.1 \pm 0.1 \times 10^{-5}. \quad (4.25)$$

Given these assumptions, the loss of the surface layer damaged by polishing, after annealing, is found to be approximately a factor of 4 higher than the loss of the surface of a flame-pulled ribbon. Heat treatment is known to reduce the loss of silica [171], therefore it is likely that a mechanically polished surface which was not heat treated would have a higher loss. This calculation is only an estimate, and relies on several assumptions. More accurate measurements of the surface loss of a polished surface could be obtained by using identically sized samples to ensure that the weld loss and clamp loss between the two samples would be closer to being identical. An alternative method used by another postgraduate student in Glasgow is to attempt to remove the damaged surface layer by chemical etching, and measure the resulting change in loss of the sample [216]. The loss of a polished silica surface is of interest to allow accurate calculation of the thermal noise associated with the polished front face of the test mass mirrors in gravitational wave detectors, as discussed by Reid [159].

4.4.4 Coating loss measurements

After the loss factors of the uncoated welded membranes discussed above had been measured, they were sent to LMA for coating with single layers of tantalum and silica. Most of the coated membranes were studied by colleagues at LMA; however, the loss factors of two of the coated samples were measured in Glasgow. These membranes, whose loss factors had been measured prior to coating, were coated with variants of the LMA Formula 5 coating (Ta_2O_5 doped with 14.5 % TiO_2) known as Formula 5** (F5**) and Formula 5*** (F5***). These variants were produced using a method in which a commercially sensitive deposition parameter was varied in an attempt to reduce the mechanical loss of the coating [220], and are otherwise identical to the doped Formula 5 coating measured elsewhere [214]. The loss factors measured for the

F5** and F5*** coatings are shown in Figure 4.20. It can be seen that lower loss factors were measured for the F5** coating for three of the four modes measured. At 350 Hz, the F5*** coating has a marginally lower loss, although it is within experimental error of the loss factor for the F5** coating. It is likely that the high loss of $\sim 1 \times 10^{-3}$ measured for the F5*** coating at 2 kHz was influenced by energy coupling to a mode of the clamp during the measurements of the coated sample.

In addition to these welded membranes, several coated silica membranes which were not welded to clamping blocks were measured by the author and Paul Holt during a visit by collaborators from LMA to the lab in Glasgow. A silica coating, an undoped tantala coating and a further variant of the LMA Formula 5 titania-doped coating known as Formula 5* were measured; each coating was 0.5 μm thick. All of the coated cantilevers which were studied are listed in Table 4.3. The coating loss was calculated using the loss measurements for the uncoated cantilever in the LMA clamp shown in Figure 4.19. The calculated coating losses are shown in Figure 4.21. The silica coating loss was found to be significantly lower than the loss of the tantala as expected, with a mean value (for the two modes studied) of $\sim 9.7 \times 10^{-5}$. The loss factors for the F5* coating are approximately a factor of 1.4 lower than those for the undoped tantala.

If the loss measurements using the welded and unwelded substrates are compared, it can be seen that all of the TiO_2 -doped Ta_2O_5 coatings have a lower loss than the undoped coating, with Formula 5** having the lowest loss. While this comparison is not ideal, as the welded cantilevers have been shown to be better isolated from the clamp, it may be valid if it is assumed that the frictional clamping losses are approximately equal for both the coated and uncoated cantilevers. If this is the case, the effects of the frictional loss could be expected to be removed when the loss factors of the coated and uncoated cantilevers are subtracted.

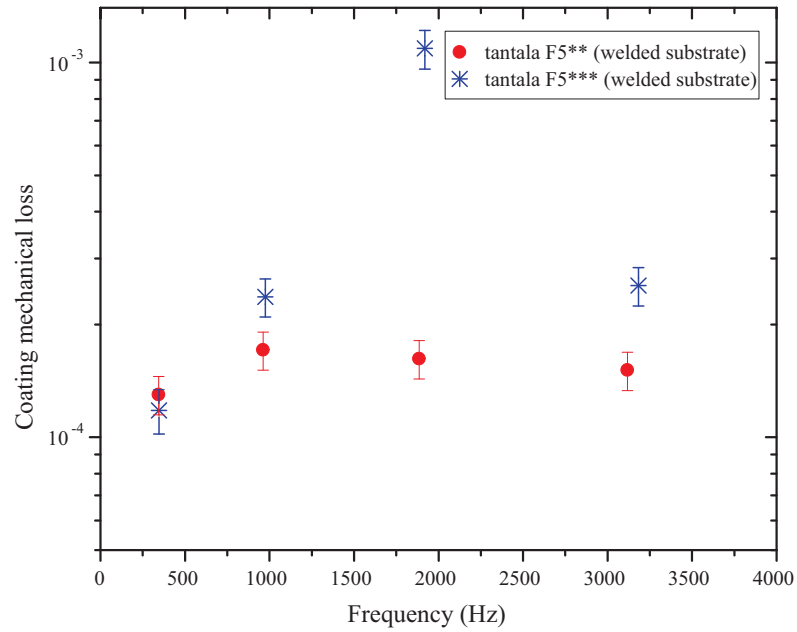


Figure 4.20: Plot of the coating loss factors for LMA F5** and F5*** tantalum, measured using silica membrane substrates welded to silica clamping blocks.

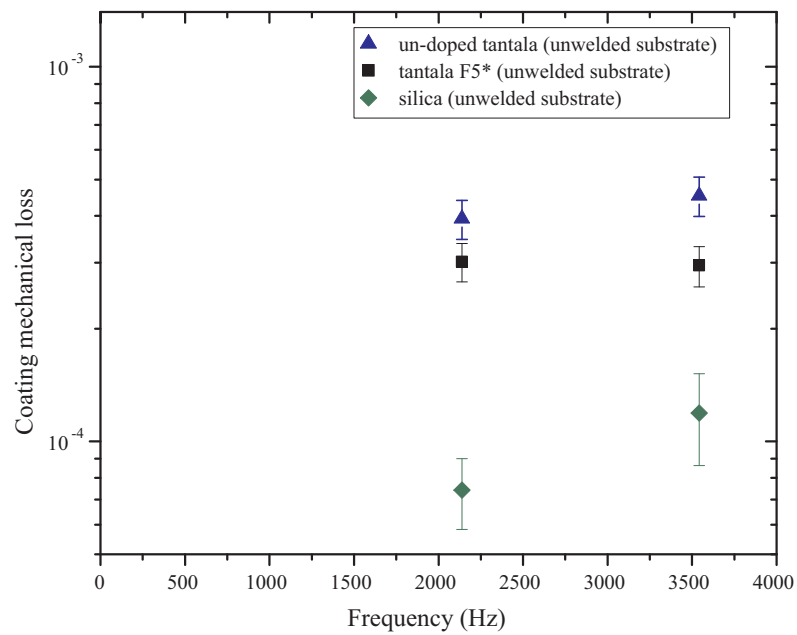


Figure 4.21: Plot of the coating loss factors for undoped tantalum, LMA F5* doped tantalum and silica coatings, measured using unwelded membranes in the clamp developed by LMA.

Coating	Substrate	Mean mechanical loss
Undoped Ta ₂ O ₅	Un-welded SiO ₂ membrane	$(4.2 \pm 0.3) \times 10^{-4}$
Doped Ta ₂ O ₅ F5*	Un-welded SiO ₂ membrane	$(3.0 \pm 0.01) \times 10^{-4}$
Doped Ta ₂ O ₅ F5**	Welded SiO ₂ membrane	$(1.5 \pm 0.1) \times 10^{-4}$
Doped Ta ₂ O ₅ F5***	Welded SiO ₂ membrane	$(2.0 \pm 0.4) \times 10^{-4}$
SiO ₂	Un-welded SiO ₂ membrane	$(0.97 \pm 0.02) \times 10^{-4}$

Table 4.3: *The average mechanical loss (calculated for all mode frequencies studied) of several coatings applied to silica membranes. All coatings were 0.5 μm thick: the membranes were 110 μm thick.*

The results indicate that the deposition parameter which is altered to produce the different variants of Formula 5 Ta₂O₅ tantala may significantly affect the mechanical loss of the coating. Without knowing what this parameter is, the results are hard to analyse further: however, it is clear that the loss of Ta₂O₅ coatings with the same level of doping can be significantly reduced by optimising the conditions under which they are deposited.

The following chapter describes a series of experiments designed to study the mechanism by which energy is dissipated in Ta₂O₅ coatings, and the effect of TiO₂ doping on this mechanism. In addition, this technique may be of value for a systematic study of the effects of various deposition parameters on the dissipation in these coatings.

4.5 Conclusion

Thermal noise arising from dissipation in the mirror coatings is expected to limit the sensitivity of the next generation of gravitational wave detectors at their most sensitive frequencies. In recent years, studies have shown that the dissipation in SiO₂/Ta₂O₅ coatings is dominated by the Ta₂O₅ layers, and that the dissipation can be significantly reduced by doping the Ta₂O₅ with TiO₂. However, further studies of the level of dissipation in the various coating mate-

rials are of considerable interest. Charging of the test masses in gravitational wave detectors can cause excess noise and affect the operation of control systems in the interferometers. The mechanical properties of conductive coatings for use in mitigating charging effects is thus of interest.

Methods of fabricating and clamping silica cantilevers for mechanical loss measurements of coating materials have been investigated. It has been shown that welding a section of silica ribbon to a thicker silica clamping block can provide isolation from the clamping structure, with evidence of the reduction of slip-stick losses in the clamp. These cantilevers have been used to study the loss of conductive tin oxide coatings, the loss of single layers of the materials used in the mirror coatings and the loss associated with the damaged silica surface layer caused by polishing.

Results have shown that tin oxide coatings applied by spray pyrolysis with a maximum thickness of 4 - 8 nm would meet the thermal noise requirements for Advanced LIGO. Further study of a possible relationship between the dissipation and the coating thickness is required.

Preliminary measurements of the dissipation in single layers of SiO_2 and Ta_2O_5 at room temperature have been carried out. The results suggest that varying a particular (undisclosed) deposition parameter can reduce the dissipation in Ta_2O_5 coating layers doped with 14.5 % TiO_2 by up to $\approx 50\%$. The variant of this coating found to have the lowest loss at room temperature is Formula 5**. In the remainder of this thesis, investigations of the temperature dependence of the dissipation in single layers of ion-beam sputtered silica and tantala coatings are presented.

Chapter 5

Temperature dependence of the mechanical dissipation in tantalum pentoxide coatings

5.1 Introduction

As discussed in Chapter 4, thermal noise arising from the mechanical loss in the ion-beam sputtered mirror coatings is expected to limit the sensitivity of the next generation of gravitational wave detectors at frequencies between several tens and several hundreds of Hertz. In the case of the proposed Advanced LIGO detectors, coating thermal noise is predicted to be the dominant noise source between approximately 40 and 400 Hz. This frequency band will coincide with the peak sensitivity of the detectors. Reduction of the level of coating thermal noise has therefore become one of the most significant challenges to be overcome in the design and development of future generations of detectors.

In general, as can be seen from Equation 2.51, thermal noise can be reduced by reducing the mechanical dissipation of the materials used or by reducing the temperature of the mirror. These approaches aim to reduce the thermal motion of the mirror in the frequency band of interest. A third method currently under investigation is the reduction of the effect of the thermal motion on the sensitivity of the interferometer through the use of different laser beam

profiles, such as a flat-topped ‘mesa beam’ instead of a standard Gaussian beam [134, 135, 136, 137, 138, 139].

For the second generation detectors, such as Advanced LIGO, research has focussed on reducing the dissipation of the current $\text{SiO}_2/\text{Ta}_2\text{O}_5$ coatings. Studies have indicated that at room temperature the dissipation of these coatings is dominated by the dissipation of the Ta_2O_5 layers, and can be reduced by up to 40% by doping the Ta_2O_5 with TiO_2 . However, neither the mechanism responsible for the dissipation nor the process by which it is reduced by doping with TiO_2 is clearly understood. A better understanding of the process responsible for the dissipation in Ta_2O_5 may allow it to be further reduced.

One method of probing the dissipation mechanisms in a material is to measure the dissipation as a function of temperature. Many materials exhibit temperature dependent dissipation peaks, occurring at particular temperatures associated with the activation energy of the process responsible for the dissipation. A well-known example of such a material is fused silica, which has a large dissipation peak at around 40 to 60 K. Studies by several authors have associated this peak with energy dissipation arising from thermally activated transitions of oxygen atoms between two energy states in the amorphous SiO_2 network [93, 221, 222]. The broad nature of this peak has been associated with the distribution of bond angles in the disordered network of SiO_2 molecules [172, 173]. The form of the temperature dependence of the dissipation in fused silica is thus strongly associated with the dissipation mechanism. Low temperature dissipation peaks have also been observed in several other amorphous oxides and disordered crystalline materials, including GeO_2 and B_2O_3 [223]. The ion-beam-sputtered Ta_2O_5 used in reflective coatings is also an amorphous oxide (see Figure 5.31), and it is therefore of considerable interest to study its dissipation as a function of temperature.

Cooling the mirror is perhaps the most intuitive method of reducing thermal motion, and generally a direct reduction in thermal noise is expected on

lowering the operating temperature of a material. However, as discussed above, mechanical dissipation is often strongly dependent on temperature and fused silica, the most commonly used test mass material in current detectors, has a large, broad dissipation peak centered on approximately 40 to 60 K [93]. Silica is therefore not a promising material for use in a low temperature gravitational wave interferometer.

In contrast, other materials such as silicon are known to have low dissipation at cryogenic temperature [224, 225], making a further reduction in substrate thermal noise possible by operation at low temperatures. The thermal expansion coefficient and thermal conductivity of silicon also make it attractive for use as a mirror substrate in a low temperature detector using a high circulating laser power [94]. Currently, a European Commission design study for a third generation gravitational wave detector is underway [98], and this includes significant research into the use of cryogenically cooled silicon mirrors. It is therefore important to study the temperature dependence of the dissipation of the appropriate mirror coatings to allow the coating thermal noise contribution to the sensitivity of a low temperature interferometer to be calculated.

The study of coating loss as a function of temperature therefore has two purposes: firstly, the performance of the coating materials at low temperatures must be evaluated for use in possible future cryogenic detectors; secondly, the temperature dependence of the dissipation of Ta_2O_5 may help to understand the underlying dissipation mechanism.

5.1.1 Measurements of the temperature dependence of coating dissipation

As in Chapter 4, to ease interpretation, single layers of Ta_2O_5 were applied to thin cantilever substrates. Ideally the loss of the substrate used for coating loss measurements should be as low as possible, to ensure high sensitivity to the loss of the coating material. This precluded the use of silica cantilevers, as the

low temperature dissipation peak in silica may have made interpretation of the results more difficult. Thin silicon substrates of order 50 to 100 μm in thickness were chosen, as the loss of silicon is known to decrease at low temperature [224], thus minimising the contribution of the substrate to the total measured loss. Silicon is also a particularly interesting substrate material as it is a likely candidate material for the test masses future cryogenic gravitational wave detectors [94, 95].

Yamamoto et al [226] have recently measured the temperature dependence of the mechanical dissipation of multi-layer silica-tantala coatings applied to sapphire substrates, with data taken at room temperature (300 K) and at a small number of temperatures between 80 K and 4 K . The tantala layers of these coatings were not doped. These results show a small variation in coating loss across the entire temperature range, between approximately 2×10^{-4} and 4×10^{-4} . Yamamoto suggests that the temperature dependence of the coating loss is therefore essentially flat: however, with only five temperature points measured, this experiment is not conclusive.

In the remainder of this chapter studies of the mechanical loss of various tantala coatings as a function of temperature are presented. The experimental apparatus is described, and initial measurements of two coating samples between 290 and 80 K are presented. Measurements below 80 K were initially carried out by the author at Freidrich-Schiller University in Jena, Germany. The cryostat in Glasgow was then modified by the author to allow cooling to liquid helium temperatures and the loss factors of several additional samples were measured at temperatures between 10 K and 300 K.

5.2 Initial measurements of the loss of doped tantalum pentoxide

5.2.1 Sample preparation

The silicon cantilever substrates were fabricated, by colleagues at Stanford University, from approximately 0.5 mm thick single-crystal silicon wafers by a hydroxide etching process. Suitable masking during this process allowed one end of the cantilever to remain un-etched, forming a thicker block by which the cantilever could be clamped, as shown in Figure 5.1. This clamping block was intended to reduce energy loss into the clamping structure through frictional processes such as stick-slip loss [174, 225].

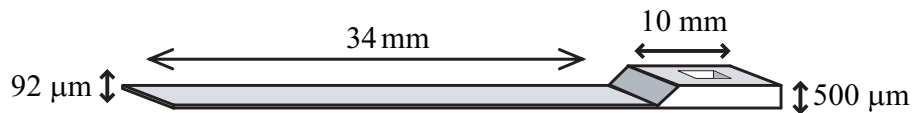


Figure 5.1: *Schematic diagram of cantilever sample A, 34 mm long, 10 mm wide and 92 μm thick. The cantilever length is parallel to the $\langle 110 \rangle$ crystal axis and the surface is on the (100) plane.*

Initial measurements were carried out on a doped tantala coating layer provided by LMA [215], a vendor involved in the development of coatings for the Advanced LIGO mirrors. The dissipation in the coating layer can be calculated from measurements of the mechanical loss of the cantilever before and after the application of the coating, as described in Section 4.3.5. It should be noted that the coating process involved two heat treatment steps which could potentially change the loss of the silicon cantilever itself. Firstly, to enable the coating to adhere properly to the silicon surface, it was necessary to grow a thermal oxide layer on the cantilever surfaces. A dry-oxidation process was used, in which the cantilevers were heated to 900°C in air for ten hours, resulting in an SiO₂ layer (~ 20 to 30 nm) thick [220]. Secondly, after

deposition of the coating, the cantilevers were put through a heat treatment procedure at 600°C for 24 hours under atmospheric conditions. Post-deposition heat treatment is standard practice to reduce absorption losses and to relieve the internal stress in ion-beam sputtered multi-layer coatings [203].

Initially two cantilevers, known as cantilevers ‘A’ and ‘B’, were coated; the properties of each cantilever are given in Table 5.1. It was possible to measure the length of the cantilevers to an accuracy of ± 0.5 mm without contacting the cantilever surface. The thickness of each cantilever was calculated from measurements of its resonant mode frequencies at room temperature using Equation 4.3. Cantilevers A and B were found to be (92 ± 1) μm and (52 ± 2) μm thick respectively. This method of calculating the thickness gave excellent agreement with measurements using a Wyko NT1100 Optical Profiler, which showed cantilever A to be (92 ± 2) μm thick [159].

The loss of cantilever A had been studied as a function of temperature by a colleague, prior to the application of the coating [227]. These loss values have been used as the uncoated measurements for this sample. However, both of the heat treatment steps described above may possibly change the loss of a cantilever substrate, so that the previously measured uncoated loss of cantilever A may not be appropriate to use as the substrate loss in these studies. While the effect on the calculated coating loss was likely to be small, a second cantilever (cantilever B) with a nominally identical uncoated partner (cantilever C), etched from the same silicon wafer, was also coated. Cantilever C remained uncoated but was subject to identical thermal oxidation and post-deposition heat treatment. This ensured that in principle the only difference between cantilevers B and C was the presence of the coating layer. Previous measurements have shown the mechanical loss of uncoated cantilevers to be consistent to within 10 % for samples of the same dimensions etched from the same wafer [227].

Cantilevers A and B were coated with a 0.5 μm thick layer of Ta₂O₅ doped

with TiO_2 to a level of $(14.5 \pm 1) \%$, applied by ion-beam sputtering using argon as the sputtering gas. This coating is of interest as it is currently one of the lowest loss tantala coatings at room temperature [214] and it was deposited in a coating chamber which is suitable to produce the Advanced LIGO mirror coatings. During the coating procedure, the cantilevers were masked to prevent the coating extending onto the clamping block. After coating, both cantilevers were heated at 600°C for 24 hours. As noted above, the uncoated partner to cantilever B underwent the same thermal oxidation process and heat treatment as the coated cantilevers.

	Cantilever A	Cantilever B	Cantilever C
Length	34 ± 0.54 mm	57 ± 0.5 mm	57 ± 0.5 mm
Thickness	92 ± 1 μm	52 ± 1 μm	52 ± 1 μm
Doping	p-type	n-type	n-type
Dopant	Boron	Phosphorous	Phosphorous
Resistivity	$10\text{-}20 \Omega\text{cm}^{-1}$	$5\text{-}10 \Omega\text{cm}^{-1}$	$5\text{-}10 \Omega\text{cm}^{-1}$
Clamping block thickness	$500 \mu\text{m}$	$350\mu\text{m}$	$350\mu\text{m}$
Coating thickness	500 nm	500 nm	uncoated

Table 5.1: *Properties of the silicon cantilevers A, B and C.*

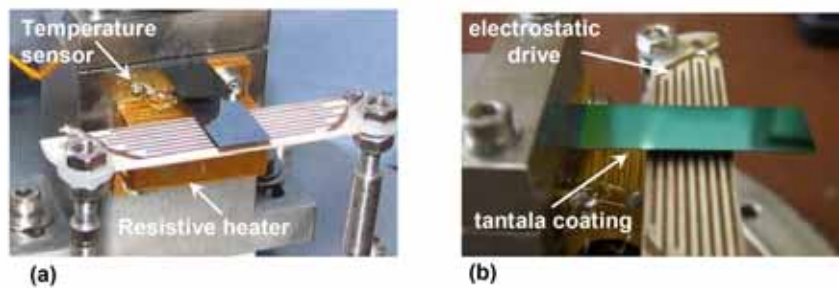


Figure 5.2: (a) *Cantilever A before coating.* (b) *Cantilever A after coating, clamped in preparation for mechanical loss measurements.*

5.2.2 Experimental method

Each silicon cantilever was held horizontally in a stainless steel clamp identical to the clamp used for the room temperature measurements described in Chapter 4. Figure 5.2 shows cantilever A in the clamp, both before and after coating. The clamp was rigidly attached to the base-plate of the vacuum chamber of a cryostat, which could be cooled by submersion in liquid nitrogen, as shown in Figure 5.3. As described in Section 4.2.4, the experimental chamber was evacuated to a pressure of less than 1×10^{-6} mb to ensure that gas damping effects were negligible. A resistive heater mounted on the clamp

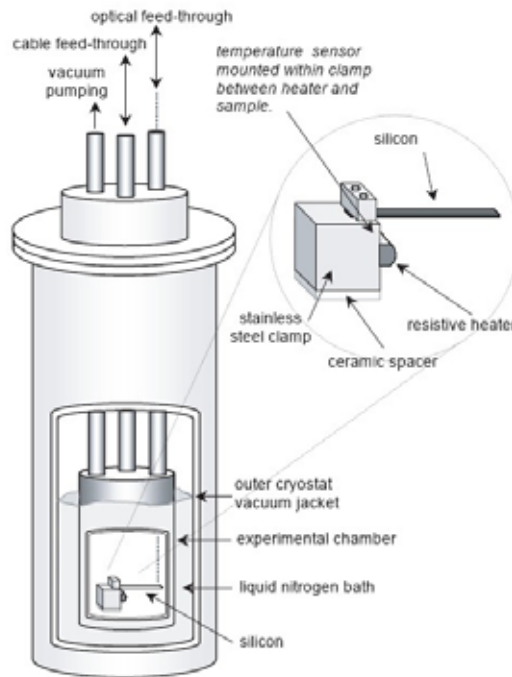


Figure 5.3: Schematic diagram of the cryostat, with an inset showing details of the clamp used to hold the cantilever samples.

was used to control the temperature of the clamp and cantilever. The temperature was measured using a silicon diode temperature sensor mounted within the clamp directly below the cantilever. Typically the temperature variation during measurements was less than ± 0.2 K. After the temperature of the

clamp had stabilised at each measurement point, the system was left for approximately five minutes before measurements commenced, to ensure that the cantilever was in thermal equilibrium with the clamp.

5.2.2.1 Readout system

For the room temperature measurements presented in Chapter 4, it was possible to position the clamped cantilever in the path of a laser beam and to measure the displacement of the resulting shadow. This arrangement was not straightforward to implement in the cryostat, as the optical feed-through pipe was located directly above the cantilever. Therefore the cantilever motion was sensed using a laser beam reflected from the surface of the cantilever and directed onto a photodiode sensor outside the cryostat. The movement of the cantilever displaced the reflected laser spot vertically. Due to the long path length between the cantilever and the photodiode, the motion of the reflected laser spot was typically too large to be sensed with a split-photodiode as used in Chapter 4. Thus a single rectangular photodiode, masked so that only a thin triangular strip of the surface was exposed, was used (see Figure 5.4). As the

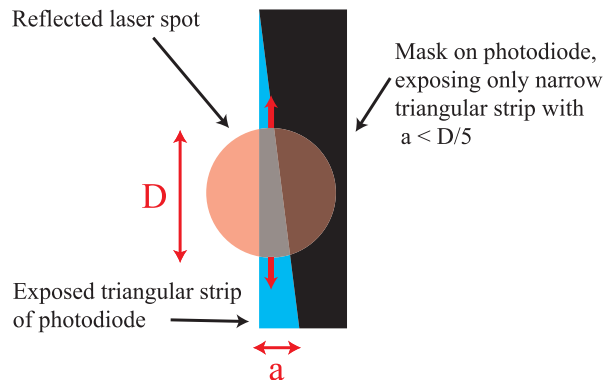


Figure 5.4: *Diagram of the photodiode sensor used to measure the displacement of the cantilever. The mask was made from electrical insulating tape, and the maximum width of the exposed photodiode (labelled a) was 1 mm. The laser spot diameter D was measured to be approximately 5 mm.*

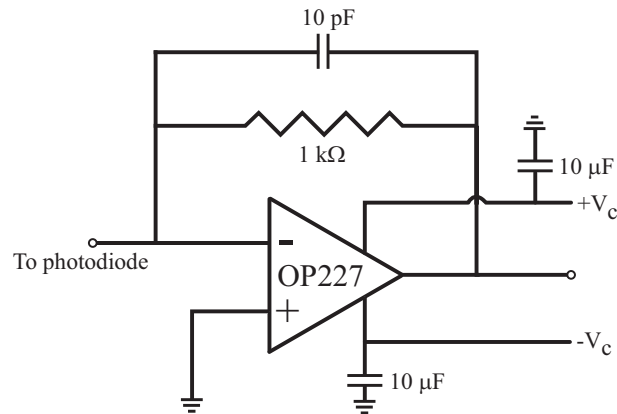


Figure 5.5: *Circuit diagram for the photodiode circuit used to measure the amplitude of the cantilever displacement.*

cantilever vibrated, the reflected laser spot moved up and down, illuminating a variable area of the photodiode and producing a photocurrent proportional to the amplitude of motion of the spot. To ensure linearity, the base of the triangle (labelled ‘a’ in Figure 5.4) was designed to be less than a fifth of the diameter of the laser spot. This readout system has the advantage of a significantly larger dynamic range than a split photodiode, allowing the large movement of the laser spot to be measured. The circuit used to amplify the signal from the photodiode is shown in Figure 5.5. The photodiode readout was constructed by S. Reid. A calibration plot and sensitivity curves for the sensor are shown in Figures 5.6 and 5.7 respectively.

The mechanical loss factors of several resonant modes of each cantilever were measured over a range of temperatures between 85 K and 292 K, with an electrostatic actuator being used to excite the modes as described in Chapter 4. Due to the long distance travelled by the reflected laser light between the cantilever and the sensor, it was often not possible to excite the fundamental mode of a cantilever to a suitable amplitude above the background noise without saturating the photodiode readout. The inclusion of a lens to reduce the range of motion of the reflected laser spot was found to reduce this prob-

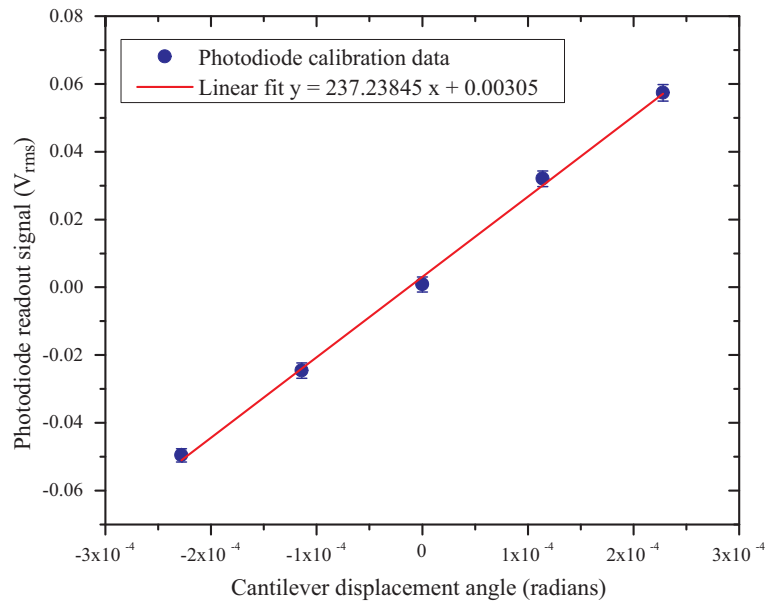


Figure 5.6: Plot of the response of the photodiode readout system used to measure the amplitude of the cantilever displacement.

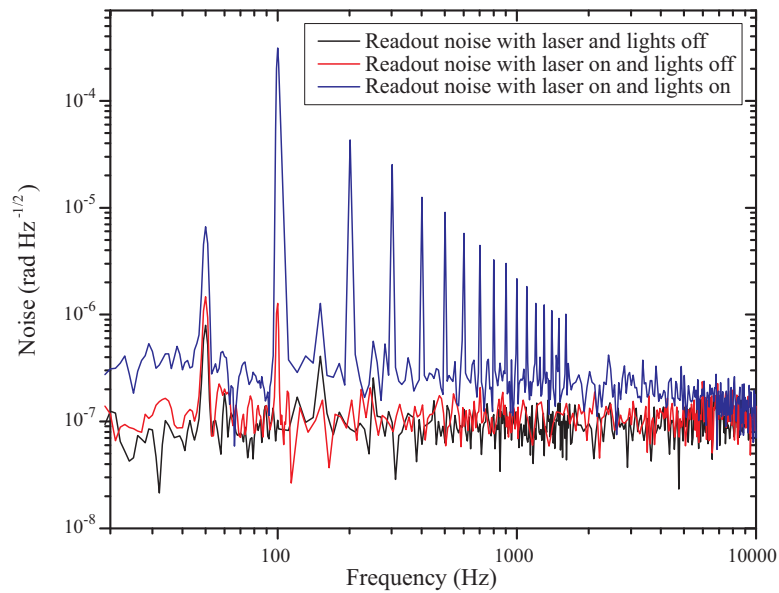


Figure 5.7: Noise plots for the photodiode sensor. The noise level was measured three times: with no incident laser spot and with the room lights turned off; with an incident laser spot and the room lights turned off and with an incident laser spot with the room lights switched on.

lem, but the ringdowns obtained were often noisy, possibly as a consequence of low frequency background noise in the system. Also, the diameter of the optical feed-through limited the maximum excitation amplitude which could be achieved before the reflected laser spot was truncated by the walls of the beam tube.

5.2.2.2 Thermoelastic loss as a function of temperature

Thermoelastic loss (see Section 2.4) is one of the dominant dissipation mechanisms in silicon cantilevers of these dimensions at room temperature. Figure 5.8 shows the thermoelastic loss at 290 K, calculated using Equation 2.40, for cantilevers A (92 μm thick) and B (52 μm thick). The peak thermoelastic loss occurs at ~ 16.4 kHz for the (thicker) cantilever A and at ~ 51.2 kHz for the (thinner) cantilever B. Over the frequency range at which measurements were

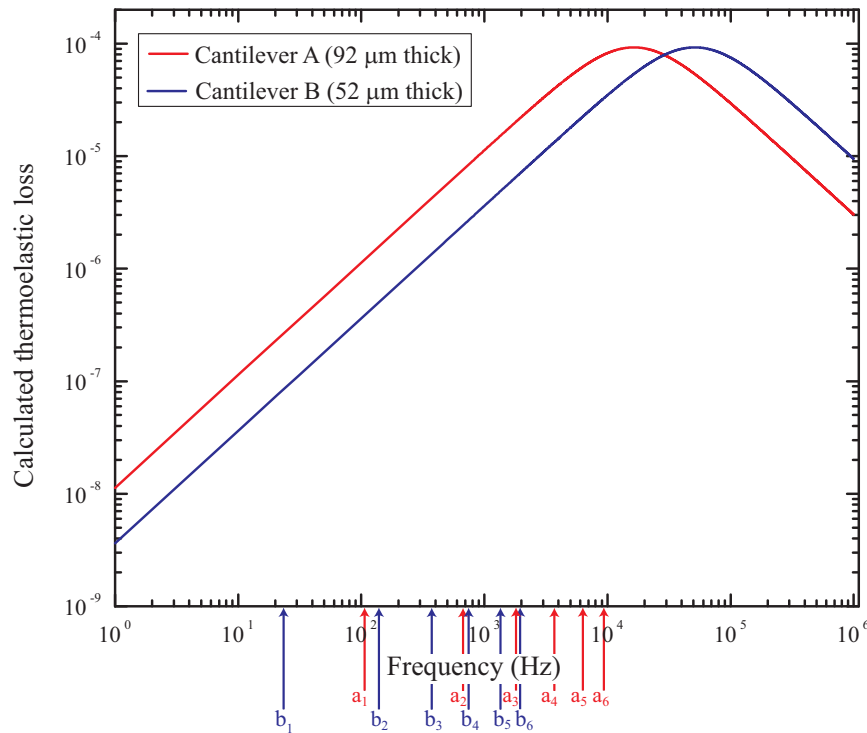


Figure 5.8: *The frequency dependence of the calculated thermoelastic loss for cantilevers A and B (92 μm and 52 μm thick respectively). The arrows mark the first 6 bending frequencies of the samples.*

taken (< 6 kHz), far from the peak, the level of thermoelastic loss in cantilever B is approximately a factor of three lower than that in cantilever A.

Thermoelastic loss in silicon is a strong function of the temperature, largely due to the temperature dependence of the thermal expansion co-efficient which has two zeros at approximately 125 K and 18 K, leading to nulls in the thermoelastic loss at these temperatures. This is illustrated in Figure 5.9, which shows the calculated temperature dependence of the thermoelastic loss for three modes of cantilever B, again using material properties from Touloukian [228]. Thermoelastic loss effects can also arise from the differing thermo-mechanical properties of the coating and substrate [141, 142]. The magnitude of this ‘coating thermoelastic loss’ is not significant for the Ta_2O_5 coatings studied here, but is discussed in detail for silica coatings in Chapter 6.

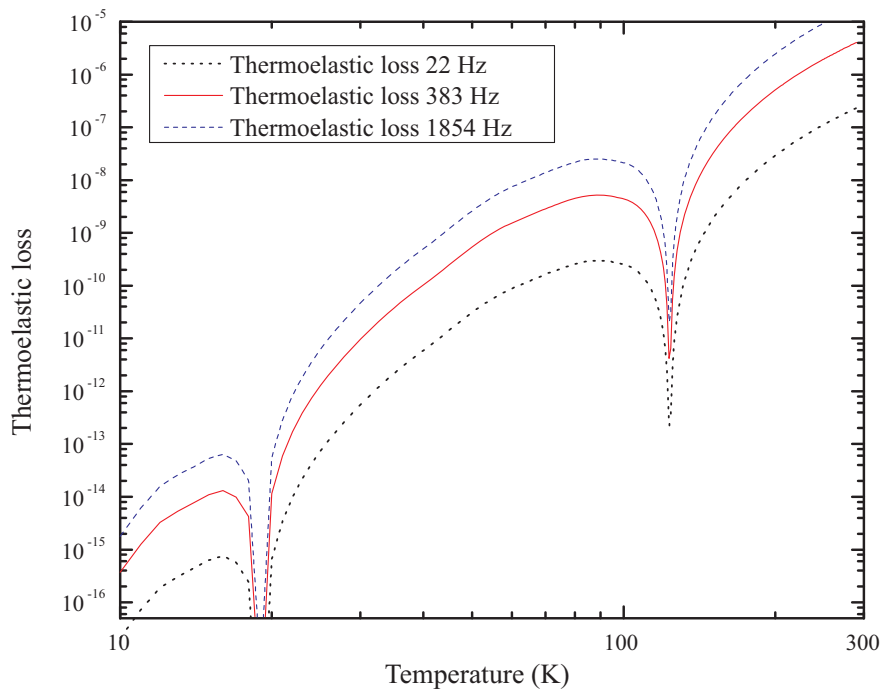


Figure 5.9: *Calculated thermoelastic loss as a function of temperature for three modes of silicon cantilever B.*

5.2.3 Results for cantilever A

5.2.3.1 Room temperature results

The mechanical loss factors of three modes (the second, third and fourth bending modes at 670 Hz, 1.9 kHz and 3.7 kHz respectively) of cantilever A had been studied as a function of temperature by a colleague [159, 227] before application of the coating. These measurements were used as the uncoated control data for cantilever A. Initially, the losses of the coated and uncoated cantilevers were compared at room temperature, as shown in Figure 5.10. It

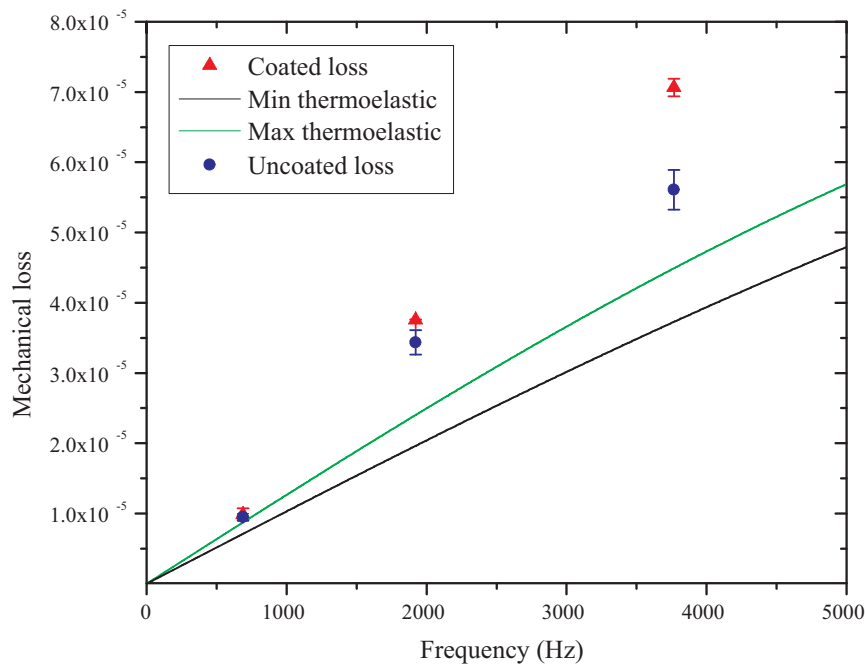


Figure 5.10: *Plot of room temperature loss measurements of cantilever A before and after coating with a 500 nm thick film of Ta₂O₅ doped with TiO₂.*

can be seen that the presence of the coating increases the loss of the cantilever, although at low frequencies the increase in loss of 8 % is relatively small and only slightly larger than the uncertainty in the measured losses. The previous data taken at low temperature for the second bending mode (670 Hz) showed significant evidence of clamping loss [159], therefore only the third and fourth bending modes of the coated cantilever were studied here.

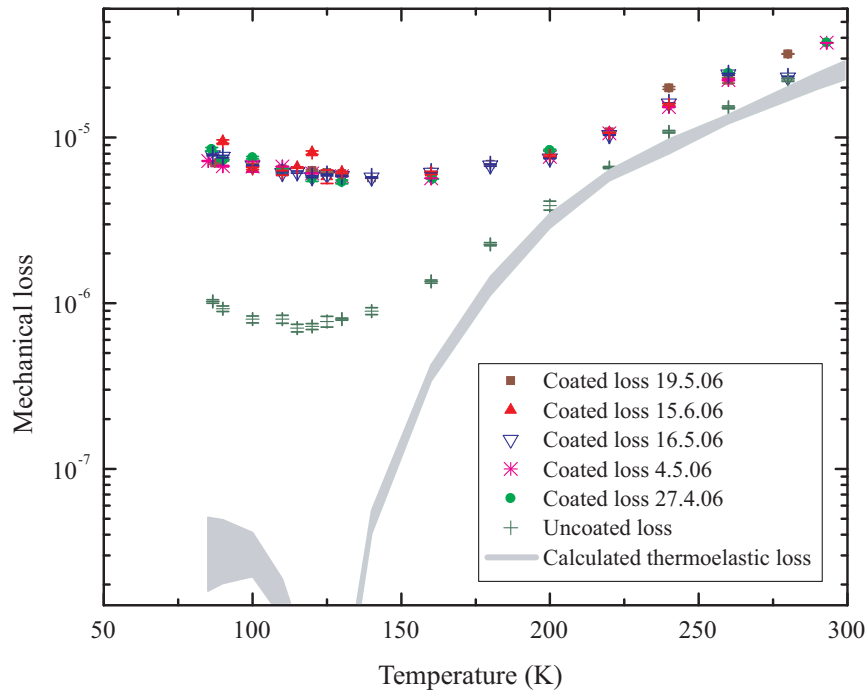


Figure 5.11: *Plot of the measured mechanical loss against temperature for the third bending mode of cantilever A before and after coating.*

5.2.3.2 Measured loss as a function of temperature

The mechanical loss factors of the third and fourth bending modes of the coated cantilever were measured as a function of temperature between 84 K and 290 K. As with all of the measurements in this chapter, the cantilever was allowed to cool to the lowest attainable temperature before measurements commenced, with the heater attached to the clamp then being used to heat the sample to a desired temperature. At each temperature at which data were taken the loss of each mode was measured at least three times and an average loss calculated. The uncertainties presented here in the average measured loss is the standard error.

Figures 5.11 and 5.12 show the temperature dependence of the measured loss factors of the third and fourth bending modes, at 1.9 kHz and 3.7 kHz respectively, both before and after coating. At temperatures above ~ 200 K the

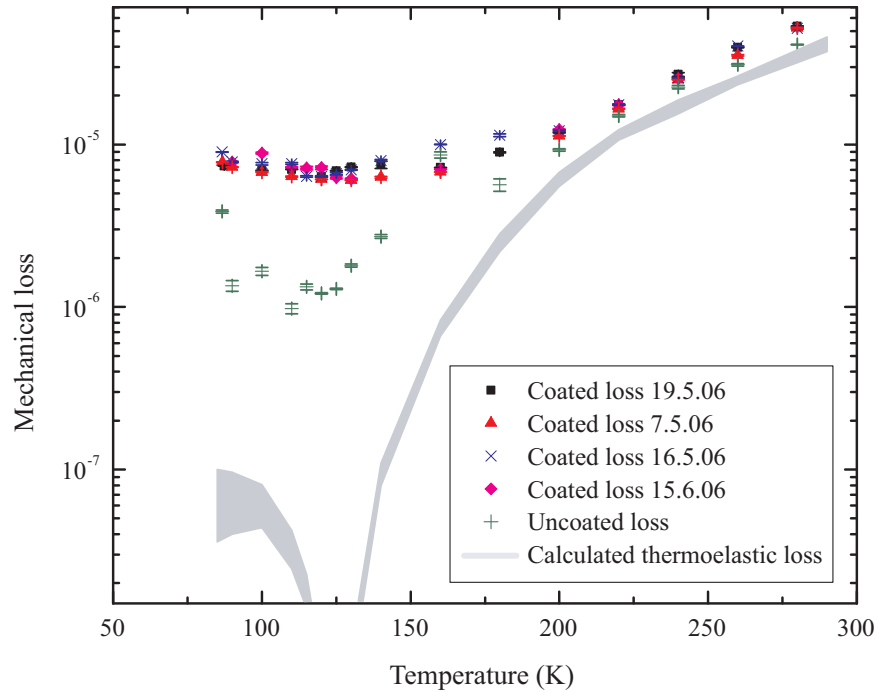


Figure 5.12: *Plot of the measured mechanical loss of the fourth bending mode of cantilever A, before and after coating.*

mechanical loss of the uncoated cantilever is dominated by thermoelastic loss, while at lower temperatures some other loss mechanism, perhaps associated with the surface of the silicon [163, 225] is dominant. The application of the coating to the sample significantly increased the mechanical loss factor by between a factor of 2 at room temperature and a factor of ~ 10 at 120 K. The losses measured for these modes of the coated sample over several temperature cycles are shown in Figure 5.12 where it can be seen that the losses in each run were reasonably consistent, with small variations probably attributable to slight variations in the levels of clamping loss.

5.2.4 Coating loss results for cantilever A

Using the data shown in Figures 5.11 and 5.12, the mechanical loss of the coating was calculated for both the third and fourth modes using Equation 4.14.

The Young's modulus of tantala was taken to be (140 ± 15) GPa [229]. The ratio of the energy stored in the coating to the energy stored in the cantilever substrate was calculated to be $E_{\text{coating}}/E_{\text{substrate}} = 1.39 \times 10^{-2}$ using Equation 4.7.

The calculated coating loss for the third and fourth modes is shown in Figures 5.13 and 5.14 respectively. The coating loss appears to decrease as the temperature decreases from room temperature to 200 K. At lower temperatures however, the coating loss shows a steady increase with decreasing temperature. The large losses at room temperature, in the order of 9×10^{-4} , are larger by a factor of ~ 3 than the losses measured for a tantala coating (with the same level of doping) applied to a silica cantilever presented in Chapter 4. The measurements close to room temperature were less repeatable than those at lower temperatures, and showed a larger degree of scatter with no obvious trend. These facts suggest that some form of excess loss associated with the

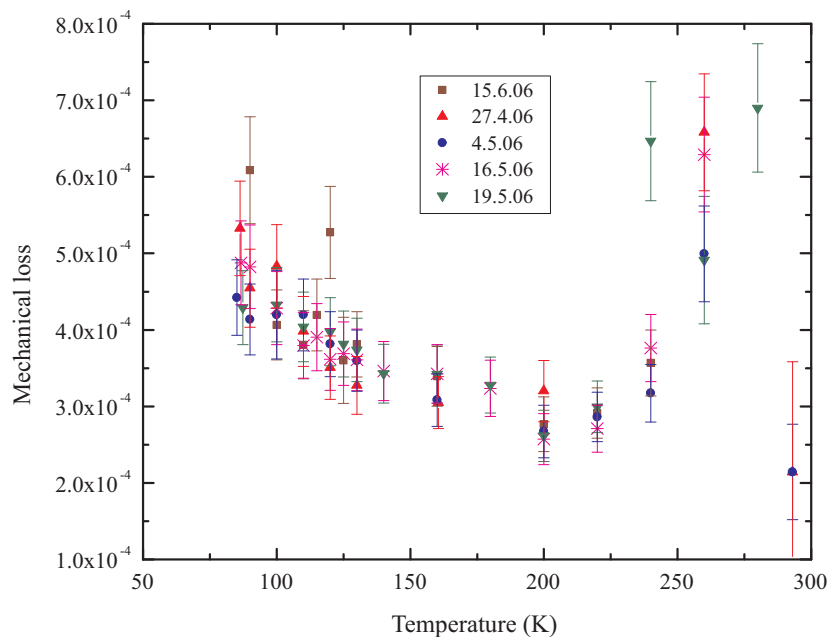


Figure 5.13: *Plot of the calculated coating loss as a function of temperature for 3rd mode of cantilever A.*

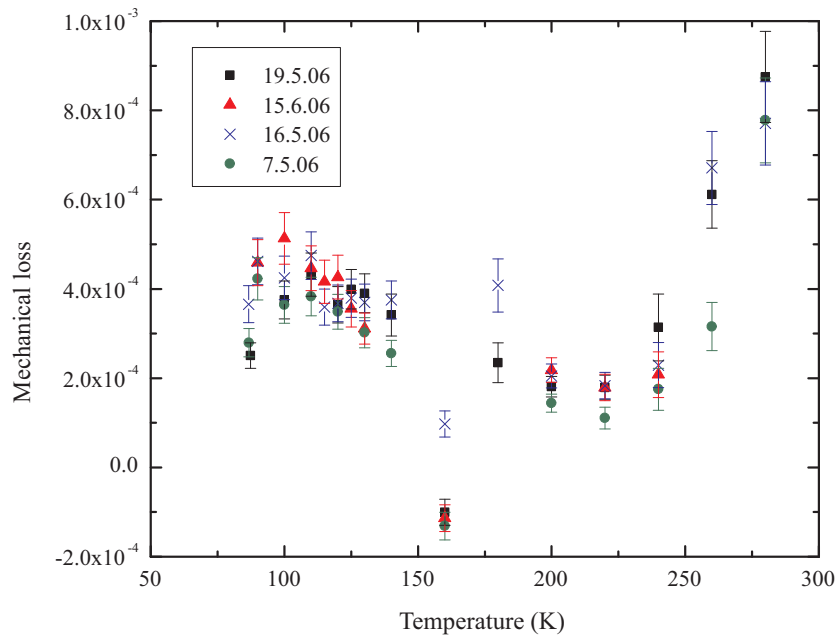


Figure 5.14: *Plot of the calculated coating loss as a function of temperature for 4th mode of cantilever A.*

clamp might have been present at these temperatures, possibly due to energy from the cantilever coupling into a nearby resonance of the clamp.

To test this hypothesis, a piezo-electric sensor was used to measure the magnitude of any motion of the clamp. The piezo was attached to the top clamping block and the signal at the cantilever mode frequency was recorded at the start of each ring-down measurement. To account for variations in excitation amplitude, the piezo signal was normalised by dividing it by the measured amplitude of the excited motion of the cantilever immediately after excitation.

At temperatures above 200 K, where the large and more variable losses were measured, significantly higher levels of clamp motion were detected. Figure 5.15 shows both the measured loss of the 1.9 kHz mode over the course of one temperature run and the amplitude of the clamp motion at the same frequency. It can be seen that the clamp motion remained relatively constant

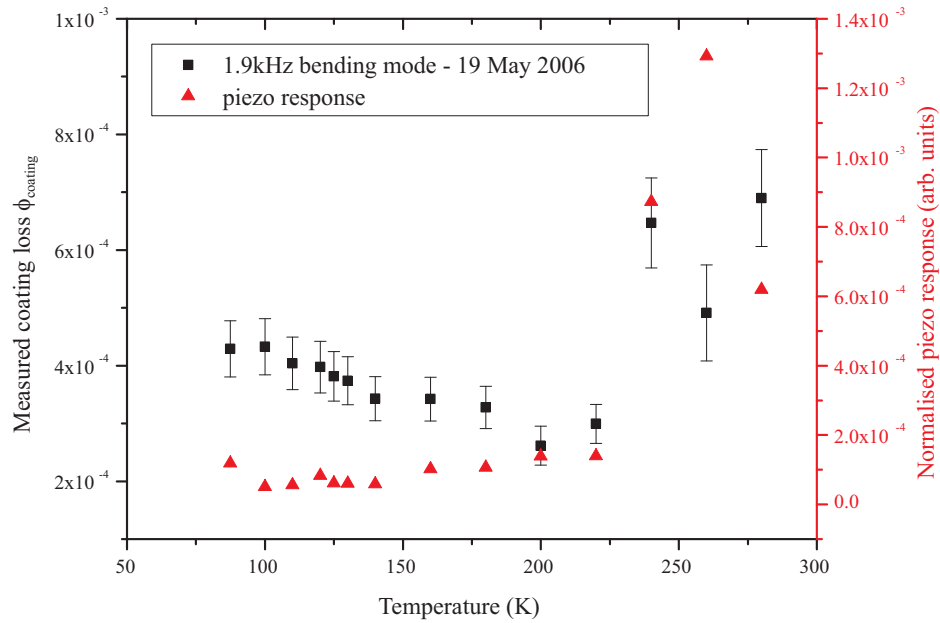


Figure 5.15: Plot of the measured coating loss at approximately 1.9 kHz and the amplitude of the piezo signal detected at the start of each ringdown.

below ≈ 225 K, and that the mechanical loss follows quite a smooth trend in this temperature range. At higher temperatures, both the motion in the clamp and the measured loss factor increase substantially.

These results suggest that a resonance of the clamping structure may be close in frequency to this mode of the cantilever, and at temperatures above 225 K, the two resonant frequencies become close enough to allow the motion of the cantilever to excite the mode of the clamp, resulting in excess loss of energy from the cantilever. Similar data were obtained for the fourth bending mode, indicating that it was also affected by energy loss into the clamping structure at temperatures above ~ 225 K. Thus it is likely that the calculated coating loss above 225 K for both modes is higher than the intrinsic loss of the coating material.

5.2.5 Coating loss results for cantilever B

Cantilever B was coated in the same coating run as cantilever A. However this cantilever had a separate, identical control sample (cantilever C) which underwent the same oxidation and annealing processes as the coated cantilever. The properties of these cantilevers are given in Table 5.1. The factor of ≈ 6.7 between the thickness of the cantilever and the clamping block (compared to a factor of ≈ 5.4 for cantilever A) should enable greater isolation of the cantilever from the clamp. The energy ratio for cantilever B was calculated to be $E_{\text{coating}}/E_{\text{substrate}} = 2.46 \times 10^{-2}$. The mechanical loss factors of the the fourth and fifth modes, at ~ 777 Hz and ~ 1280 Hz respectively, of cantilevers B and C were measured as a function of temperature; the results are shown in Figures 5.16 and 5.17. For both modes the loss of the uncoated sample follows the trend of the expected thermoelastic loss above 200 K. The loss of the 777

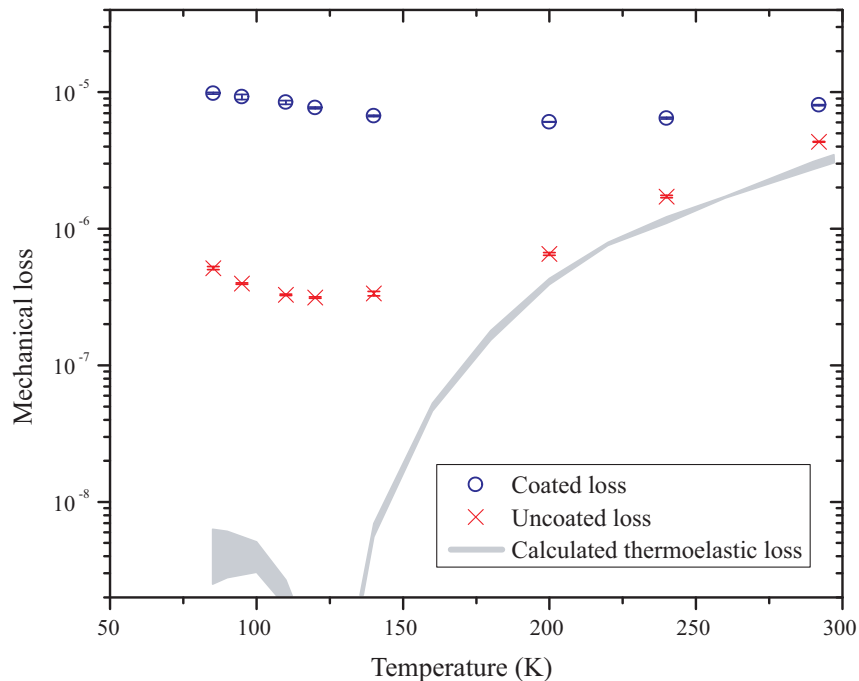


Figure 5.16: Plot of the measured loss for the fourth mode of cantilever B and its identical uncoated control sample.

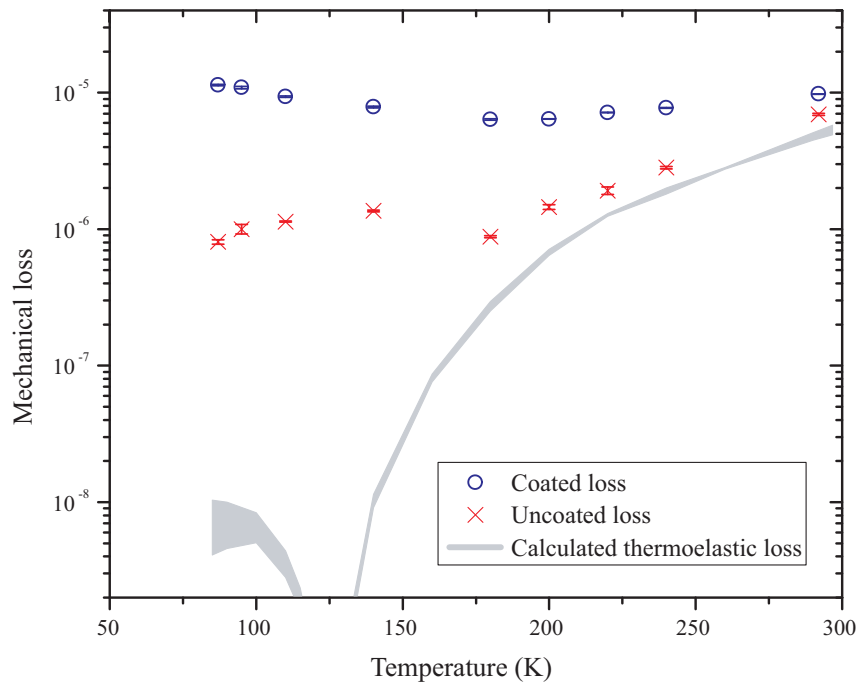


Figure 5.17: *Plot of the measured loss for the fifth mode of cantilever B and its identical uncoated control sample.*

Hz mode continues to decrease to a minimum of 3.1×10^{-7} at 120 K, where the loss begins to increase quite steeply. The loss of the mode at 1280 Hz appears to have a small, broad peak at approximately 120 to 140 K. The piezo sensor on the upper clamping block did not show any indication of excess loss into the clamping structure. It is possible, therefore, that this small peak may be intrinsic to the silicon. Other authors have observed peaks in the loss of silicon in this temperature range [224], and this would be of interest for further study.

The loss of the coated cantilever for both the 777 Hz and 1280 Hz modes was found to decrease smoothly with temperature to a minimum at approximately 160 K where the loss begins to increase with decreasing temperature.

Figure 5.18 shows the calculated coating loss for both of the modes. The coating loss was found to increase as the temperature decreases, rising from a level of approximately 1.5×10^{-4} at 290 K to 3.8×10^{-4} at 85 K. There is evidence of a plateau in the loss between 175 and 225 K, although more

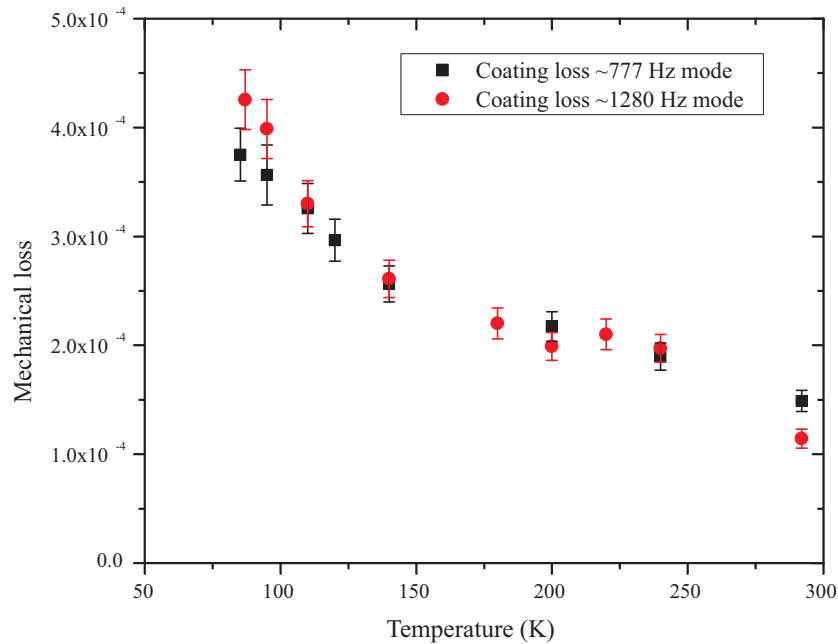


Figure 5.18: *Plot of the coating loss for cantilever B at 777 Hz and 1280 Hz.*

measurements would be required to examine this feature more thoroughly. Below 175 K, the slope of the loss curve increases. The coating loss results for both modes studied agree to within experimental error at every point except at room temperature. However, below 150 K, the loss of the 1280 Hz mode appears to increase more rapidly than that of the 777 Hz mode, suggesting that the coating loss may have some frequency dependence.

The loss measurements for cantilever B were repeatable to within 5 % over several measurement runs and did not show evidence of energy coupling to the clamp, unlike the results for cantilever A. This is possibly due to cantilever B being better isolated from the clamp due to the larger clamping block to cantilever thickness ratio. It is also possible that the mode frequencies of cantilever B were further away from the resonances of the clamp, making coupling between the sample and the support structure less likely. For ease of comparison, the lowest coating losses found at each temperature for cantilever A are shown in Figure 5.19. Generally, the losses measured for cantilever A were

slightly higher than those measured in cantilever B. Several anomalously low losses measured in cantilever A (e.g. at 87 and 160 K) can be attributed to excess clamp loss in the data measured prior to application of the coating (see Figure 5.12).

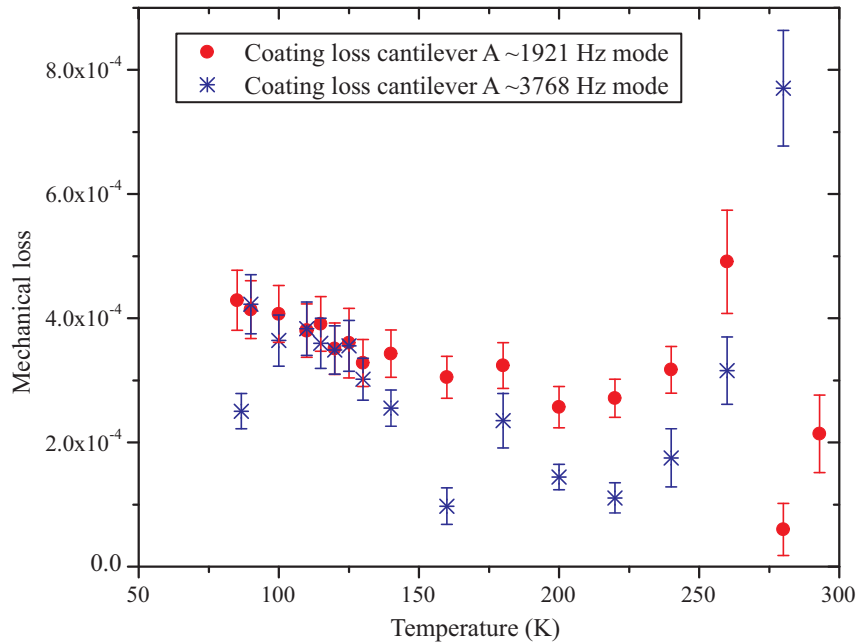


Figure 5.19: Plot of the coating loss for cantilever A at 1920 Hz and 3768 Hz, calculated using the lowest loss factors measured for the coated cantilever at each temperature.

5.2.6 Conclusion

These initial loss measurements demonstrated that it was possible to use the technique described here to measure the temperature dependence of the mechanical loss of a coating. The loss of the ion-beam sputtered Ta₂O₅ film doped with 14.5 % TiO₂ was observed to increase significantly as its temperature was reduced from room temperature to 84 K. Since the loss of the Ta₂O₅ layers is known to be the main source of loss in SiO₂/Ta₂O₅ multi-layer coatings at room temperature, this result is potentially of significance for the operation of

gravitational wave interferometers at cryogenic temperatures.

If the coating loss continues to increase below 84 K, then it is possible that the coating thermal noise may actually be increased by operating a gravitational wave detector at these temperatures. It was therefore clearly of interest to continue these measurements at lower temperatures. In addition, the results of similar studies of a silica coating are presented in Chapter 6, enabling a calculation of the expected loss in a multi-layer SiO₂/Ta₂O₅ coating from the measured loss of the individual coating materials.

Initial measurements of the loss of single-layer coatings at temperatures approaching liquid helium temperature were carried out during a visit to collaborators at Jena University, and are detailed in Section 5.3. Concurrent modifications (described in Section 5.6.1) were made to the cryostat experiment in Glasgow to allow cooling with liquid helium, after which several undoped Ta₂O₅ coatings were studied as described in Sections 5.6 and 5.7.

5.3 Dissipation of a TiO₂-doped Ta₂O₅ coating between 7 K and 300 K

5.3.1 Sample preparation

The mechanical loss of a tantalum coating of identical doping to that described in the previous section was measured between 7 and 300 K during a visit to Jena University. The previous pair of samples could not be used because cantilever C (the uncoated control sample) was found to have cracked in the clamp during the final measurement run. While only the clamping block was damaged, it was no longer possible to clamp the cantilever properly or repeatably, and no other control sample for cantilever B was available.

Therefore a new pair of cantilevers, of approximately the same thickness and with the same clamping block dimensions as cantilever B, were used. These cantilevers were fabricated from n-type, antimony-doped single-crystal silicon

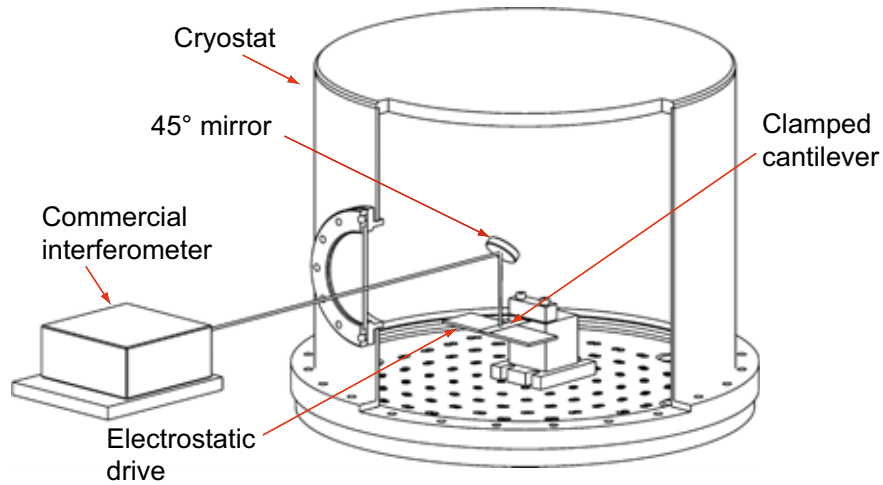


Figure 5.20: *Schematic diagram of the cryostat used to measure the doped tantala coating at Jena University, showing the laser interferometer readout system used.*

of resistivity 0.005-0.25 Ωcm and were (34 ± 0.5) mm long. The thickness, again calculated from the measured mode frequencies of the uncoated cantilever using Equation 4.3, was found to be (47.7 ± 0.5) μm .

Subsequent to the previous coating run, LMA had developed the Ta₂O₅ coating process by changing a commercially sensitive (and therefore undisclosed) deposition parameter. The new variant of coating, which LMA have found to have a lower mechanical loss at room temperature [220], is known as Formula 5**. The TiO₂ doping level remained unchanged at a cation concentration of 14.5 %. A loss factor of $(1.5 \pm 0.1) \times 10^{-4}$ was measured for Formula 5** tantala applied to a silica cantilever, as presented in Chapter 4.

As before, two identical cantilevers were sent to LMA. A thermal oxide layer approximately 20-30 nm thick was grown on both samples, before one was coated with 500 nm of Formula 5** Ta₂O₅ by ion-beam sputtering. Both the coated cantilever and the control sample were then heat treated at 600°C for twenty-four hours.

5.3.2 Experimental method

The cryostat used in Jena University is shown in Figure 5.20. In place of the laser and photodiode sensor described in Section 5.2.2.1, a commercial laser interferometer (SIOS model SPS-120/500) was used to measure the displacement of the cantilever, with the laser beam reflected from one surface of the sample. Due to the design of the cryostat, with a short optical path between the cantilever and the interferometer, it was possible to measure the fundamental mode of the cantilevers.

5.4 Results

The measured mechanical loss factors for the first five bending modes of both the sample coated with doped tantala and the uncoated control sample are shown in Figures 5.21 to 5.25. Each point represents the average loss calculated from at least three ring-down measurements and typically has an experimental error of less than 3 %. Error bars have been omitted for clarity.

The most striking feature of this plot is a clearly defined peak in the dissipation of the coated sample centred at approximately 20 K. This peak is present for all of the modes studied, suggesting that it is unlikely to be related to any frequency dependent energy loss into the clamp. This was confirmed through the use of a piezo-electric sensor attached to the clamp, as described in 5.2.4, which showed no evidence of energy coupling into the clamping structure associated with the dissipation peak.

The first two modes both show some evidence of a second, smaller peak in the dissipation at approximately 90 K (see Figures 5.21 and 5.22). However, there is no evidence of this feature in the data for the third and fourth modes, which show the loss increasing smoothly with decreasing temperature.

The measured dissipation of the fifth mode appears to be anomalously high and to have apparent structure above 100 K. Unfortunately few measurements

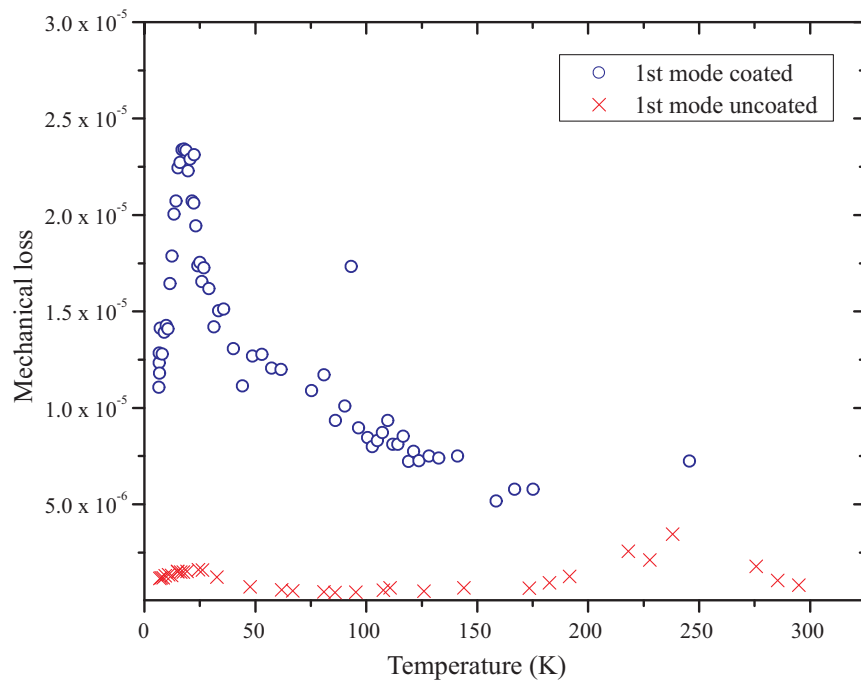


Figure 5.21: Plot showing the temperature dependence of the measured mechanical loss of the first mode (~ 55 Hz) of the coated and uncoated cantilevers.

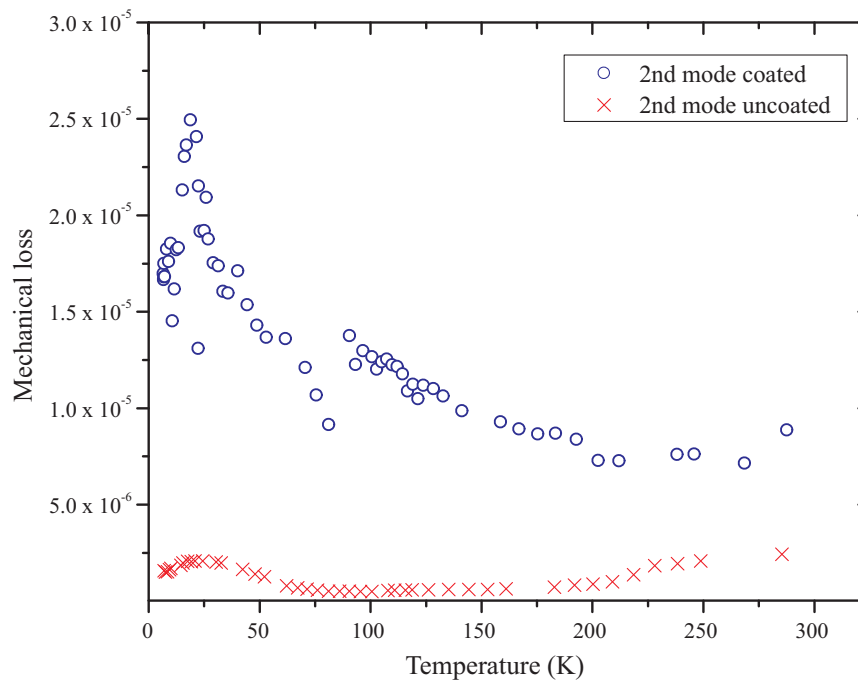


Figure 5.22: Temperature dependence of the measured mechanical loss of the second mode (~ 350 Hz) of the coated and uncoated cantilevers.

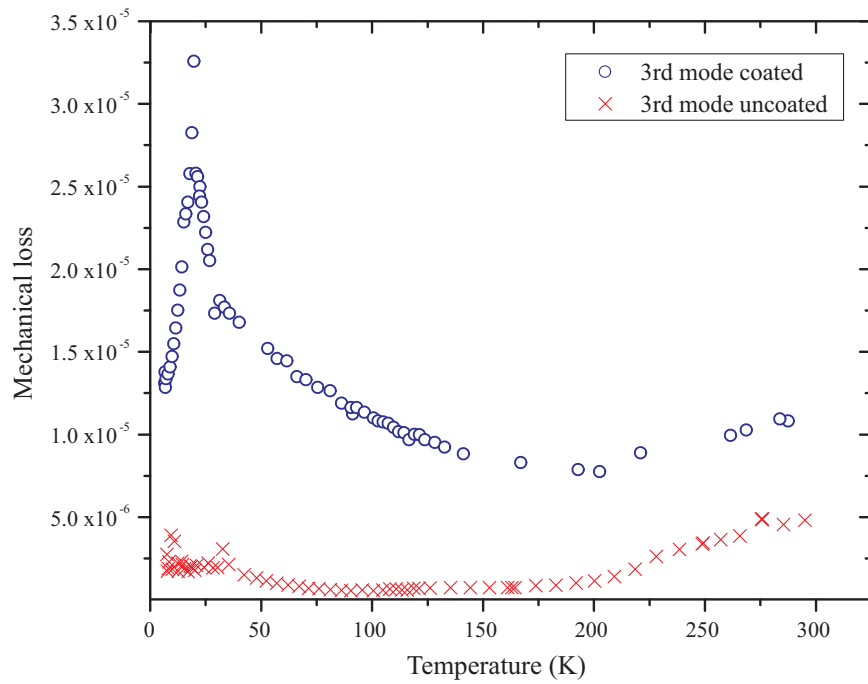


Figure 5.23: *Temperature dependence of the measured mechanical loss of the third mode (~ 989 Hz) of the coated and uncoated cantilevers.*

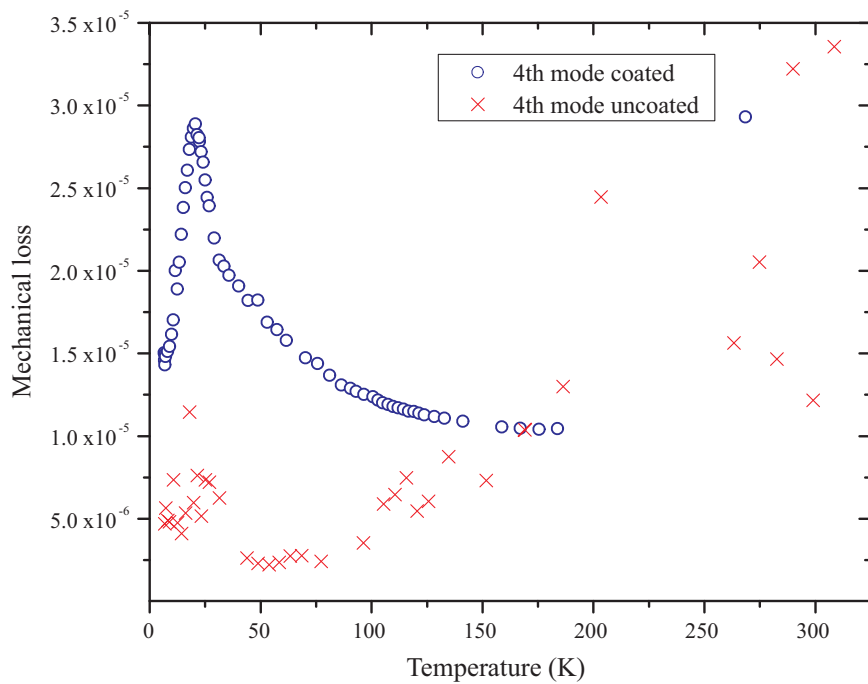


Figure 5.24: *Temperature dependence of the measured mechanical loss of the fourth mode (~ 1939 Hz) of the coated and uncoated cantilevers.*

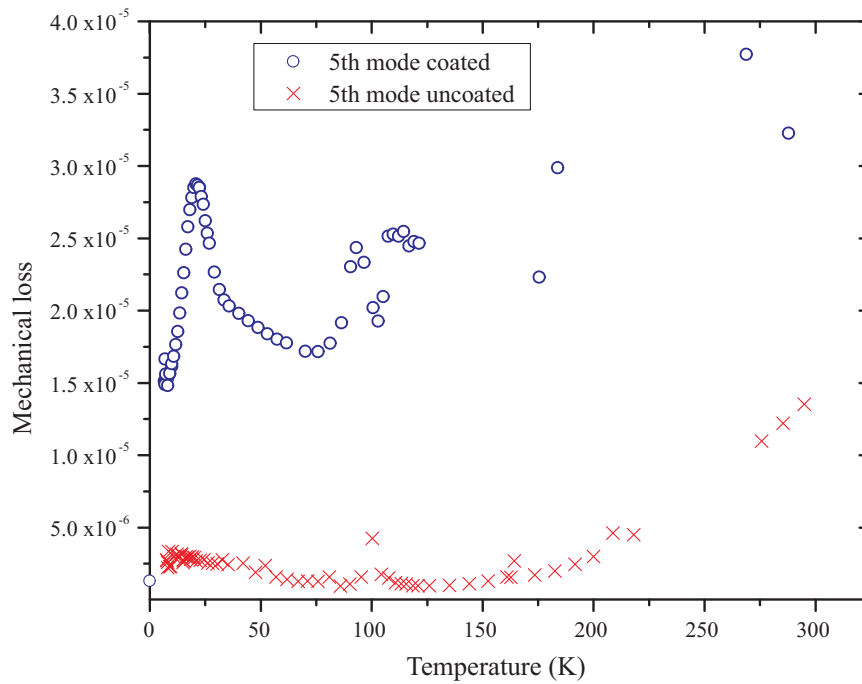


Figure 5.25: *Temperature dependence of the measured mechanical loss of the fifth mode (~ 3184 Hz) of the coated and uncoated cantilevers.*

of the clamp motion using the piezo sensor were obtained for this mode below 150 K, although excess motion of the clamp at this frequency was detected at higher temperatures. It is therefore likely that the anomalously high dissipation measured close to room temperature was due to energy coupling into the clamp. However, the possibility that the high loss measured at 90 K - 100 K may be intrinsic to the sample cannot be ruled out.

Each graph also shows the measured loss of the uncoated cantilever. For each mode, the loss of the uncoated sample decreases to a plateau between approximately 175 K and 110 K, below which the loss rises to a relatively small broad peak at ~ 25 K. Above 200 K, the loss of the second, third and fifth modes of the uncoated sample follow the trend of the thermoelastic loss. The loss of the first and fourth modes, however, do not follow the expected thermoelastic trend, with the loss of the fourth mode in particular being significantly higher and more scattered than would be expected. Indeed, the

measured losses were actually larger than those measured for the same mode of the coated sample. The piezo sensor clearly showed evidence of excess clamp motion during ring-down measurements of this mode of the uncoated cantilever at temperatures above 200 K, suggesting that the high losses measured were explained by energy loss into the clamp.

It should be noted again that the peak in the dissipation of the coated sample at 20 K is well defined for all of the modes measured, and that no evidence of energy coupling to the clamping structure was observed around this peak.

5.4.1 Calculation of the coating loss

The mechanical loss of the doped tantala layer was calculated for each of the first five modes of the cantilever using Equation 4.14. Due to its low mechanical loss the ring-downs of the uncoated cantilever took a considerable time, resulting in data being taken at fewer temperatures than for the coated cantilever. At temperatures where the uncoated loss had not been measured, interpolated values were used.

As shown in Figure 5.26, the coating loss was generally found to steadily increase with decreasing temperature, from approximately 2×10^{-4} at 292 K to a peak of approximately 1×10^{-3} , at ~ 20 K. The two exceptions to the general trend occur for the fourth and fifth modes at temperatures above 75 K. At these temperatures the calculated coating loss has been affected by the clamping loss effects observed for the fourth and fifth modes, as discussed in Section 5.4. The level of loss measured above 77 K is broadly consistent with that measured in the other, similar coatings presented in Section 5.2.

5.5 Analysis and Interpretation

A dissipation peak at a particular temperature usually arises from a specific loss mechanism within the material. If it is assumed that the dissipation has

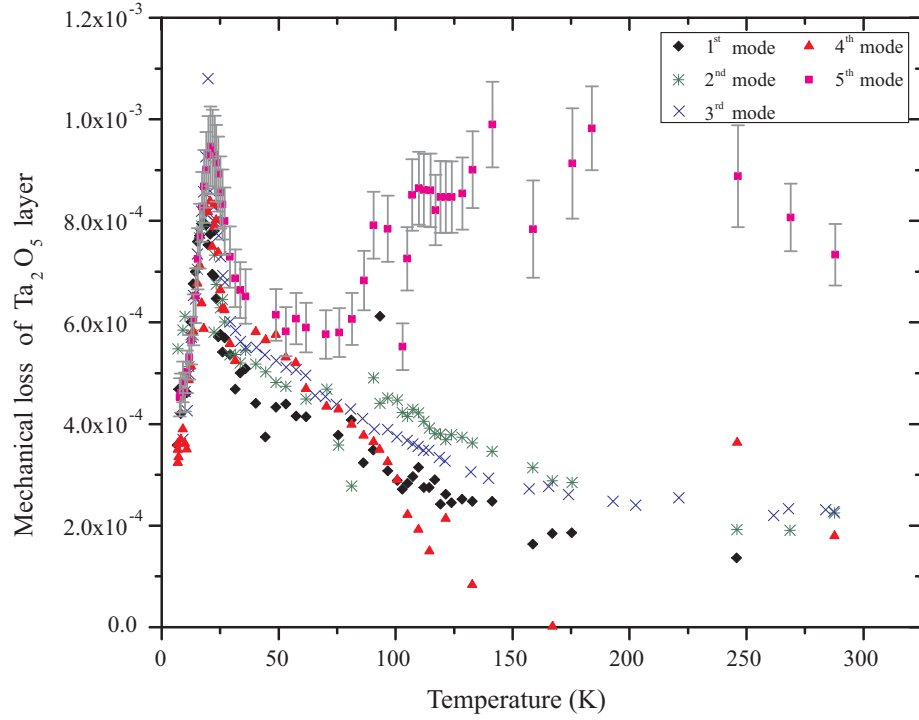


Figure 5.26: *Temperature dependence of the dissipation of the doped Ta_2O_5 coating.*

the form of a Debye peak, as is the case for most dissipation mechanisms [110], then the loss can be expressed as:

$$\phi(\omega) = \Delta \frac{\omega\tau}{1 + (\omega\tau)^2} \quad (5.1)$$

where Δ is a constant related to the magnitude of the dissipation[110]. For clarity, the loss of each of the modes at temperatures around the peak is shown in more detail in Figure 5.27. The temperature at the point of maximum dissipation can be seen to increase with the mode frequency. This is characteristic of dissipation arising from a thermally activated relaxation process, in which the relaxation time τ is related to the activation energy E_a of the process by the Arrhenius equation:

$$\tau^{-1} = \tau_0^{-1} e^{-E_a/k_B T}, \quad (5.2)$$

where τ_0 is the relaxation constant of the dissipation mechanism and k_B is Boltzmann's constant [93]. From Equation 5.1 it is clear that at the dissipation

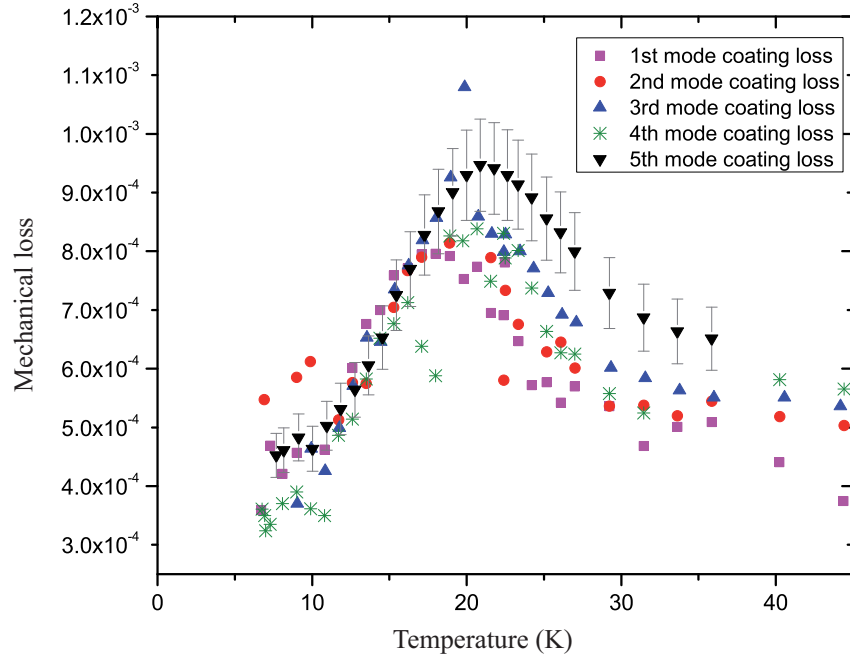


Figure 5.27: *The mechanical loss peak measured in the doped Ta_2O_5 coating. For clarity, error bars are only shown for the fifth mode: these are typical of the errors in all of the points.*

peak, $\omega\tau = 1$ and thus Equation 5.2 can be written as:

$$\omega = \tau_0^{-1} e^{-E_a/k_B T_{peak}}, \quad (5.3)$$

and thus :

$$\ln \omega = \ln \tau_0^{-1} - \frac{E_a}{k_B T_{peak}}. \quad (5.4)$$

Therefore a plot of the natural logarithm of the angular frequency of each mode against the reciprocal of the peak temperature (known as an Arrhenius plot) should be a straight line of slope E_a/k_B .

To determine the temperature of each peak accurately, a fourth order polynomial function was fitted to each data set in the immediate vicinity of the peak (approximately between 12 and 25 K), and the position of the peak was found by calculating the roots of the derivative of the fit function. The fits used are shown in Figure 5.28. The temperature at which the dissipation peaks can be seen to increase with increasing frequency. With the exception of the third

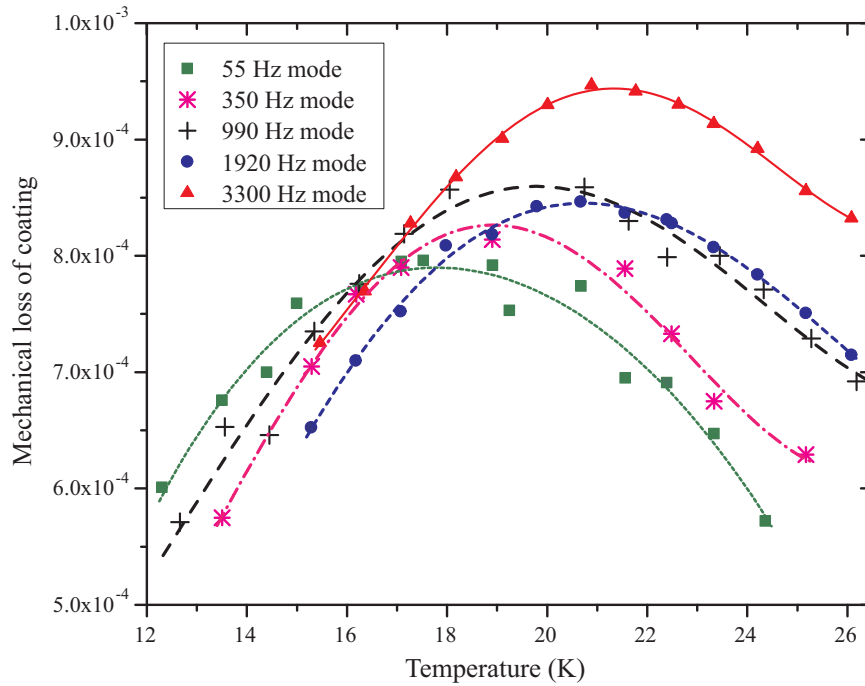


Figure 5.28: *The fits used to determine the position of the mechanical loss peak in the doped Ta_2O_5 coating. Note the temperature at which the peak occurs increases with increasing mode frequency.*

Mode	Frequency	T_{peak}	ϕ_{peak}
1	55 Hz	17.81K	7.9×10^{-4}
2	355 Hz	18.91 K	8.3×10^{-4}
3	989 Hz	19.78 K	8.6×10^{-4}
4	1920 Hz	20.72 K	8.5×10^{-4}
5	3175 Hz	21.33 K	9.4×10^{-4}

Table 5.2: *The temperature at which the dissipation peak occurs and the peak magnitude of the dissipation for each mode of the cantilever coated with doped Ta_2O_5 measured in Jena.*

mode at ~ 990 Hz, the magnitude of the loss peak can also be seen to increase at higher frequencies. The third mode displayed the highest peak loss of all (although in the fitted curve this is not apparent), possibly due to the effect of clamping loss at this frequency. Table 5.2 shows both the temperature and

magnitude of the dissipation peak obtained from the fit for each mode. The Arrhenius plot of this data, which is shown in Figure 5.29, yields a straight line with a fitted gradient of 430.6 and intercept of $\ln(\omega) = 30.3$. Comparison with Equation 5.4 allows an activation energy of (39.5 ± 2.7) meV and a relaxation constant of $(1.7 \pm 0.1) \times 10^{-14}$ s to be calculated.

Following the analysis of Cannelli et al [230], the values of E_a and τ_0^{-1} can be substituted into Equations 5.2 and 5.1, which can be used to calculate the theoretical shape of the mechanical loss peak, as shown in Figure 5.30. The theoretical peak is substantially narrower than the observed experimental peak. This is characteristic of strongly interacting or disordered systems in which there is a range of values of E_a [230]. As the Ta_2O_5 coating is amorphous (see Figure 5.31), it is possible that a distribution of values of E_a could arise from the disordered structure of the material. The calculated activation energy of 39.5 ± 2.7 meV would therefore correspond to the average activation energy

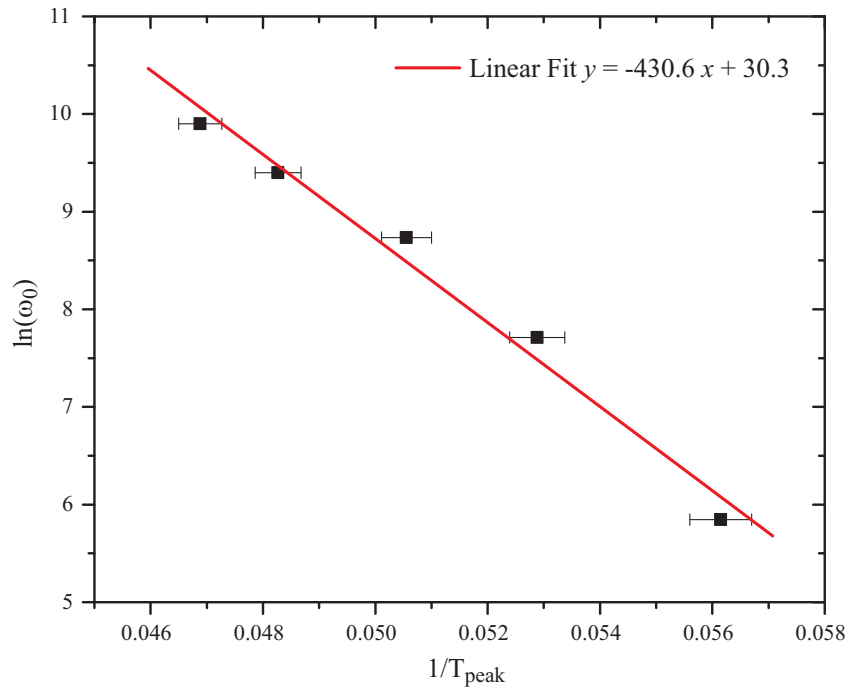


Figure 5.29: Arrhenius plot, showing a linear fit of $\ln(\omega_0)$ against $1/T_{\text{peak}}$ for the dissipation peak.

in this distribution.

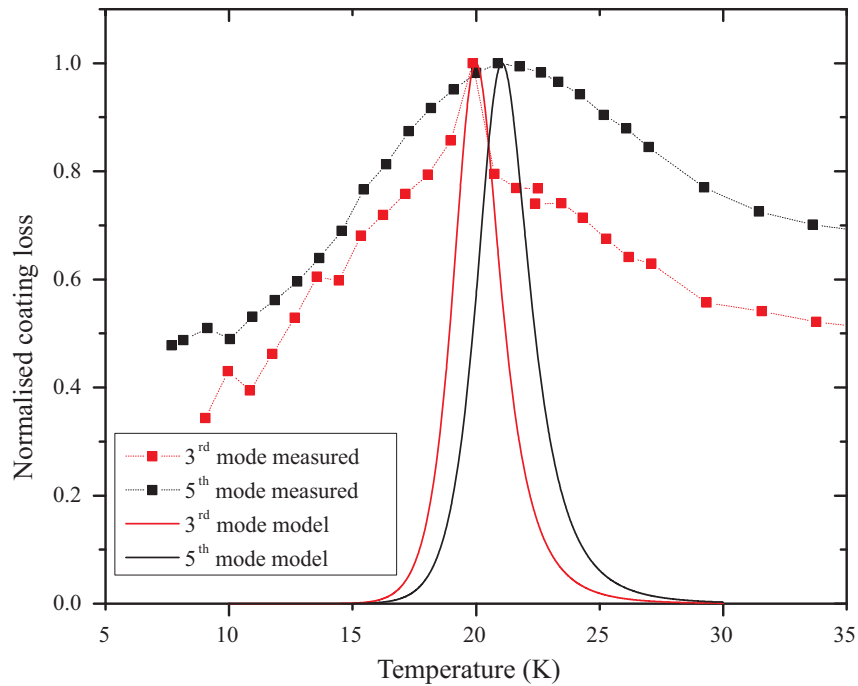


Figure 5.30: Comparison of the measured dissipation peak to the theoretical peak obtained from the Arrhenius fit.

5.5.1 Possible interpretation

It is interesting to note that the activation energy of the well-known low temperature dissipation peak in fused silica, also an amorphous oxide material, has been measured to be 44 meV using a method similar to the one described above [172]. However, the dissipation peak in silica is significantly wider than the simple Debye peak predicted to arise from a single activation energy of 44 meV (see Equation 5.1), implying that there is a distribution of activation energies. The activation energy of 44 meV extracted from the Arrhenius-type analysis therefore actually corresponds to the most probable activation energy in this distribution.

Fine et al first suggested that the spectrum of activation energies, and thus the width of the dissipation peak, might arise from the disorder in the structure

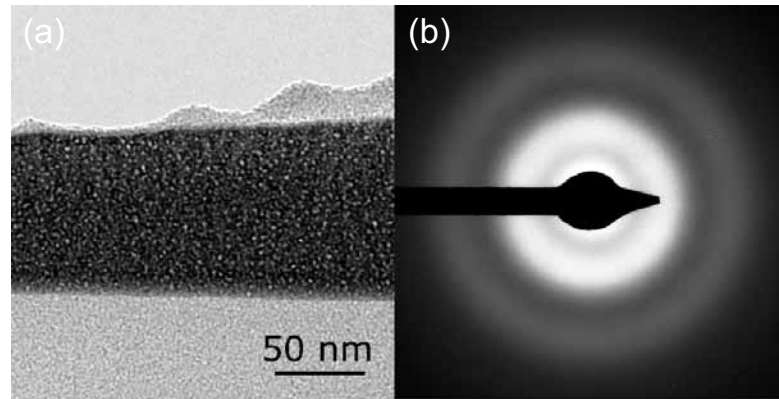


Figure 5.31: (a) *Bright field TEM image of a tantalum layer (dark) and a silica layer (light) in a $\text{SiO}_2 / \text{Ta}_2\text{O}_5$ multi-layer coating, where the Ta_2O_5 layers are doped with 8% TiO_2* (b) *convergent beam electron diffraction from a Ta_2O_5 layer showing just diffuse rings of intensity, confirming that this layer is amorphous. Both images were taken by Ian MacLaren of the solid state physics group at Glasgow University.*

of fused silica [231]. Over the following two decades, various models for the specific dissipation mechanism were proposed. Anderson and Bommel [172] suggested that the dissipation arose from certain oxygen atoms (the ‘bridge’ oxygen atoms, linking together ring-like formations in the silica) moving between two possible bond angles. The width of the dissipation peak is attributed to the distribution of Si-O bond angles in the disordered silica network.

Strakna proposed a similar model in which certain Si-O-Si bonds are naturally elongated [222]. If the two end atoms in a linear chain of three atoms are sufficiently far apart, the middle atom will have two possible equilibrium positions separated by an energy barrier [169]. The loss arises from vibrations of the oxygen atom between these two potential minima positions in the elongated bond. The width of peak is again related to the wide distribution of bond angles and bond lengths in the disordered silica structure.

Vukcevic [232] proposed a third model, in which the low temperature dissipation occurs when neighbouring SiO_4 tetrahedral structures rotate between

two stable states. The activation energy of this process depends on the microscopic environment of individual tetrahedra, again resulting in a spectrum of activation energies and a correspondingly wide dissipation peak.

In all of the above models, changes in Si-O-Si bond angles are postulated to be responsible for the low temperature dissipation peak in silica. The three models differ only in describing which type of motion occurs and the nature of the associated potential barrier which must be overcome. In each model, the atom, or group of atoms, involved in the dissipation process sits in a double-well potential: that is, there are two possible positions which can be occupied with almost equal probability. Energy dissipation can occur if an atom gains enough energy (the activation energy) to surmount the potential barrier which separates the two equilibrium positions.

The theory of dissipation in silica was further developed when Gilroy and Phillips [233] pointed out that for a dissipation peak to occur, the double-well potential had to be asymmetric. Although most previous analysis had assumed the potential well was symmetric, the asymmetric double-well potential (ADWP) was thought to be a more realistic physical model, and had already been used to explain various types of anomalous low temperature behaviour in amorphous solids, including silica [234, 235]. The ADWP model has since been corroborated by low frequency light scattering measurements [173].

The average activation energy of 39.5 ± 2.7 meV obtained here for the dissipation mechanism in doped tantala is of a similar order to the activation energy of the dissipation mechanism in fused silica. Furthermore, several other amorphous materials are known to exhibit dissipation peaks similar to the peak in silica [223, 236]. Therefore, one possible dissipation mechanism responsible for the peak observed in tantala may be thermally activated transitions of oxygen atoms between two states in a double well potential. As in silica, it is possible that these transitions may involve bond angles flipping between energetically stable states, or perhaps rotational movement of micro-

scopic structures consisting of a small number of atoms. The wide distribution of activation energies, implied by the width of the dissipation peak (see Figure 5.30), suggests that there is a distribution of potential barrier heights, possibly related to the distribution of Ta-O bond angles in the amorphous network. However further studies are required to gain a better understanding of the dissipation mechanism.

5.6 Undoped tantalum loss measurements

Doping ion-beam sputtered Ta₂O₅ with TiO₂ has been shown to significantly reduce the mechanical loss at room temperature [214]. Following the discovery of the low temperature dissipation peak in TiO₂-doped Ta₂O₅, subsequent studies of an undoped Ta₂O₅ coating were carried out in an attempt to determine what effect, if any, the presence of doping has on the characteristics of the dissipation peak.

5.6.1 Experimental setup for cooling with liquid helium

Before cooling the cryostat with liquid helium, several modifications were made to minimise unwanted heating and allow temperatures close to 4 K to be attained. Initially, when cooling with liquid nitrogen, the lowest clamp temperature obtained was ~ 84 K. One possible source of heating is thermal radiation from warmer areas of the cryostat, especially the top parts of the three feed-through pipes, which were always close to room temperature. To reduce this effect, a narrow band optical filter (transparent at 633 nm to allow the laser beam to be transmitted) was attached to the top-plate of the experimental chamber beneath the optical read-out port (see Figure 5.32), thus preventing the cantilever from ‘seeing’ room temperature. Similarly, the lower ends of the electrical and vacuum feed-through pipes were screened with thin copper plates thermally linked to the cold top-plate of the vacuum chamber. These

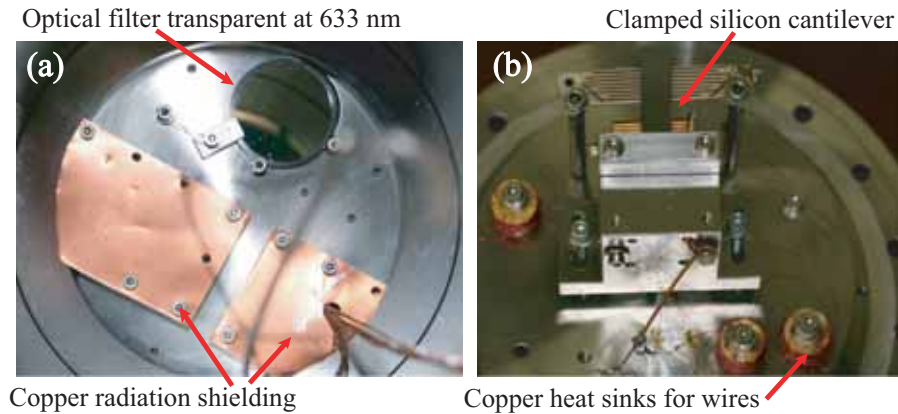


Figure 5.32: *The addition of radiation shielding across the feed-through ports in the roof of the experimental chamber (a) and thermally anchoring wires to the base-plate (b) allowed the clamp to cool to 78 K, 6 degrees lower than the previous lowest temperature obtained.*

radiation shields allowed the clamp to cool to 80 K, 4 K lower than the previous minimum temperature.

The wiring in the cryostat was initially anchored onto the back of the clamp, providing a direct conduction path between the sample and the ends of the wires at room temperature. Furthermore, to allow better temperature control the clamp was thermally insulated from the base-plate by Macor (a machinable ceramic) spacers. To prevent heating through the wires, the anchor point was removed from the clamp and the lower stages of the wiring replaced with very thin enamelled copper wire, which was wound around copper bobbins bolted to the base plate and covered in thermally conductive cryogenic varnish. This heat sinking method was used for the wires connecting the temperature sensors and the resistive heater, but was not thought necessary for the high voltage wires, which did not touch the clamp. On cooling with liquid nitrogen after these wiring changes, the base plate of the experimental chamber reached 77.5 K while the clamp cooled to 78 K.

5.6.2 Loss measurements of undoped tantalum

In this section, measurements of the temperature dependence of the dissipation of undoped tantalum are presented, and compared to the results for doped tantalum in Section 5.3. An identical silicon cantilever to the pair used in the previous section was coated with a 0.5 μm thick layer of undoped Ta_2O_5 , and heated to 600°C for 24 hours. The losses of the 2nd, 3rd, 4th and 5th bending modes were measured between 11 and 300 K and the coating loss calculated using the uncoated control data from Section 5.4. The calculated coating loss factors of each mode are shown in Figures 5.33 to 5.39.

A peak in the dissipation was found to occur at almost identical temperatures to the peak in the titania doped coating. However, for three of the four modes studied, the peak dissipation was larger for the undoped coating. For the third mode, the peak dissipation was approximately 1.1×10^{-3} for both coatings. It is interesting to note that for this mode the peak dissipation in the titania doped coating was abnormally high in comparison to the other modes, perhaps suggesting that the true dissipation was lower than that measured.

The second bending mode of the cantilever was measured only between 11 and 23 K. At higher temperatures this mode proved difficult to measure because the frequency of the first torsional mode became very close to the frequency of the second bending mode. While no evidence of direct energy coupling between the two modes was observed, the torsional mode was often excited in parallel with the bending mode, perhaps as a result of some asymmetry in the electrostatic drive plate. The resulting torsional vibration of the cantilever moved the laser spot from side to side on the photodiode readout, making it very difficult to obtain a clean ringdown of the amplitude of motion of the bending mode. This effect is likely to be responsible for the large amount of scatter observed in the measurements of the loss of the second bending mode. The data for the second mode of the cantilever coated with TiO_2 -doped Ta_2O_5 in Section 5.3 showed no evidence of this problem. It is possible that, due to

small differences in the geometry of the cantilever, the thickness of the coating or the rigidity of the clamp, the frequency of the torsional mode was more widely separated from the frequency of the second bending mode. However, the most likely explanation is the longer optical path between the cantilever and the sensor in the Glasgow cryostat effectively amplified the apparent torsional motion of the cantilever as sensed at the photodiode.

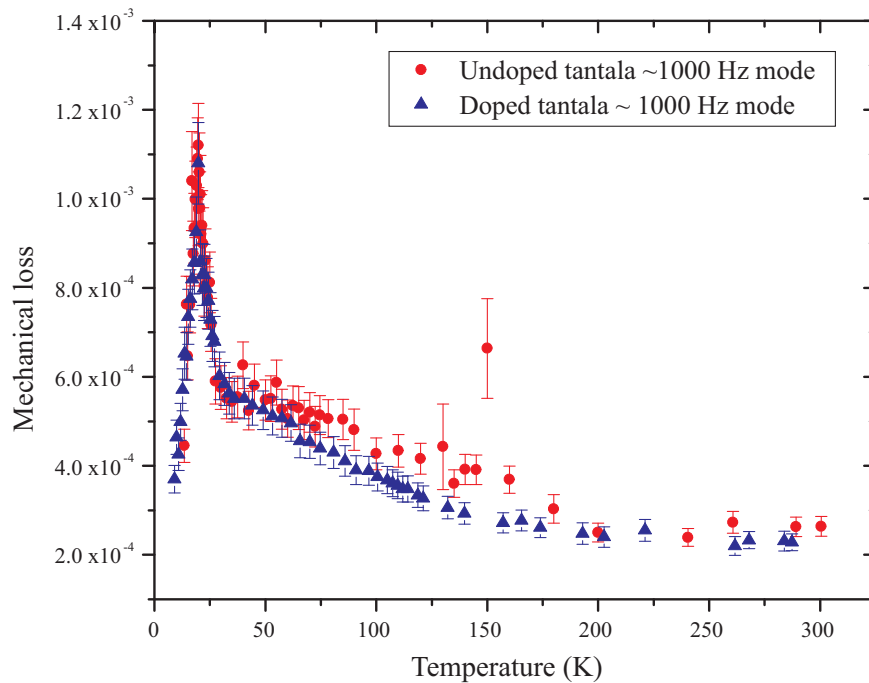


Figure 5.33: Comparison of the loss of an undoped Ta_2O_5 and a Ta_2O_5 coating doped with 14.5 % TiO_2 at ~ 1000 Hz.

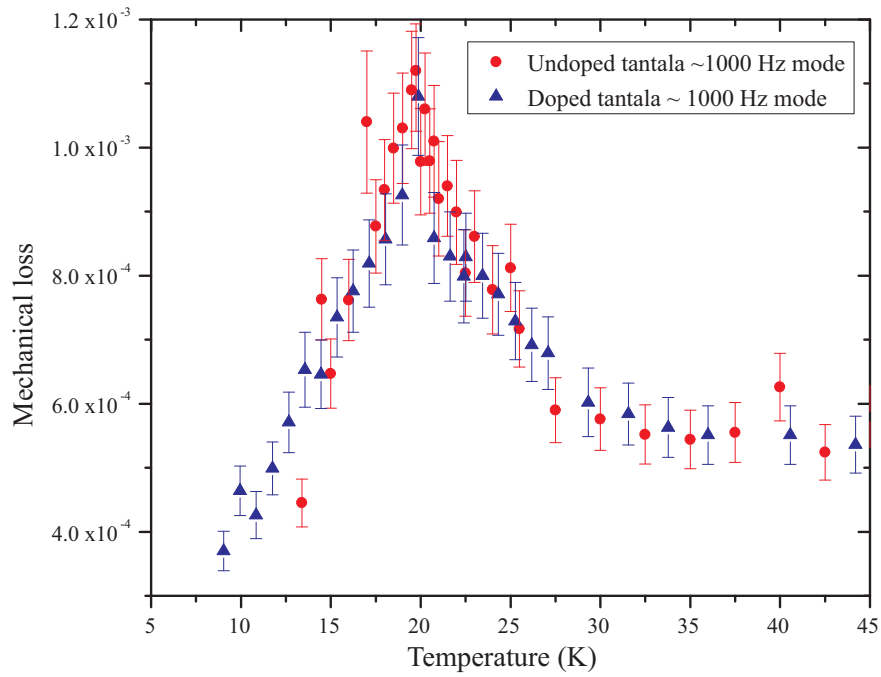


Figure 5.34: Comparison of the loss peak for an undoped Ta_2O_5 and a Ta_2O_5 coating doped with 14.5% TiO_2 at ~ 1000 Hz.

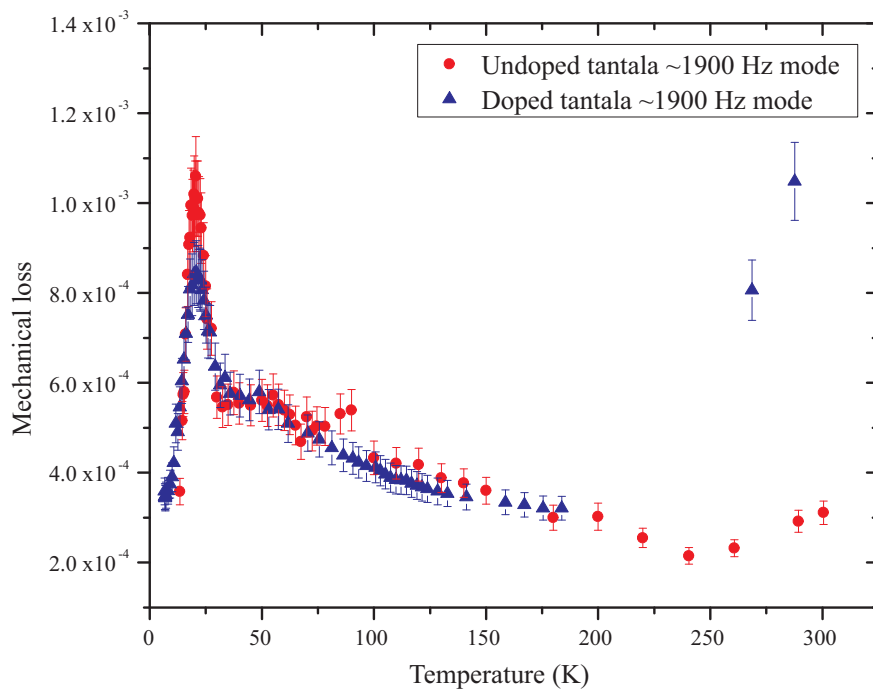


Figure 5.35: Comparison of the loss of an undoped Ta_2O_5 and a Ta_2O_5 coating doped with 14.5% TiO_2 at ~ 1900 Hz.

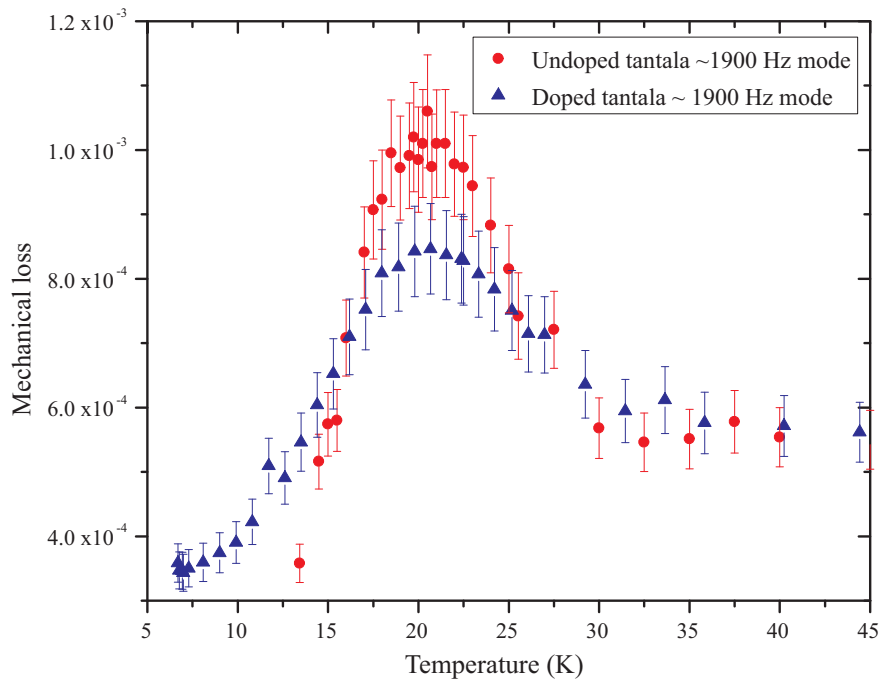


Figure 5.36: Comparison of the loss peak for an undoped Ta_2O_5 with a Ta_2O_5 coating doped with 14.5% TiO_2 at ~ 1900 Hz.

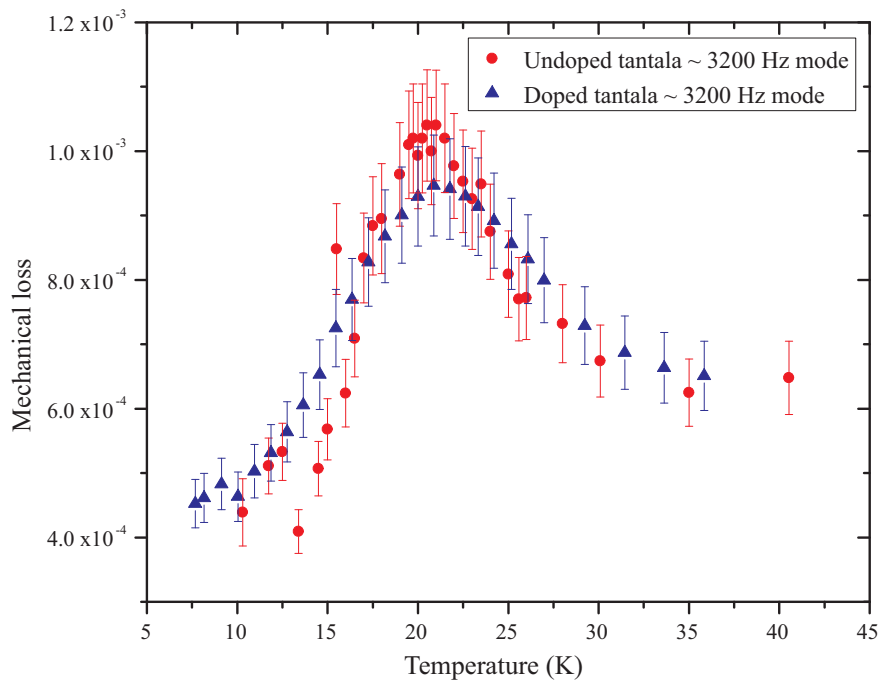


Figure 5.37: Comparison of the loss peak for an undoped Ta_2O_5 with a Ta_2O_5 coating doped with 14.5% TiO_2 at ~ 3200 Hz.

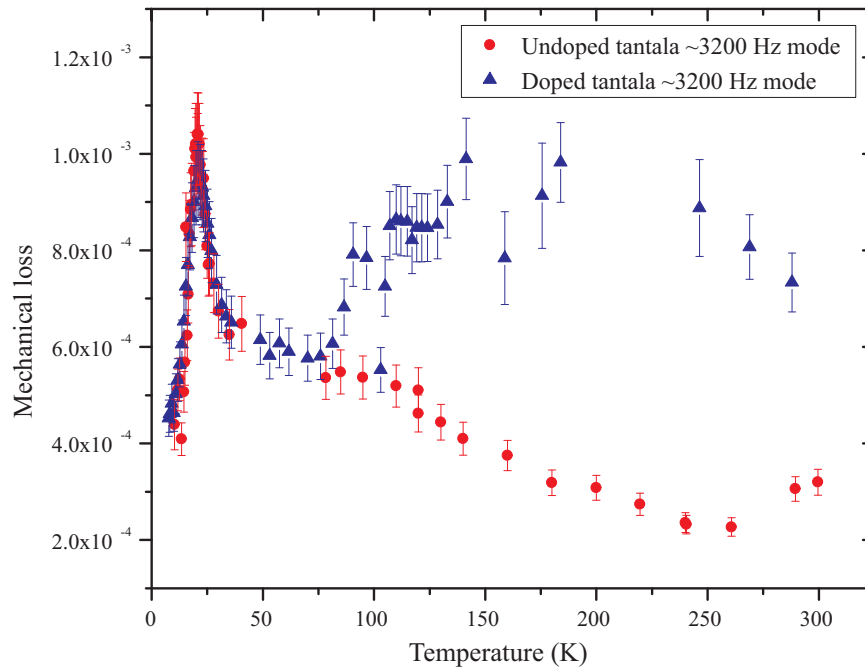


Figure 5.38: Comparison of the loss of an undoped Ta_2O_5 and a Ta_2O_5 coating doped with 14.5% TiO_2 at ~ 3200 Hz.

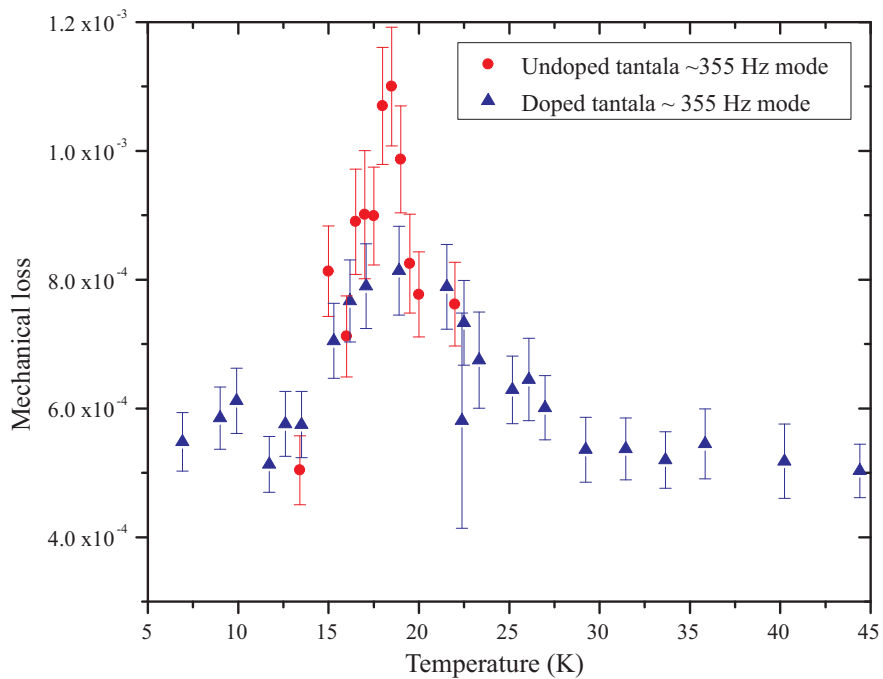


Figure 5.39: Comparison of the loss peak for an undoped Ta_2O_5 with a Ta_2O_5 coating doped with 14.5% TiO_2 at ~ 355 Hz.

5.6.3 Arrhenius plot analysis

Polynomial fitting was again used to enable the temperature at which the peak occurs to be estimated. The polynomial fits used are shown in Figures 5.40 and 5.41. The data show considerably more scatter than the previous data for the doped coating, and the fits are therefore correspondingly poorer. As with the doped coating (see Section 5.5) the third bending mode proved difficult to fit, seeming to have a different shape with a sharper peak than the other modes.

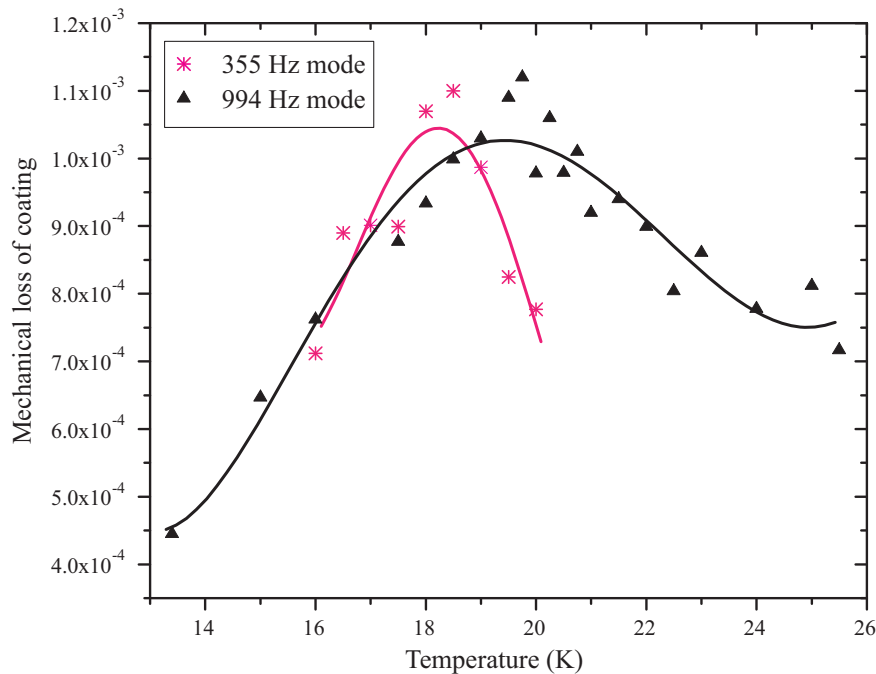


Figure 5.40: *The polynomial fits used to determine the position of the dissipation peak for the second and third bending modes.*

An Arrhenius plot for this peak is shown in Figure 5.42, from which an activation energy $E_a = (28.6 \pm 1.2)$ meV and a rate factor of $\tau_0 = (5.9 \pm 0.2) \times 10^{-12}$ s were calculated. Also shown is the data for the doped coating, for which the activation energy and relaxation constant were (39.5 ± 2.7) meV and $(1.7 \pm 0.1) \times 10^{-14}$ s respectively. The results suggest that doping Ta_2O_5 with TiO_2 increases the average value of the activation energy of the process

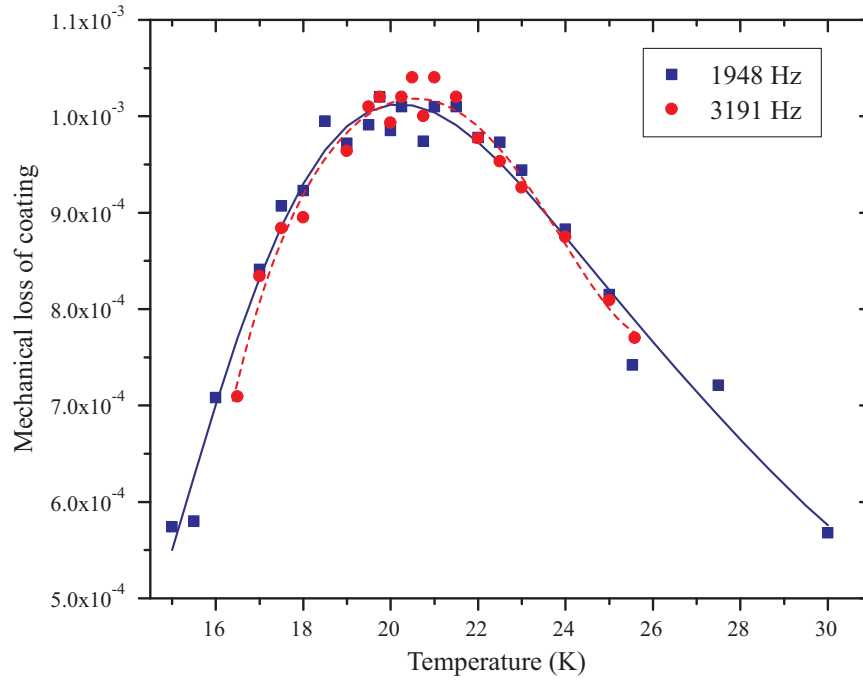


Figure 5.41: *The polynomial fits used to determine the position of the dissipation peak for the fourth and fifth bending modes.*

responsible for the dissipation by approximately 33 % and decreases the rate factor by three orders of magnitude.

The peak temperature for the fundamental mode ($1/T_{peak} = 0.0625 \text{ K}^{-1}$) of the undoped coating was obtained from measurements taken by Eleanor Chalkley [237] using a second cryostat with a shadow sensor readout similar to that described in Section 4.2.2. This arrangement allowed the fundamental mode of the cantilever to be measured without the saturation problems observed previously.

While the losses of this coating show significantly more scatter than those for the doped coating, it is possible to be confident of the position of the peak to within approximately 0.2 K for three of the five modes studied. It is unlikely that the data for the second mode could be improved using the current cryostat, as the proximity of the torsional mode at $\sim 365 \text{ Hz}$ makes obtaining a clean ringdown challenging.

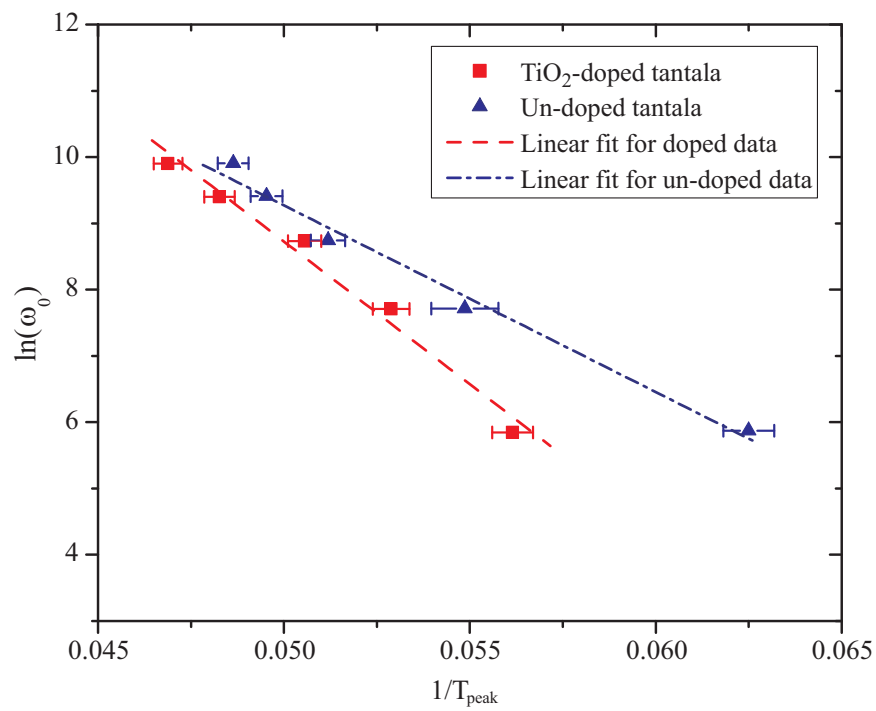


Figure 5.42: Comparison of the Arrhenius plots of $\ln(\omega_0)$ against $1/T_{\text{peak}}$ for the dissipation peaks in TiO_2 doped Ta_2O_5 and undoped Ta_2O_5 .

5.6.4 Analysis of the distribution of potential barrier heights

As noted previously, mechanical dissipation peaks occurring at temperatures above 10 K in many amorphous solids [238], such as fused silica, are thought to arise from thermally activated transitions of atoms or molecules between stable orientations. These stable orientations can be represented by a double well potential, with two minimum energy states separated by a potential energy barrier of height V [172]. The amorphous nature of these materials results in a wide distribution of potential barrier heights, explaining the broad nature of the dissipation peaks observed in these materials. Initial models were based on the assumption that the double-well potentials were symmetric, with the potential barrier separating states of equal potential energy [172, 222, 232, 236]. Gilroy and Phillips [233] pointed out several drawbacks of this model. Firstly, for a peak in dissipation to occur, a low energy cut-off in the distribution of barrier heights must be included in the model. Secondly, the symmetric model fails to explain the observed linear scaling of the peak loss in fused silica with

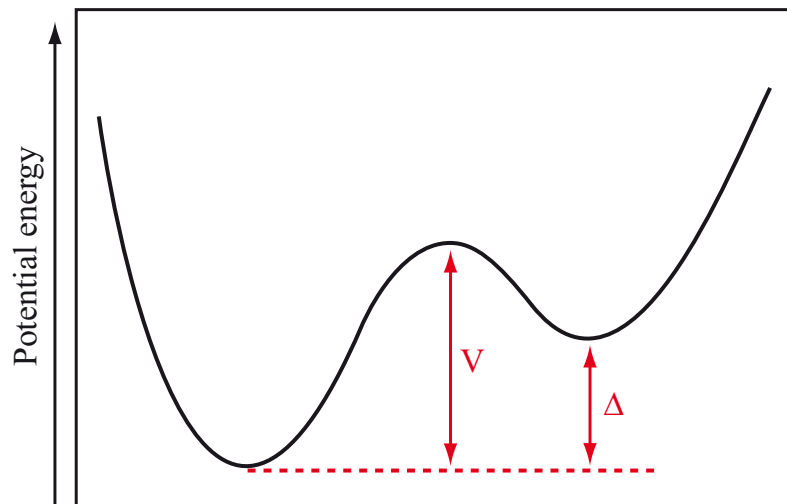


Figure 5.43: A schematic diagram of an asymmetric double well potential, with a potential barrier V and an asymmetry Δ .

the measurement frequency. Thirdly, Gilroy and Phillips suggest that the same structural variations which give rise to the distribution of potential barrier heights would also be expected to produce asymmetric potential wells.

Figure 5.43 shows a model of an asymmetric double-well potential (ADWP), with a barrier height V and an asymmetry Δ in the energies of the wells. In an amorphous solid there will be a distribution of potential barrier heights, $g(V)$, and also a distribution of the asymmetries $f(\Delta)$ in the energies of adjacent potential wells. Gilroy and Phillips showed that the dissipation predicted by this model is given by the following double integral over Δ and V [233]:

$$\phi = \frac{\gamma^2}{k_B T C_{ii}} \int_0^\infty \int_0^\infty \frac{\omega \tau}{1 + (\omega \tau)^2} \operatorname{sech}^2 \left(\frac{\Delta}{2k_B T} \right) f(\Delta) g(V) d\Delta dV, \quad (5.5)$$

where ω is the angular frequency of measurement, C_{ii} is the appropriate elastic constant, γ is the elastic coupling constant which represents the coupling between the defect (e.g. the atom re-orienting within the ADWP) and the applied strain. The relaxation time τ associated with a barrier height V is given by the Arrhenius equation (Equation 5.2).

Starting with this integral, and assuming that $g(V)$ is independent of temperature and that $f(\Delta) = f_0 = \text{constant}$ [233], Topp and Cahill [223] derive the following expression relating the mechanical loss to the function $g(V)$:

$$\phi = \frac{\pi \gamma^2 f_0}{C_{ii}} k_B T g(V), \quad (5.6)$$

where

$$V = k_B T \ln \left(\frac{1}{\omega \tau_0} \right). \quad (5.7)$$

Thus the distribution of barrier heights, $g(V)$, can be calculated from the measured temperature dependence of the mechanical loss. This calculation was carried out for the doped and undoped tantala loss data measured at ~ 1900 Hz, using the values of τ_0 obtained from the Arrhenius fits: $\tau_0 = 5.9 \times 10^{-12}$ s for undoped tantala and $\tau_0 = 1.7 \times 10^{-14}$ s for doped tantala. For

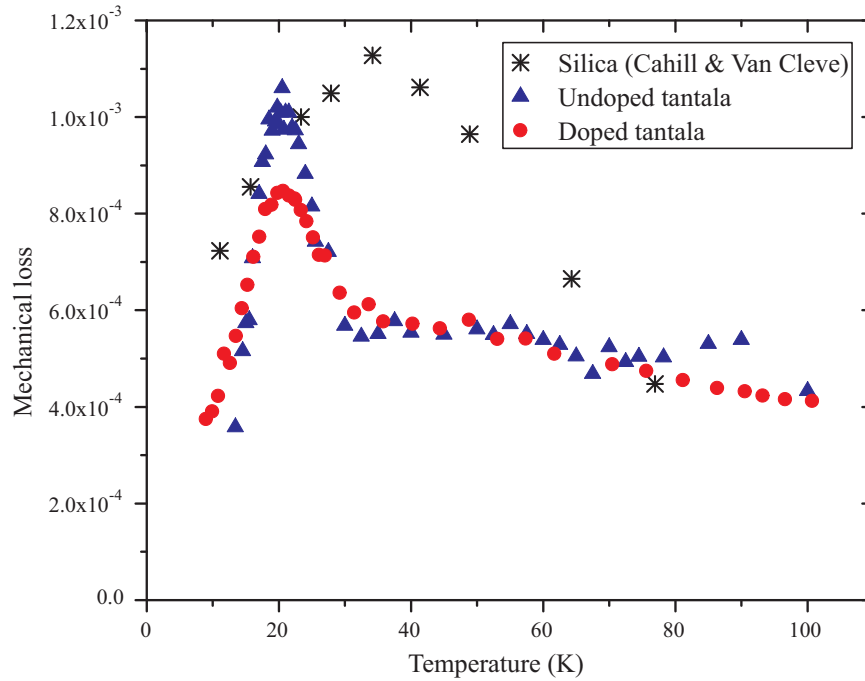


Figure 5.44: *Plot of the loss data used to calculate the barrier height distribution. The silica data is taken from Cahill and Van Cleve [239] and was measured at 100 kHz.*

comparison, the calculation of $g(V)f_0$ for fused silica in Topp and Cahill was repeated, using experimental loss data from Cahill and Van Cleve [239]. The data used for the calculation are shown in Figure 5.44.

The value of the coupling coefficient γ for tantalum could not be found in the literature. However, experimental data in Topp and Cahill [223] suggests that for most amorphous solids $0.6 \text{ eV} < \gamma < 1.1 \text{ eV}$. It was decided to use the value of γ measured in fused silica, $\gamma = 0.9 \text{ eV}$. Data for the elastic constants C_{ii} of various amorphous materials are given in Topp and Cahill, all falling in the range $1.4 \times 10^4 < C_{ii} < 7.8 \times 10^4 \text{ MPa}$. C_{ii} for tantalum was approximated by scaling the value for silica, $C_{ii} = 3.3 \times 10^4 \text{ MPa}$ [240], by the ratio of the Young's moduli of tantalum and silica, giving $C_{ii} = 6.42 \times 10^4$. It should be noted that, while every effort was made to make reasonable approximations of C_{ii} and γ , these constants are likely to be similar for both doped and undoped tantalum, and the precise values are thus of little importance for comparing the

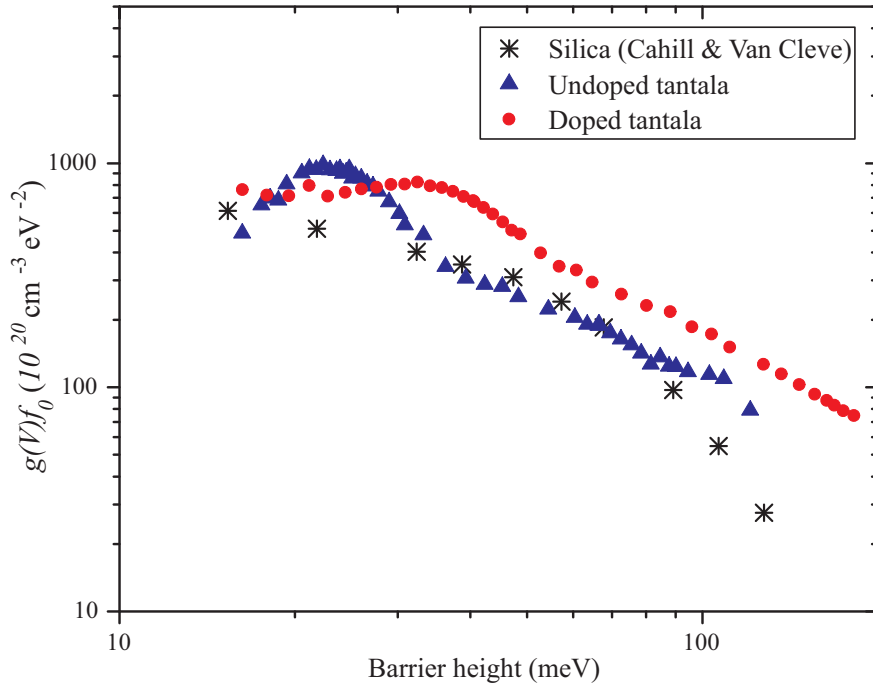


Figure 5.45: Plot of the calculated potential barrier height distribution function $g(V)f_0$ as a function of barrier height for pure tantalum, titania-doped tantalum and silica. The silica data used in the calculation was taken from Cahill and Van Cleve [239].

two materials. Moreover, the constants do not affect the shape of the barrier height distribution function, which is of primary interest.

The calculated function $g(V)f_0$ for doped tantalum, undoped tantalum and fused silica [223, 239] is shown in Figure 5.45. This plot allows the distribution of barrier heights (i.e. activation energies for the transition between potential wells in the ADWP) to be compared.

Both forms of tantalum have a peak in the barrier height distribution: in both cases this peak corresponds closely to the average activation energy calculated from the Arrhenius equation. The presence of titania doping appears to shift peak in the distribution to a higher potential barrier energy. In addition, the titania doping appears to increase the width of the peak in the distribution function.

5.6.5 Comparison of tantalum coatings at room temperature

The mechanical loss of three types of tantalum coating supplied by LMA have been studied: TiO₂-doped Formula 5, TiO₂-doped Formula 5** and undoped tantalum. Formula 5 tantalum was used in one of the multi-layer coatings studied by Harry et al [214] to determine the effect of TiO₂ doping on the dissipation at room temperature. LMA claimed to have reduced the dissipation of the Formula 5 material by changing an unspecified coating deposition parameter; resulting in the Formula 5** coating. The results presented in Chapter 4, measured using silica substrates, suggested that the Formula 5** coating did indeed have a lower than than Formula 5 tantalum. Figure 5.46 compares the dissipation measured in each of these coatings as a function of frequency at room temperature. It can be seen that the Formula 5** coating measured on

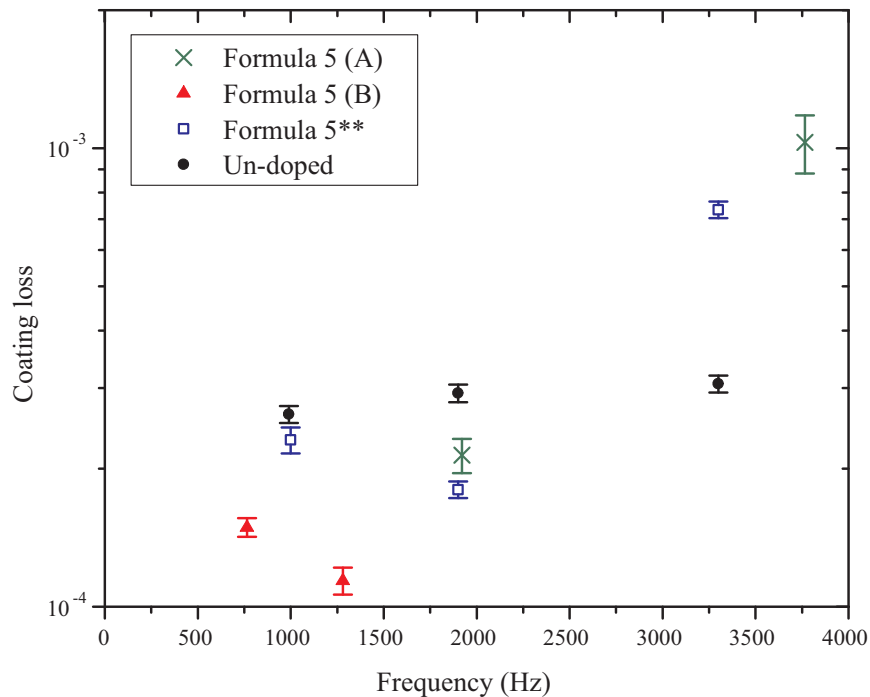


Figure 5.46: Comparison of the coating losses measured at room temperature for Formula 5, Formula 5** and undoped Ta₂O₅ coatings.

a silicon substrate has slightly higher dissipation at room temperature than the Formula 5 coating. TiO_2 doping can be seen to reduce the loss by approximately 11 % at 1 kHz and 28 % at 1.9 kHz. This is a significantly smaller decrease in loss than the factor of almost two reported by Harry et al [214] in multi-layer coatings. At room temperature, the silicon cantilever experiment has large errors because the loss difference between the coated and uncoated cantilevers is typically very small. It is possible that these errors are responsible for the discrepancy between the single layer and multi-layer coating loss results. Further investigation of the coating loss at room temperature would be of interest.

5.7 The effect of heat treatment

Heat treatment of fused silica can significantly reduce the observed mechanical loss at both room temperature and cryogenic temperature [171]. Heating is believed to reduce the internal stresses in silica, resulting in a narrowing of the distribution of Si-O bond angles, which corresponds to a narrowing of the distribution of potential barrier heights in the double-well systems. The height and width of the dissipation peak are also related to the fictive temperature [241] i.e. the temperature at which the glass formed by freezing from a molten liquid structure. The dissipation peak is found to become higher and narrower as the fictive temperature decreases. It is thought that silica formed at lower temperatures has a lower concentration of stressed ring structures, and that the distribution of bond angles and therefore potential barrier heights is also reduced, resulting in a higher, narrower dissipation peak.

If the dissipation mechanism in tantala is indeed analogous to that in silica, heat treatment may also be effective in reducing the dissipation in this material. To investigate this, it was decided to measure the mechanical loss of tantala films which had been heat treated at different temperatures. A set of nominally identical cantilevers were sent to CSIRO, a coating vendor in Australia [242].

As before, a thermal oxide layer approximately 15 to 20 nm thick was grown on all of the samples. Eight cantilevers were coated with undoped tantala. These coated cantilevers were heat treated in pairs at each of the following temperatures: 300, 400, 600 and 800°C. An oxidised but uncoated control cantilever was included in each of the heat treatment runs. The heat treatment was carried out in standard atmosphere.

Ion-beam sputtered tantala films are known to crystallise when heated to $\approx 650^\circ\text{C}$, to the detriment of their optical properties. However, it was thought to be interesting to study the mechanical loss on either side of this transition temperature in order to gain a better understanding of the physics involved.

As yet, uncoated control samples have not been measured and therefore the loss of the coatings has not been calculated. However, the cantilevers are nominally identical and thus the only difference between them is the temperature at which the post-coating heat treatment was carried out. Each cantilever had been heated to $\sim 900^\circ\text{C}$ prior to coating for the growth of the thermal oxide layer, so it is perhaps reasonable to assume that the further post-coating heat treatment will not substantially alter the mechanical loss of the silicon substrate. Even if the substrate loss was changed substantially by the heat treatment, it would only be expected to significantly affect the measured loss of the coated samples at temperatures above approximately 200 K. It is therefore of significant interest to compare the losses of the coated samples at low temperature.

Figures 5.47 to 5.50 show the measured loss of the second, third, fourth and fifth modes of the coated cantilevers which had been heat treated at 300 and 800°C. Also shown are the results from Section 5.6 for the LMA undoped tantala coating, which was heat treated at 600°C. The most striking features of the results are the absence of a dissipation peak at ~ 20 K for the coating heat treated at 300°C and the large, broad peak in the dissipation of the coating heated to 800°C.

The dissipation of the coated cantilever heat treated at 300°C peaks at

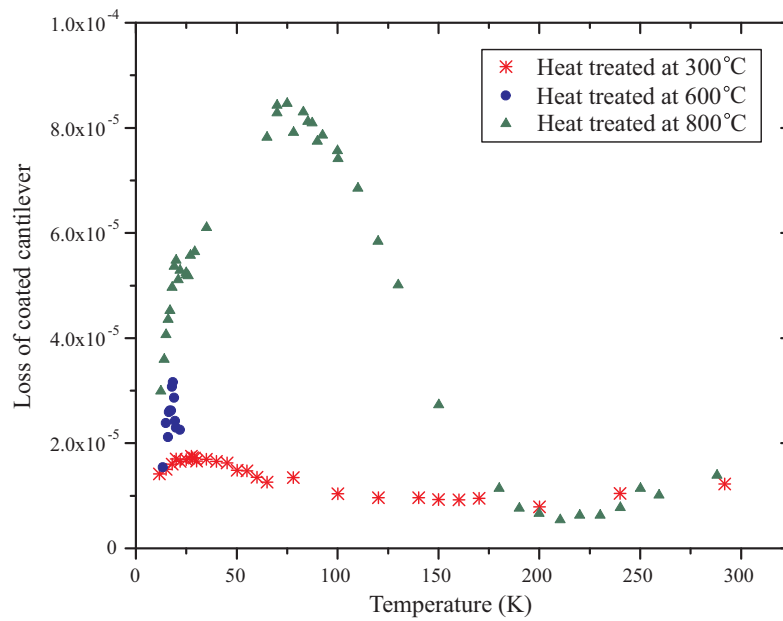


Figure 5.47: *Measurements of the mechanical loss of the second bending mode (at approximately 350 Hz) of three cantilevers coated with undoped Ta_2O_5 and heated to 300, 600 and 800 °C respectively.*

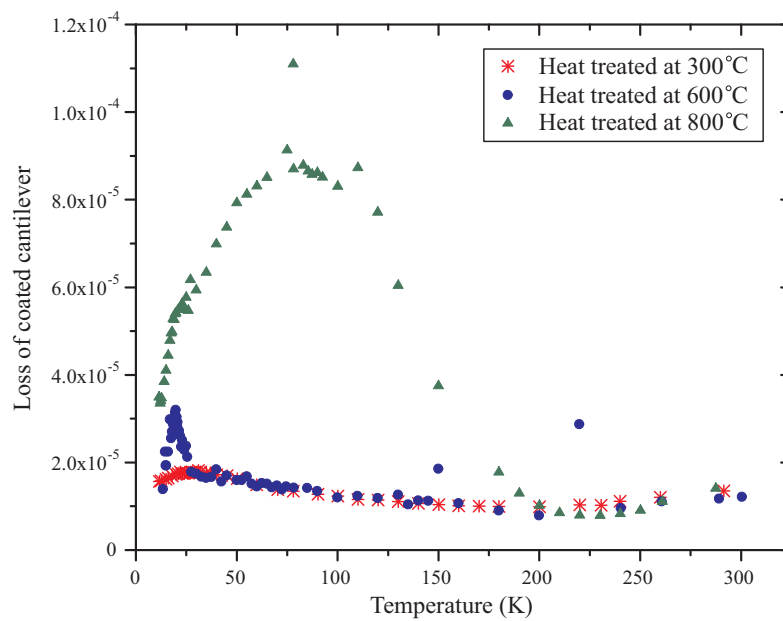


Figure 5.48: *Measurements of the mechanical loss of the third bending mode (at approximately 1000 Hz) of three cantilevers coated with undoped Ta_2O_5 and heated to 300, 600 and 800 °C respectively.*

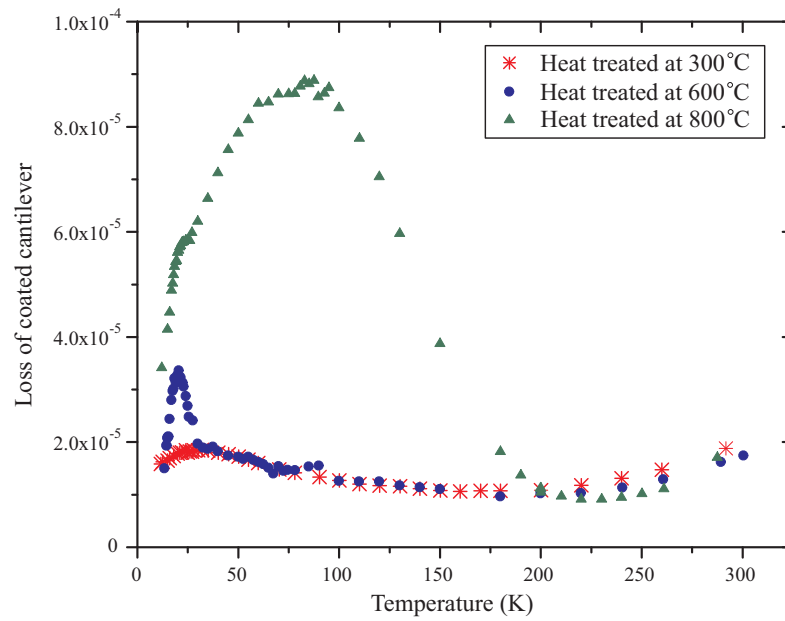


Figure 5.49: *Measurements of the mechanical loss of the fourth bending mode (at approximately 1960 Hz) of three cantilevers coated with undoped Ta_2O_5 and heated to 300, 600 and 800 °C respectively.*

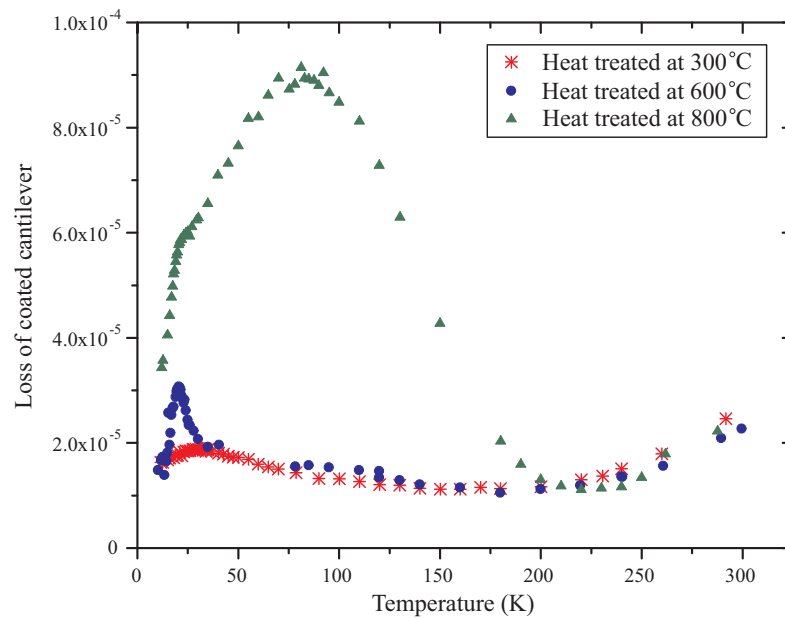


Figure 5.50: *Measurements of the mechanical loss of the fifth bending mode (at approximately 3200 Hz) of three cantilevers coated with undoped Ta_2O_5 and heated to 300, 600 and 800 °C respectively.*

approximately 30 K for each mode studied. The peak is significantly smaller and broader than the peak at 20 K previously observed in tantala coatings which had been heat treated at 600 °C. Analysis of the Arrhenius plot for this peak, which is shown in Figure 5.51, yielded an activation energy and relaxation constant (138 ± 4) meV and $(3.5 \pm 0.1) \times 10^{-27}$ s respectively. It is possible that the two peaks arise from the same dissipation mechanism and that heating the Ta_2O_5 to 600°C altered the distribution of potential barrier heights, resulting in a lower average activation energy. However, the dissipation at (and above) 30 K is almost identical for both samples, suggesting that the 30 K peak may also be present in the coatings treated at 600°C, although partially obscured by the larger peak at 20 K. At temperatures above the dissipation

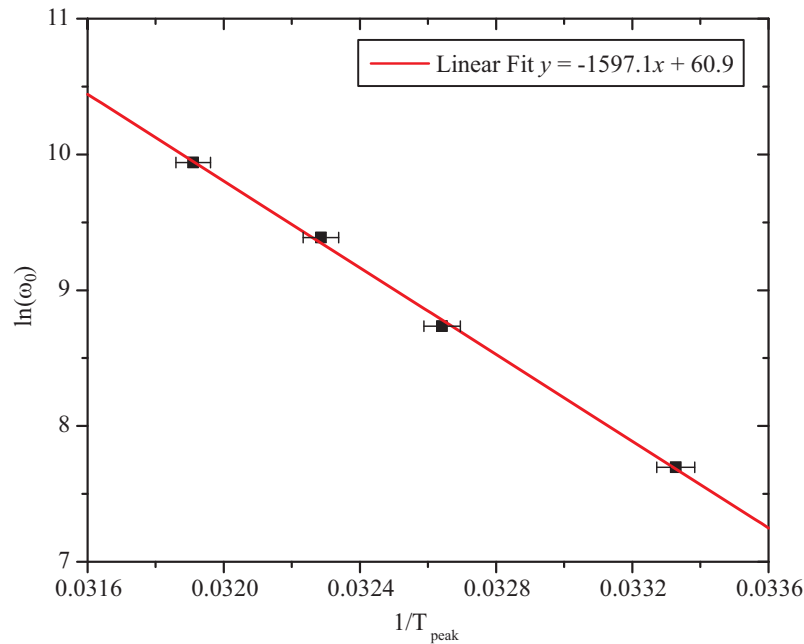


Figure 5.51: Arrhenius plot for the dissipation peak observed at ~ 30 K for an undoped tantala coating heat treated at 300 °C

peak, between ~ 40 and 200 K, the dissipation of the coatings treated at 300 and 600 °C follow a similar trend and, for the third and fourth modes of the samples, have the same magnitude to within experimental error. Between

~ 200 K and room temperature, the loss of the cantilever treated at 600°C appears to be significantly lower. In this region, however, the thermoelastic loss of the cantilever substrate becomes increasingly dominant and thus the effect of the coating on the measured loss becomes smaller. It is therefore difficult to draw conclusions in this temperature range until the dissipation of the uncoated control samples has been measured.

The cantilever treated at 800°C exhibits a large and very broad dissipation peak at ~ 80 to 90 K and a smaller, narrower peak at ~ 20 K. As noted above, ion-beam sputtered tantalum is known to crystallise at approximately 650°C . To confirm that the coating was polycrystalline, a silica disk which had been coated and heat treated at the same time as the cantilever was studied under a transmission electron microscope by R. Bassiri and J. Scott. Both the microscope images and the results of electron diffraction measurements, shown in Figure 5.52, indicate that the tantalum coating has a crystalline structure. It is likely, therefore, that the large dissipation peak centered on 80 to 90 K is associated with the polycrystalline structure of the tantalum. Dissipation peaks in polycrystalline materials can arise from phonon scattering at the grain boundaries [110], and this dissipation mechanism may be responsible for the peak observed at 90 K.

The effects of the dissipation peak at 20 K can be seen as a small plateau in the low temperature edge of the 90 K peak in the loss data for each mode of the sample heat treated at 800°C . At temperatures between ≈ 200 and 250 K, this cantilever has a lower loss than those heat treated at 300 and 600°C , while closer to room temperature, it has the largest loss of the three cantilevers. The lower loss between 200 and 250 K may be caused by the heat treatment at 800°C reducing the loss of the silicon substrate, perhaps by removing contaminants from the surface or by driving water out of the thermal oxide layer. Measurements of the control samples which underwent the same heat treatment will be required to fully understand the behaviour of

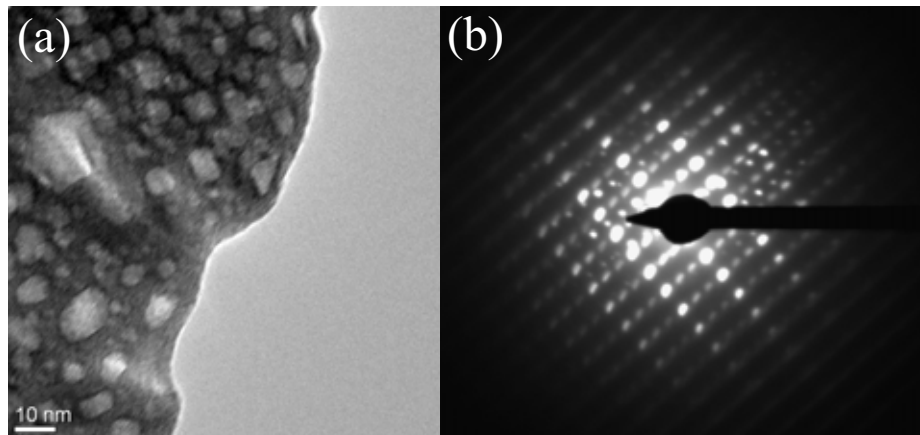


Figure 5.52: (a) Transmission electron microscope image of the tantala coating annealed to 800°C, showing evidence of crystal structure with features up to 15 nm across. (b) Electron energy loss diffraction pattern from the same coating, showing clear diffraction spots confirming the crystalline structure of the coating. Images taken by Riccardo Bassiri and Jamie Scott [243].

the dissipation above 200 K.

5.8 Conclusions

A peak in the dissipation of 500 nm thick films of tantalum pentoxide heat-treated at 600°C has been discovered at approximately 20 K. The peak is present in both undoped tantala and in tantala doped with (14.5 ± 1) % titania. The frequency dependence of the temperature at which the peak occurs implies that the dissipation arises from a Debye-type thermally activated relaxation process which can be described by the Arrhenius equation.

The presence of titania doping in the tantala, which is known to reduce the loss of multi-layer $\text{SiO}_2/\text{Ta}_2\text{O}_5$ coatings at room temperature, was found to reduce the dissipation throughout the entire temperature range studied, with the exception of the wings of the peak, where the loss dissipation of the undoped coating was slightly higher. Analysis of the dissipation peaks observed in the doped and undoped coatings suggests that the TiO_2 doping increases the activation energy of the dissipation mechanism by approximately

33 % from 28.6 ± 1.2 meV to 39.5 ± 2.7 meV.

Given the magnitude of the activation energy and the amorphous structure of ion-beam sputtered tantala, it has been postulated that the dissipation mechanism may be similar to that observed in fused silica, where the dissipation is thought to arise from thermally activated transitions of oxygen atoms between stable states in a double-well potential system. The dissipation peak observed in tantala is significantly wider than a Debye peak, suggesting that there may be a wide distribution of activation energies for the energy loss mechanism. This distribution may be related to the amorphous structure of the coating. Following the asymmetric double-well potential model of Gilroy and Phillips and its extension by Topp and Cahill, the distribution of activation energy barriers has been calculated for doped and undoped tantala. The results suggest that the presence of TiO_2 doping broadens this distribution and shifts it towards a higher average activation energy.

Heat treatment is believed to increase the height and reduce the width of the dissipation peak in fused silica by reducing the distribution of Si-O bond angles. Initial studies of ion-beam sputtered Ta_2O_5 have shown that the position, height and width of the dissipation peak are very strongly related to the heat treatment temperature. A second, very broad dissipation peak has been observed in a Ta_2O_5 film which had crystallised after heat treatment at 800°C .

The identification of this low temperature dissipation peak provides the first evidence of the mechanism responsible for mechanical dissipation in ion-beam sputtered Ta_2O_5 coatings. Further study of the effects of doping and heat treatment on the dissipation, and particularly on the characteristics of the dissipation peak, may facilitate the development of lower loss coatings for use at both room and cryogenic temperatures, thus enabling the sensitivity of future gravitational wave detectors to be significantly enhanced. In addition, these results are of direct interest to a variety of optical measurements and may,

for example, be of use in the choice of coatings and operating temperatures for future ultra-stable laser cavities.

Chapter 6

Temperature dependence of the mechanical dissipation in silica coatings

6.1 Introduction

In the preceding chapter, the temperature dependence of the mechanical loss of single layers of ion-beam sputtered tantalum pentoxide was studied, resulting in a possible identification of one of the loss mechanisms in this material. To evaluate the coating thermal noise in a cryogenic gravitational wave detector, it is also necessary to study the low temperature loss in a silica coating layer. For multi-layer silica/tantala coatings the tantala layers are known to be the dominant source of the coating loss at room temperature [130, 131], as discussed in the previous chapter. However, it is known that the loss of bulk silica increases significantly at low temperatures [93]. It is therefore important to investigate the temperature dependence of the dissipation in ion-beam sputtered silica coatings.

Low temperature dissipation in thin silica films grown by thermal oxidation and electron beam evaporation has been studied [244], but to the author's knowledge, the temperature dependence of the dissipation in single layers of ion-beam sputtered silica coatings has not previously been investigated. Mea-

measurements of the loss of a single layer of silica deposited on a silicon cantilever by ion-beam sputtering are presented in this chapter. The losses measured at room temperature are compared with those obtained by Penn for ion-beam sputtered silica deposited on a silica disk and found to be higher, and any possible role of coating thermoelastic loss in this observed difference evaluated. These results are combined with the tantala dissipation results from Chapter 5 to calculate the expected loss in a multi-layer coating as a function of temperature. Finally, these results are compared with direct measurements of the loss in a multi-layer coating by Yamamoto et al [226].

6.2 Coating thermoelastic loss

Thermoelastic loss in a material arises when heat flows between regions of different temperature. In a vibrating cantilever an oscillating differential temperature distribution occurs leading to energy dissipation from heat flow across the thickness of the cantilever, as described in Section 2.4.

A further source of thermoelastic loss occurs in a coated sample from the differing thermo-mechanical properties of the coating and substrate materials. This effect is described in detail by Fejer et al [142], where the following equations for the ‘coating thermoelastic loss’ are derived. It should be noted that this is a misnomer as this loss is not solely dependent on the properties of the coating and arises from the differences in the properties of the coating and substrate materials. For a uniform film of thickness l on a much thicker substrate, the coating thermoelastic loss is described by the following four equations:

$$\phi_{te} = \frac{2Y_c\alpha_c^2T}{C_c(1-\nu_c)} \left(1 - \frac{\alpha_s Y_s (1-\nu_c) C_c}{\alpha_c Y_c (1-\nu_s) C_s} \right)^2 g(\omega), \quad (6.1)$$

where Y is Young’s modulus, α is the coefficient of thermal linear expansion, C is specific heat capacity and ν is Poisson’s ratio and the subscripts ‘s’ and ‘c’ refer to properties of the substrate and the coating film respectively. The

function $g(\omega)$ describes the frequency dependence:

$$g(\omega) = \text{Im} \left\{ -\frac{1}{\sqrt{i\omega\tau_c}} \frac{\sinh(\sqrt{i\omega\tau_c})}{\cosh(\sqrt{i\omega\tau_c}) + R\sinh(\sqrt{i\omega\tau_c})} \right\}, \quad (6.2)$$

in which τ_c and R are defined as:

$$R = \sqrt{\frac{k_c C_c}{k_s C_s}}, \quad (6.3)$$

and

$$\tau_c = l^2 / \kappa_c, \quad (6.4)$$

and $\kappa_c = k_c / C$ is the thermal diffusivity of the coating. Upon examination of Equation 6.1 it can be seen that if the coating and substrate materials are identical then the combination of material properties in brackets becomes zero and there is no thermoelastic loss from this effect. Since the magnitude of the dissipation has a quadratic dependence on the difference between the properties of the coating and the substrate, the loss can be very sensitive to small changes in the properties of the coating.

	Silicon	Silica	Tantala
Young's modulus	166 GPa	72 GPa	140 GPa
Linear thermal expansion coefficient	$2.6 \times 10^{-6} \text{K}^{-1}$	$5.1 \times 10^{-7} \text{K}^{-1}$	$3.6 \times 10^{-6} \text{K}^{-1}$
Specific heat capacity	$705 \text{Jkg}^{-1} \text{K}^{-1}$	$746 \text{Jkg}^{-1} \text{K}^{-1}$	$306 \text{Jkg}^{-1} \text{K}^{-1}$
Poisson's ratio	0.27	0.17	0.23
Thermal conductivity	$140 \text{Wm}^{-1} \text{K}^{-1}$	$1.38 \text{Wm}^{-1} \text{K}^{-1}$	$33 \text{Wm}^{-1} \text{K}^{-1}$
Density	2330kgm^{-3}	2202kgm^{-3}	6850kgm^{-3}

Table 6.1: *Material properties for silicon [228], silica [142] and tantala [142] at 290 K, used in the calculation of the coating thermoelastic loss.*

The calculated magnitudes and frequency dependence of the coating thermoelastic loss for 500 nm thick single layer silica and tantala coatings on silicon substrates is compared in Figure 6.1. The material properties used in this calculation are shown in Table 6.1. The coating thermoelastic loss peaks at

approximately 1 MHz for the cantilever coated with silica and 20 MHz for the samples coated with tantala. The different shape of the peaks is explained by the differing values of R , as discussed by Fejer [142]. The thermoelastic loss is significantly higher in the case of the cantilever coated with silica. At frequencies above 100 Hz it is of the same order as the measured loss of the uncoated silicon cantilever, and thus might be expected to have a small effect on the measured coating loss at room temperature. To allow correct calculation of the intrinsic loss of the coating material, the coating thermoelastic loss must be subtracted from the measured coating loss. The formula for calculating the intrinsic coating loss (Equation 4.14) now becomes:

$$\phi(\omega_0)_{\text{coating}} = \frac{Y_s a}{3Y_c t} (\phi(\omega_0)_{\text{coated}} - \phi(\omega_0)_{\text{substrate}}) - \phi(\omega_0)_{\text{coating thermoelastic}}, \quad (6.5)$$

where $\phi(\omega_0)_{\text{coating thermoelastic}}$ is the coating thermoelastic loss calculated from Equation 6.1.

The temperature dependence of the coating thermoelastic loss was calculated for the cantilever coated with silica, and is shown in Figure 6.2. The temperature dependent values of all of the material properties were taken from Touloukian [228] and White [245]. Over the temperature range studied, the coating thermoelastic loss is highest at room temperature.

In the frequency range at which loss measurements were carried out (below 5 kHz) the tantala coating thermoelastic loss is approximately two orders of magnitude smaller than the loss of the uncoated silicon cantilever, and thus has no significant effect on the loss of the coated sample. It was therefore not necessary to correct the measurements in Chapter 5 for coating thermoelastic loss.

6.3 Results

A 492 nm thick silica coating was applied by ion-beam sputtering to a silicon cantilever by LMA [215]. The cantilever was identical to those used to

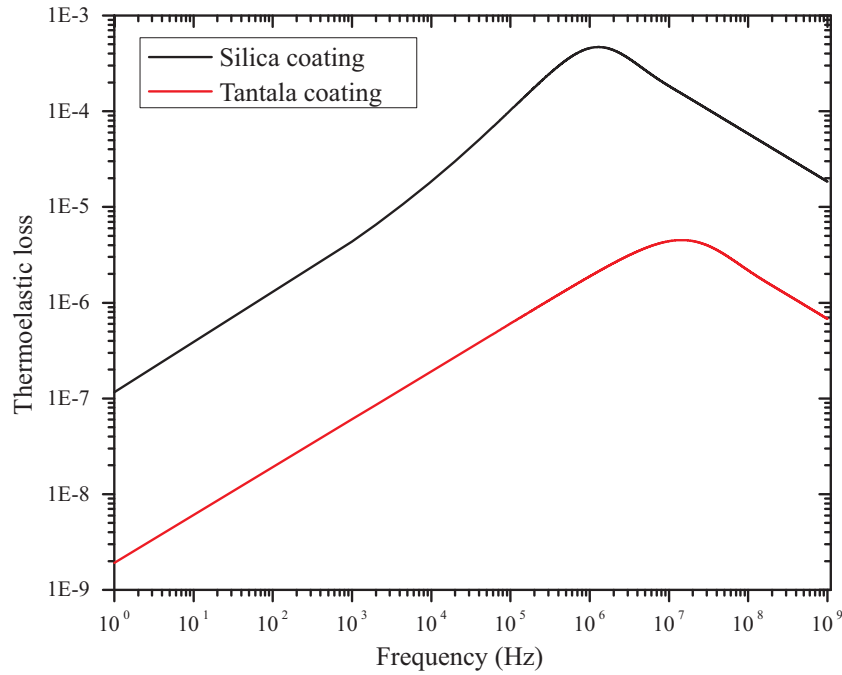


Figure 6.1: Comparison of the coating thermoelastic loss at 290 K calculated for a 500 nm thick SiO_2 coating and a 500 nm thick Ta_2O_5 coating.

measure the loss of a doped tantalum coating to liquid helium temperature (see Section 5.3) and underwent the same pre-coating thermal oxidation process and post-coating heat treatment at 600 °C. The temperature dependence of the mechanical loss of the coated cantilever was measured using the method and apparatus described in Section 5.3.2. The measured dissipation is shown as a function of temperature in Figures 6.3 to 6.7. Each point represents the average loss calculated from at least three ring-down measurements and has a standard error of typically less than 3%. The uncoated control data set is identical to that used in Section 5.3: it has, however, been interpolated onto the same temperature points as the measurements of the silica coating sample.

Loss of the coated cantilever

Each mode of the coated cantilever shows some evidence of a broad dissipation peak at approximately 21 K, which will be discussed further in the next section.

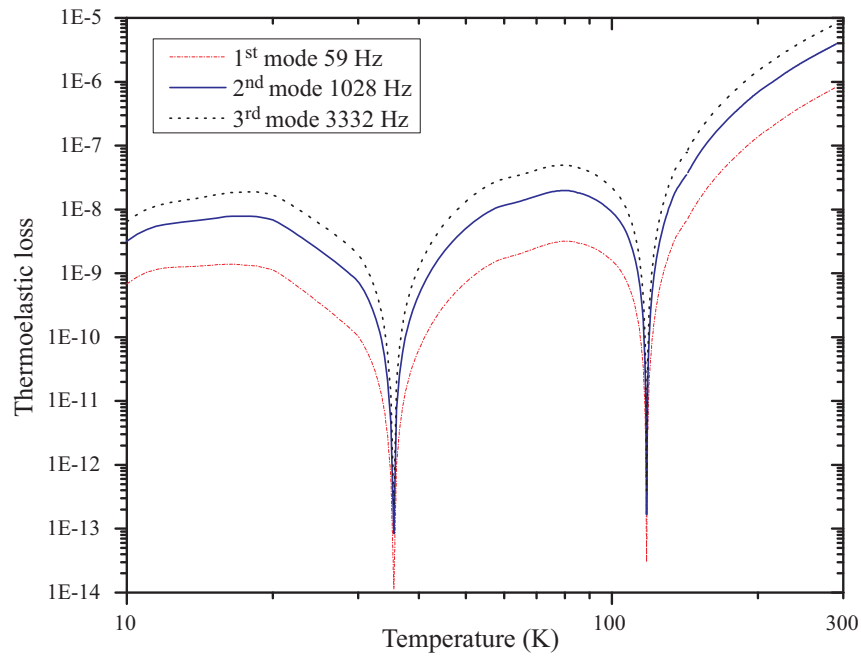


Figure 6.2: Temperature dependence of the coating thermoelastic loss calculated for three modes of the SiO_2 coated silicon cantilever.

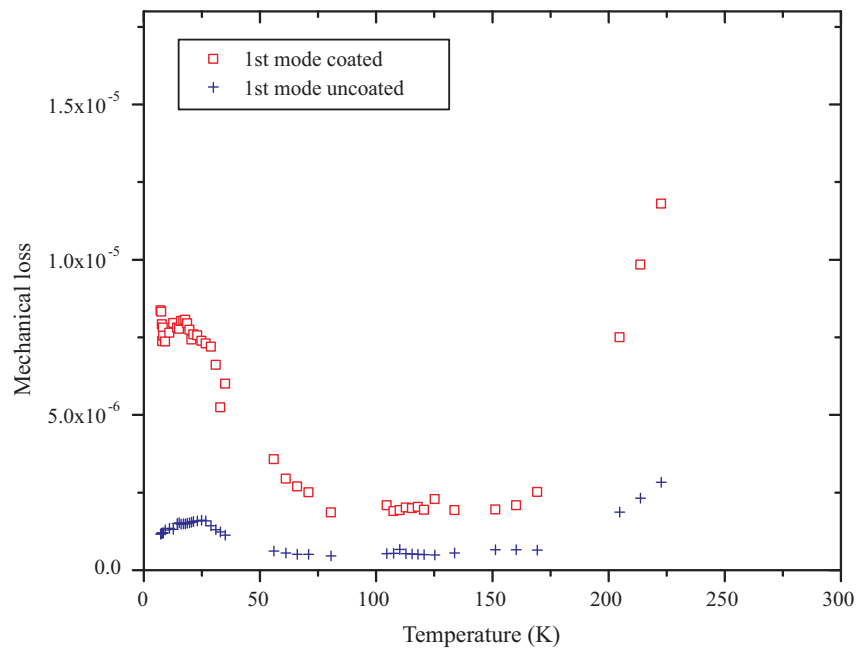


Figure 6.3: Plot of the measured loss for the first mode of the cantilever coated with silica and of the uncoated control sample.

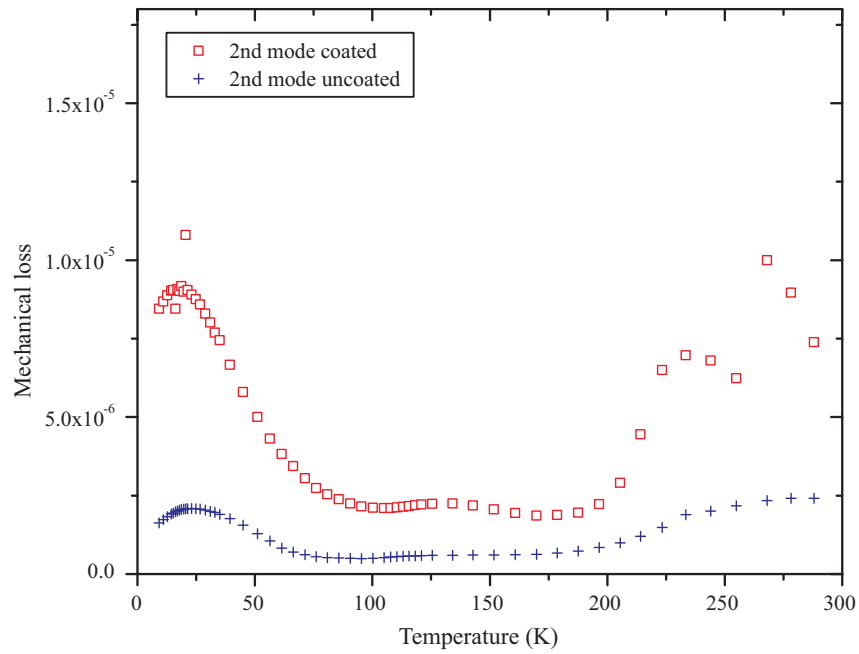


Figure 6.4: Plot of the measured loss for the second mode of the cantilever coated with silica and of the uncoated control sample.

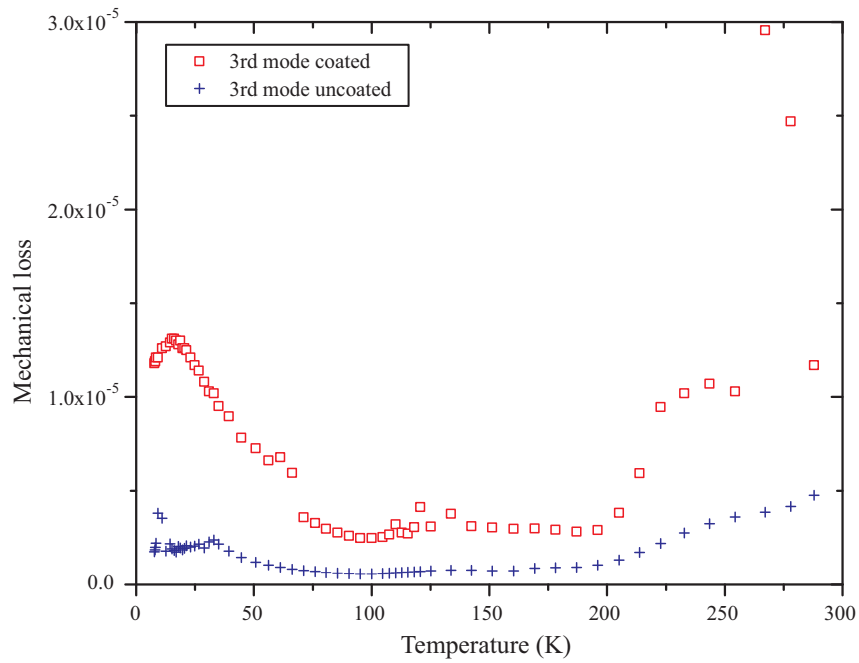


Figure 6.5: Plot of the measured loss for the third mode of the cantilever coated with silica and of the uncoated control sample.

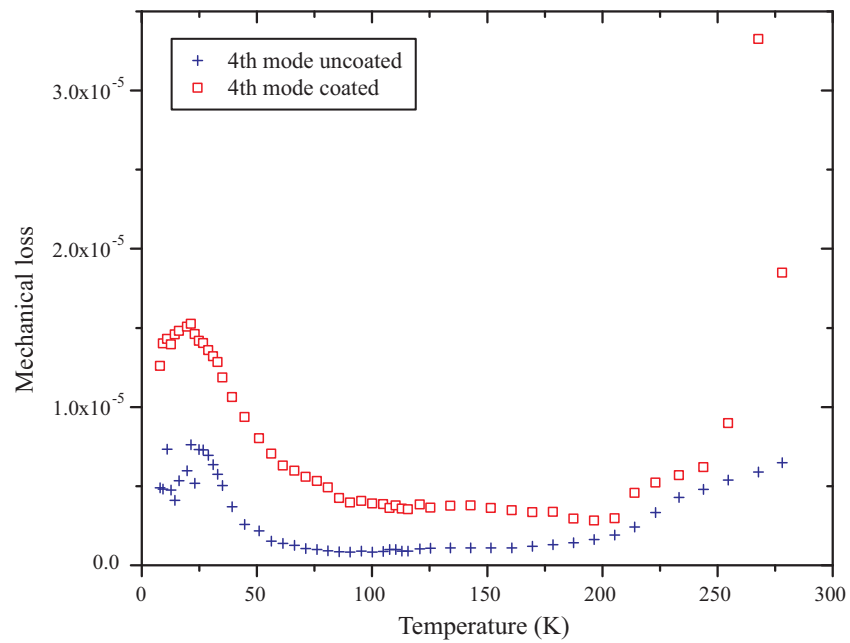


Figure 6.6: Plot of the measured loss for the fourth mode of the cantilever coated with silica and of the uncoated control sample.

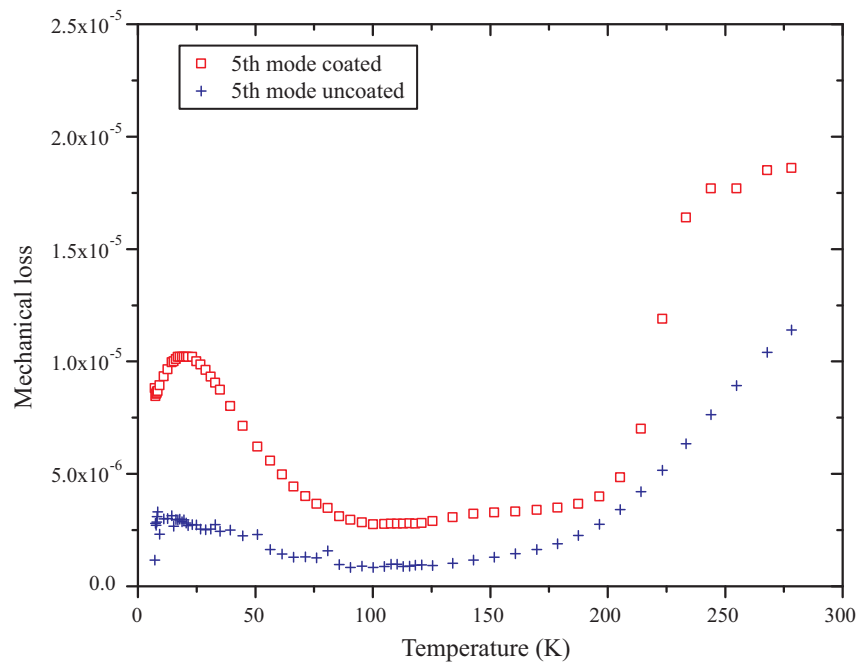


Figure 6.7: Plot of the measured loss for the fifth mode of the cantilever coated with silica and of the uncoated control sample.

Limited data were obtained for the first mode above 175 K, as clean ringdowns were difficult to obtain, possibly due to low frequency background noise. At temperatures above 200 K the dissipation of each mode rises rapidly, with broad peak or plateau structures apparent for all of the modes studied. The data for the second and third modes show a broad peak centred on ~ 235 K and a narrower, higher peak at ~ 270 K. Immediately above 200 K, the dissipation of the fourth mode follows the trend of the uncoated sample more closely with no peak at 235 K, but does show evidence of the higher peak at ~ 270 K. The data for the fifth mode show a steep increase in loss between 200 and 240 K. However, the loss does not peak, but continues to increase, less steeply, towards room temperature.

The very high losses measured for three of the modes at temperatures around ~ 270 K may be indicative of energy coupling into modes of the clamp. However, it seems unlikely that this type of clamping loss would have such a similar effect on three modes separated widely in frequency. It is possible that the cantilever was clamped such that a degree of frictional stick-slip loss was present close to room temperature. Thermal contraction of the clamp could eliminate this effect at lower temperatures: certainly the measured loss is generally smooth below 200 K. It is possible that the broad peaks observed between 200 and 240 K are intrinsic to the coating, although the absence of this structure in the data for the fourth mode would weigh against this possibility.

Loss of the uncoated cantilever

A small peak, centred on 20 - 25 K, was observed in the dissipation of the uncoated cantilever. It is possible that this peak arises from the 20-30 nm thick thermal oxide layer grown on the cantilevers by the coating vendor. Measurements of a 500 nm thick thermal oxide layer on a silicon substrate at 5 kHz by White and Pohl [244] have shown a dissipation peak at 35 K, a somewhat

higher temperature than the peak observed in the dissipation of the uncoated cantilever (see Section 6.5). However, in addition to being more than a factor of 10 thicker, the thermal oxide layer measured by White and Pohl was grown using a wet oxidation process, whereas the cantilevers studied by the author underwent a dry oxidation process. Given these differences, it may be possible that the peak at 25 K is related to the dissipation peak of the oxide layer. Further investigation of the loss of thermal oxide layers on silicon cantilevers at cryogenic and ultra-cryogenic temperatures is planned, in collaboration with the INFN laboratory at Legnaro, Italy. However, the peak should not affect the calculated coating loss, as the effects of the peak would be expected to be present in the dissipation of both the coated and uncoated cantilevers and thus will be removed when the losses are subtracted.

6.4 Coating loss

The dissipation of the silica coating was calculated using Equation 6.5. For the level of loss measured in the silica coating the thermoelastic correction term had an almost negligible effect. The coating thermoelastic loss was calculated to increase with temperature and frequency. For the highest frequency mode studied (the fifth mode at ~ 3300 Hz) at room temperature, the thermoelastic correction was found to reduce the coating loss by $\sim 1.3\%$. As expected, the effect decreased at low temperatures, falling to a reduction of $\sim 0.015\%$ at 100 K and $\sim 0.003\%$ at 20 K. While the thermoelastic correction had an insignificant effect on the results presented here, it is likely to be important for the correct interpretation of loss measurements of thicker coatings, or measurements carried out at higher frequencies.

The coating loss results for each of the modes of the cantilever are shown in Figures 6.8 to 6.12. The loss of the silica film has quite a complex shape and follows a similar trend below 225 K for each of the cantilever modes studied. Generally, between 225 K and 190 K the dissipation of the film drops sharply

to a minimum, before rising slightly to a low and broad peak centred on 150 K. A second minima or an inflection point is reached at approximately 100 to 110 K. Below this temperature the loss rises steadily to a peak at approximately 17 K.

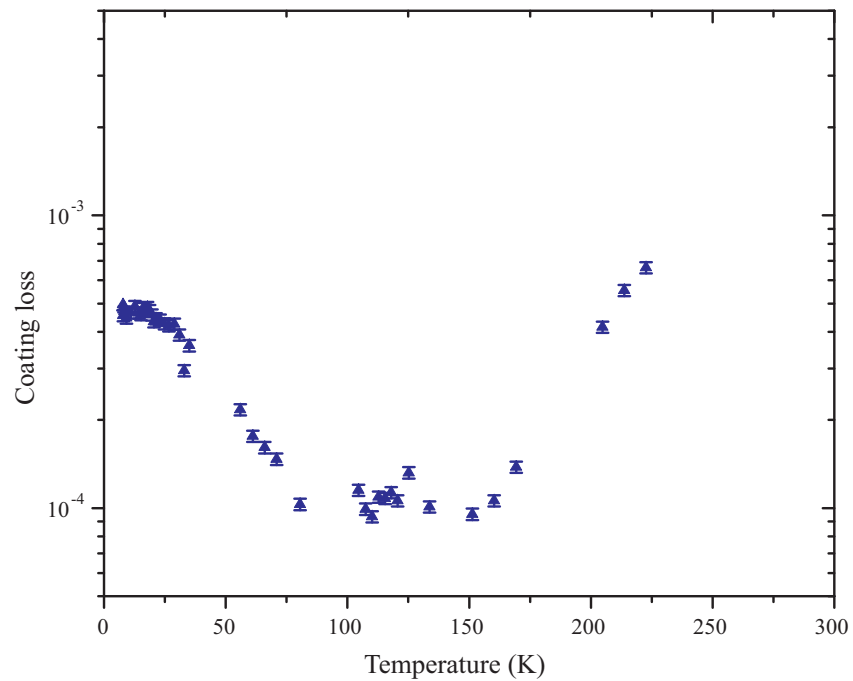


Figure 6.8: *Calculated dissipation of the silica coating for the first mode at 59 Hz.*

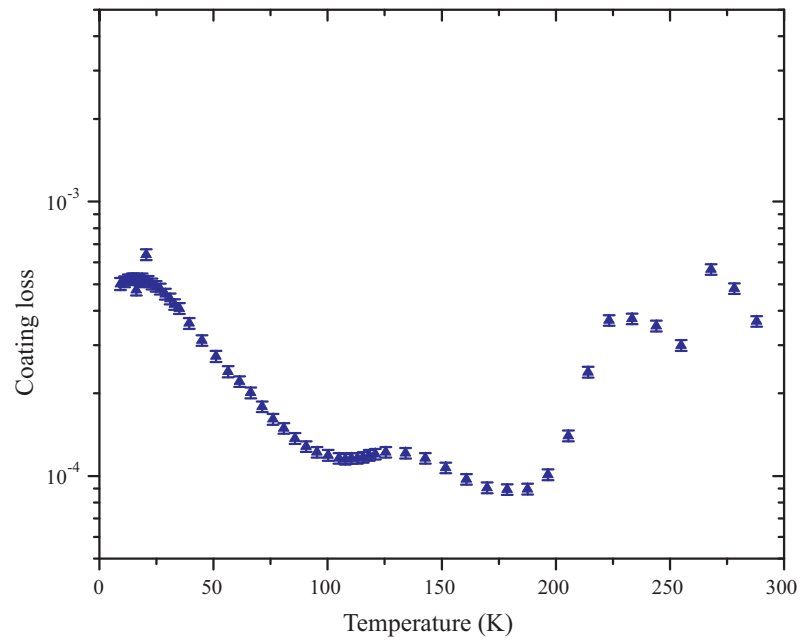


Figure 6.9: *Calculated dissipation of the silica coating for the second mode at 355 Hz.*

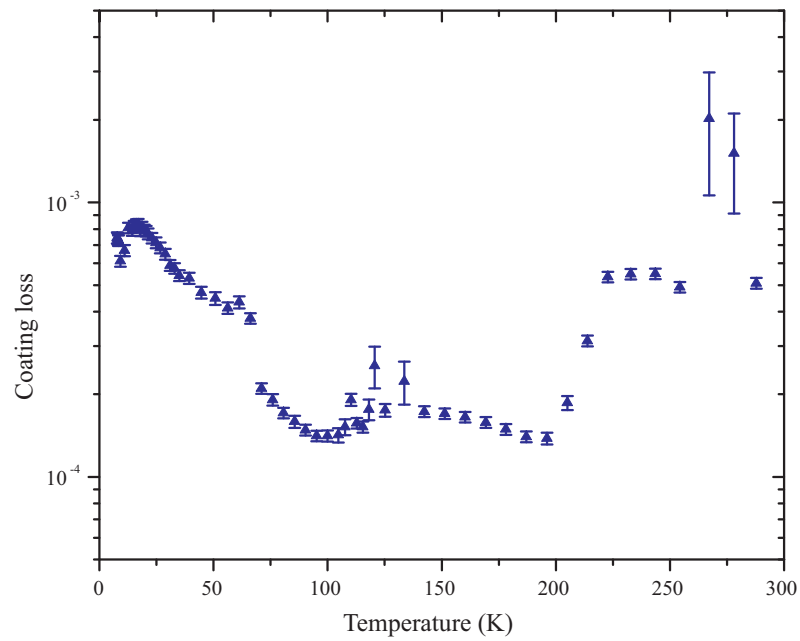


Figure 6.10: *Calculated dissipation of the silica coating for the third mode at 995 Hz.*

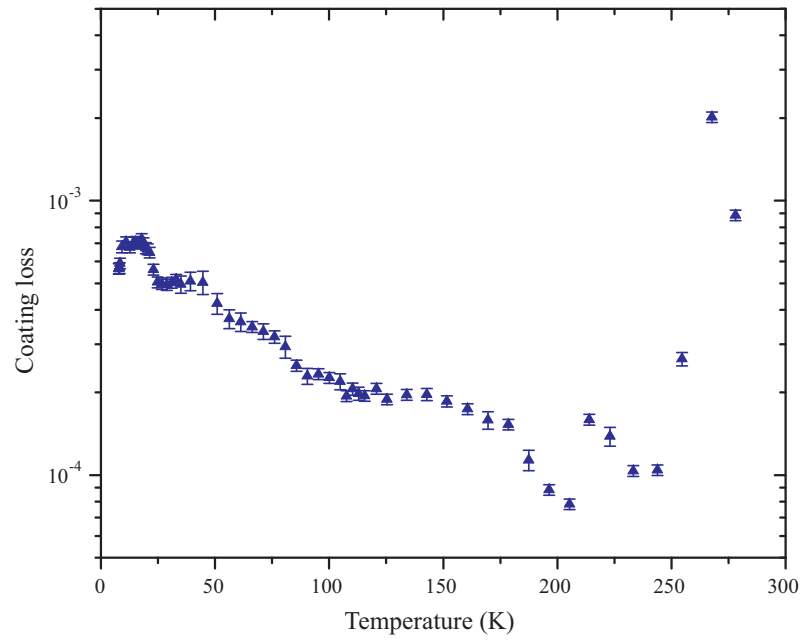


Figure 6.11: *Calculated dissipation of the silica coating for the fourth mode at 1920 Hz.*

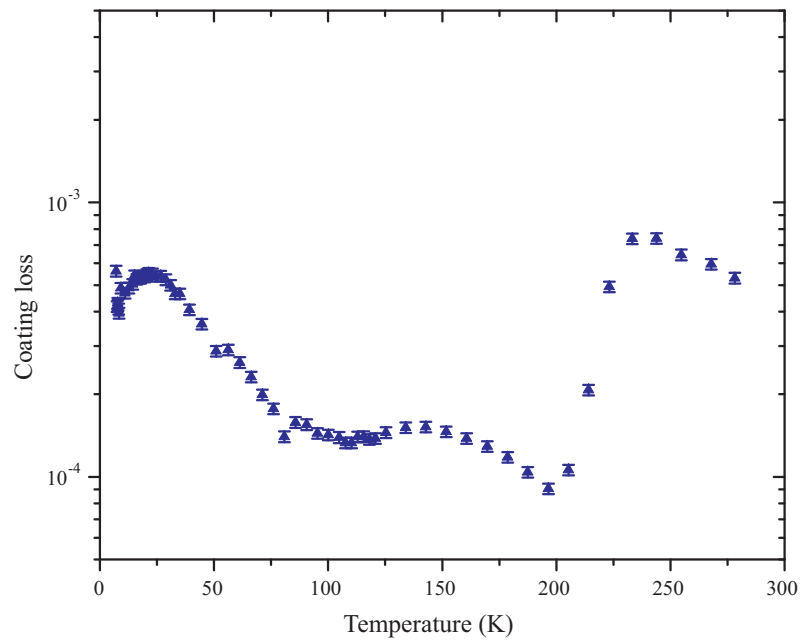


Figure 6.12: *Calculated dissipation of the silica coating for the fifth mode at 3175 Hz.*

6.4.1 Dissipation peak analysis

The method described in Section 5.5 was used to construct an Arrhenius plot for the low temperature dissipation peak at ~ 17 K, shown in Figure 6.13. As shown on this graph, there is a reasonable linear relationship ($R^2 = 0.93$) between $\ln(\omega)$ and $1/T_{\text{peak}}$ for the first, second, third and fourth bending modes. However the data for the fifth mode at ~ 3175 Hz did not fit this trend. If the fifth mode is neglected, the data for the remaining four modes can be used to calculate an activation energy associated with the dissipation peak of 54.4 ± 5.5 meV. This is somewhat higher than the activation energy of 44 meV measured in bulk silica by Anderson and Bommel [172].

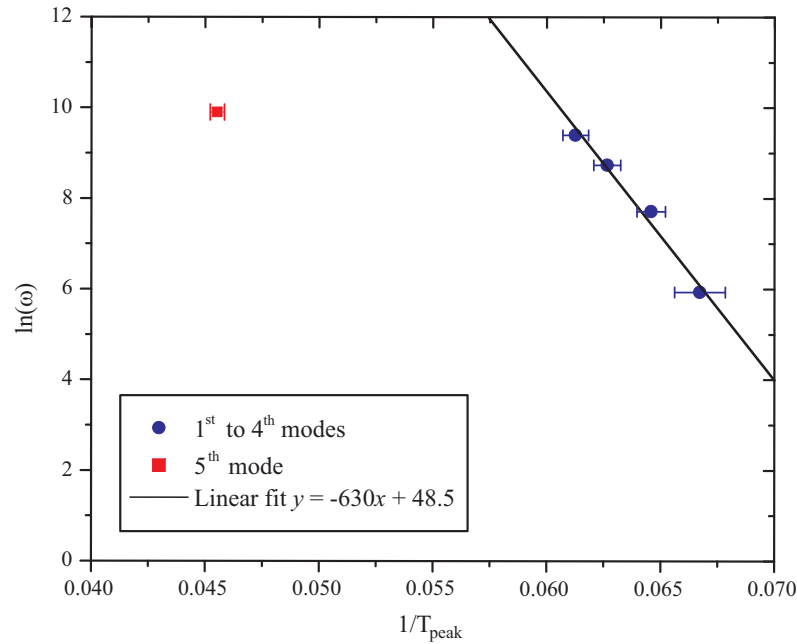


Figure 6.13: *Arrhenius plot for the low temperature dissipation peak in the silica coating.*

The coating loss for the fifth mode was observed to peak at 21.9 K, approximately 5.5 K higher than predicted by the linear fit for the other four modes. It is possible that this discrepancy is related to the effect of the loss of the uncoated cantilever on the calculated coating loss. The small peak in the loss of the uncoated cantilever centred on 20 to 25 K, which is present in the

data for the first four modes, is not clearly observed in the data for the fifth mode, possibly due to the effect of clamping loss. For each of the other modes, on subtraction of the loss of the uncoated sample from the loss of the coated sample, the temperature at which the peak occurred was found to decrease by up to 2 K. This is due to the effect of the small peak in the loss of the uncoated cantilever. In contrast, on calculation of the coating loss for the fifth mode the temperature at which the peak occurred increased by approximately 2 K.

Further measurements of the fifth mode of both the coated and uncoated cantilevers are required to fully investigate this anomalous point. Study of the dissipation of higher order modes would also be of interest to investigate if the linear trend for the first four modes in the Arrhenius plot continues at higher frequency. However, measurements of the sixth (and higher frequency) bending modes of the coated cantilever proved difficult due to very short ring-down times.

6.4.2 Silica coating loss above 200 K

Recent measurements of the loss of a 1 μm thick silica coating (deposited by CSIRO [242]) on a silica substrate carried out by Penn [246] suggest that at room temperature the loss may be as low as 1 to 3×10^{-5} at ≈ 3 -4 kHz. This is approximately an order of magnitude lower than the room temperature losses presented in this chapter at similar frequencies, and approximately a factor of 3 lower than the losses measured at 355 Hz and 1 kHz. This difference may be related to the possible clamping loss peaks in the measurements of the coated cantilever which were noted above. To investigate further, the cantilever was re-clamped and the measurements repeated at room temperature. The losses were found to be substantially lower than the previous results. For example, the new measurement of the loss factor of the third mode at 290 K was 6.4×10^{-6} , which is a factor of 1.9 lower than the previous measurement of 1.2×10^{-5} . The calculated coating losses were also correspondingly lower. Figure 6.14 shows

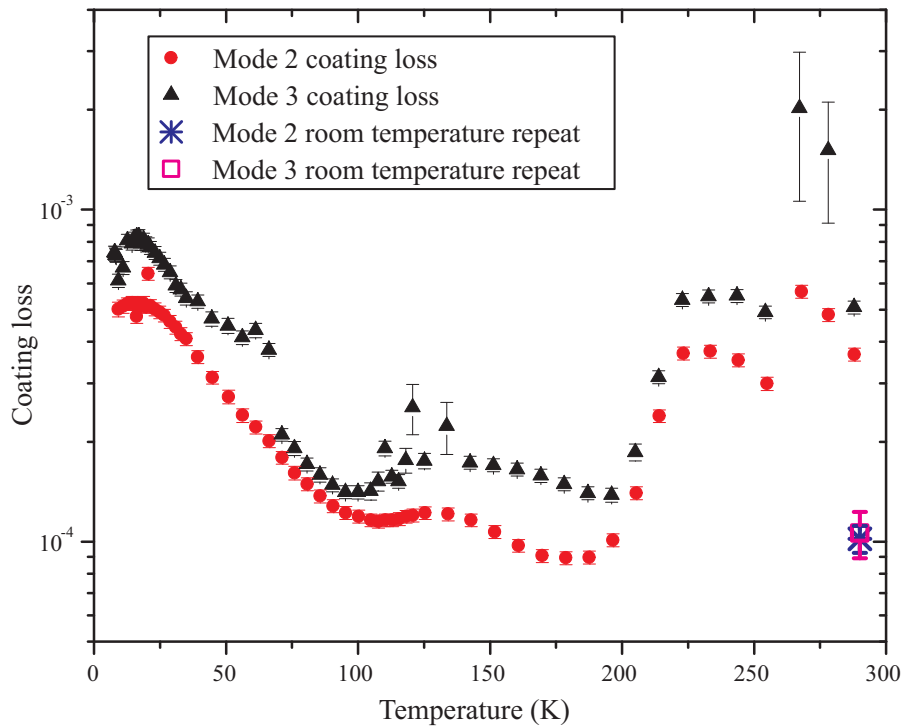


Figure 6.14: *Plot comparing the initial measurements of the temperature dependence of the coating loss with the measurements repeated at room temperature.*

both the original temperature dependent coating loss and the repeated room temperature measurements for the second and third modes. The new coating loss factor at 290 K was found to be $(1.0 \pm 0.1) \times 10^{-4}$ for the second mode, $(1.1 \pm 0.2) \times 10^{-4}$ for the third mode and $(2.3 \pm 0.2) \times 10^{-4}$ for the third mode (see Table 6.2). These values are lower than the previous values measured in Jena by factors of ~ 2 , ~ 4.8 and ~ 3.9 respectively. The repeated measurements of the fifth mode yielded the same loss as originally measured, and the coating loss for this mode remained unchanged at $(5.4 \pm 0.3) \times 10^{-4}$.

It seems likely therefore that the high losses initially measured above 200 K were indeed related to the clamp.

The repeated measurements of the coating loss factors are compared to Penn's data and to the silica coating loss factors presented in Chapter 4 (for a 500 nm thick SiO_2 coating on a silica cantilever substrate) in Figure 6.15. Between 2 kHz and 4 kHz, the coating loss measured using the silicon can-

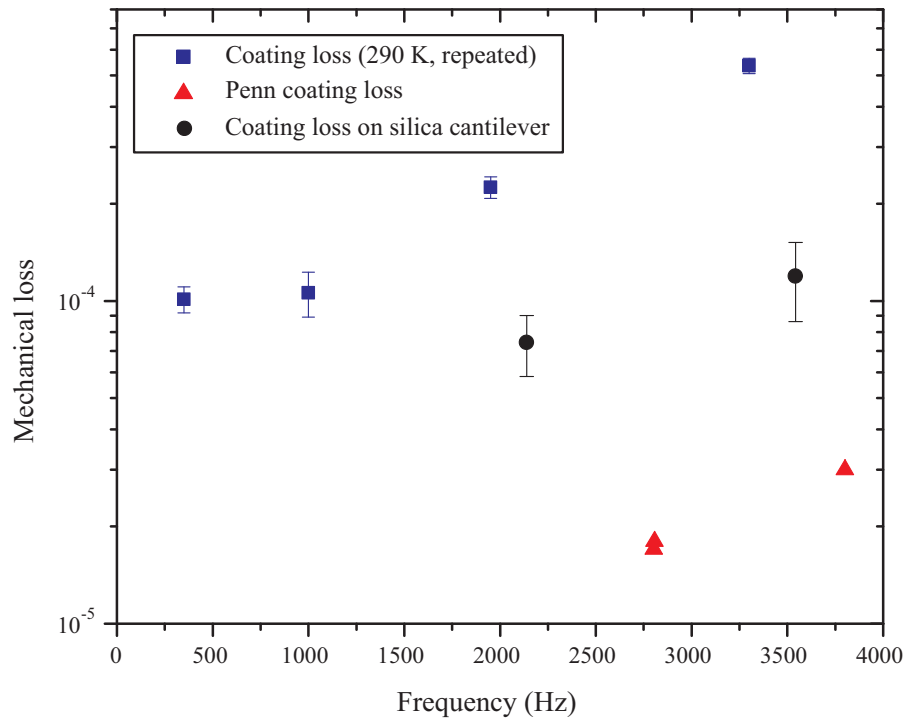


Figure 6.15: *Plot of the repeated room temperature measurements of the coating loss. Also shown is Penn's coating loss data, measured at room temperature using silica substrates [246].*

Mode	Coating loss	Thermoelastic correction
355 Hz	$(1.0 \pm 0.1) \times 10^{-4}$	2.1×10^{-6}
989 Hz	$(1.1 \pm 0.2) \times 10^{-4}$	3.8×10^{-6}
1920 Hz	$(2.3 \pm 0.2) \times 10^{-4}$	4.8×10^{-6}
3175 Hz	$(5.4 \pm 0.3) \times 10^{-4}$	6.9×10^{-6}

Table 6.2: *The coating loss factors for each mode at room temperature, calculated using the data from the repeated loss measurements of the coated cantilever. Also shown is the calculated thermoelastic coating loss for each mode frequency.*

tilever substrate is significantly higher than the loss measured using the silica cantilever substrate, which in turn is 3 to 4 times higher than the coating loss measured by Penn.

There are several possible explanations of these differences. The coatings

were supplied by different vendors (Penn's coating was produced by CSIRO [242], while the coatings studied by the author were supplied by LMA [215]) so it is possible that the differences in the mechanical loss are related to variations in the coating material or in the deposition process. Penn's coating was approximately twice as thick as the coatings applied to the cantilevers, so a dependence of the loss on the thickness of the coating could also explain the differences in the results.

The coated silicon cantilever is likely to have a higher level of internal stress than the other two samples, due to the differences in the material properties of the coating and substrate. It is possible that this could increase the mechanical loss of the coated cantilever, resulting in an artificially high coating loss.

Another possibility is that the coating thermoelastic loss for the silicon cantilever coated with silica is higher than was calculated. As noted previously, the magnitude of the calculated thermoelastic loss is very sensitive to the material properties used. Thus if the properties of the ion-beam sputtered silica film differ from those of bulk silica, it is possible that the coating thermoelastic loss correction could be more significant than shown in Table 6.2, reducing the calculated intrinsic loss of the coating.

Further study of the dependence of the dissipation of silica coatings on coating thickness and substrate material is clearly desirable to enable these results to be fully explained.

6.5 Discussion - low temperature loss in silica

The dissipation in bulk pieces of silica has been extensively studied as a function of temperature and a dissipation peak centred on approximately 40 to 60 K has been well characterised by many authors [93, 172, 222, 239]. White and Pohl have studied the dissipation of silica coatings deposited by electron beam evaporation and by thermal oxidation of silicon substrates [244]. This experiment used a silicon double paddle oscillator vibrating at 5.5 kHz to measure the

loss of several thicknesses of e-beam films, and a 500 nm thick thermal oxide layer, between 10^{-2} K and 100 K. The loss of the thermal silica was found to closely resemble that observed in bulk silica samples, with a dissipation peak at 35 K. However, no evidence of a similar dissipation peak was observed in the e-beam coatings. For coatings under 10 nm thick the loss was essentially constant below 20 K. At approximately 5 K, the loss of bulk, thermal and the thin (under 10 nm) e-beam coatings was found to be almost identical, lying between 3×10^{-4} and 4×10^{-4} . Thicker e-beam coatings were found to have a significantly higher loss throughout the temperature range studied, with the loss increasing rapidly above 10 K, perhaps towards a peak at a temperature above 100 K.

These results suggest that thicker e-beam coatings might have a different

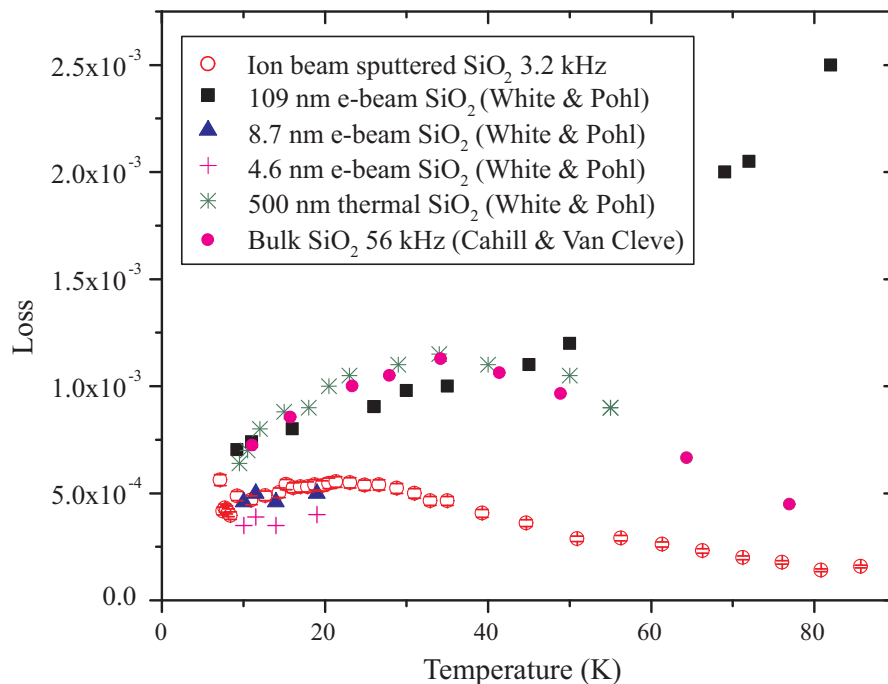


Figure 6.16: A comparison of the dissipation measured for the ion-beam sputtered silica coating at 3.3 kHz with the loss at 5.5 kHz of silica coatings grown by wet thermal oxidation and electron beam evaporation (from White and Pohl [244]) and with the loss of bulk silica at 56 kHz (from Cahill and Van Cleve [239].)

structure, and thus a different dissipation mechanism, than the e-beam films less than 10 nm in thickness. White and Pohl suggest that macroscopic disorder, possibly related to porosity, in the thicker films may be related to the higher losses and different temperature behaviour observed [247].

The mechanical loss of the ion-beam sputtered silica coating studied here, also shown in Figure 6.16, can be seen to have significantly lower loss than the same thickness (500 nm) of thermal oxide measured by White and Pohl at a similar frequency. Furthermore, the peak loss in the ion-beam sputtered coating occurs at a lower temperature - about 21 K - than the peak observed in bulk silica and thermal oxide. Below 25 K, the loss of the ion-beam sputtered coating is very close to the loss of the thinnest (less than 10 nm thick) e-beam coatings, while the loss of the 100 nm thick e-beam coating is almost an order of magnitude higher.

While more work is required, particularly to measure the dependence of the mechanical dissipation on coating thickness for ion-beam sputtered silica, this comparison suggests that both thickness and coating deposition method can have a very significant effect on the low temperature loss in silica coatings. The results also indicate that ion-beam sputtered coatings appear to have significantly lower loss than similar thicknesses of e-beam coatings. It is known that ion-beam sputtered coatings tend to be more dense and have better stoichiometry than e-beam deposited films [204], and it is possible that the different losses are related to structural differences associated with the deposition method.

6.6 Multi-layer coating loss calculation

If it is assumed that the loss of ion-beam sputtered silica and tantalum are independent of the coating thickness, the experimental results from this chapter and Chapter 5 can be used to calculate the expected loss in a multi-layer $\text{SiO}_2/\text{Ta}_2\text{O}_5$ coating. This calculated loss is compared with measurements of

a multi-layer coating on a sapphire disk by Yamamoto et al [226].

6.6.1 The mechanical loss of a multi-layer coating

For a multi-layer coating the loss ϕ , Young's modulus Y and thickness t are related to the properties of the individual component materials as follows [197]:

$$Y_{\text{coating}} t_{\text{coating}} \phi_{\text{coating}} = Y_{\text{SiO}_2} t_{\text{SiO}_2} \phi_{\text{SiO}_2} + Y_{\text{Ta}_2\text{O}_5} t_{\text{Ta}_2\text{O}_5} \phi_{\text{Ta}_2\text{O}_5}, \quad (6.6)$$

where t_{SiO_2} and $t_{\text{Ta}_2\text{O}_5}$ are the total thickness of silica and tantalum present in the coating. Hence the loss of a multi-layer coating is related to the individual losses of its constituent materials as follows:

$$\phi_{\text{coating}} = \frac{Y_{\text{SiO}_2} t_{\text{SiO}_2} \phi_{\text{SiO}_2} + Y_{\text{Ta}_2\text{O}_5} t_{\text{Ta}_2\text{O}_5} \phi_{\text{Ta}_2\text{O}_5}}{Y_{\text{coating}} t_{\text{coating}}}. \quad (6.7)$$

It can be shown from composite materials theory that the effective Young's modulus in an isotropic multi-layer coating consisting of two materials is given by [248]:

$$Y_{\text{coating}} = \frac{Y_1 t_1 + Y_2 t_2}{t_1 + t_2}, \quad (6.8)$$

where the subscripts '1' and '2' refer to properties of the different materials. The optical thickness, $\delta = nt$ (see Section 4.4.1), of each layer of silica and tantalum is 266 nm (i.e. $\lambda/4$ for a wavelength of 1064 nm), where the refractive indices are $n_{\text{silica}} = 1.45$ and $n_{\text{tantalum}} = 2.03$ [131]. Thus the physical layer thickness can be calculated to be ~ 180 nm and ~ 130 nm for silica and tantalum respectively.

If it is assumed that the loss of the coating materials is independent of the coating thickness, Equation 6.7 can be used to calculate the loss in a multi-layer coating from the measured losses of the individual coating materials.

The measured dissipation for the undoped tantalum coating (see Section 5.6) and the silica coating at 1 kHz was used to calculate the expected loss in a 31 layer silica / tantalum coating (with the same reflectivity as the coating measured by Yamamoto et al). The single layer coating loss data used are

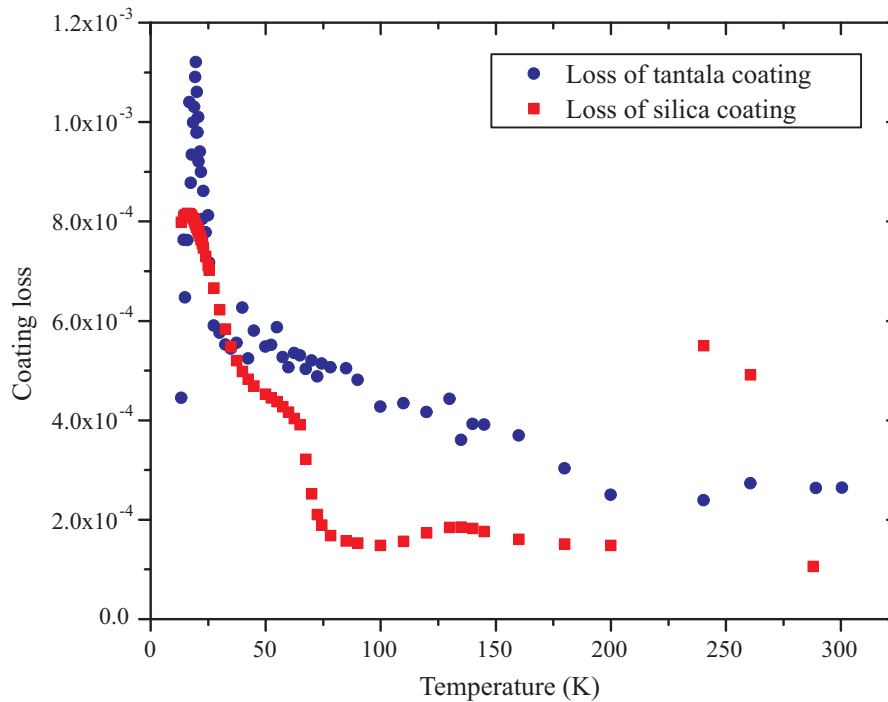


Figure 6.17: *The measured coating loss for the silica and tantala coatings at ~ 1 kHz which was used in the multi-layer coating loss calculation.*

shown in Figure 6.17. Figure 6.18 compares the predicted loss in a multi-layer coating calculated using Equation 6.7 with the loss measured in three multi-layer coatings by Yamamoto et al at approximately the same frequency. Two of the multi-layer coatings were not heat treated and these display higher losses at room temperature than the third coating, which was heat treated at several hundred $^{\circ}$ C. The exact temperature of the heat treatment is not known [249]. Close to room temperature, the multi-layer loss calculated from the single layer results presented here is very similar to the loss measured by Yamamoto for the heat treated coating.

At low temperature, the calculated multi-layer loss is dominated by the dissipation peak observed in Ta_2O_5 . This peak does not appear to be present in Yamamoto's experimental results. While there are not enough data points from Yamamoto's work to allow a full comparison, it can be seen that the calculated peak loss at approximately 20 K is almost a factor of two higher than the

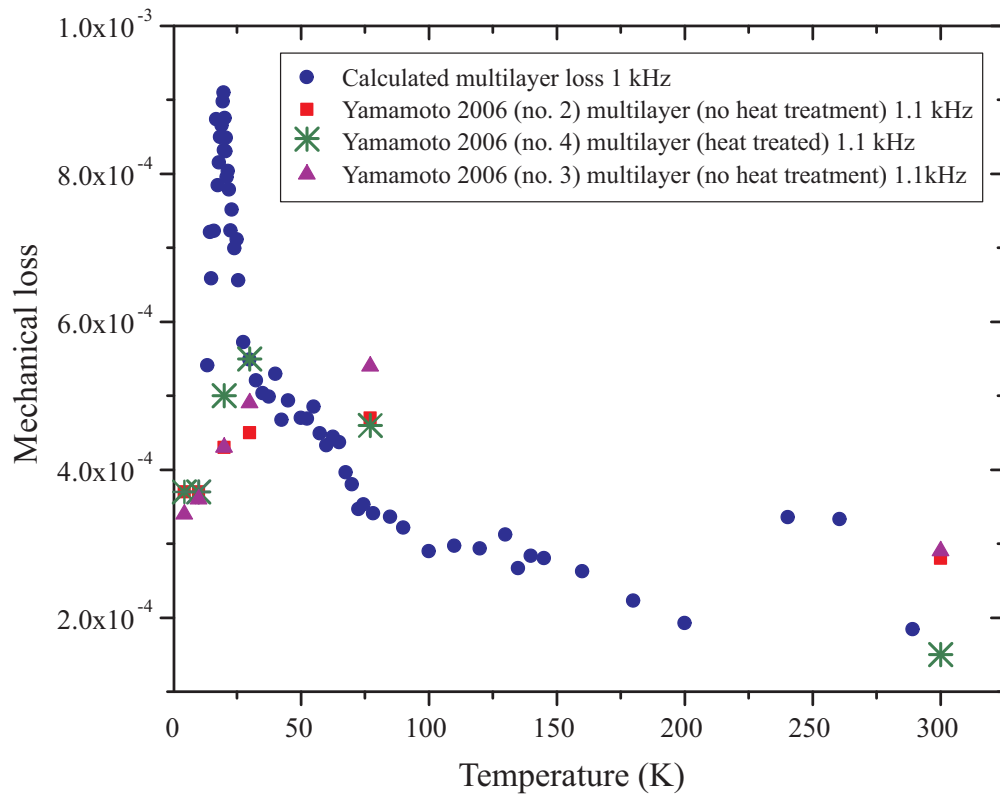


Figure 6.18: *The expected loss in a 31 layer $\text{SiO}_2\text{Ta}_2\text{O}_5$ coating, calculated from the single layer results, compared with the loss measured in such a multi-layer coating by Yamamoto et al [226]*

loss measured by Yamamoto in the heat treated coating at this temperature. However, the experimental multi-layer data do show some evidence of a peak in the dissipation at higher temperatures, with the peak occurring at a lower temperature in the heat treated coating.

The calculated multi-layer coating loss around 250 K is significantly higher than expected from the general trend of the data. These high loss values are a result of the high losses measured in the silica coating at these temperatures, which are likely to be due to clamping loss effects and therefore not intrinsic to the coating material.

6.6.2 Coating thermoelastic loss

It has been shown that, at the frequencies of interest, the coating thermoelastic loss at room temperature in a 500 nm silica or tantala coating on a silicon substrate does not have a significant contribution to the measured coating loss. Further, the coating thermoelastic loss of the silica sample has been shown to be negligible at all temperatures between 10 and 300 K. This calculation could not be carried out for tantala as the temperature dependence of the relevant material properties could not be found in the literature. However, at room temperature the coating thermoelastic loss of the cantilever coated with tantala is approximately two orders of magnitude lower than that of the silica coating sample, and it is therefore unlikely that it will become significant at low temperature.

However, Fejer et al [142] have shown that, at room temperature, the coating thermoelastic loss arising from a silica/tantala multilayer coating applied to a sapphire substrate may be of the same order as the intrinsic loss of the coating materials. As the coatings studied by Yamamoto had sapphire substrates, it is of interest to calculate and correct for the expected level of thermoelastic loss in these samples.

The coating thermoelastic loss of a multilayer coating can be calculated using a form of Equation 6.1, adapted to be applicable to a multilayer coating consisting of alternating layers of two materials, where a suitable volume averaging operator (Equation 2.56) is applied to obtain the average material properties of the multilayer [141, 142].

The thermoelastic contribution to the coating loss measured by Yamamoto at room temperature was calculated using the material properties of silica and tantala given in Table 6.1 and the properties of sapphire given in Table 6.3.

To allow an estimate of the thermoelastic loss at low temperatures to be made, the properties of tantala were approximated by those of sapphire, for which the required temperature dependent properties were obtained from

Coefficient of thermal linear expansion	$5.4 \times 10^{-6} \text{ K}^{-1}$
Young's modulus	$4 \times 10^{11} \text{ Nm}^{-2}$
Specific heat capacity	$777 \text{ Jkg}^{-1}\text{K}^{-1}$
Thermal conductivity	$33 \text{ Wm}^{-1}\text{K}^{-1}$
Poisson's ratio	0.23
Density	3980 kgm^{-3}

Table 6.3: *Material properties of sapphire used to calculate coating thermoelastic loss [142].*

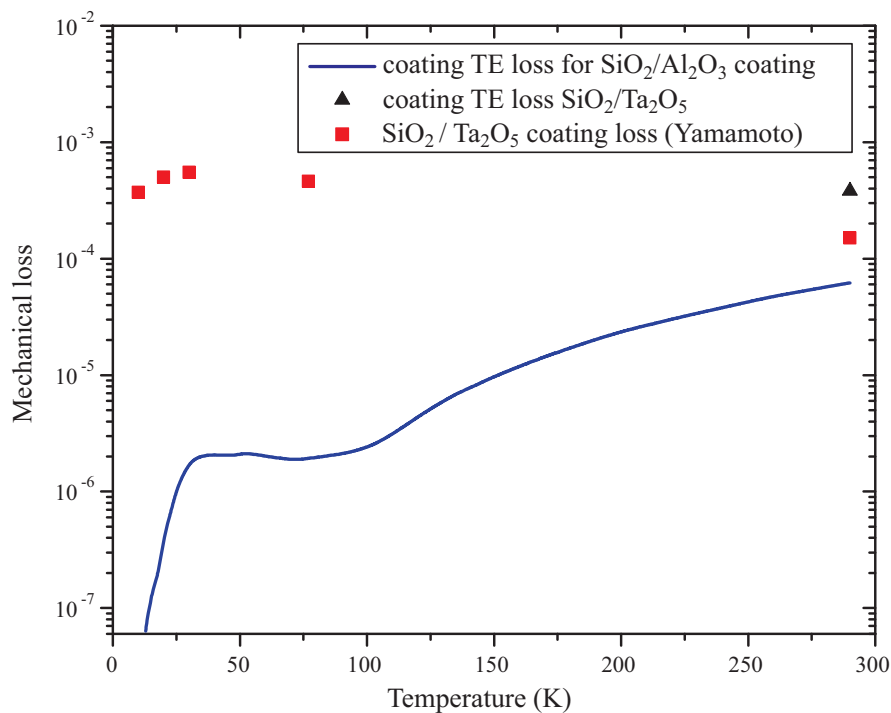


Figure 6.19: *Plot showing Yamamoto's coating loss measurements at 1.1 kHz [226] and the calculated coating thermoelastic loss in (i) a 31 layer $\text{SiO}_2/\text{Ta}_2\text{O}_5$ coating on a sapphire substrate at room temperature and (ii) a $\text{SiO}_2/\text{Al}_2\text{O}_3$ coating on a sapphire substrate as a function of temperature.*

Touloukian [228]. The density, Poisson's ratio and Young's modulus were assumed not to vary significantly with temperature.

The calculated coating thermoelastic loss is shown in Figure 6.19, alongside Yamamoto's measured coating loss factors. At room temperature, the

thermoelastic loss calculated for the silica/tantala coating on sapphire is 3.8×10^{-4} , more than twice as high as the coating loss measured by Yamamoto. This implies that the residual intrinsic loss of the coating, $\phi_{\text{coating intrinsic}} = \phi_{\text{coating}} - \phi_{\text{coating thermoelastic}}$, is negative, which is not a physically possible result. This implies that the material properties of the actual coating and substrate may differ from the properties used in the calculation.

When the properties of tantala are approximated by those of sapphire, the calculated coating thermoelastic loss at room temperature is approximately 50 % lower than the measured coating loss, resulting in a residual coating loss of 8.8×10^{-5} . While this is a substantial correction at room temperature, it can be seen that below 100 K the calculated coating thermoelastic loss is more than two orders of magnitude lower than the measured coating loss factors. For this approximation, the thermoelastic correction at low temperature is therefore negligible.

It is clearly of significant interest to measure the temperature dependence of α , k and C for ion-beam sputtered tantala and silica films to allow more accurate calculation of the coating thermoelastic loss.

6.6.3 Discussion

There are several possible explanations for the differences between the results. It is possible that systematic experimental factors such as variations in the coating materials from different vendors or thermometry errors between different experiments could result in the measured dissipation peaking at different temperatures. The multi-layer data of Yamamoto are not inconsistent with there being a narrow dissipation peak located between 20 and 30 K. The individual layers of silica and tantala studied in this thesis were 500 nm thick, whereas in a standard multi-layer coating the layers of silica and tantala are approximately 180 nm and 130 nm thick respectively. The difference in coating thickness, and therefore in surface to volume ratio, may also result in a

difference in the mechanical loss. It is also possible that differences in the temperature at which the coatings were heat treated could result in the loss peaking at a different temperature.

An alternative explanation is that a single layer of coating material does not display the same dissipation properties as a layer of the same material as part of a multi-layer stack. It has been shown that the coating layer interfaces are not a significant source of dissipation [130]. However, the stress exerted on each layer of a multi-layer coating may be significantly different to the internal stress in a single layer of silica or tantala, possibly resulting in differing levels of dissipation.

Further work is required to understand if the loss in a multi-layer coating can be accurately modelled from measurements of the losses of single layers of the individual materials. In addition it would be very interesting to repeat the multi-layer coating loss measurements in significantly more detail.

6.7 Conclusion

The temperature dependence of the dissipation in a silica coating applied by ion-beam sputtering to a silicon cantilever has been measured. The results show that the dissipation decreases to two broad minima centred on approximately 180 K and 115 K, separated by a small and broad peak at approximately 140 K. Below 100 K the dissipation increases to a peak at between 16 K and 20 K. This activation energy of the dissipation mechanism responsible for this peak was calculated to be 54.4 ± 5.5 meV using the data from the first four bending modes. However, the data from the fifth bending mode did not lie on the same line on the Arrhenius plot as the other modes. The most likely explanation is that the calculated coating loss was ‘contaminated’ by clamping loss effects in the data for the uncoated control sample, altering the temperature at which the coating loss appeared to peak. This requires further investigation.

Broad peaks in the loss of the coated cantilever close to room temperature

and around 225 K were observed and the coating loss calculated at room temperature was significantly higher than expected. Repeated measurements at room temperature yielded a lower loss, and it seems likely that the original losses measured above 200 K were artificially high due to clamping effects. However, the loss factors measured at room temperature were still up to an order of magnitude higher than Penn's results for an ion-beam sputtered silica coating on a silica substrate.

The single layer coating loss results for silica and tantalum have been used to calculate the expected loss in a multi-layer coating of the type measured by Yamamoto et al. The calculated multi-layer coating loss peaks at ~ 20 K, with a maximum loss of $\sim 9.2 \times 10^{-4}$. This is almost a factor of 2 higher than the multi-layer coating loss of $\sim 5 \times 10^{-4}$ measured at 20 K by Yamamoto. Further comparison is difficult due to the limited experimental data for the multi-layer coating. However, Yamamoto's data are not inconsistent with the presence of a similar dissipation peak between 20 and 30 K. Further investigations of the temperature dependence of the dissipation in multi-layer coatings, and its relationship to the dissipation of the individual coating materials, is clearly of great interest.

Chapter 7

Conclusions

The first generation of long baseline interferometric gravitational wave detectors have reached their design sensitivities and acquired data for extended periods of time. Data analysis from the various science runs has allowed constraints to be placed on astrophysical models of sources of gravitational radiation. The adoption of the silica suspension technology and signal recycling techniques pioneered in the GEO 600 detector by the longer baseline LIGO and VIRGO detectors, alongside an increase in the circulating light power, will allow the sensitivity of these instruments to be increased by approximately a factor of ten. It is widely expected that these second generation detectors will make the first direct detection of gravitational waves.

Investigations into some aspects of the materials and processes which may be used in future gravitational wave detectors have been presented in this thesis. In particular, much of the research was aimed at understanding the mechanical dissipation associated with the dielectric mirror coatings, allowing reduction of the coating thermal noise in future detectors.

Studies of hydroxide catalysis bonding have shown that the bond settling time can be increased by carrying out the bonding procedure at 0°C. This result may be of use in future space missions, such as LISA, to allow more time for the alignment of bonded components on an optical bench. The settling time data allowed calculation of the activation energy of the chain of chemical

reactions involved in the bond formation. Similar studies may be useful to allow comparison of the chemistry of hydroxide catalysis bonds between oxidised silicon surfaces, which may be required in third generation gravitational wave detectors.

Brownian thermal noise arising from the reflective mirror coatings is likely to limit the sensitivity of the next generation gravitational wave detectors in their most sensitive frequency band. The magnitude of the coating thermal noise is related to the mechanical dissipation factor of the coating materials. It is thus important to determine the exact level of dissipation expected from specific coatings, to understand the mechanism responsible for the dissipation and to find methods of reducing it.

A method of measuring the dissipation in various coating materials at room temperature using silica cantilever substrates has been developed. It has been shown that a silica ribbon welded to a thicker silica clamping block can provide isolation from the clamping structure, reducing excess energy loss into the clamp. Silica cantilevers have been used to measure the mechanical loss of tin oxide coatings deposited by spray pyrolysis. It has been shown that tin oxide coatings applied by spray pyrolysis with a maximum thickness of 4 - 8 nm would meet the thermal noise requirements for second generation detectors. Preliminary measurements of the dissipation in single layers of ion-beam sputtered silica and tantala, the materials used in the reflective coatings, have been carried out at room temperature. The results suggest that altering a particular (undisclosed) deposition parameter can reduce the dissipation in tantala coating layers doped with 14.5 % TiO_2 by 40 to 50%.

Silicon cantilevers, which have a low mechanical loss at cryogenic temperatures in comparison to silica, have been used to measure the temperature dependence of the dissipation in 500 nm thick films of silica and tantala. Studies of single layers of tantala, heat treated at the same temperature as the standard multi-layer coatings, have shown the presence of a dissipation peak

at approximately 20 K. Analysis of this peak has provided the first evidence of the nature of the mechanical dissipation mechanism in this material, suggesting that it may be analogous to the double-well potential loss mechanism observed in fused silica, with the loss arising when molecules cross energy barriers whilst undergoing changes in configuration. The width of the dissipation peak is indicative of a broad distribution of energy barrier heights. Doping tantala with titania to a level of 14.5 % cation concentration has been shown to reduce the magnitude of dissipation at the peak, and to increase the average activation energy by $\sim 33\%$.

Initial studies suggest that the form of the low temperature dissipation in ion-beam sputtered tantala is strongly related to the temperature at which the post-deposition heat treatment is carried out. Measurements of a coating heat treated at 300 °C showed no dissipation peak at 20 K and a smaller, broader dissipation peak at ~ 35 K. Both a peak at ~ 20 K and a second, very broad dissipation peak at ~ 90 K were observed in a tantala coating which had crystallised after heat treatment at 800 °C. It is likely that the broad peak centred on 90 K is related to the onset of polycrystalline structure in this coating. The temperature dependence of the loss of an ion-beam sputtered silica coating has also been measured, and a dissipation peak at ~ 17 K was observed. The peak is at a lower temperature, and has a somewhat higher activation energy, than the well-known dissipation peak in bulk silica. Comparison with the literature suggests that the method of fabrication can significantly affect the mechanical dissipation in silica films.

The loss factors measured for silica and tantala coatings have been used to calculate the expected loss in a multi-layer coating. The calculated multi-layer coating loss peaks at ~ 20 K, with a maximum loss of $\sim 9.2 \times 10^{-4}$. This is almost a factor of 2 higher than Yamamoto's multi-layer coating loss factor of $\sim 5 \times 10^{-4}$ measured at 20 K. However, Yamamoto's data are not inconsistent with the presence of a similarly high dissipation peak between 20 and 30 K.

Further investigations of the temperature dependence of the dissipation in multi-layer coatings, and its relationship to the dissipation of the individual coating materials, is an important topic of further research.

In summary, the source of mechanical dissipation in ion-beam sputtered tantala coatings has been probed for the first time and the results suggest that the dissipation mechanism may involve structural reorientations in double-well potentials. It has been shown that the dissipation of the tantala layers is likely to dominate the total dissipation of a multi-layer silica / tantala coating between 10 K and 300 K. Further study of the effects of doping and heat treatment on the low temperature dissipation peaks in tantala may facilitate the development of lower loss coatings for use at both room and cryogenic temperatures, thus enabling the sensitivity of future gravitational wave detectors to be significantly enhanced.

Bibliography

- [1] A. Einstein, *Die Grundlage der allgemeinen Relativitätstheorie*, Annalen der Physik **49** (1916) 769.
- [2] J. Weber, *Detection and generation of gravitational waves*, Physical Review **117** (1960) 306–313.
- [3] R. A. Hulse, J. H. Taylor, *Discovery of a pulsar in a binary system*, The Astrophysical Journal **195** (1975) L51–L53.
- [4] J. H. Taylor, R. A. Hulse, L. A. Fowler, G. E. Gullahron, J. M. Rankin, *Further observations of the binary pulsar PSR 1913 + 16*, The Astrophysical Journal **206** (1976) L53–L58.
- [5] J. H. Taylor, L. A. Fowler, P. M. McCulloch, *Measurements of general relativistic effects in the binary pulsar PSR 1913 + 16*, Nature **277** (1979) 437–440.
- [6] J. H. Taylor, J. M. Weisberg, *A new test of general relativity - Gravitational radiation and the binary pulsar PSR 1913+16*, The Astrophysical Journal **253** (1982) 908–920.
- [7] J. M. Weisberg, J. H. Taylor, *Relativistic binary pulsar B1913+16: Thirty years of observations and analysis*, in: F. A. Rasio, I. H. Stairs (Eds.), Binary Radio Pulsars: Proc. Aspen Conference, Vol. **328** of ASP Conf. Series, Astronomical Society of the Pacific, 2004, pp. 25–31.

-
- [8] H. Lück, et al., *Status of the GEO 600 detector*, Classical and Quantum Gravity **23** (2006) S71–S78.
- [9] A. Abramovici, W. E. Althouse, R. W. P. Drever, Y. Gursel, et al., *LIGO: The laser interferometer gravitational-wave observatory*, Science **256** (1992) 325–333.
- [10] F. Acernese, P. Amico, M. Al-Shourbagy, S. Aoudia, et al., *The status of VIRGO*, Classical and Quantum Gravity **23** (2006) S63–S69.
- [11] R. Takahashi, the TAMA Collaboration, *Status of TAMA300*, Classical and Quantum Gravity **21** (2004) S403–S408.
- [12] B. Abbot, R. Abbot, R. Adhikari, J. Agresti, et al., *Searches for periodic gravitational waves from unknown isolated sources and Scorpius X-1: Results from the second LIGO science run*, Physical Review D **76** (2007) 082001.
- [13] R. X. Xu, *Solid quark stars?*, The Astrophysical Journal Letters **596** (2003) L59–L62.
- [14] B. J. Owen, *Maximum elastic deformations of compact stars with exotic equations of state*, Physical Review Letters **95** (2005) 211101.
- [15] C. Cutler, *Gravitational waves from neutron stars with large toroidal B fields*, Physical Review D **66** (2002) 084025.
- [16] N. Andersson, *A new class of unstable modes of rotating relativistic stars*, The Astrophysical Journal **502** (1998) 708–713.
- [17] B. J. Owen, L. Lindblom, C. Cutler, B. F. Schutz, et al., *Gravitational waves from hot young rapidly rotating neutron stars*, Physical Review D **58** (1998) 084020.

-
- [18] C. Van Den Broeck, *The gravitational wave spectrum of non-axisymmetric, freely precessing neutron stars*, Classical and Quantum Gravity **22** (2005) 1825–1839.
- [19] D. I. Jones, N. Andersson, *Gravitational waves from freely precessing neutron stars*, Monthly Notices of the Royal Astronomical Society **331** (2002) 203–220.
- [20] B. Abbott, R. Abbott, R. Adhikari, P. Ajith, et al., *Beating the spin-down limit on gravitational wave emission from the Crab pulsar*, The Astrophysical Journal Letters **683** (2008) L45–L49.
- [21] L. Bildsten, *Gravitational radiation and rotation of accreting neutron stars*, The Astrophysical Journal Letters **501** (1998) L89–L93.
- [22] R. V. Wagoner, *Gravitational radiation from accreting neutron stars*, The Astrophysical Journal **278** (1984) 345–348.
- [23] S. Chandrasekhar, *Solutions of two problems in the theory of gravitational radiation*, Physical Review Letters **24** (1970) 611–615.
- [24] J. L. Friedman, B. F. Schutz, *Secular instability of rotating Newtonian stars*, The Astrophysical Journal **222** (1978) 281–296.
- [25] B. F. Schutz, *Gravitational-wave sources*, Classical and Quantum Gravity **13** (1996) A219–A238.
- [26] B. Schutz, *Determining the Hubble constant from gravitational wave observations*, Nature **323** (1986) 310–311.
- [27] L. Blanchet, B. R. Iyer, C. M. Will, A. G. Wiseman, *Gravitational waveforms from inspiralling compact binaries to second-post-Newtonian order*, Classical and Quantum Gravity **13** (1996) 575–584.

- [28] C. L. Fryer, D. E. Holz, S. A. Hughes, *Gravitational wave emission from core collapse of massive stars*, The Astrophysical Journal **565** (2002) 430–446.
- [29] A. A. Penzias, R. W. Wilson, *A measurement of excess antenna temperature at 4080 Mc/s*, The Astrophysical Journal **142** (1965) 419–421.
- [30] R. H. Dicke, P. J. E. Peebles, P. G. Roll, D. T. Wilkinson, *Cosmic black-body radiation*, The Astrophysical Journal **142** (1965) 414–419.
- [31] B. Allen, *The stochastic gravity-wave background: Sources and detection*, in: J.-A. Marck, J.-P. Lasota (Eds.), *Relativistic Gravitation and Gravitational Radiation*, Cambridge Univ. Press, Cambridge, 1997, p. 373.
- [32] B. Abbott, R. Abbott, R. Adhikari, J. Agresti, et al., *Searching for a stochastic background of gravitational waves with the laser interferometer gravitational-wave observatory*, The Astrophysical Journal **659** (2007) 918–930.
- [33] R. L. Forward, D. Zipoy, J. Weber, S. Smith, et al., *Upper limit for interstellar millicycle gravitational radiation*, Nature **189** (1961) 473.
- [34] J. Weber, *Observation of the thermal fluctuations of a gravitational-wave detector*, Physical Review Letters **17** (1966) 1228–1230.
- [35] J. Weber, *Gravitational-wave-detector events*, Physical Review Letters **20** (1968) 1307–1308.
- [36] J. Weber, *Evidence for discovery of gravitational radiation*, Physical Review Letters **22** (1969) 1320–1324.
- [37] J. Weber, *Anisotropy and polarization in the gravitational-radiation experiments*, Physical Review Letters **25** (1970) 180–184.

- [38] J. L. Levine, R. L. Garwin, *Absence of gravity-wave signals in a bar at 1695 Hz*, Physical Review Letters **31** (1973) 173–176.
- [39] R. L. Garwin, J. L. Levine, *Single gravity-wave detector results contrasted with previous coincidence detections*, Physical Review Letters **31** (1973) 176–180.
- [40] J. A. Tyson, *Null search for bursts of gravitational radiation*, Physical Review Letters **31** (1973) 326–329.
- [41] V. B. Braginsky, A. B. Manukin, E. I. Popov, V. N. Rudenko, et al., *Upper limit of the density of extraterrestrial gravitational radiation*, Soviet Physics, JETP **39** (1974) 387.
- [42] R. W. P. Drever, J. Hough, R. Bland, G. W. Lessnoff, *Search for short bursts of gravitational radiation*, Nature **246** (1973) 340–344.
- [43] I. S. Heng, E. Daw, J. Giaime, W. O. Hamilton, et al., *Allegro: noise performance and the ongoing search for gravitational waves*, Classical and Quantum Gravity **19** (2002) 1889–1895.
- [44] P. Astone, M. Bassan, P. Bonifazi, P. Carelli, et al., *Long-term operation of the Rome ‘Explorer’ cryogenic gravitational wave detector*, Physical Review D **47** (1993) 362–375.
- [45] M. Bassan, P. Carelli, V. Fafone, Y. Minenkov, et al., *A new capacitive read-out for EXPLORER and NAUTILUS*, Journal of Physics: Conference Series **32** (2006) 89–93.
- [46] I. S. Heng, D. G. Blair, E. M. Ivanov, M. E. Tobar, *Long term operation of a niobium resonant bar gravitational wave antenna*, Physics Letters A **218** (1996) 190–196.

- [47] M. Cerdonio, et al., *The ultracryogenic gravitational-wave detector AURIGA*, Classical and Quantum Gravity **14** (1997) 1491–1494.
- [48] A. Vinante, R. Mezzena, G. A. Prodi, S. Vitale, et al., *Thermal noise in a high Q ultracryogenic resonator*, Review of Scientific Instruments **76** (2005) 074501.
- [49] M. P. McHugh, W. W. Johnson, W. O. Hamilton, J. Hanson, et al., *Calibration of the ALLEGRO resonant detector*, Classical and Quantum Gravity **22** (2005) S965–S973.
- [50] A. de Waard, M. Bassan, Y. Benzaim, V. Fafone, et al., *Preparing for science run 1 of MiniGRAIL*, Classical and Quantum Gravity **23** (2006) S79–S84.
- [51] S. R. Furtado, O. D. Aguiar, D. S. Almeida, *Progress report on the development of a very high sensitivity parametric transducer for the Mario Schenberg Gravitational wave detector*, Journal of Physics: Conference Series **32** (2006) 439–444.
- [52] M. Cerdonio, L. Conti, J. A. Lobo, A. Ortolan, et al., *Wideband dual sphere detector of gravitational waves*, Physical Review Letters **87** (2001) 031101.
- [53] S. E. Whitcomb, *Ground-based gravitational-wave detection: now and future*, Classical and Quantum Gravity **25** (2008) 114013 (15pp).
- [54] M. E. Gertsenshtein, V. I. Pustovoit, *On the detection of low frequency gravitational waves*, Soviet Physics, JETP **16** (1962) 433.
- [55] R. Weiss, *Electromagnetically coupled broadband gravitational antenna*, Quarterly Progress Report 105, Electronics research laboratory, MIT (1972).

-
- [56] G. E. Moss, L. R. Miller, R. L. Forward, *Photon-noise-limited laser transducer for gravitational antenna*, Applied Optics **10** (1971) 2495.
- [57] R. L. Forward, *Wideband laser-interferometer gravitational-radiation experiment*, Physical Review D **17** (1978) 379–390.
- [58] H. Billing, K. Maischberger, A. Rudiger, R. Schilling, et al., *An argon laser interferometer for the detection of gravitational radiation*, Journal of Physics E: Scientific Instruments **12** (1979) 1043–1050.
- [59] R. W. P. Drever, J. R. Pugh, W. A. Edelstein, H. Ward, et al., Proceedings of the Royal Society of London **A368** (1979) 11–18.
- [60] H. Ward, J. Hough, G. P. Newton, B. J. Meers, et al., *Laser interferometric sensing techniques for very small displacements with applications to gravitational radiation detectors*, IEEE Transactions on Instrumentation and Measurement **34**(1985) 261–265.
- [61] D. Shoemaker, R. Schilling, L. Schnupp, W. Winkler, et al., *Noise behavior of the Garching 30-meter prototype gravitational-wave detector*, Physical Review D **38** (1988) 423–432.
- [62] P. R. Saulson, *Terrestrial gravitational noise on a gravitational wave antenna*, Physical Review D **30** (1984) 732–736.
- [63] S. A. Hughes, K. S. Thorne, *Seismic gravity-gradient noise in interferometric gravitational-wave detectors*, Physical Review D **58** (1998) 122002.
- [64] M. Beccaria, et al, *Relevance of Newtonian seismic noise for the VIRGO interferometer sensitivity*, Classical and Quantum Gravity **15** (1998) 3339–3362.
- [65] P. R. Saulson, *Fundamentals of Interferometric Gravitational Wave Detectors*, World Scientific, Singapore, 1994.

- [66] S. Rowan, J. Hough, *Gravitational wave detection by interferometry*, Living Reviews in Relativity **3** (2000) 1.
- [67] M. E. Husman, C. I. Torrie, M. V. Plissi, N. A. Robertson, et al., *Modeling of multistage pendulums: Triple pendulum suspension for GEO 600*, Review of Scientific Instruments **71** (2000) 2546–2551.
- [68] M. V. Plissi, C. I. Torrie, M. E. Husman, N. A. Robertson, et al., *GEO 600 triple pendulum suspension system: Seismic isolation and control*, Review of Scientific Instruments **71** (2000) 2539–2545.
- [69] S. Braccini, C. Bradaschia, R. D. Fabbro, A. D. Virgilio, et al., *Seismic vibrations mechanical filters for the gravitational waves detector VIRGO*, Review of Scientific Instruments **67** (1996) 2899–2902.
- [70] N. A. Robertson, et al., *Seismic isolation and suspension systems for Advanced LIGO*, in: J. Hough, G. Sanders (Eds.), Gravitational Wave and Particle Astrophysics Detectors. Proceedings of the SPIE, Vol. **5500**, 2004, pp. 81–91.
- [71] W. A. Edelstein, J. Hough, J. R. Pugh, W. Martin, *Limits to the measurement of displacement in an interferometric gravitational radiation detector*, Journal of Physics E: Scientific Instruments **11** (1978) 710–712.
- [72] C. M. Caves, *Quantum-mechanical radiation-pressure fluctuations in an interferometer*, Physical Review Letters **45** (1980) 75–79.
- [73] C. M. Caves, *Quantum-mechanical noise in an interferometer*, Physical Review D **23** (1981) 1693–1708.
- [74] W. G. Unruh, in: P. Meystre, M. O. Scully (Eds.), Proceedings of the NATO Advanced Study Institute on Quantum Optics and Experimental General Relativity, Vol. **B94**, Plenum Press, Newyork, 1983, p. 647.
- [75] V. B. Braginsky, Y. I. Vorontsov, *Quantum mechanical limitations in macroscopic experiments and modern experimental technique*, Soviet Physics - Uspekhi **17** (1975) 644–650.

- [76] T. Corbitt, N. Mavalvala, *Review: Quantum noise in gravitational-wave interferometers*, *Journal of Optics B: Quantum and Semiclassical Optics* **6** (2004) S675–S683.
- [77] V. B. Braginsky, F. Y. Khalili, *Nonlinear meter for the gravitational wave antenna*, *Physics Letters A* **218** (1996) 167–174.
- [78] V. B. Braginsky, M. L. Gorodetsky, F. Y. Khalili, *Optical bars in gravitational wave antennas*, *Physics Letters A* **232** (1997) 340–348.
- [79] A. Buonanno, Y. Chen, *Quantum noise in second generation, signal-recycled laser interferometric gravitational-wave detectors*, *Physical Review D* **64** (2001) 042006.
- [80] H. J. Kimble, Y. Levin, A. B. Matsko, K. S. Thorne, et al., *Conversion of conventional gravitational-wave interferometers into quantum non-demolition interferometers by modifying their input and/or output optics*, *Physical Review D* **65** (2001) 022002.
- [81] B. J. Meers, *Recycling in laser-interferometric gravitational-wave detectors*, *Physical Review D* **38** (1988) 2317–2326.
- [82] K. A. Strain, B. J. Meers, *Experimental demonstration of dual recycling for interferometric gravitational-wave detectors*, *Physical Review Letters* **66** (1991) 1391–1394.
- [83] B. Meers, *The frequency response of interferometric gravitational wave detectors*, *Physics Letters A* **142** (1989) 465–470.
- [84] K. A. Strain, *Techniques in laser interferometry for the detection of gravitational radiation*, Ph.D. thesis, University of Glasgow (1990).
- [85] J. Mizuno, K. A. Strain, P. G. Nelson, J. M. Chen, et al., *Resonant sideband extraction: a new configuration for interferometric gravitational wave detectors*, *Physics Letters A* **175** (1993) 273–276.
- [86] H. Grote, A. Freise, M. Malec, G. Heinzel, et al., *Dual recycling for GEO 600*, *Classical and Quantum Gravity* **21** (2004) S473–S480.

- [87] D. Tatsumi, R. Takahashi, K. Arai, N. Nakagawa, et al., *Current status of Japanese detectors*, Classical and Quantum Gravity **24** (2007) S399–S403.
- [88] T. Uchiyama, K. Kuroda, M. Ohashi, S. Miyoki, et al., *Present status of large-scale cryogenic gravitational wave telescope*, Classical and Quantum Gravity **21** (2004) S1161–S1172.
- [89] B. Abbott, R. Abbott, R. Adhikari, J. Agresti, et al., *Search for gravitational waves associated with 39 gamma-ray bursts using data from the second, third, and fourth LIGO runs*, Physical Review D **77** (2008) 062004.
- [90] B. Abbott, R. Abbott, R. Adhikari, J. Agresti, et al., *Implications for the origin of GRB 070201 from LIGO observations*, The Astrophysical Journal **681** (2008) 1419–1430.
- [91] B. Abbott, R. Abbott, R. Adhikari, J. Agresti, et al., *Search for gravitational wave radiation associated with the pulsating tail of the SGR 1806-20 hyperflare of 27 December 2004 using LIGO*, Physical Review D (Particles, Fields, Gravitation, and Cosmology) **76** (2007) 062003.
- [92] Advanced LIGO team, *Advanced LIGO reference design*, LIGO document LIGO M060056-08-M (2007).
- [93] V. B. Braginsky, V. P. Mitrofanov, V. I. Panov, *Systems with small dissipation*, University of Chicago Press, Chicago, 1985.
- [94] W. Winkler, K. Danzmann, A. Rüdiger, R. Schilling, *Heating by optical absorption and the performance of interferometric gravitational-wave detectors*, Physical Review A **44** (1991) 7022–7036.
- [95] S. Rowan, R. L. Byer, M. M. Fejer, R. Route, et al., *Test mass materials for a new generation of gravitational wave detectors*, Proceedings of SPIE **292** (2003) 4856.
- [96] R. W. P. Drever, *Concepts for extending the ultimate sensitivity of interferometric gravitational wave detectors using non-transmissive optics*

- with diffractive or holographic coupling*, in: M. Keiser, R. T. Jantzen (Eds.), *Proceedings of the Seventh Marcel Grossman Meeting on General Relativity*, World Scientific, 1995, pp. 1401–1406.
- [97] K.-X. Sun, R. L. Byer, *All-reflective Michelson, Sagnac, and Fabry–Perot interferometers based on grating beam splitters*, *Optics Letters* **23** (1998) 567–569.
- [98] *Einstein Gravitational Wave Telescope*, proposal to the European Commission, Framework Programme 7 (2007), <http://www.ego-gw.it/ILIAS-GW/FP7-DS/fp7-DS.htm>.
- [99] R. Brown, *A brief account of microscopical observations made in the months of June, July and August, 1827, on the particles contained in the pollen of plants; and on the general existence of active molecules in organic and inorganic bodies.*, *Philosophical Magazine* **4** (1828) 161–173.
- [100] M. Gouy, *Note sur le mouvement brownien*, *Journal de Physique* **7** (1888) 561.
- [101] F. M. Exner, *Notiz. zu. Brown's molecularbewegung*, *Annalen der Physik* **2** (1900) 843.
- [102] A. Einstein, *On the movement of small particles suspended in a stationary liquid demanded by the molecular-kinetic theory of heat*, *Annalen der Physik* **17** (1900) 549.
- [103] J. B. Johnson, *Thermal agitation of electricity in conductors*, *Nature* **119** (1927) 50.
- [104] J. B. Johnson, *Thermal agitation of electricity in conductors*, *Physical Review* **32** (1928) 97–109.
- [105] H. Nyquist, *Thermal agitation of electric charge in conductors*, *Physical Review* **32** (1928) 110–113.
- [106] H. B. Callen, T. A. Welton, *Irreversibility and generalized noise*, *Physical Review* **83** (1951) 34–40.

- [107] R. F. Greene, H. B. Callen, *On the formalism of thermodynamic fluctuation theory*, Physical Review **83** (1951) 1231–1235.
- [108] H. B. Callen, R. F. Greene, *On a theorem of irreversible thermodynamics*, Physical Review **86** (1952) 702–710.
- [109] G. Cagnoli, L. Gammaitoni, J. Hough, J. Kovalik, et al., *Very high Q measurements on a fused silica monolithic pendulum for use in enhanced gravity wave detectors*, Physical Review Letters **85** (2000) 2442–2445.
- [110] A. Nowick, B. Berry, *Anelastic Relaxation in Crystalline Solids*, Academic Press, New York, 1972.
- [111] P. Saulson, *Thermal noise in mechanical experiments*, Physical Review D **42** (1990) 2437.
- [112] S. Arrhenius, *On the reaction velocity of the inversion of cane sugar by acids*, Zeitschrift für physikalische Chemie **4** (1889) 226.
- [113] C. Zener, *Elasticity and Anelasticity in Metals*, University of Chicago Press, 1948.
- [114] A. L. Kimball, D. E. Lovell, *Internal friction in solids*, Physical Review **30** (1927) 948–959.
- [115] T. J. Quinn, C. C. Speake, L. M. Brown, *Materials problems in the construction of long-period pendulums*, Philosophical Magazine A **65** (1992) 261–276.
- [116] P. R. Saulson, R. T. Stebbins, F. D. Dumont, S. E. Mock, *The inverted pendulum as a probe of anelasticity*, Review of Scientific Instruments **65** (1994) 182–191.
- [117] Y. Huang, P. R. Saulson, *A method for measuring the dependence of internal friction on strain*, Review of Scientific Instruments **65** (1994) 2102–2106.

- [118] K. Yuki, M. A. Barton, K. N., K. Kuroda, *Measuring the anelasticity of Cu-Be film under tensile stress using the X-pendulum*, Physics Letters A **223** (1996) 149–154.
- [119] J. L. Routbort, H. S. Sack, *Background internal friction of some pure metals at low frequencies*, Journal of Applied Physics **37** (1966) 4803–4805.
- [120] G. I. Gonzalez, P. R. Saulson, *Brownian motion of a mass suspended by an anelastic wire*, The Journal of the Acoustical Society of America **96** (1994) 207–212.
- [121] C. Zener, *Internal friction in solids I. Theory of internal friction in reeds*, Physical Review, **52**, (1937) 230–235.
- [122] C. Zener, *Internal friction in solids II. General theory of thermoelastic internal friction*, Physical Review **53** (1938) 90–99.
- [123] G. Cagnoli, P. A. Willems, *Effects of nonlinear thermoelastic damping in highly stressed fibers*, Physical Review B **65** (2002) 174111.
- [124] A. Gillespie, F. Raab, *Thermally excited vibrations of the mirrors of laser interferometer gravitational-wave detectors*, Physical Review D **52**, (1995) 577–585.
- [125] Y. Levin, *Internal thermal noise in the LIGO test masses: A direct approach*, Physical Review D **57** (1998) 659.
- [126] F. Bondu, P. Hello, Y.-Y. Vinet, *Mirror thermal noise in interferometric gravitational wave detectors*, Physics Letters A **246** (1998) 227–236.
- [127] Y. T. Liu, K. S. Thorne, *Thermoelastic noise and homogeneous thermal noise in finite sized gravitational-wave test masses*, Physical Review D **62** (2000) 122002.
- [128] G. Harry, A. Gretarsson, P. Saulson, S. Kittelberger, et al., *Thermal noise in interferometric gravitational wave detectors due to dielectric optical coatings*, Classical and Quantum Gravity **19** (2002) 897–917.

- [129] D. R. M. Crooks, P. Sneddon, G. Cagnoli, J. Hough, et al., *Excess mechanical loss associated with dielectric mirror coatings on test masses in interferometric gravitational wave detectors*, *Classical and Quantum Gravity* **19** (2002) 883–896.
- [130] S. D. Penn, P. H. Sneddon, H. Armandula, J. C. Betzwieser, et al., *Mechanical loss in tantala/silica dielectric mirror coatings*, *Classical and Quantum Gravity* **20** (2003) 2917–2928.
- [131] D. Crooks, G. Cagnoli, M. Fejer, A. Gretarsson, et al., *Experimental measurements of coating mechanical loss factors*, *Classical and Quantum Gravity* **21** (2004) 1059–1065.
- [132] A. Ageev, B. C. Palmer, A. Felice, S. D. Penn, et al., *Very high quality factor measured in annealed fused silica*, *Classical and Quantum Gravity* **21** (2004) 3887–3892.
- [133] N. Nakagawa, A. M. Gretarsson, E. K. Gustafson, M. M. Fejer, *Thermal noise in half-infinite mirrors with nonuniform loss: A slab of excess loss in a half-infinite mirror*, *Physical Review D* **65** (2002) 102001.
- [134] K. Thorne, *Beam reshaping to reduce thermoelastic noise*, LIGO document LIGO-G000223-00-D (2000).
URL <http://www.ligo.caltech.edu/docs/G/G000223-00.pdf>
- [135] E. D’Ambrosio, *Nonspherical mirrors to reduce thermoelastic noise in advanced gravitational wave interferometers*, *Physical Review D* **67** (2003) 102004.
- [136] E. D’Ambrosio, R. O’Shaughnessy, K. Thorne, P. Willems, et al., *Advanced LIGO: non-Gaussian beams*, *Classical and Quantum Gravity* **21** (2004) S867–S873.
- [137] R. O’Shaughnessy, S. Strigin, S. Vyatchanin, *The implications of Mexican-hat mirrors: calculations of thermoelastic noise and interferometer sensitivity to perturbation for the Mexican-hat-mirror proposal for advanced LIGO*, gr-qc/0409050. (2004).
URL <http://arxiv.org/abs/gr-qc/0409050>

- [138] M. Bondarescu, K. S. Thorne, *New family of light beams and mirror shapes for future LIGO interferometers*, Physical Review D **74** (2006) 082003.
- [139] J. Agresti, *Researches on non-standard optics for advanced G.W. interferometers*, LIGO document LIGO-T040225-00-R (2005).
URL <http://www.ligo.caltech.edu/docs/T/T040225-00.pdf>
- [140] V. B. Braginsky, M. L. Gorodetsky, S. P. Vyatchanin, *Thermodynamical fluctuations and photo-thermal shot noise in gravitational wave antennae*, Physics Letters A **264** (1999) 1–10.
- [141] V. B. Braginsky, S. P. Vyatchanin, *Thermodynamical fluctuations in optical mirror coatings*, Physics Letters A **312** (2003) 244–255.
- [142] M. Fejer, S. Rowan, G. Cagnoli, D. Crooks, et al., *Thermoelastic dissipation in inhomogeneous media: Loss measurements and displacement noise in coated test masses for interferometric gravitational wave detectors*, Physical Review D **70** (2004) 082003.
- [143] J. E. Logan, J. Hough, N. A. Robertson, *Aspects of the thermal motion of a mass suspended as a pendulum by wires*, Physics Letters A **183** (1993) 145–152.
- [144] D. H. Santamore, Y. Levin, *Eliminating thermal violin spikes from LIGO noise*, Physical Review D **64** (2001) 042002.
- [145] S. Goßler, G. Cagnoli, D. R. M. Crooks, H. Lück, et al., *Damping and tuning of the fibre violin modes in monolithic silica suspensions*, Classical and Quantum Gravity **21** (2004) S923–S933.
- [146] S. Rowan, J. Hough, D. R. M. Crooks, *Thermal noise and material issues for gravitational wave detectors*, Physics Letters A **347** (2005) 25–32.
- [147] D. Gwo, *Ultra-precision bonding for cryogenic fused silica optics*, in: J. Heaney, L. Burriesci (Eds.), Proc. of SPIE, Cryogenic optical systems and instruments VIII, Vol. **3435**, 1998, p. 136.

- [148] D. Gwo, U.S. Patent no. US 6,284,085 b1.
- [149] D. Gwo, *Hydroxide-catalysed bonding*, U.S. Patent no. US 6,548,176 B1.
- [150] S. Twyford, S. Rowan, J. Hough, D. Gwo, *Losses associated with the bonding of fused quartz fibres to fused quartz test masses*, in: G. P. E. Coccia, G. Veneziano (Eds.), *Proceedings from the Second Edoardo Amaldi Conference on Gravitational Waves*, Vol. 4, World Scientific, Singapore, 1997, pp. 479–484.
- [151] S. Rowan, S. M. Twyford, J. Hough, D. H. Gwo, *Mechanical losses associated with the technique of hydroxide-catalysis bonding of fused silica*, *Physics Letters A* **246** (1998) 471–476.
- [152] P. Amico, L. Bosi, L. Carbone, L. Gammaitoni, et al., *Fused silica suspension for the VIRGO optics: status and perspectives*, *Classical and Quantum Gravity* **19** (2002) 1669–1674.
- [153] K. Danzmann, for the LISA Study Team, *LISA - an ESA cornerstone mission for a gravitational wave observatory*, *Classical and Quantum Gravity* **14** (1997) 1399–1404.
- [154] K. Danzmann, A. Rudiger, *LISA technology - concept, status, prospects*, *Classical and Quantum Gravity* **20** (2003) S1–S9.
- [155] C. Cutler, K. S. Thorne, *An overview of gravitational-wave sources*, in: N. Bishop (Ed.), *Proceedings of the GR16 Conference on General Relativity and Gravitation*, World Scientific, Singapore, 2002.
- [156] P. McNamara, S. Vitale, K. Danzmann, (on behalf of the LISA Pathfinder Science Working Team), *LISA Pathfinder*, *Classical and Quantum Gravity* **25** (2008) 114034 (8pp).
- [157] S. Anza, M. Armano, E. Balaguer, M. Benedetti, et al., *The LTP experiment on the LISA Pathfinder mission*, *Classical and Quantum Gravity* **22** (2005) S125–S138.

- [158] E. J. Elliffe, J. Bogenstahl, A. Deshpande, J. Hough, et al., *Hydroxide-catalysis bonding for stable optical systems for space*, Classical and Quantum Gravity **22** (2005) S257–S267.
- [159] S. Reid, *Studies of materials for future ground-based and space-based interferometric gravitational wave detectors*, Ph.D. thesis, University of Glasgow (2006).
- [160] P. Murray, *Measurement of the mechanical loss of test mass materials for advanced gravitational wave detectors*, Ph.D. thesis, University of Glasgow (2008).
- [161] V. Davydov, A. Kiselev, L. Zhuravlev, *Study of the surface and bulk hydroxyl groups of silica by infrared spectra and D₂O-exchange*, Transactions of the Faraday Society **60** (1964) 2254–2264.
- [162] R. K. Iler, *The Chemistry of Silica*, John Wiley and Sons, 1979.
- [163] S. Reid, G. Cagnoli, E. Elliffe, J. Faller, et al., *Influence of temperature and hydroxide concentration on the settling time of hydroxy-catalysis bonds*, Physics Letters A **363** (2007) 341–345.
- [164] K. A. Connors, *Chemical Kinetics: Study of Reaction Rates in Solution*, John Wiley & Sons, 1998.
- [165] J. H. van't Hoff, *Etudes de dynamique chimique*, J. Muller, Amsterdam, 1884.
- [166] A. W. Heptonstall, *Characterisation of mechanical loss in fused silica ribbons for use in gravitational wave detector suspensions*, Ph.D. thesis, University of Glasgow (2004).
- [167] S. Rowan, R. Hutchins, A. McLaren, N. A. Robertson, et al., *The quality factor of natural fused quartz ribbons over a frequency range from 6 to 160 Hz*, Physics Letters A **227** (1997) 153–158.
- [168] N. W. McLachlan, *Theory of Vibrations*, Dover, 1952.

- [169] D. J. McLachlan, L. L. Chamberlain, *Atomic vibrations and melting point in metals*, Acta Metallurgica **12** (1964) 571–576.
- [170] S. D. Penn, A. Ageev, D. Busby, G. M. Harry, et al., *Frequency and surface dependence of the mechanical loss in fused silica*, Physics Letters A **352** (2006) 3–6.
- [171] B. S. Lunin, *Physical and Chemical Bases for the Development of Hemispherical Resonators for Solid-State Gyroscopes*, Moscow Aviation Institute, Moscow, 2005.
- [172] O. L. Anderson, H. E. Bommel, *Ultrasonic absorption in fused silica at low temperatures and high frequencies*, Journal of the American Ceramic Society **38** (1955) 125–131.
- [173] J. Wiedersich, S. V. Adichtchev, E. Rössler, *Spectral shape of relaxations in silica glass*, Physical Review Letters **84** (2000) 2718–2721.
- [174] T. J. Quinn, C. C. Speake, R. S. Davis, W. Tew, *Stress dependent damping in Cu-Be torsion and flexure suspensions at stresses up to 1.1GPa*, Physics Letters A **197** (1995) 197–208.
- [175] S. M. Tywford, *Developements towards low loss suspensions for laser interferometric gravitational wave detectors*, Ph.D. thesis, University of Glasgow (1998).
- [176] A. Heptonstall, Private communication, 2007.
- [177] R. Weiss, *Note on Electrostatics in the LIGO suspensions*, LIGO technical note T960137-00-E (1995).
- [178] M. Hewitson, K. Danzmann, H. Grote, S. Hild, et al., *Charge measurement and mitigation for the main test masses of the GEO 600 gravitational wave observatory*, Classical and Quantum Gravity **24** (2007) 6379–6391.
- [179] V. P. Mitrofanov, L. G. Prokhorov, K. V. Tokmakov, *Variation of electric charge on prototype of fused silica test mass of gravitational wave antenna*, Physics Letters A **300** (2002) 370–374.

- [180] V. Mitrofanov, L. Prokhorov, K. Tokmakov, P. Willems, *Investigation of effects associated with variation of electric charge on a fused silica test mass*, Classical and Quantum Gravity **21** (2004) S1083–S1089.
- [181] V. Braginsky, O. Ryazhskaya, S. Vyatchanin, *Notes about noise in gravitational wave antennas created by cosmic rays*, Physics Letters A **350** (2006) 1–4.
- [182] S. Rowan, S. Twyford, R. Hutchins, J. Hough, *Investigations into the effects of electrostatic charge on the Q factor of a prototype fused silica suspension for use in gravitational wave detectors*, Classical and Quantum Gravity **14** (1997) 1537–1541.
- [183] V. P. Mitrofanov, N. A. Styazhkina, K. V. Tokmakov, *Damping of the test mass oscillations caused by multistrip electrostatic actuator*, Physics Letters A **278** (2000) 25–29.
- [184] M. J. Mortonson, C. C. Vassiliou, D. J. Ottaway, D. H. Shoemaker, et al., *Effects of electrical charging on the mechanical Q of a fused silica disk*, Review of Scientific Instruments **74** (2003) 4840–4845.
- [185] D. Ugolini, R. McKinney, G. M. Harry, *Developing an optical chopper-modulated capacitive probe for measuring surface charge*, Review of Scientific Instruments **78** (2007) 046102.
- [186] R. S. Amin, *Brief of the May 2006 LIGO charging event*, LIGO document G070572-00 (2007).
URL <http://www.ligo.caltech.edu/docs/G/G070572-00/G070572-00.pdf>
- [187] A. L. Dawar, J. C. Joshi, *Review Semiconducting transparent thin films: their properties and applications*, Journal of Materials Science **19** (1984) 1–23.
- [188] J. B. Mooney, S. B. Radding, *Spray pyrolysis processing*, Annual Review of Materials Science **12** (1982) 81–101.

- [189] J. F. Jordan, S. P. Albright, *Large-area CdS/CdTe photovoltaic cells*, Bulletin of Materials Science **23** (1988) 107–113.
- [190] J. Hirunlabh, S. Suthateeranet, K. Kirtikara, R. D. Pynn, *Development of a Spray Pyrolysis Coating Process for Tin Oxide Film Heat Mirrors*, Thammasat International J. of Science and Technology **3** (1998) 10–20.
- [191] J. M. Mochel, U.S. Patents 2,564,707; 2,564,987; 2,564,709; 2,564,710; 2,564,708; 2,564,706 (1951).
- [192] A. E. Rakhshani, Y. Makdisi, H. A. Ramazaniyan, *Electronic and optical properties of fluorine-doped tin oxide films*, Journal of Applied Physics **83** (1998) 1049–1057.
- [193] T. Fukano, T. Motohiro, T. Ida, H. Hashizume, *Ionization potentials of transparent conductive indium tin oxide films covered with a single layer of fluorine-doped tin oxide nanoparticles grown by spray pyrolysis deposition*, Journal of Applied Physics **97** (2005) 084314.
- [194] T. Ishida, H. Kouno, H. Kobayashi, Y. Nakato, *Dependence of photovoltages of spray-deposited indium tin oxide/silicon oxide/silicon junction solar cells on spray solvents*, Journal of the Electrochemical Society **141** (1994) 1357–1361.
- [195] K. S. Shamala, L. C. S. Murthy, K. N. Rao, *Studies on tin oxide films prepared by electron beam evaporation and spray pyrolysis methods*, Bulletin of Materials Science **27** (2004) 295–301.
- [196] A. Markosyan, Private communication, 2007.
- [197] D. R. M. Crooks, *Mechanical loss and its significance in the test mass mirrors of gravitational wave detectors*, Ph.D. thesis, University of Glasgow (2003).
- [198] D. Crooks, Private communication, 2005.
- [199] P. Lemoine, D. Mariotti, P. Maguire, J. A. McLaughlin, *Depth-sensitive analysis of a degraded tin oxide electrode surface in a plasma device application*, Thin Solid Films **401** (2001) 196–202.

- [200] V. I. Mitrokhin, S. I. Rembeza, E. S. Rembeza, A. A. Rudenko, *Inelastic relaxation in tin dioxide thin films*, Solid State Phenomena **115** (2006) 275–278.
- [201] H. A. MacLeod, *Thin-film Optical Filters*, Adam Hilger Ltd., Bristol, 1986.
- [202] O. S. Heavens, *Thin Film Physics*, Methuen and Co. Ltd, London, 1970.
- [203] R. P. Netterfield, M. Gross, F. N. Baynes, K. L. Green, et al., *Low mechanical loss coatings for LIGO optics: progress report*, in: M. L. Fulton, J. D. T. Kruschwitz (Eds.), Proceedings of SPIE, Advances in Thin-Film Coatings for Optical Applications II, Vol. **5780**, 2005, p. 58700.
- [204] K. Seshan (Ed.), *Handbook of Thin-Film Deposition Processes and Techniques - Principles, Methods, Equipment and Applications*, William Andrew Publishing/Noyes, Norwich, NY, 2002.
- [205] N. A. Robertson, K. A. Strain, J. Hough, *Measurements of losses in high reflectance mirrors coated for $\lambda = 514.5$ nm*, Optics Communications **69** (1989) 345–348.
- [206] K. Numata, A. Kemery, J. Camp, *Thermal-noise limit in the frequency stabilization of lasers with rigid cavities*, Physical Review Letters **93** (2004) 250602.
- [207] M. Notcutt, L.-S. Ma, A. D. Ludlow, S. M. Foreman, et al., *Contribution of thermal noise to frequency stability of rigid optical cavity via Hertz-linewidth lasers*, Physical Review A **73** (2006) 031804.
- [208] R. J. Rafac, B. C. Young, J. A. Beall, W. M. Itano, et al., *Sub-dekahertz ultraviolet spectroscopy of $^{199}\text{Hg}^+$* , Physical Review Letters **85** (2000) 2462–2465.
- [209] A. D. Ludlow, M. M. Boyd, T. Zelevinsky, S. M. Foreman, et al., *Systematic study of the ^{87}Sr clock transition in an optical lattice*, Physical Review Letters **96** (2006) 033003.

- [210] S. A. Webster, M. Oxborrow, P. Gill, *Subhertz-linewidth Nd:YAG laser*, Optics Letters **29** (2004) 1497–1499.
- [211] F. Schmidt-Kaler, S. Gulde, M. Riebe, T. Deuschle, et al., *The coherence of qubits based on single Ca^+ ions*, Journal of Physics B: Atomic, Molecular and Optical Physics **36** (2003) 623–636.
- [212] D. R. M. Crooks, G. Cagnoli, M. M. Fejer, G. Harry, et al., *Experimental measurements of mechanical dissipation associated with dielectric coatings formed using SiO_2 , Ta_2O_5 and Al_2O_3* , Classical and Quantum Gravity **23** (2006) 4953–4965.
- [213] J. Agresti, G. Castaldi, R. DeSalvo, V. Galdi, et al., *Optimized multilayer dielectric mirror coatings for gravitational wave interferometers*, in: M. J. Ellison (Ed.), Proceedings of SPIE, Advances in Thin-Film Coatings for Optical Applications III, Vol. **6266**, 2006, p. 628608.
- [214] G. M. Harry, M. R. Abernathy, A. E. Becerra-Toledo, H. Armandula, et al., *Titania-doped tantala/silica coatings for gravitational-wave detection*, Classical and Quantum Gravity **24** (2007) 405–415.
- [215] Laboratoire des Matériaux Avancés, LMA, CNRS-IN2P3, France, <http://lma.in2p3.fr>.
- [216] P. Holt, *Quantifying surface loss of mechanically polished silica cantilevers*, Master's thesis, University of Glasgow (2007).
- [217] A. Heptonstall, G. Cagnoli, J. Hough, S. Rowan, *Characterisation of mechanical loss in synthetic fused silica ribbons*, Physics Letters A **354** (2006) 353.
- [218] A. Gretarsson, G. Harry, *Dissipation of mechanical energy in fused silica fibers*, Review of Scientific Instruments **70** (1999) 4081–4087.
- [219] <http://einstein.stanford.edu/content/topics/pg4.html>.
- [220] N. Morgado, Private Communication (2006).

- [221] H. E. Bömmel, W. P. Mason, A. W. Warner, *Dislocations, relaxations, and anelasticity of crystal quartz*, Physical Review **102** (1956) 64–71.
- [222] R. E. Strakna, *Investigation of low temperature ultrasonic absorption in fast-neutron irradiated SiO₂ glass*, Physical Review **123** (1961) 2020–2026.
- [223] K. A. Topp, D. G. Cahill, *Elastic properties of several amorphous solids and disordered crystals below 100 K*, Zeitschrift für Physik B **101** (2004) 235–245.
- [224] D. H. McGuigan, C. C. Lam, R. Q. Gram, A. W. Hoffman, et al., *Measurements of the mechanical Q of single-crystal silicon at low temperatures*, Journal of Low Temperature Physics **30** (1978) 621–629.
- [225] K. Y. Yasamura, T. D. Stowe, E. M. Chow, T. Pfafman, et al., *Quality factors in micron and sub-micron thick cantilevers*, Journal of Microelectromechanical Systems **9** (2000) 117.
- [226] K. Yamamoto, S. Miyoki, T. Uchiyama, H. Ishitsuka, et al., *Measurement of the mechanical loss of a cooled reflective coating for gravitational wave detection*, Physical Review D **74** (2006) 022002.
- [227] S. Reid, G. Cagnoli, D. R. M. Crooks, J. Hough, et al., *Mechanical dissipation in silicon flexures*, Physics Letters A **351** (2006) 205.
- [228] Y. S. Touloukian, E. H. Buyco, *Thermo-physical Properties of Matter*, Plenum, New York, 1970.
- [229] P. Martin, et al., *Mechanical and optical properties of thin films of tantalum pentoxide deposited by ion-assisted deposition*, in: J. S. P. Townsend, T. Weihs, P. Borgesen (Eds.), Materials Research Society Symposium Proceedings, Vol. **308**, Materials Research Society, 1993, pp. 583–588.
- [230] G. Cannelli, R. Cantelli, F. Cordero, F. Trequattrini, M. Ferretti, *Strong dependence on doping of a low-activation-energy relaxation process in YBa₂Cu₃O_{6+x}: Possible polaron relaxation*, Physical Review B **54** (1996) 15537–15542.

- [231] M. E. Fine, H. van Duyn, N. T. Kenney, *Low-Temperature internal friction and elasticity effects in vitreous silica*, Journal of Applied Physics **25** (1954) 402–405.
- [232] M. R. Vukcevic, *A new interpretation of the anomalous properties of vitreous silica*, Journal of Non-Crystalline Solids **11** (1972) 25–63.
- [233] K. S. Gilroy, W. A. Phillips, *An asymmetric double-well potential model for structural relaxation processes in amorphous materials*, Philosophical Magazine B **43** (1981) 735–746.
- [234] W. A. Phillips, *Tunneling states in amorphous solids*, Journal of Low Temperature Physics **7** (1972) 351–360.
- [235] P. W. Anderson, *Anomalous low-temperature thermal properties of glasses and spin glasses*, Philosophical Magazine **25** (1972) 1–9.
- [236] J. Y. Duquesne, G. Bellessa, *Internal-friction peak in amorphous selenium at low temperature*, Journal of Physics C: Solid State Physics **13** (1980) L215–L219.
- [237] E. Chalkley, Ph.D. thesis, University of Glasgow (in preparation).
- [238] M. Goldstein, *Amorphous Materials*, Wiley, New York, 1970.
- [239] D. G. Cahill, J. E. V. Cleve, *Torsional oscillator for internal friction data at 100 kHz*, Review of Scientific Instruments **60** (1989) 2706–2710.
- [240] J. E. V. Cleve, A. K. Raychaudhuri, R. O. Pohl, *Glasslike elastic properties in the ω - β alloys*, Zeitschrift für Physik B **93** (1994) 479–490.
- [241] J. T. Krause, Variables affecting the acoustic loss and velocity of vitreous silica from 4 to 300k, Journal of Applied Physics **42** (1971) 3035–3037.
- [242] Materials Science and Engineering Division, CSIRO, Bradfield Road, West Lindfield, Sydney, NSW, 2070, Australia, <http://www.csiro.au/>.
- [243] R. Bassiri, *Probing the microscopic properties of the materials used for advanced gravitational wave detectors*, First year PhD report, University of Glasgow (2008).

-
- [244] B. E. White, R. O. Pohl, *Internal friction of subnanometer α -SiO₂ films*, Physical Review Letters **75** (1995) 4437–4439.
- [245] G. K. White, *Thermal expansion of reference materials: copper, silica and silicon*, Journal of Physics D: Applied Physics **6** (1973) 2070–2078.
- [246] S. Penn, Private communication, 2008.
- [247] B. E. White, R. O. Pohl, *How do two-level-systems come about?*, Physica B **219-220** (1996) 267–269.
- [248] R. M. Jones, *Mechanics of Composite Materials*, Scripta Book Company,, Washington DC, 1975.
- [249] K. Yamamoto, Private communication, 2008.